eman ta zabal zazu

Universidad del País Vasco
Euskal Herriko Unibertsitatea

NAZIOARTEKO BIKAINTASUN CAMPUSA
CAMPUS DE EXCELENCIA INTERNACIONAL

Topological quantum chemistry description of interacting-electron systems

Department of Physics
Faculty of Science and Technology

Mikel Iraola Iñurrieta

Supervised by
Professor Maia García Vergniory
Professor Juan Luis Mañes Palacios

Donostia-San Sebastián
January 31, 2023

Contents

Acknowledgments

"Seme baten etorkizuna beti da amaren lanaren fruitu", Napoleonen hitzen arabera. Eskerrik asko aita eta ama, nigan konfidantza izateagatik eta hainbeste zaintzeagatik. Idazluma nire eskuek mugitu duten arren, zuena da lan honen emaiza, nirea bezainbeste. Eskerrik asko nire anai Josuri, jaio nintzenetik alboan egoteagatik. Agur bero bat Iraola eta Iñurrieta familiako kide guztiei, eman didazuen maitasunagatik: iraganaren parte zaretenei, alde batetik; ni bezalaxe oraina zaretenei, bestetik; geure saihetsetatik jaio eta etorkizuna osatuko duzuenei, azkenik.

Muchas gracias a mis supervisores por creer en mí, por compartir conmigo su conocimiento y por tener conmigo una paciencia infinita. Maia, ojalá llegue algún día a desarrollar la perspicacia que manejas y el coraje que despliegas. Nunca olvidaré que si he podido desarrollar esta tesis de forma digna, es gracias a ti. Juan Luis, siempre admiraré tu visión para abordar los misterios de la naturaleza. Espero que algun día mi intuición para la física alcance a ser mitad de poderosa que la tuya. Inscribirme en tus asignaturas ha sido, sin duda, la mejor decisión que he tomado en mi carrera como estudiante y científico.

I would like to thank the DIPC for its generosity, for giving me access to the marvelous formation courses they organize (thank you, Aitzol!), and for accepting me in such a nice research environment.

I want to thank the bright scientists I have had the pleasure to collaborate with during these work. Thank you Dr. Roser Valentí for directing my international stay, and for sharing with me your wide knowledge. Thank you Dr. Titus Neupert, Dr. Barry Bradlyn, Dr. Frank Pollman and the rest of scientists who have given me academic advice. Thank you Dr. Stepan Tsirkin for your patience and for letting me work with you. I have learnt a lot from you and I am sure I will continue doing so. I would like to thank also all the people I have met during my stays abroad, to Marti in particular, for her advice and for being so kind with me. I hope she will enjoy the sets in this thesis; that in Eq. (4.21) looks particularly nice...

Me gustaría dar las gracias a los demás compañeros del grupo de investigación. Gracias Iñigo y Chiara por estar aquí desde el principio, Martín, Mikel, Irián y Antonio.

También quiero agradecer a toda la gente con la que he coincidido en el DIPC, especialmente a los compañeros de despacho: María, Irene, Nathan, "the Dutchman" Tim. Gracias Sofía por ser como una hermana mayor en el doctorado y por compartir conmigo tantos "trucos".

Labur geratuko nintzateke paragrafo oso bat zuri dedikatuko ez banizu, Unai. Duela 9 urte ezagutu genuen elkar graduan hasi ginenean eta orduz geroztik, elkarrekin egin dugu bide hau. Elkarrekin masterrean, elkarrekin doktoregoan. Benetako plazera izan da kafe garaian zurekin euskaraz mintzatzea, euskaraz bazkaltzea, momentu zail hauetan zu lagun izatea eta termodinamikari buruz luze aritzea. Orain bide desberdinak hartuko

ditugun arren, Donostia eta Zarautz beti egongo dira gertu. Zorte on bizitzan, lagun!

Ez litzateke zilegi gradu eta masterreko kideei hitzik ez dedikatzea. Herabe abiatu ginen fisikaren eremuan 2013an eta aurrez aurre egin genuen topo errealitatearekin. Benetan bizigarria izan zen egunez egunekoaren deman zuen alboan esertzea eta zuen bromekin barre egitea. Eskerrik asko, bereziki, Iban Turumbay eta Jon Zurutuzari. Lagun eta euskarri bikainak izan zineten eta egiaz diotsuet zuek zaretela graduari buruz dudan oroitzapen onena.

Ni puedo, ni quiero olvidarme de mis compañeros del Karate. Hemos compartido tantas horas descalzos sobre el tatami. Me habéis visto crecer y algunos habéis crecido conmigo. Me ha aportado tanto el karate y me habéis aportado tanto vosotros, que no me imagino mi vida sin este arte y sin vuesta compañía. Muchas gracias Jesús, Javier, Agus, Patricia, David, Dani, Markel, Nahia, Maddi, Carlos, Ekain, Sandra y todos a los que no puedo mencionar por culpa de mi limitada memoria. Aunque las circustancias de la vida puedan separarnos por algún tiempo, no tengáis la menor duda de que, siempre que esté en Donostia, me tendréis en el tatami.

Eskerrik asko, bihotz-bihotzez, kuadrilako lagunei. Eskerri kasko Ander, Ekain, Jon Beñat, Harri, Nabas eta Unai, naizen bezala onartzeagatik. Aspalditik ezagutzen dugu elkar eta hamaika bizitakoak gara. Espero dezagun beste hainbeste bizitzeko aukera izatea. Nahiz eta balitekeen bizitzaren joan-etorriek munduan zehar sakabanatzea, jakin ezazue beti izango duzuela teilatu bat ni nagoen tokian. Besarkada bero bat Nagore, Laura, Leire eta Iñigori. Gracias Iker por mostrarme la importancia de relativizar. Es, sin duda, uno de los mejores consejos que me han dado nunca.

Testu honetako hitz garrantzitsuenak idazteko garaia heldu da, bidean nenbilela joan direnei eskerrak emateko garaia, alegia. Arbasoei zuzenduriko hitz hauek arbasoen hizkuntzan idatziko ditut, nire erraietatik irteten diren hitzak baitira:

Beti izango dut gogoan zure eskuzabaltasuna, osaba. Zure etxeko ateak zabalik izan dituzu beti guretzat eta ez gaituzu inoiz esku hutsik utzi. Eskerrik asko, amona Karmen. Argi utzi diguzu ez direla gure lorpen pertsonalak handi egiten gaituztenak, ingurukoak geure buruaren gainetik maitatzea baizik. Beti konformatu zinen gutxirekin, zenuena trukean ezer espero gabe emanez, etxekoek izan genezan. Zaratarik egin gabe. Lurrak hartu bazaitu ere, zure maitasunak beti argi bitza gure bideak.

Eskerrik asko, amona Mari Tere. Errukiaren pertsonifikazioa izan zinen, inoiz agortzen ez den errukiaren iturria. Beti jarri zinen gure lekuan eta beti barkatu zenituen gure bekatuak, asko edo larriak izanda ere. Zentzuak huts egiten ez badit behintzat, ez ditut inoiz ahaztuko zurekin igarotako udara baketsuak, ezta zein eztiki zaindu gintuzun ere. Beti izan da estua zurekin izan dudan lotura, heriotzak ere apurtuko ez duen lotura. Eskerrik asko denagatik.

Xala. Zenbat oroitzen naizen zutaz. Ez dakit zerurik existitzen ote den, baina ez dut zu onartu ez zaituen zeru batean sinisten. Baldintzarik gabeko maitasuna, leialtasun irmoa eta niganako konfidantza itsua izan zenituen, eta hau ezin dut beste inori buruz esan. Ez izan zalantzarik lortu dudan guztia emango nukeela horrek nire alb-

ora bueltatuko bazintu, baina “lur bortitz honen azpitik berriz itzultzerik ez da asmatu oraino”. Nire besoetan utzi zenuen mundu hau, nire arimaren zati bat zurekin eramanez, inoiz bueltatuko ez den zati bat, baina zaude ziur beti eramango zaitudala geratzen zaidan beste zatian. Zin dagit.

ESKERRIK ASKO

Laburpena

Fisikaren helburu nagusienetako bat inguruan dugun materiaren sailkapena da. Horretarako jarrai daitekeen irizpide zabalduenetako baten arabera, hiru multzo ezberdinetan sailka dezakegu materia: gas, likido edo solido gisa, hain zuzen ere [ikus **1.1**(a) irudia]. Besteak beste, likido eta (bereziki) solidoen propietateak aztertzeaz arduratzen den fisikaren alorrari Materia kondentsatuaren fisika deritzo.

Multzo hauetako batean barneratu bezain laster, sailkapen hau labur geratzen da. Solidoen kasuan, propietateak sistema batetik bestela aldatzen direla ikusten dugu, sailkapen-irizpide zehatzago baten beharra dugula ohartzen garelarik. Aukeretako bat solidoak metal edo isolatzaile gisa klasifikatzea da, kanpo eremu elektriko baten eraginpean duten jokaeraren arabera: baldintza horietan korronte elektrikoa garraiatzen badute, metalak direla diogu, isolatzaileak bestela [ikus **1.1**(b) irudia].

1980an K. v. Klitzing eta haren kolaboratzaileek egindako aurkikuntza batek agerian utzi zuen sailkapen hau ere ez dela nahikoa: *integer* Hall efektu kuantiko (HEK) delakoa behatu zuten [1]. Bi dimentsioko elektroi gas bat planoarekiko perpendikularra den kanpo eremu magnetiko baten eraginpean jartzean behatzen den efektu bat da hau. Druderen eredu erdi-klasikoaren arabera, zeharkako erresistibitateak eremu magnetikoaren intentsitatearekiko proportzionala izan behar luke; behaketa esperimentalen arabera, ordea, lautadak (*plateau* deritzenak) ageri dira aipaturiko menpekotasuna adierazten duen kurban, **1.2** irudiak ikus daitekeen moduan. Halaber, menpekotasun hau harritzekoa den zehaztasunaz deskriba daiteke lautada bakoitzari zenbaki arrun bat[1] esleituz. Bi urte beranduago, 1982an, J. Thouless eta haren kolaboratzaileek frogatu zutenez, zenbaki arrunt hau Chern zenbakiarekin (TKNN aldaezin bezala ere ezaguna) bat dator, *integer* HEK efektu topologikoa delarik. Aurkikuntza hauek isolatzaile tribial eta topologikoen artean bereizteko beharra azpimarratu zuten [ikus **1.1**(c) irudia]. Era honetan, *integer* HEKaren aurkikuntzak hasiera eman zion isolatzaile topologikoen ikerkuntzari.

Hamarkada batzuk geroago, 2005 eta 2006 urteetan, C. Kane eta E. J. Melek alde batetik [2,3], A. B. Bernevig eta S. C. Zhangek bestetik [4,5], spin Hall efektu kuantikoa aurkitu zuten, isolatzaile topologikoen eremuari behin-betiko bultzada emanez. *Integer* HEKan ez bezala, spin HEKan kanpo eremu magnetikoa ez da funtsezko osagaia, spin-orbita akoplamendua (SOC) baita bandak topologikoak izatea ahalbidetzen duen faktorea. Hori dela eta, spin HEKa elementu astuneko HgTe/CdTe geruzaz osaturiko sistemetan behatu zen aurrenekoz [5,6]. Efektu hau aurkitu eta berehala, haren oinarrian dagoen topologiak hiru dimentsioko sistemetan duen gauzatzea ikertu zen [7–9], topologia ahul eta sendo arteko bereizketa proposatu zelarik.

Materialaren erdiguneko topologiaren gauzatze exotikoenetako bat gainazal egoera

[1] Ingeleraz zenbaki arruntei *integer* deritze. Bertatik dator *integer* Hall efektu kuantiko izendapena.

metalikoen presentzia da [10]. Esate baterako, Chern isolatzaile topologikoek gainazal egoera egonkor kiralak dituzte lotuta; spin HEKaren fase topologiaren kasuan, aldiz, gainazal egoerak bikoteka agertzen dira eta ongi zehazturiko spin zenbaki kuantikoa dute. Kristalaren erdiguneko fase topologikoa bezalaxe, gainazal egoerak ere iraunkorrak dira perturbazio adiabatikoen aurrean, hots, energia gap-a ixten ez duten eta fasea babesten duten simetriak errespetatzen dituzten perturbazion aurrean. Ezaugarri honek isolatzaile topologikoak interesgarri bilakatzen ditu zenbait aplikazio teknologikotarako, adibidez: spintronika, konputazio kuantiko eta supereroaleen alorrean [11].

Spin HEK aurkitu eta 3-dimentsiotara hedatu bezain laster, material topologikoen aurresate eta karakterizazio esperimentalak atentzio handia bereganatu zuen. Esfortzu honek hainbat material topologikoren aurkikuntza izan zuen ondorio, esaterako $Bi_{1-x}Sb_x$ [12], Bi_2Se_3, Bi_2Te_3 eta Sb_2Te_3 [13,14]. Aldi berean, esfortzu handia dedikatu zitzation topologia eta simetrien arteko erlazioaren ikerkuntzari. Hasteko, barne-motako simetriek (denbora alderantzizkaketa kasu) fase topologikoak hainbat klasetan bereizi ditzaketela aurkitu zen eta dimentsio desberdinetan ageri diren klaseen katalogo bat plazaratu zen, *ten-fold way* bezala ezaguna [15–17]. Ondoren, kristal-motako simetriek (biraketek, esaterako) topologian izan dezaketen rola aztertu zen. Bi paper nagusi joka ditzaketela ondorioztatu zen: Alde batetik, fase topologikoen diagnosia erraztu dezakete [18]. Bestetik, simetria talde batek izan ditzakeen fase topologiko klaseen aniztasuna aberas dezakete, halako faseak babestu zein bereizteko duten gaitasuna dela eta. Kristal-motako simetriek babesten dituzten faseei *krista-motako isolatzaile topologiko* (topological-crystalline insulators ingeleraz) deritze [19, 20] eta egoera metalikoak izan ditzakete fasea babesten duen simetriak finko utzitako gainazaletan.

Kristal-motako isolatzaileen familia tipiko bat *mirror-Chern*[2] isolatzaile deritzanak dira [21–23]. Planoarekiko islapenak Hilberten espazioa bitan banatzen du, azpiespazio bakoitza simetriaren autobalio bati dagokiolarik. Horrela, azpiespazio bakoitzean Chern fase bat gauza daiteke. Nahiz eta denbora alderanzketa simetriak Chern zenbaki osoa zero izatera behartu, azpiespazio desberdinetako faseek ezin dute elkar deuseztatu, islapen simetriak babesten baititu.

Beste kristal-motako isolatzaile topologiko klase ezagun bat *ordena-altuko* isolatzaile topologikoak dira (*higher-order topological insulators*, ingeleraz). Hauen berezitasuna gainazal egoeretan aurki dezakegu: d-dimentsiotan definituriko ohiko isolatzaile topologikoek egoera metalikoak $(d-1)$-dimentsioko gainazaletak dituzten bitartean, ordena-altuko isolatzaile topologikoek $(d-2)$-dimentsioko ertz $(d=3)$ edo erpinetan $(d=2)$ erpinetan dituzte. Familia honetako material ezagunenetako bat Bismuto kristala da [24].

Nahiz eta 2000 eta 2010eko hamarkadetan zehar komunitate zientifikoak isolatzaile topologikoen azterketari dedikaturiko esfortzua handia izan, material topologikoen

[2]Euskarazko hitzez-hitzeko itzulpena *ispilu-Chern* isolatzaile litzateke. Izen hau ematen zaie fase hauek babesten dituen simetria plano batekiko islapena delako. Ingeleraz *mirror-reflection* gisa izendatzen dira simetria hauek.

iragarpen eta aurkikuntza astiro zihoazen. Alderdi teorikoari dagokionez, mantsotasunaren kausa nagusia material batek fase topologikorik ote duen aurresateko metodo sistematiko eta orokor baten falta zen. Izan ere, material bakoitzaren analisiak prozedura propio bat eska zezakeen. Gainera, orduko metodoak kalkulatzen zailak diren aldaezin topologikoetan oinarritzen ziren, oro har. Arazo honen soluzioa aipaturiko hamarkadaren bigarren zatian argitaraturiko bi formalismoren eskutik etorri zen: kimika topologikoaren kuantiko (KTK) [25–27] eta simetrian oinarrituriko adierazle topologikoen formalismoen [28, 29] eskutik, alegia. Aipatu formalismoek topologia eta kristal-motako simetrien arteko deskribapen orokorra eskaintzen dute, 230 talde-espazialentzako aplikagarria dena, SOCarekin nahiz gabe. Orokortasun honi esker, formalismo hauek *ab initio* simulazioekin konbinatu ahal izan ziren eta material topologikoen iragarpen zein analisia izugarri azeleratu ziren. Azelerazio honen erakusle da [30] artikuluan aurkezturiko analisia. Ikerkuntza honetan, *ab initio* metodo bidez 26.938 material inorganikoren banda egiturak kalkulatzen dituzte, ondoren egitura hauek KTKaren bidez aztertuz material topologikoak aurkitzeko asmoz. Bilaketaren emaitzen arabera, azterturiko materialen %12 isolatzaile topologikoak dira.

KTK formalismoaren abaintaila nagusienetako bat posizioen espazioarekin mantentzen duen erlazio estua da. Izan ere, posizioen espazioan kokaturiko orbitalek elkarrekiko espazioan elektroi bandak nola induzitzen dituzten deskribatzen du, *banda errepresentazio* izeneko egitura matematikoen kontzeptua medio [31–33]. Harreman hau bereziki interesgarria da elkarrekintza sendoko materialen ikuspuntutik, errazagoa baita sarritan halako materialak posizioen espazioan definituriko irudi batean oinarrituz deskribatzea.

Nahiz eta hasiera batean KTK formalismoa soilik ordena magnetiko gabeko sareetzako izan baliogarri, berehala hedatu zuten material magnetikoen deskribapena eskaintzeko gain izan zedin [34]. Simetrian oinarrituriko topologiaren adierazleen formalismoa ere antzera osatu zuten [35].

Orainarte aurkeztutako ikerkuntza, metodo eta formalismo denek ezaugarri berdina dute komunean: partikula independenteen hurbilketa dute oinarrian. Esate baterako, Chern zenbakia bezalako aldaezinak kalkulatzeko erabiltzen diren adierazpenak partikula-bakarreko uhin funtzioen menpe idatzi ohi dira; KTK edo simetria adierazleen formalismoen funtsa partikula-bakarreko hamiltondarraren simetria autobalio edo errepresentazio laburtezinei buruzko ezagutza da. Dena den, onartu beharra dago material orotan pairatzen dutela elektroiek Coulomben elkarrekintza bidezko aldaratzea, hein batean edo bestean. Zenbait konposatutan elkarrekintza hau ahula izan daitekeen arren, beste zenbait sistemen kasuan haien natura gobernatzera hel daitezke, adibidez: Kondo materialen [36] edo Mott isolatzaileen [37] kasuan.

Zilegi da material batek elektroi-elektroi elkarrekintza izatea ohikoa ote den geure buruari galdetzea. Fisika atomikoaren ikuspuntutik, elektroien arteko elkarrekintza bereziki sendoa izango da eletroiak nukleoaren inguruko eremu txiki batean lokalizatuta daudenean. Bi faktorek eragiten dute lokalizazio honetan: Alde batetik, elementuaren

zenbaki atomikoa zenbat (hots, protoi kopurua) eta handiagoa izan, elektroiek jasango duten elkarrekintza elektrostatikoa orduan eta sendoagoa izango da; beraz, lokalizazioa orduan eta handiagoa izango da, elektroiek elkarri eragioten dioten aldarapena sendoa izango delarik. Hau da, besteak beste, $5f$-orbitaletako elektroiek elkarrekintza sendoak pairatzearen arrazoia. Bestalde, eletroien lokalizazioa nabarmenagoa da $l = n - 1$ momentu angeluar orbitaleko egoeretan (non n zenbaki kuantiko nagusia den), haien zati erradialak ez baitu nodorik[3]; horrenbestez, elektroien arteko elkarrekintza sendoa izan ohi da $4f$ eta $3d$-orbitaletan. Irizpide honen laburpena **1.3** irudian dago adierazita. $3d$-orbitalek presentzia nabarmena izan dezakete trantsizio-metalak dituzten konposatuetan; kobredun materialen familiak, esaterako, bereziki interesgarriak dira Mott fisikaren zein tenperatura-altuko supereroankortasunaren alorretan [38]. Era berean, $4f$ eta $5f$-orbitalek paper garrantzitsua joka dezakete, hurrenez hurren, lantanido eta aktinidoz osaturiko konposatuetan. Halakoak dira Kondo eta fermioi astuneko materialak [39, 40], adibidez.

Isolatzaile topologikoen ikerkuntzan elektroi-elkarrekintzak izan dezakeen garrantzia ez da berria. C. Kane eta E. J. Melek grafenoan spin EHK aztertu zutenean jada kontsideratu zuten elkarrekintza honek izan dezakeen eragina [2]. Beste lan batzuk, berriz, elkarrekintzek gainazal egoeretan izan dezaketen eragina aztertzean zentratu ziren [41]. Lan hauen balioa ukaezina den arren, ez dute topologiak elkarrekintza sendoko materialetan duen gorpuztearen irudi oso bat eskaintzen.

2000ko hamarkadaren amaiera aldera, elkarrekintzek topologian duten eragina aztertzeko partikularki interesgarria den ikuspuntu bat proposatu zen. Perspektiba honen oinarrian Greenen funtzioak daude, elkarrekintzadun sistemen kasuan partikula bakarreko kitzikapenen dinamikari buruzko informazioa duten funtzioak, alegia. Hasiera batean, proposamenaren funtsa aldaezin topologikoak Greenen funtzioen menpe idaztea zen, partikula-bakarreko uhin funtzioen menpe idatzi beharrean. Halere, erdietsitako adierazpenak zenbakizko metodoetan inplementatzeko konplikatuegiak zirela eta, Z. Wang eta haren kolaboratzaileek elkarrekintzadun problema partikula independenteen alegiazko sistema baten problemara laburtzea proposatu zuten [42, 43]. Elkarrekintza gabeko sistema honen hamiltondarrari *hamiltondar topologiko* deritzo eta Greenen funtzioa maiztasun zehatz batean ($\omega = 0$) ebaluatuz eraiki daiteke. Zenbait baldintzapean berezko eta alegiazko sistemak topologia berdina dutela kontuan edukiz [44], berezko materialaren topologia sailkatzeko metodoa sinplea da: hamiltondar topologikoari elkarrekintza gabeko sistemen topologia ikertzeko eskuragarri ditugun metodoak aplikatzea.

Nahiz eta esfortzu handia dedikatu zaion elkarrekintza sendoko isolatzaile topologikoen bilaketari, aurkitutako material kopurua elkarrekintza ahuleko kasutik urrun dago oraindik. Aurkituriko halako kristalen artean Na_2IrO_3 [45], SmB_6 [46–54] eta elkarrekiko biraturik dauden grafenozko bi geruzaz osaturiko sistemak [55–58] daude.

[3] Zati erradialaren nodo kopurua $n - l - 1$ da, non n zenbaki kuantiko nagusia den eta l momentu-angeluar orbitalari dagokion zenbaki kuantikoa.

Azaldu dugun moduan, elkarrekintza gabeko isolatzaile topologikoen aurkikuntzak ere antzeko egora bat bizi izan zuen, KTKaren proposamenarekin arazoa gainditu eta topologia uste zena baino ohikoagoa dela konprobatu zen arte [30]. Honela, argi geratu zen arazoaren kausa simetria eta topologiaren arteko erlazioa behar bezala deskribatzen duen metodo baten falta zela. Antzekotasun honek tesi honetan KTKaren formalismoak elkarrekintza sendoko kristalen kasuan izan dezakeen aplikazioa ikertzera animatzen gaitu.

Tesi hau hiru atal nagusitan dago banatuta. Lehenengo atalean, elkarrekintza gabeko sistemen topologia dugu aztergai. Bigarren atalean, KTK formalismoa elkarrekintza sendoko materialen familia batean aplikatzen dugu: $4f$-orbital lokalizatudun lantanidoz osaturiko fermio-astuneko materialetan. Hirugarren atalean, KTK formalismoa elkarrekintza sendoko sistemen analisira hedatzeko modu bat aztertzen dugu, Greenen funtzioak eta hamiltondar topologikoa direla medio.

Jarraian, tesiaren emaitzak laburtuko ditut:

Banda egituren topologiaren deskribapen alternatiboa, garraio adiabatikoa ulertzeko ikuspuntu geometrikoan oinarritua. Perspektiba honenpean topologiaren azterketan funtsezkoak diren Berriren fase eta Wilsonen lakioak nola ageri diren frogatu dugu. Ondoren, kargaren lokalizazio eta Wilsonen lakioen arteko erlazioa landu dugu, banda-bakarreko kasura mugatu gabe. Erlazio hau biziki hezigarria da, banden izaera topologikoa karga lokalizatzeko eragozpen gisa interpretatu ohi baita [59], bereziki KTKaren argitalpenaz geroztik. Izatez, Wilsonen lakioen espektruko harilketak[4] kargaren lokalizaziorako oztopo direla frogatzen dugu, baita Chern zenbakia antzera interpretatzen ere. Horretaz gain, kristal-motako simetriek Wilsonen lakioaren espektrua nola baldintzatzen duten aurkezten dugu.

***Ab initio* banda egituren simetria-autobalio eta errepresentazio laburtezinen kalkulurako kode ireki baten garapena.** Python programazio hizkuntzan idatzitako kode honi *IrRep* izena eman diogu eta *ab initio* simulazioen bidezko materialen topologiaren azterketari egin diogun kontribuzioa da. *IrRep*-en bidez lortzen dugun informazioa KTK formalismoa jarraituz azter daiteke ondoren. Formalismo hau belazaxe, edozein 230 talde espazialen kasuan aplika daiteke *IrRep*, SOC akoplamenduarekin zein gabe. Orokortasun honi esker, material topologikoak aurresan eta aztertzeko metodo sistematiko bat aplikatzea ahalbidetzen du gure kodeak, *ab initio* simulazio eta KTK formalismoaren arteko zubi gisa jokatzen duelarik.

Une honetan, *IrRep*ek *ab initio* kode erabilienentzako interfazeak ditu, VASP [60], Abinit [61, 62], QE [63] eta Wannier90 [64] kodeentzako interfazeak, hain justu ere. Horretaz gain, interfaze berrien eta funtzio berrien inplementazioa errazteko moduan izan da egituratua, hau bere garapenerako onuragarria izango delakoan.

[4] Ingelerazko *winding* hitza *harilketa* gisa itzuli dugu, Wilsonen lakioaren autobalioak ardatz baten inguruan harilkatuko balira bezala dirudi eta.

Kimika topologiko kuantikoak fermioi-astuneko materialetan duen aplikazioaren esplorazioa. Fermioi-astuneko materialetan, elektroi arteko elkarrekintza sendoa izan ohi da, $4f$ eta $5f$-orbital lokalizatudun lantanido zein aktinidoz osatuak baitaude. Bertan, kuasipartikulan oinarrituriko deskribapena onartzen duten zenbain fase identifikatu ditugu, baita KTK formalismoa haietan aplikatu ere. Horrela, banda zabal eta ia-lauen arteko eragin-trukeari KTK formalismoaren ikuspuntutik begiratuz, fase topologikoen sorrera analizatu dugu. Orainarte garatutako analisien aldean, gure azterketaren abantaila nagusia kristal-motako simetria denak maila berean inplementatzen dituela da, ezein simetria era berezian tratatuz. Orokortasun hau dela eta, aipatu faseak KTK formalismoaren menpe aztertzeak topologiaren sailkapen xeheago bat eskuratzea ahalbidetzen digu. Ekarpen honek fermioi-astuneko materialen fase topologikoen sailkapena bultzatuko duelakoan gaude, fase berrien identifikazioa bideratuz eta aurretik burututako materialen sailkapenen berrikusketa motibatuz.

Analisi metodo hau *ab initio* kalkuluekin konbinatu dugu SmB_6 materiala aztertzeko. SmB_6 isolatzaile topologiko bortitz bat dela ondorioztatu ahal izan dugu honela. Gainera, erdietsi dugun fase topologikoa aurreko lanek lortutako klasifikazioarekin bat badator ere, gure sailkapena zehatzagoa da. Topologiaren sorrerari dagokionez, $4f$ eta $5d$-orbitaletatik induzituriko banden hibridazioaren bidez interpreta daitekeela ondorioztatu dugu.

Kimika Topogiko Kuantikoaren bidez Greenen funtzioak aztertzean oinarritzen den metodoaren aplikazioa Hubbarden Diamanteen Katearen analisian. Proiektu hau KTK formalismoa elkarrekintza sendoko sistemen analisirako hedatzeko saiakera baten parte da. Saiakeraren funtsa Greenen funtzioak medio eraikitzen den hamiltondar topologikoa KTK formalismoaren bidez aztertzea da. Bertan, metodo hau sistema zehatz batean aplikatu dugu: Hubbarden Diamanteen katean (HDK).

Analisia hiru pausutan bereizi dugu: Lehenik eta behin, elkarrekintza gabeko kasua aztertu dugu, uneoro erreferentzia gisa izan duguna. Bigarren, Matrize Dinamikoen Birnormalizazio Talde (DMRG, ingeleraz) eta Monte Carlo Bariazionalaren bidezko kalkuluak erabili ditugu, partikula-anitzeko aldaezin topologikoekin batera, elkarrekintzadun kasuko fase diagrama determinatu eta fase bakoitza sailkatzeko. Informazio hau erreferentzia gisa harturik, fase diagramaren kalkulu eta topologiaren sailkapena aztergai dugun Greenen funtzioetan oinarrituriko metodoaren bidez errepikatu dugu.

Atera dugun ondorioetako bat metodoaren aplikagarritasunaren ingurukoa da. Elkarrekintzadun faseen sailkapen topologikorako egokia dela ondorioztatu dugu, fase hauek partikula independenteen hurbilketaren barnean deskriba daitezkeen faseren bati adiabatikoki konekta daitezkeen bitartean. Are gehiago, horrelako faseen azterketa sistematiko eta eraginkorrerako bidea dela ikusi dugu.

Halaber, HDKko Mott isolatzaile fasea metodoaren aplikagarritasunetik at dagoela ikusi dugu; beraz, ezin dugu ziurtatu hamiltondar topologikoan oinarrituriko metodo hau

baliogarria denik aztergai dugun fasea elkarrekintza gabeko inongo faseri konektatuta ez dagoenean. Aipatu Mott fasearen kasuan, oztopoa auto-energiak $\omega = 0$ maiztasunean duen dibergentzia da. Honelako faseen sailkapenak partikula-anitzeko Greenen funtzioen erabilera exijitzen du, [65] kolaborazioan azaltzen dugun moduan.

HDKaren fase diagramari dagokionez, mota desberdineko faseetan aberatsa dela ikusi dugu. Elkarrekintza gabe, limite atomikodun bi fase isolatzaile (AI eta OAL izendatuak[5]) eta fase metaliko bat behatu ditugu. Elektroi-elektroi elkarrekintza kontsideratzean, AI eta OAL faseek isolatzaileak izaten jarraitzen dute eta kuasipartikulen bidez deskriba daitezke; metala, berriz, Mott isolatzaile bilakatzen da.

Spin-orbita akoplamenduak sistemaren fase diagraman duen eragina ere aztertu dugu. Gure emaitzen arabera, AI eta OAL faseetan eragina txikia bada ere, inplikazio garrantzitsua du metal fasean, isolatzaile bilakatzen baitu. SOCak eragindako isolatzaile honi SAI (*SOC atomic insulator*, ingeleraz) izena eman diogu. Horretaz gain, elektroien arteko elkarrekintza eta SOC akoplamendu arteko norgehiagoka behatu dugu HDK katean.

[5]Ingeleraz, *atomic insulator* (isolatzaile atomiko) eta *obstructed-atomic Limit* (oztopaturiko limite atomiko) izendatu ditugunak. Bien arteko desberdintasuna kargaren lokalizazioa da.

List of publications

I. *"Lecture notes on Berry phases and topology"*, Barry Bradlyn and **Mikel Iraola**, SciPost Phys. Lect. Notes 51 (2022)

II. *"IrRep: Symmetry eigenvalues and irreducible representations of ab initio band structures"*, **Mikel Iraola**, Juan Luis Mañes, Barry Bradlyn, Matthew K. Horton, Titus Neupert, Maia G. Vergniory and Stepan S. Tsirkin, Computer Physics Communications 272 (2022) 108226

III. *"Towards a topological quantum chemistry description of correlated systems: The case of the Hubbard diamond chain"*, **Mikel Iraola**, Niclas Heinsdorf, Apoorv Tiwari, Dominik Lessnich, Thomas Mertz, Francesco Ferrari, Mark H. Fischer, Stephen M. Winter, Frank Pollmann, Titus Neupert, Roser Valentí and Maia G. Vergniory, Phys. Rev. B **104**, 195125 (2021)

IV. *"Topological quantum chemistry for heavy-fermion insulators"*, Mikel Iraola *et al.*, in preparation.

V. *"Elementary band representations for single-particle Green's function of interacting topological insulators"*, Dominik Lessnich, Stephen M. Winter, **Mikel Iraola**, Maia G. Vergniory, Roser Valentí, Phys. Rev. B **104**, 085116 (2021)

VI. *"Interacting topological quantum chemistry of Mott atomic limits"*, Martina O. Soldini, Nikita Astrakhantsev, **Mikel Iraola**, Apoorv Tiwari, Mark H. Fischer, Roser Valentí, Maia G. Vergniory, Glenn Wagner, Titus Neupert, arXiv:2209.10556

VII. *"Novel family of topological semimetals with butterflylike nodal lines"*, Xiaoting Zhou, Chuang-Han Hsu, Hugo Aramberri, **Mikel Iraola**, Cheng-Yi Huang, Juan Luis Mañes, Maia G. Vergniory, Hsin Lin, Nicholas Kioussis, Phys. Rev. B **104**, 125135 (2021)

VIII. *"Glide symmetry protected higher-order topological insulators from semimetals with butterfly-like nodal lines"*, Xiaoting Zhou, Chuang-Han Hsu, Cheng-Yi Huang, **Mikel Iraola**, Juan Luis Mañes, Maia G. Vergniory, Hsin Lin, Nicholas Kioussis, npj Computational Materials **7**, 202 (2021)

IX. *"Prediction of double-Weyl points in the iron-based superconductor $CaKFe_4As_4$"*, Niclas Heinsdorf, Morten H. Christensen, **Mikel Iraola**, Shang-Shun Zhang, Fan Yang, Turan Birol, Cristian D. Batista, Roser Valentí and Rafael M. Fernandes, Phys. Rev. B **104**, 075101 (2021)

X. *"Fractional corner charge in spin-orbit coupled crystals"*, Frank Schindler, Marta Brzezińska, Wladimir A. Benalcazar, **Mikel Iraola**, Adrien Bouhon, Stepan S. Tsirkin, Maia G. Vergniory and Titus Neupert, Phys. Rev. Research **1**, 033074 (2019).

1 Introduction

The classification of matter is one of the principal tasks of physics. The most widely known criterion consists in classifying materials among three groups: solids, liquids or gases [see Fig. **1.1**(a)]. Condensed Matter physics is indeed the field of physics which takes care, among other duties, of investigating the properties of liquids and, especially, solids.

As soon as we dive deeper into one of these groups, this classification scheme turns out to be too broad. In particular, we soon become conscious that the properties of a solid might vary from system to system, which creates the need to adopt a more detailed classification for them. A possibility is to label a solid either as a metal or an insulator, depending on its behavior under an external electric field: if under that condition the (bulk of the) system carries charge current, we say that it is a metal; otherwise, we label it as an insulator [see Fig. **1.1**(b)].

In 1980, one of the most striking discoveries manifested the necessity for an even more detailed criterion to classify insulators: K. v. Klitzing *et al.* reported for the first time the integer quantum Hall effect (QHE) [1]. In this effect, a two dimensional electron gas is subjected to an off-plane magnetic field. While Drude's theory predicts that the

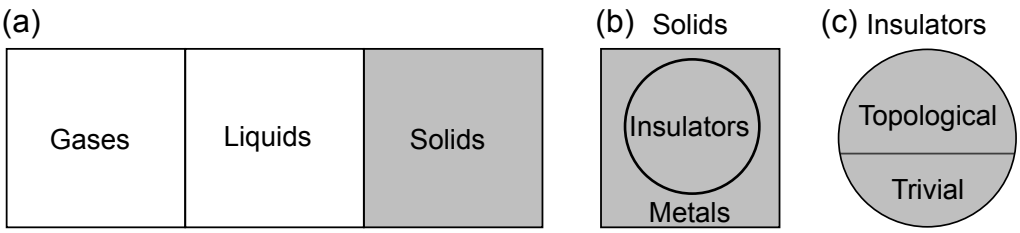

Figure 1.1: Historical classification of matter, with the focus on topological insulators. (a) In general terms, matter can be classified in three main groups: gas, liquid or solid. (b) Solids can be further classified as insulators or metals, depending on their behavior under an electric field. (c) In modern condensed matter field, insulators can be further labeled as trivial or topological.

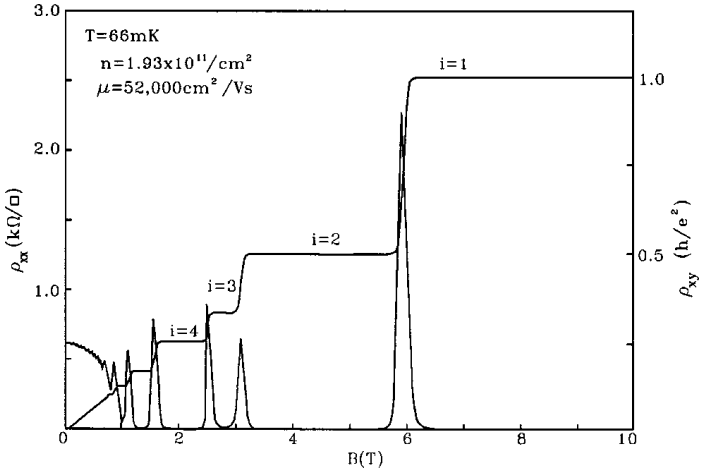

Figure 1.2: Dependence of the transverse resistivity on the magnetic field in the integer QHE. Source: [68].

transverse resistivity should be proportional to the strength of the magnetic field [66], experimental evidences show plateaus in this dependence [see Fig. **1.2**]. Furthermore, it turns out that the relation is governed, with a surprising accuracy, by a factor that takes an integer value for each plateau. Two years later, in 1982, D. J. Thouless *et al.* demonstrated that this integer number is a topological invariant, known currently as Chern number or TKNN invariant [67]. These discoveries emphasized the need for a more meticulous classification of insulators which consists in differentiating between topological and trivial insulators [see Fig. **1.1**(c)]. Furthermore, the integer QHE was the first step in the research on topological insulators, and the beginning of the field known as topological condensed matter physics.

The discovery by C. Kane and E. J. Mele [2, 3] – and by A. B. Bernevig and S. C. Zhang [4, 5] – of the quantum spin Hall effect gave a firm push to the topological consensed matter physics. Unlike the integer QHE, an external magnetic field is not required to realize the quantum spin Hall effect. The key ingredient for the band topology in this case is the spin-orbit coupling (SOC) effect. Consequently, the quantum spin Hall effect was first predicted [4, 5] and then observed [6] in systems consisting of HgTe/CdTe layers. Soon after the discovery of the quantum spin Hall phenomenon, the basic topology of this effect was extended to three dimensions, yielding a classification based on weak and strong topological indices [7–9].

One of the most exotic manifestation of the bulk's band topology is the presence of gapless boundary states [10]. For instance, Chern insulators display chiral edge modes prevented from backscattering, whereas quantum spin Hall insulators show pairs of spin-filtered gapless edge modes dubbed helical modes. As well as the topology of the bulk,

these boundary modes are robust against adiabatic perturbations, *i.e.* perturbations which neither close the bulk gap nor break any protecting symmetry. Featuring such boundary states turns topological insulators into promising platforms not only for the achievement of a fundamental understanding of topological phenomena, but also for practical applications in fields like spintronics, quantum computation or superconductivity [11].

The prediction and experimental characterization of topological materials, together with the analysis of the robustness of edge states, attracted intense attention during the years following to the discovery of the quantum spin Hall effect and its extension to three dimensions. This effort lead to the discovery of some topological materials, like $Bi_{1-x}Sb_x$ [12], Bi_2Se_3, Bi_2Te_3 or Sb_2Te_3 [13, 14]. In parallel, the interplay between symmetries and topology also attracted notable consideration. The study of the role played by internal symmetries in topology led to a catalog of topological classes in many dimensions [15–17], known as the *ten-fold way* classification. Concerning crystal symmetries, they might play two roles: On the one hand, they might facilitate the diagnosis of topology; for instance, inversion eigenvalues might be used to simplify the identification of strong and weak topological phases in centrosymmetric crystals [18]. On the other hand, crystal symmetries might enrich the variety of topological phases that a symmetry group can host, owing to their capacity to protect topological phases from adiabatic deformations and to differentiate between distinct phases. An insulator whose phase is protected by a crystal symmetry is called *topological-crystalline insulator* (TCI) [19]. These insulators show gapless modes in the boundaries left invariant by the protecting symmetry. A pedagogical introduction to TCIs can be found in Refs. [20].

A prototypical family of TCIs are mirror-Chern insulators [21], which have been identified in actual materials like SnTe [22, 23]. Basically, the Hilbert space of a system with mirror symmetry can be split into two, so that each subspace has in correspondence an eigenvalue of the reflection operation, and hosts a Chern insulator phase. Even if time-reversal symmetry forces the sum of Chern numbers of both subspaces – that is, the total Chern number – to vanish, mirror symmetry protects the value of each of this individual invariants, and hence protects the topological phase.

Another type of TCIs that have attracted much attention recently are the so-called *higher-order topological insulators* (HOTIs) [69]. These materials are known for their particular bulk-boundary correspondence: while a typical topological insulator in a d-dimensional lattice shows gapless modes in certain boundaries of $(d-1)$-dimensions, HOTIs display gapless modes in $(d-2)$-dimensional boundaries. Three-dimensional HOTIs show gapless hinge-modes, while the gapless states are corner modes in HOTIs defined in two dimensions. Bismuth is famous for being the first material realization of a HOTI, which was supported by theoretical and experimental evidences [24].

Although intense effort was devoted in the past decades to the investigation of topological insulators and this effort was reflected in the development of the conceptual understanding of these systems, the prediction and identification of topological phases

in actual materials was slow. Regarding the theoretical aspect of the problem, its main cause was the lack of a general and systematic approach for the prediction of band topology in materials. The analysis of every material and every phase could require its own method, which used to consist in the numerically subtle calculation of topological invariants. The parallel development of the formalisms of topological quantum chemistry (TQC) by B. Bradlyn *et al.* [25–27] and symmetry-based indicators of topology [28, 29] set the solution to this problem. Each of these frameworks describes the interplay between crystal symmetries and band topology based on an approach that is applicable on the same footing to all 230 space groups, with and without SOC. This feature allowed for the implementation of both formalisms together with *ab initio* simulations of band structures, which turned out to be a systematic method for the analysis of topological materials.

The development of these *ab initio* based methods accelerated the diagnosis and classification of topological materials. A work that emphasizes this acceleration is the high-throughput search of topological materials in an extense list of 26,938 high-quality materials performed in Ref. [30] via the combined application of TQC and Density Functional Theory (DFT) calculations. This search identified as topological insulators the 12 per cent of the materials included in the database, and thus suggested that band topology is more common than previously believed. Therefore, both the consideration of crystal symmetries and the implementation of an effective TQC-based method took down the idea that topological materials were scarce. Alternative searches based on the formalism of symmetry-indicators of topology yielded similar results [70, 71].

An advantage of the formalism of TQC is that not only provides us with a powerful framework for the diagnosis of topological phases, but also with a description of how bands in reciprocal space inherit their properties from localized Wannier functions in real space. This description is based on the concept of *band representation* introduced by J. Zak [31–33], which is basically the representation of the space group induced from a set of Wannier orbitals located in the lattice. This strong connection with a real-space picture of the crystal makes the TQC framework particularly interesting for a theory to explain the topology of interacting materials.

Despite the fact that TQC was first devised for non-magnetic (grey) space groups, it was later extended to crystals showing magnetic order [34]. Moreover, inspired by success of the aforementioned high-throughput search performed for paramagnetic materials, a similar search for topological phases in magnetically-ordered compounds was also carried out based on magnetic TQC [72]. The formalism of symmetry-based indicators of topology was also extended to account for magnetic space groups [35].

All the research, methods and formalisms mentioned above have something in common: they have been developed within the framework of the independent-electron approximation. For instance, the expressions for the Berry connection, Wilson loops and invariants like the Chern number are written in terms of single-particle wave functions; TQC and the formalism of symmetry-based indicators of topology are also rooted in the

symmetry eigenvalues and irreducible representations corresponding to the eigenstates of the single-particle Hamiltonian. Nevertheless, the reality is that Coulomb interaction is present in all materials. Whereas, the independent-electron picture might be adequate for materials where electron-electron interactions are weak, in some systems these effects are strong enough to govern their physics, *e.g.* in Kondo materials [36] or Mott insulators [37]. It is therefore vital and natural to address the effect that electron interactions might have in topological insulators.

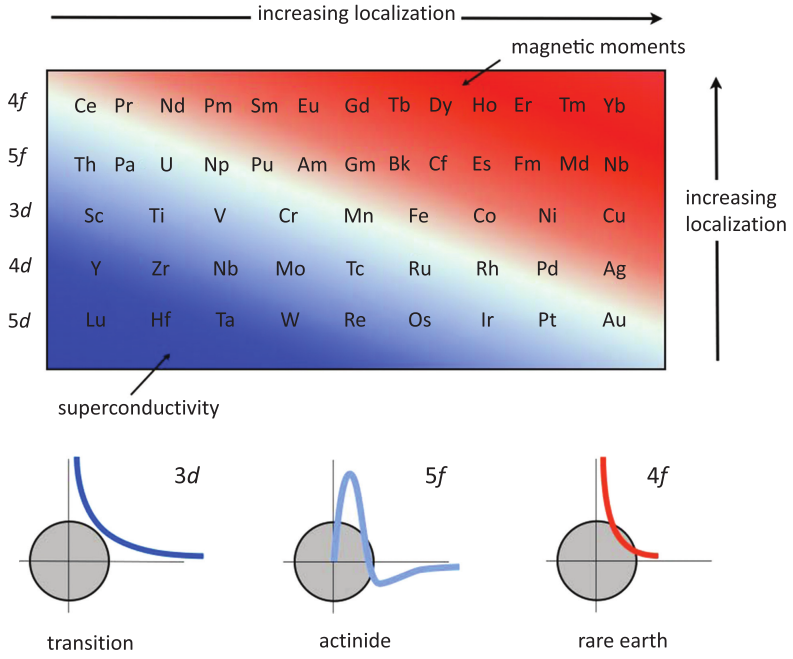

Figure 1.3: Kmetko-Smith diagram illustrating the tendency towards electron localization in d and f-orbitals. Source: [38].

We might ask ourselves how common the presence of strong electron interactions in actual materials is. From an atomistic point of view, the Coulomb interaction between electrons tends to be large in orbitals which are very localized around the nucleus. There are two main factors which influence the localization: on the one hand, the bigger the atomic number of the atom, the stronger the attraction felt by electrons, and hence the more localized are the electrons around the nucleus; this is the reason why electrons in $5f$-orbitals tend to feel strong Coulomb repulsion between them. On the other hand, the localization tends to be bigger in orbitals with $l = n - 1$ quantum number for the orbital-angular momentum, since the number of nodes in the radial part of the wave function is given by $n - l - 1$, and the smaller the number of nodes, the closer the

charge is from the nucleus; accordingly, repulsion between electrons tends to be large in $4f$ and $3d$-orbitals. These arguments are illustrated in Fig. **1.3**. $3d$-electrons play an important role in many compounds, like in cuprates, which attract intense attention for being platforms to study Mott physics and high-temperature superconductity [38]. Lanthanide and actinide elements containing $4f$ and $5f$-orbitals are also common in a variety of compounds, *e.g.* heavy-fermion insulators and Kondo materials [39, 40]. This discussion emphasizes the need to consider the effect of electron interactions in topological insulators.

C. Kane and E. J. Mele already realized the importance of electron interactions in their seminal work about the quantum spin Hall effect in graphene [2]. They concluded that electron-electron repulsion strengthens the spin-orbit coupling, which enlarges the spectral gap.

Other works focused on the effect of electron interaction on surface states [41], which turns out to be especially interesting for potential technological applications. However, such an approach is not suitable to achieve a picture of the influence of interactions over the bulk topology.

A particularly promising direction where interactions were consider consists in analyzing the topology via single-particle Green's functions. This approach is motivated by the fact that Green's functions contain information about the dynamics of particle excitations in interacting media; moreover, they become equivalent to the single-particle Hamiltonian in the non-interacting limit, which ensures that the topology of independent electrons is properly recovered in this limit. This research direction was begun with the proposal of expressions for certain topological invariants written in terms of Green's functions [73–75]. The limited practical applicability of these expressions, which stems from their complicated form, motivated an alternative approach based on a mapping of the interacting problem to an auxiliary non-interacting system. This mapping is performed by constructing an independent-particle Hamiltonian, dubbed *topological Hamiltonian*, out of single-particle Green's function of the original interacting system. Z. Wang *et al.* proposed that the topology of the genuine interacting system could be determined by diagnosing the topology of the topological Hamiltonian via the aformentioned conventional methods developed within the independent-particle framework [42, 43]. The extension of this approach to account for the role of crystal symmetries in the topology was still to be explored when I began working on this thesis.

In spite of the the intense effort devoted to the search of topological materials, the number of predicted strongly interacting topological compounds is very scarce compared to the weakly-interacting case. Examples of interacting topological materials include Na_2IrO_3 [45], SmB_6 [46–54] and twisted-bilayer graphene [55–58]. As we explained above, a similar situation regarding non-interacting topological insulators was solved by the proposal of TQC, which lead to the conclusion that topology is more common than previously thought [30], and thus pointed out that the source of the problem was the lack of a formalism able to describe in detail the interplay between crystal symmetries and

topology. This encourages us to investigate in this work the applicability and possible extension of TQC to interacting crystals.

1.1 General objectives and structure

The objectives of this thesis are the following:

Description of an alternative formulation of band topology, based on a geometrical approach to adiabatic transport. This formulation is based on the work we presented in Ref. [76], and allows us to explore the capacity of Wilson loops for diagnosing band topology. Furthermore, we provide a mathematical relation between non-trivial band topology and obstruction to charge localization in crystals, which is especially interesting since this interpretation is widely accepted [25, 28, 59] nowadays.

Development of an open-source software to calculate symmetry eigenvalues and irreducible representations of Bloch states in *ab initio* band structures. As we mentioned, the TQC based analysis of *ab initio* band structures is a powerful method for the theoretical classification and prediction of topological materials. Motivated by the scarcity of numerical tools available for such an analysis, we have developed the code *IrRep*: a Python software that calculates the symmetry eigenvalues and irreducible representations of wave functions obtained via *ab initio* simulations. We reported this development in Ref. [77]. Unlike other codes with similar capabilities [78, 79], the applicability of *IrRep* is not limited to a single DFT code, as it contains interfaces to the most popular DFT softwares, namely VASP [60], Abinit [61, 62], QE [63], and to the post-processing tool Wannier90 [64]. Furthermore, it is built upon the idea of keeping the interaction with the user as simple as possible, and written with a structure that facilitates the implementation of new features and interfaces.

Exploration of the application of topological quantum chemistry to heavy-fermion insulators. Heavy-fermion insulators are strongly-interacting systems due to the presence of lanthanide and actinide elements with localized $4f$ and $5f$-orbitals in their chemical composition. We have focused here on interacting phases which admit a description in terms of quasiparticle bands. By applying TQC to their analysis, we have derived a description of the origin of topological bands as the result of the interplay between dispersive $5d$ and (almost-)flat $4f$-bands. This approach (i) allows for a rigorous classification that accounts on an equal footing for the role of all crystal symmetries of the space group, (ii) has lead us to a new and more exhaustive classification of the topology in SmB_6, and (iii) explains the origin of topology in SmB_6 in terms of the hybridization-mediated interplay of bands.

Application to the Hubbard diamond chain of the TQC based analysis of single-particle Green's functions. Encouraged by the approach consisting in the analysis of topology in interacting phases through Green's functions [42, 43, 73–75], we consider the extension of the method to account for all crystal symmetries, and test it in the Hubbard diamond chain. After solving the phase diagram with state-of-the-art numerical methods and many-body topological invariants, we explore the classification of the interacting phases by analyzing the spectrum of single-particle Green's functions within the framework of TQC. This work, whose results we reported in Ref. [80], led us to (i) a picture of the applicability and limitations of the approach, (ii) the identification of a new type of interacting topological phase, namely *Mott atomic limits*, which might serve as atomic limits for a future extension of TQC to interacting phases. In addition, we have studied the Hubbard diamond chain with SOC, which allows us to gain insight about the interplay between SOC effects and electron interactions.

This manuscript is separated in three main parts: Part I is devoted to the presentation of our contributions to the field of band topology in non-interacting systems. Within this part, chapter 3 contains our alternative perspective to look into band topology, while chapter 6 consists of the description of the code *IrRep*. Part II accommodates the analysis of heavy-fermion insulators in terms of TQC. Finally, Part III contains our work on the extension of TQC to interacting systems in terms of single-particle Green's functions. The theoretical background of each contribution is included in the corresponding part.

Part I

Topology of non-interacting band insulators

We will begin this part by introducing in chapter 2 the fundamentals of band theory, namely the independent-electron approximation and Bloch's theorem. In chapter 3, we will present one of the works published during this thesis, which consists in a formulation of the theory of band topology from a geometrical point of view for adiabatic transport. This chapter will also serve as an introduction to band topology. In chapter 4, we will provide the basic knowledge about group theory needed to follow the discussions included in this work. Chapter 5 could be seen as a continuation of the previous section, since it contains a formal description of topological quantum chemistry which is indeed based on group theory considerations. Finally, chapter 6 contains a complete characterization of *IrRep*, a Python software we have developed to calculate the irreducible representations of electron bands.

2 Independent electrons in periodic lattices

This brief chapter is devoted to the introduction of the basic concepts about electrons in periodic lattices. We will begin by introducing the independent electron approximation, which is the cornerstone of the theory of topological band structures. Then, we will describe the fundamental features of the energy levels and states of electrons in periodic crystals, namely that the energy levels form a discrete spectrum called **band structure** and that the corresponding wave functions are delocalized in the crystal. In the way, we will define important concepts like Bloch's theorem, the reciprocal lattice and the Brillouin zone.

2.1 Independent-electron approximation

Let us consider a crystal made of M ions, whose positions are given by vectors $\boldsymbol{R}_1$, $\boldsymbol{R}_2$,..., $\boldsymbol{R}_M$. The electronic Hamiltonian of such a system contains three terms:

$$H = -\sum_i \frac{1}{2}\nabla_i^2 + \sum_i \sum_{j\neq i} \frac{1}{|\boldsymbol{r}_i - \boldsymbol{r}_j|} + \sum_i V(\boldsymbol{r}_i, \boldsymbol{R}_1, \boldsymbol{R}_2, ..., \boldsymbol{R}_M), \tag{2.1}$$

where $\boldsymbol{r}_i$ indicates the position of the i^{th} electron and the indices i and j run over all electrons in the system. We set $\hbar = m = e = 1$ in the expressions given in this section to keep the notation simple. The first term is the kinetic energy of electrons. The second one is the electron-electron Coulomb interaction and the third term is the attractive Coulomb interaction between electrons and ions. Since the mass of electrons is $\sim 10^4$ smaller than the mass of ions, we can consider that they adapt almost immediately to lattice distortions. This fact motivates us to treat the array of ions as a static lattice, where the positions of ions play the role of parameters, rather than degrees of freedom. This assumption is called Born-Oppenheimer approximation. Accordingly, the electron-

ion interaction acts as a static potential where the only degrees of freedom correspond to the position of the electron. Let us thus stop indicating the positions of ions:

$$H = -\sum_i \frac{1}{2}\nabla_i^2 + \sum_i \sum_{j\neq i} \frac{1}{|\boldsymbol{r}_i - \boldsymbol{r}_j|} + \sum_i V(\boldsymbol{r}_i). \tag{2.2}$$

Note that the electron-electron interaction couples the degrees of freedom of different electrons, so that the dynamics of an electron depends on the rest of electrons. This fact makes the calculation of eigenvalues and eigenvectors of the Hamiltonian in Eq. (2.2) one of the most challenging and crucial problems of condensed matter physics. In mathematical terms, the electron-electron interaction prevents us from writing the electronic Hamiltonian as a sum of single-electron Hamiltonians. For instance, let us consider that the electron interaction is weak enough to neglect it. Then, the electronic Hamiltonian becomes:

$$H = -\sum_i \frac{1}{2}\nabla^2 + \sum_i V(\boldsymbol{r}) = \sum_i H_i, \tag{2.3}$$

where $H_i = -\nabla^2/2 + V(\boldsymbol{r})$ is the single-electron Hamiltonian. The eigenvalues of the Hamiltonian in Eq. (2.3) are constructed as sums of eigenvalues of H_i; similarly, the eigenstates of H are constructed as products of the eigenstates of H_i. Therefore, neglecting the electron-electron interaction reduces the eigenvalue/eigenstate problem of H to that of H_i.

The key question is the following: is neglecting the electron-electron interaction always a good approximation? Unfortunately, the answer is no. This approximation breaks down for the so-called **strongly correlated systems**, as it does not lead to a realistic description of their electronic properties. Nevertheless, it works well for a big number of materials. Furthermore, it sets a starting point to later study the effect of strong correlations. The investigation of the electronic structure of weakly-interacting materials is therefore an important task of condensed matter physics.

2.2 Eigenstates and spectrum of the single-particle periodic Hamiltonian

From now on, let us denote H the independent-particle Hamiltonian H_i, i.e. $H_i \to H$:

$$H = -\frac{1}{2}\nabla^2 + V(\boldsymbol{r}). \tag{2.4}$$

We might wonder about how the spectrum and eigenstates of H look like. Even though the details depend on the actual material, there are some features that are common to all crystals. Let us anticipate some of them.

The bound states of the hydrogen atom form a discrete energy spectrum and they are localized on the actual position of the atom. In the next step of complexity, atoms get together to form molecules. The energy levels of molecules are also discrete, but the corresponding states are not localized on a single atom. Instead, they might contain contributions from many atoms, which physically means that there is a finite probability to find an electron around different sites. In the same spirit, when atoms form a crystal arrangement, we might expect that the spectrum of H will also be discrete and that the corresponding eigenstates might be delocalized through the whole crystal.

Let us now support our intuition with mathematically rigorous arguments. An important difference between molecules (or an isolated atom) and a crystal is that, in the later, atoms form a periodic arrangement. For the sake of simplicity, let us consider a 1D chain of atoms that repeats $\mathcal{N}$ times with periodicity a, as illustrated in Fig. **2.1**(a). Note that the length L of the chain is $\mathcal{N}a$. The fact that the pattern is periodic means that the electron-ion potential $V(r)$ [also H] in Eq. (2.4) is invariant under the translation by a distance a, i.e. $V(r-a) = V(r)$. As a consequence, H must commute with the operator T_a corresponding to the translation by a distance a: $[H, T_a] = 0$. Therefore, there exists a set of functions $\psi_k(r)$ that are at the same time eigenstates of H and T_a:

$$\begin{aligned} H\psi_k(r) &= \epsilon_k \psi_k(r), \\ T_a\psi_k(r) &= \varphi_k \psi_k(r), \end{aligned} \tag{2.5}$$

We consider now that the translation is applied N times:

$$T_a^{\mathcal{N}}\psi_k(r) = \varphi_k^{\mathcal{N}}\psi_k(r). \tag{2.6}$$

On the other hand,

$$T_a^{\mathcal{N}}\psi_k(r) = \psi_k(r - \mathcal{N}a). \tag{2.7}$$

Since we are more interested in the bulk of the system than on the boundaries, we can adopt periodic boundary conditions by assuming that the $\mathcal{N}^{\text{th}}$ site of the lattice is identical to the beginning of the chain, as it is illustrated in Fig. **2.1**(b). Then, $\psi_k(r - \mathcal{N}a) = \psi_k(r)$, and Eqs. (2.6) and (2.7) to be compatible:

$$\varphi_k = e^{i2\pi n/\mathcal{N}} = e^{i(2\pi n/L)a} = e^{ik\cdot a}, \tag{2.8}$$

where $n = 0, ..., \mathcal{N}-1$ and $k = 2\pi n/L$. Therefore, there exist $\mathcal{N}$ different states $\psi_k(r)$, so that each of these has in correspondence the eigenvalue $e^{ik\cdot a}$ of translation T_a and an energy level ϵ_k. The set of energy levels ϵ_k forms thus a discrete spectrum, as we anticipated.

It is not difficult to extend this result to higher dimensions. For instance, let us say that in 3D the primitive lattice translations are given by vectors $\boldsymbol{a}_1$, $\boldsymbol{a}_2$ and $\boldsymbol{a}_3$. Each of these translations has in correspondence a set of eigenvalues $e^{i(2\pi n_i/L_i)a_i}$,

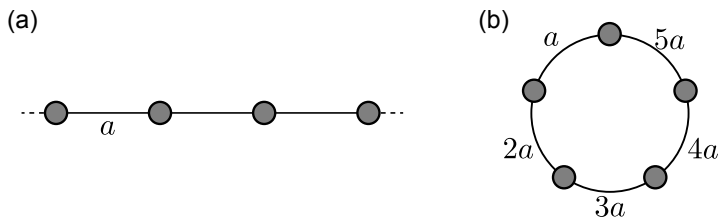

Figure 2.1: (a) 1D chain of periodicity a considered for the demonstration of Bloch's theorem. (b) Illustration of periodic boundary conditions for a 1D chain of $\mathcal{N} = 5$ cells and length $L = 5a$.

where $n_i = 0, ..., \mathcal{N}_i$ and L_i is the length of the crystal along the i^{th}-direction. Since translations commute[1], the eigenvalue of the operator of a general lattice translation $t = m_1\boldsymbol{a}_1 + m_2\boldsymbol{a}_2 + m_3\boldsymbol{a}_3$ is:

$$\varphi_{\boldsymbol{k}}(\boldsymbol{t}) = e^{i(2\pi n_1/L_1)\cdot m_1 a_1} e^{i(2\pi n_2/L_2)\cdot m_2 a_2} e^{i(2\pi n_3/L_3)\cdot m_3 a_3}. \tag{2.9}$$

Let $\boldsymbol{b}_1$, $\boldsymbol{b}_2$ and $\boldsymbol{b}_3$ denote the dual vectors of $\boldsymbol{a}_1$, $\boldsymbol{a}_2$ and $\boldsymbol{a}_3$, which are defined as to satisfy the following relations:

$$\boldsymbol{b}_i \cdot \boldsymbol{a}_j = 2\pi\delta_{ij}. \tag{2.10}$$

The vectors $\boldsymbol{b}_i$ form the so-called **reciprocal lattice**. We can then rewrite the translation eigenvalue in Eq. (2.9) as:

$$\varphi_{\boldsymbol{k}}(\boldsymbol{t}) = e^{i\boldsymbol{k}\cdot\boldsymbol{t}}, \tag{2.11}$$

where $\boldsymbol{k} = n_1/\mathcal{N}_1\ \boldsymbol{b}_1 + n_2/\mathcal{N}_2\ \boldsymbol{b}_2 + n_3/\mathcal{N}_3\ \boldsymbol{b}_3$. In conclusion, the eigenstates of the Hamiltonian of an electron in a periodic lattice are labeled by $\boldsymbol{k}$. This vector belongs to the **reciprocal space** where the reciprocal lattice formed by vectors $\boldsymbol{b}_i$ is defined. Like in the 1D case, two vectors $\boldsymbol{k}$ and $\boldsymbol{k}'$ which differ by a vector $\boldsymbol{G} = \sum_{i=1}^{3} n_i\boldsymbol{b}_i$ (with $n_i = 0, ..., \mathcal{N}_i - 1$) of the reciprocal lattice have in correspondence the same eigenvalues of translation and are hence equivalent, in the sense that they have in correspondence the same state $\psi_{\boldsymbol{k}}(\boldsymbol{r})$. This equivalence relation allows us to adopt as domain of definition of $\boldsymbol{k}$ a connected region centered around the origin $\boldsymbol{k} = \boldsymbol{0}$ which contains all non-equivalent $\boldsymbol{k}$-vectors but not equivalent vectors. When this region is chosen to have the same point group symmetries as the crystal, it is called 1^{st} Brillouin zone (BZ). Another possible choice is a parallelepiped with a vertex sitting at the origin whose edges are parallel and equal in length to $\boldsymbol{b}_1$, $\boldsymbol{b}_2$ and $\boldsymbol{b}_3$. Even if these choices do not coincide for many crystals, we will refer as Brillouin zone to any region defined in either of this forms.

In order to look in more detail into the form of a state $\psi_{\boldsymbol{k}}(\boldsymbol{r})$, let us suppose that it can be written as $\psi_{\boldsymbol{k}}(\boldsymbol{r}) = \exp(-i\boldsymbol{k}\cdot\boldsymbol{r})u_{\boldsymbol{k}}(\boldsymbol{r})$. If we consider the action of the translation

[1] In terms of group theory, the group of translations is abelian.

by a vector $\boldsymbol{t}$ of the Bravais lattice, which is given by the operator $T_{\boldsymbol{t}}$:

$$T_{\boldsymbol{t}}\psi_{\boldsymbol{k}}(\boldsymbol{r}) = \psi_{\boldsymbol{k}}(\boldsymbol{r}-\boldsymbol{t}) = \exp(i\boldsymbol{k}\cdot\boldsymbol{t})\exp(-i\boldsymbol{k}\cdot\boldsymbol{r})u_{\boldsymbol{k}}(\boldsymbol{r}-\boldsymbol{t}). \tag{2.12}$$

On the other hand, $\psi_{\boldsymbol{k}}(\boldsymbol{r})$ is an eigenstate of $T_{\boldsymbol{t}}$ with eigenvalue (2.11), which sets the following constrain on $u_{\boldsymbol{k}}(\boldsymbol{r})$:

$$u_{\boldsymbol{k}}(\boldsymbol{r}-\boldsymbol{t}) = u_{\boldsymbol{k}}(\boldsymbol{r}). \tag{2.13}$$

We have thus shown that the eigenstates of the periodic Hamiltonian can be written as the product of a plane wave and a function with the same periodicity as the Bravais lattice. This result is known as **Bloch's theorem**.

The probability $P(\boldsymbol{r})$ for an electron in the state $\psi_{\boldsymbol{k}}(\boldsymbol{r})$ to be found around the position $\boldsymbol{r}$ is given by $P(\boldsymbol{r}) = |u_k(\boldsymbol{r})|^2$. This probability has thus the same periodicity as the lattice of atoms, which means that the electron is delocalized through the whole crystal, as we predicted based on our intuition.

Let us summarize the key ideas presented in this section. First, we have shown that every eigenstate $\psi_{\boldsymbol{k}}(\boldsymbol{r})$ of the Hamiltonian of an electron in a periodic lattice has in correspondence a vector $\boldsymbol{k}$. This vector belongs to the reciprocal space; furthermore, it can be chosen to belong to the BZ. The energy levels $\epsilon_{\boldsymbol{k}}$ corresponding to the states $\psi_{\boldsymbol{k}}(\boldsymbol{r})$ are discrete[2] and form a band structure defined in reciprocal space. Second, we have given a proof of Bloch's theorem, which states that $\psi_{\boldsymbol{k}}(\boldsymbol{r})$ can be written as $\psi_{\boldsymbol{k}}(\boldsymbol{r}) = \exp(-i\boldsymbol{k}\cdot\boldsymbol{r})u_{\boldsymbol{k}}(\boldsymbol{r})$, where $u_{\boldsymbol{k}}(\boldsymbol{r})$ is a function with the same periodicity as the crystal lattice. An electron sitting on such a state is delocalized through the whole crystal, rather than being bound to a particular atom.

[2]It should be mentioned that, in practical terms, it is often considered that the energy levels $\epsilon_{\boldsymbol{k}}$ form a continuum, based on the thermodynamic limit where the number of cells is taken to infinity ($\mathcal{N} \to \infty$).

3 Alternative derivation of band topology from a geometrical perspective of adiabatic transport

In this chapter, we will present the result of a collaboration with Dr. Barry Bradlyn, from the University of Illinois Urbana-Champaign. It consists in an alternative perspective to look into the topology of band structures. Basically, we will show how Berry phases and Wilson loops arise within the framework of adiabatic transport, to later focus on their capacity for diagnosing topology and their relation with the localization of electrons in crystals.

The content of the chapter is organized in the following way: In Sec. 3.1, we will present the Berry connection and holonomy in terms of adiabatic transport. The way in which adiabatic transport relates to the band structure of crystals will also be explained. Then, in Sec. 3.2, we will come in contact with the physical consequences of the Berry phase by relating it to the electric polarization in a one-dimensional chain. Wannier and hybrid-Wannier functions will be introduced in Sec. 3.3, which will allow us to get a grasp on the relation between real-space localization of charge and Berry phases. Finally, Sec. 3.4 will be devoted to Wilson loops; apart from giving a definition for them, we will show how symmetries set constrains on them. Moreover, we will give a demonstration of the capacity of Wilson loops for differentiating topologically distinct sets of bands, and we will show how the fact that topological bands present an obstruction to charge localization manifests itself in the Wilson loop.

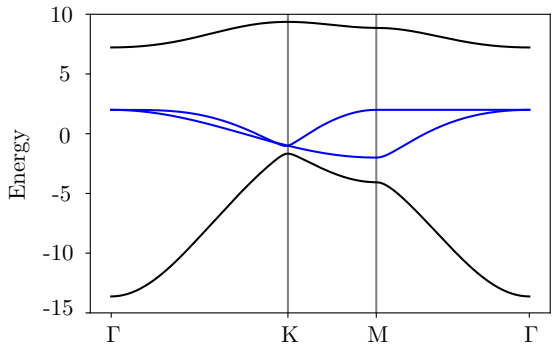

Figure 3.1: The concept of adiabatic transport is applicable to band structures defined in the reciprocal space of a periodic system, where the vector $\boldsymbol{k}$ in the Brillouin zone plays the role of the set of parameters $\boldsymbol{\lambda}$. In this figure, we show an example of such an application: the blue bands form the family of states $\mathcal{R}(\boldsymbol{k})$ in the image of the projector $P(\boldsymbol{k})$, which are separated from states belonging to the rest of bands (black).

3.1 Parametric Hamiltonians and parallel transport

We will start this section by presenting the formalism of adiabatic transport quite generally, where the concepts of parallel transport, Berry connection and holonomy defined in parameter space will arise. The point of view we will adopt is slightly more geometrical than that given in introductory books – more details about this approach can be found in Refs. [81, 82]. Then, we will show how these concepts apply in a particular example: spin-1/2 in a magnetic field. Finally, we will show that the set of Bloch Hamiltonians written as a function of crystal momentum $\boldsymbol{k}$ forms the kind of parametric family of Hamiltonian considered in the quantum adiabatic theorem.

3.1.1 Adiabatic transport

Let us assume that the Hamiltonian H of our system depends on a set of parameters λ_i, i.e. $H = H(\lambda_1, \lambda_2, \cdots, \lambda_M)$, where $i = 1, \cdots, M$. We can think that every particular choice of these parameters is represented by a vector $\boldsymbol{\lambda} = (\lambda_1, \lambda_2, \cdots, \lambda_M)$ which belongs to a smooth space $\mathcal{M}$ of dimension M called **parameter space**. When considering the application to crystals, the role of parameter space and $\boldsymbol{\lambda}$ will be played by the Brillouin zone and vectors $\boldsymbol{k}$ belonging to it, respectively.

We can also consider that our Hamiltonian forms a family of parametric Hamiltonians $\{H(\boldsymbol{\lambda}),\ \boldsymbol{\lambda} \in \mathcal{M}\}$. We will take $H(\boldsymbol{\lambda})$ to have a discrete spectrum for every $\boldsymbol{\lambda}$. Furthermore, let us suppose we have a collection of N states

$$\mathcal{R}(\boldsymbol{\lambda}) = \{\, |\psi_n(\boldsymbol{\lambda})\rangle\,,\ n = 1, ..., N\}, \tag{3.1}$$

so that

$$H(\boldsymbol{\lambda})\,|\psi_n(\boldsymbol{\lambda})\rangle = E_n(\boldsymbol{\lambda})\,|\psi_n(\boldsymbol{\lambda})\rangle\,, \tag{3.2}$$

and that there exists a $\Delta > 0$ such that for every $\boldsymbol{\lambda}$ and $|\varphi\rangle \notin \mathcal{R}(\boldsymbol{\lambda})$ satisfying $H(\boldsymbol{\lambda})\,|\varphi\rangle = E(\boldsymbol{\lambda})\,|\varphi\rangle$ we have

$$\min_n |E(\boldsymbol{\lambda}) - E_n(\boldsymbol{\lambda})| \geq \Delta, \tag{3.3}$$

i.e. our family $\mathcal{R}(\boldsymbol{\lambda})$ is gapped from all other states in the spectrum for all $\boldsymbol{\lambda} \in \mathcal{M}$.

At the same time, we can define the hermitian operator $P(\boldsymbol{\lambda})$ as

$$P(\boldsymbol{\lambda}) = \frac{1}{2\pi i} \oint_{C(\boldsymbol{\lambda})} \frac{\mathbb{1}}{z - H(\boldsymbol{\lambda})} dz, \tag{3.4}$$

where $C(\boldsymbol{\lambda})$ is a contour in the complex plane enclosing all the $E_n(\boldsymbol{\lambda})$ and no other eigenvalues of $H(\boldsymbol{\lambda})$. The fact that our family of states is gapped allows us to choose such a contour. We denote $|\phi_i\rangle$ an eigenstate of $H(\boldsymbol{\lambda})$ with energy $E_i(\boldsymbol{\lambda})$ and let us act on this state with $P(\boldsymbol{\lambda})$:

$$P(\boldsymbol{\lambda})\,|\phi_i\rangle = \frac{1}{2\pi i} \oint_{C(\boldsymbol{\lambda})} \frac{\mathrm{d}z}{z - E_i(\boldsymbol{\lambda})}\,|\phi_i\rangle = \begin{cases} |\phi_i\rangle & \text{if } E_i(\boldsymbol{\lambda}) \in C(\boldsymbol{\lambda}), \\ 0 & \text{otherwise.} \end{cases} \tag{3.5}$$

where we have applied Cauchy's integral theorem. It immediately follows from Eq. 3.5 that $P^2(\boldsymbol{\lambda}) = P(\boldsymbol{\lambda})$, i.e. $P(\boldsymbol{\lambda})$ is idenpotent. Therefore, $P(\boldsymbol{\lambda})$ is a **projection operator**. Apart from idenpotence, the following properties also follow from the definition in Eq. (3.4):

Property 1: $[H, P(\boldsymbol{\lambda})] = 0$,

Property 2: $P(\boldsymbol{\lambda})\,|\psi_n(\boldsymbol{\lambda})\rangle = |\psi_n(\boldsymbol{\lambda})\rangle,\ \forall \boldsymbol{\lambda} \in \mathcal{M}$ and $|\psi_n(\boldsymbol{\lambda})\rangle \in \mathcal{R}(\boldsymbol{\lambda})$,

Property 3: rank $P(\boldsymbol{\lambda}) = N$.

On the one hand, by virtue of these properties, $P(\boldsymbol{\lambda})$ could have been defined in terms of the states $\mathcal{R}(\boldsymbol{\lambda})$ as:

$$P(\boldsymbol{\lambda}) = \sum_{n=1}^{N} |\psi_n(\boldsymbol{\lambda})\rangle\langle\psi_n(\boldsymbol{\lambda})|\,. \tag{3.6}$$

On the other hand, it is clear that $\mathcal{R}(\boldsymbol{\lambda})$ span the image of $P(\boldsymbol{\lambda})$ and hence we could define our set of states $\mathcal{R}(\boldsymbol{\lambda})$ from $P(\boldsymbol{\lambda})$:

$$\mathcal{R}(\boldsymbol{\lambda}) = \mathrm{Im}[P(\boldsymbol{\lambda})]. \tag{3.7}$$

It is not particularly relevant that $P(\boldsymbol{\lambda})$ was defined from a Hamiltonian. What is important is that we have a well defined family of states and a projection onto the subspace spanned by these. Indeed, the formalism we will introduce below holds equally well for projectors onto families of quantum states, projectors onto the tangent spaces of manifolds, as well as more general fiber bundles [83, 84].

In the language of projectors, the well-known adiabatic theorem takes a particularly geometrical form, first illustrated by Kato [85]: consider a path $\boldsymbol{\lambda}(t),\ t \in [0, \tau]$ in the parameter space $\mathcal{M}$, such that $\tau \to \infty$ ($\Delta\tau >> 1$) for fixed endpoints of the path. Notice that t can be interpreted as a scalar playing the role of time. Then the quantum adiabatic theorem is the statement that the exact projector $P(t)$ at time t is approximately equal to our projector $P(\boldsymbol{\lambda}(t))$ onto the space spanned by $R(\boldsymbol{\lambda}(t))$:

$$P(t) = U(t)P(0)U^{\dagger}(t) \approx P(\boldsymbol{\lambda}(t)), \tag{3.8}$$

where $U(t)$ is the time-evolution operator corresponding to the Hamiltonian $H(\boldsymbol{\lambda}(t))$.

We might ask ourselves how could the projector $P(t)$ be different from $P(\boldsymbol{\lambda}(t))$. Let us suppose that at $t = 0$ the operator $P(\boldsymbol{\lambda}(0))$ is the projector onto the states $\mathcal{R}(\boldsymbol{\lambda}(0))$ we are interested in, i.e. $P(0) = P(\boldsymbol{\lambda}(0)) = \sum_{n=1}^{N} |\psi_n(0)\rangle\langle\psi_n(0)|$. At time $t > 0$, after the system is taken along the path parametrized by $\boldsymbol{\lambda}(t)$, the operator $P(t)$ could in principle contain projections into states $|\psi_n(\boldsymbol{\lambda}(t))\rangle \notin \mathcal{R}(\boldsymbol{\lambda}(t))$ and thus be different from $P(\boldsymbol{\lambda}(t))$. In other words, the space into which $P(t)$ projects might be different from $\mathcal{R}(\boldsymbol{\lambda}(t))$. The quantum adiabatic theorem in Eq. (3.8) consists in assuming that, as the system is driven along a path in parameter space, the exact projector $P(t)$ does not involve projections out of $R(\boldsymbol{\lambda}(t))$ and can thus be substituted by $P(\boldsymbol{\lambda}(t))$.

Following Kato's approach [85], let us introduce an adiabatic evolution operator $U_A(t)$ which drives the evolution of $P(\boldsymbol{\lambda}(t))$:

$$P(\boldsymbol{\lambda}(t)) = U_A(t)P(0)U_A^{\dagger}(t). \tag{3.9}$$

In order to obtain an expression for $U_A(t)$, we will first derive the differential equation that it satisfies. Let us for that differentiate in both sides of Eq. (3.9) and apply the identity $U_A\dot{U}_A^{\dagger} = -\dot{U}_A U_A^{\dagger}$, which follows from the unitarity of $U_A(t)$:

$$\begin{aligned} i\dot{P} &= i\Big[\dot{U}_A P(0)U_A^{\dagger} + U_A P(0)\dot{U}_A^{\dagger}\Big] \\ &= i\Big(\dot{U}_A U_A^{\dagger} U_A P(0)U_A^{\dagger} - U_A P(0)U_A^{\dagger}\dot{U}_A U_A^{\dagger}\Big) \\ &= \Big[i\dot{U}_A U_A^{\dagger}, P\Big]. \end{aligned} \tag{3.10}$$

By applying the property $P\dot{P}P = 0$, it can be shown [76] that Eq. (3.10) is satisfied by

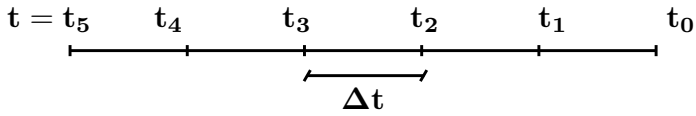

Figure 3.2: Time-slicing adopted in the discretization of the path ordered exponential of Eq. (3.14), for $N = 5$. Note that time increases to the left.

any $U_A(t)$ which also satisfies the following equation:

$$\dot{U}_A U_A^\dagger = [\dot{P}, P] + f(H(\boldsymbol{\lambda})). \tag{3.11}$$

Eq. (3.11) is the differential equation for $U_A(t)$ that we were looking for. Here, $f(x)$ is an arbitrary function of x. Choosing $f(x) = x$ leads to an adiabatic evolution operator that correctly accounts for the dynamical phase individual states acquire during evolution [82, 86]. For this choice it is possible to derive an expression of the difference between $U_A(t)$ and $U(t)$ [82]:

$$U_A^\dagger(t)U(t) - \mathbb{1} = \mathcal{O}(1/\tau). \tag{3.12}$$

This equation is a quantitative expression for the quantum adiabatic theorem stated in Eq. (3.9): when the time needed to complete the path in parameter space is large ($\tau \to \infty$), the evolution governed by $U(t)$ may be substituted by the adiabatic evolution described by $U_A(t)$. Equivalently, the exact projector $P(t)$ can be substituted by the projector $P(\boldsymbol{\lambda}(t))$ into the subspace $\mathcal{R}(\boldsymbol{\lambda}(t))$.

Since we are interested primarily in the behavior of the subspace $\mathcal{R}(\boldsymbol{\lambda})$, however, we can make the simpler choice $f = 0$. This leads to the following simplified differential equation for the adiabatic evolution operator:

$$\dot{U}_A = [\dot{P}, P]U_A \equiv \mathcal{A}_s U_A. \tag{3.13}$$

The solution of this equation is a path-ordered exponential:

$$U_A(t) = \mathcal{P}e^{\int_0^t \mathcal{A}_s dt'} \equiv \lim_{\Delta t \to 0} e^{\mathcal{A}_s(t_N)\Delta t} e^{\mathcal{A}_s(t_{N-1})\Delta t} \dots e^{\mathcal{A}_s(t_0)\Delta t}, \tag{3.14}$$

where $t_N = t$, $t_j = j\Delta t$ and $j = 0, ..., N$ (see Fig. **3.2**). Note that since

$$\mathcal{A}_s dt = [\partial_{\boldsymbol{\lambda}} P, P] \cdot \dot{\boldsymbol{\lambda}}(t) dt = [\partial_{\boldsymbol{\lambda}} P, P] \cdot d\boldsymbol{\lambda}, \tag{3.15}$$

the integral expression for $U_A(t)$ is **independent** of the rate at which t is varied, and only depends on the particular adiabatic path from the initial point $\boldsymbol{\lambda}_i = \boldsymbol{\lambda}(t = 0)$ to the final point $\boldsymbol{\lambda}_f = \boldsymbol{\lambda}(t)$ in parameter space. Thus, U_A is a **geometric** quantity and it is purely determined from the geometry of the projectors $P(\boldsymbol{\lambda})$.

This discussion becomes even nicer if we restrict our attention to states $|\varphi(\boldsymbol{\lambda})\rangle \in$

$\mathrm{Im}[P(\boldsymbol{\lambda})]$. Consistent with the facts that $P(\boldsymbol{\lambda}) = U_A P(0) U_A^\dagger$ and $P(\boldsymbol{\lambda})\,|\varphi(\boldsymbol{\lambda})\rangle = |\varphi(\boldsymbol{\lambda})\rangle$, we have

$$|\varphi(\boldsymbol{\lambda})\rangle = U_A\,|\varphi(0)\rangle\,. \tag{3.16}$$

This looks like the time-evolution of states in the Schrödinger picture, with U_A playing the role of time-evolution operator. Differentiating this expression yields:

$$\partial_{\boldsymbol{\lambda}}\,|\varphi(\boldsymbol{\lambda})\rangle = \partial_{\boldsymbol{\lambda}} U_A\,|\varphi_0\rangle = [\partial_{\boldsymbol{\lambda}} P, P]\,|\varphi(\boldsymbol{\lambda})\rangle = [\partial_{\boldsymbol{\lambda}} P, P]P\,|\varphi(\boldsymbol{\lambda})\rangle\,, \tag{3.17}$$

and hence

$$[\partial_{\boldsymbol{\lambda}} - (\partial_{\boldsymbol{\lambda}} P)P]\,|\varphi(\boldsymbol{\lambda})\rangle = 0. \tag{3.18}$$

Eq. (3.17) is known as the **parallel transport** equation. It tells us that under adiabatic evolution, the projection of states into the subspace of interest does not change; thus it is a generalization of transporting a vector along a curve such that the angle of the vector with a line tangent to the curve is constant. The quantity $[\partial_{\boldsymbol{\lambda}} P, P]P$ [or equivalently, $(\partial_{\boldsymbol{\lambda}} P)P$] is known as the **adiabatic (Berry) connection**, analogous to the Christoffel Levi-Civita connection in General Relativity. Note also that the adiabatic connection is precisely $\boldsymbol{\mathcal{A}}_s = (\partial_{\boldsymbol{\lambda}} P)P$ from Eq. (3.15).

This operator form of the connection is closely related to the more conventional form, which expresses Eq. (3.17) in a fixed coordinate system: let $\{|\psi_n(\boldsymbol{\lambda})\rangle\}$ be a basis for $\mathrm{Im}[P(\boldsymbol{\lambda})]$, with $n = 1, ..., N$, so that $P(\boldsymbol{\lambda})$ can be written as in Eq. (3.6). Then, by applying $|\varphi(\boldsymbol{\lambda})\rangle = \sum_{n=1}^{N} a_n(\boldsymbol{\lambda})\,|\psi_n(\boldsymbol{\lambda})\rangle$ in Eq. (3.18):

$$\begin{aligned} 0 &= \partial_{\boldsymbol{\lambda}}\,|\varphi\rangle - (\partial_{\boldsymbol{\lambda}} P)\,|\varphi\rangle \\ &= \sum_{n=1}^{N}\left[(\partial_{\boldsymbol{\lambda}} a_n)\,|\psi_n\rangle + a_n\,|\partial_{\boldsymbol{\lambda}}\psi_n\rangle - a_n\,|\partial_{\boldsymbol{\lambda}}\psi_n\rangle - \sum_{m=1}^{N}|\psi_m\rangle\,\langle\partial_{\boldsymbol{\lambda}}\psi_m|\psi_n\rangle\,a_n\right] \\ &= \sum_{n=1}^{N}\left[\partial_{\boldsymbol{\lambda}} a_n + \sum_{m=1}^{N}\langle\psi_n|\partial_{\boldsymbol{\lambda}}\psi_m\rangle\,a_m\right]|\psi_n\rangle = 0, \end{aligned} \tag{3.19}$$

where we have applied the relation $\langle\partial_{\boldsymbol{\lambda}}\psi_m|\psi_n\rangle = -\langle\psi_m|\partial_{\boldsymbol{\lambda}}\psi_n\rangle$ to go from the second line to the third line, and we have suppressed the explicit dependence on $\boldsymbol{\lambda}$ of coefficients and states for the sake of clarity. Since the states $\{|\psi_n(\boldsymbol{\lambda})\rangle\}$ form a basis of the subspace $\mathrm{Im}[P(\boldsymbol{\lambda})]$, they are linearly independent, which means that a linear combination of them could be zero if and only if all the coefficients are zero. The parallel transport equation then implies

$$\partial_{\boldsymbol{\lambda}} a_n - i\sum_{m=1}^{N}\mathbf{A}_{nm}(\boldsymbol{\lambda})a_m = 0, \tag{3.20}$$

where $\mathbf{A}_{nm}(\boldsymbol{\lambda}) = i\,\langle\psi_n|\partial_{\boldsymbol{\lambda}}\psi_m\rangle$ is the usual Berry connection. Whether we use $\boldsymbol{\mathcal{A}}_s$ or $\mathbf{A}_{nm}$ depends on whether we view our adiabatic transformation as acting on basis vectors

or coordinate functions: when we use $\boldsymbol{\mathcal{A}}_s$, we view the adiabatic transformation as a unitary operator on the (basis) states of our Hilbert space. Contrarily, we use $\mathbf{A}_{nm}$ when we view the adiabatic transformation as a matrix acting on the coordinate vector for a state in the space

$$\mathcal{R} = \bigcup_{\boldsymbol{\lambda}} \mathrm{Im}[P(\boldsymbol{\lambda})]. \tag{3.21}$$

Both approaches contain equivalent information when restricted to the subspaces $\mathrm{Im}[P(\boldsymbol{\lambda})]$. However, note that we must find a differentiable basis for $\mathrm{Im}[P(\boldsymbol{\lambda})]$ in order to define $\mathbf{A}_{nm}(\boldsymbol{\lambda})$, while no such choice is needed to define $\boldsymbol{\mathcal{A}}_s(\boldsymbol{\lambda})$.

In terms of coordinates, we can solve Eq. (3.20) to find:

$$a_n(\boldsymbol{\lambda}) = \left[\mathcal{P} e^{i\int_0^{\boldsymbol{\lambda}} \boldsymbol{A}(\boldsymbol{\lambda}')\cdot d\boldsymbol{\lambda}'}\right]_{nm} a_m(\mathbf{0}) \equiv W_{nm}(\boldsymbol{\lambda}) a_m(\mathbf{0}). \tag{3.22}$$

In particular, by choosing $|\varphi(0)\rangle = |\psi_m(\mathbf{0})\rangle$ in Eq. (3.16) and applying Eq. (3.22), we derive:

$$\langle \psi_n(\boldsymbol{\lambda}) | U_A | \psi_m(\mathbf{0})\rangle = W_{nm}(\boldsymbol{\lambda}). \tag{3.23}$$

The matrix W is not invariant under $U(N)$ basis rotations. In fact, it transforms in the following way under the basis transformation represented by the matrix $\mathcal{U}(\boldsymbol{\lambda}) \in U(N)$:

$$W'_{nm}(\boldsymbol{\lambda}) = [\mathcal{U}^\dagger(\boldsymbol{\lambda}) U_A \mathcal{U}(\mathbf{0})]_{nm}, \tag{3.24}$$

Nevertheless, this expression becomes a similarity relation if we consider a **closed path** with $|\psi_n(\boldsymbol{\lambda})\rangle = |\psi_n(\mathbf{0})\rangle$. This implies that for closed paths the spectrum of W is basis independent. We call the matrix W for a closed path the **holonomy** of the adiabatic connection around that path.

We will now derive a particularly useful expression for $W(\boldsymbol{\lambda})$ that does not depend on the basis states. Let us for that define the operator $\mathcal{W}(\boldsymbol{\lambda})$ as:

$$\mathcal{W}(\boldsymbol{\lambda}) \equiv P(\boldsymbol{\lambda}) U_A P(\mathbf{0}), \tag{3.25}$$

which implements the parallel transport on $\mathcal{R}$. Eq. (3.23) shows that $\mathcal{W}(\boldsymbol{\lambda})$ and $W(\boldsymbol{\lambda})$ share the same nonzero spectrum in the fixed basis[1] $\{|\psi_n(\boldsymbol{\lambda})\rangle\}$. Furthermore, W_{nm} can be understood as a matrix element of $\mathcal{W}$ in the subspace $\mathcal{R}$.
Note that since $P(\boldsymbol{\lambda}) = U_A(\boldsymbol{\lambda}) P(\mathbf{0}) U_A^\dagger(\boldsymbol{\lambda})$, we can write

$$\mathcal{W}(\boldsymbol{\lambda}) = P(\boldsymbol{\lambda}) U_A(\boldsymbol{\lambda}) P(\mathbf{0}) = U_A(\boldsymbol{\lambda}) P(\mathbf{0}) U_A^\dagger(\boldsymbol{\lambda}) U_A(\boldsymbol{\lambda}) P(\mathbf{0}) = U_A(\boldsymbol{\lambda}) P(\mathbf{0}). \tag{3.26}$$

By taking a derivative and using Eq. (3.13) for U_A, we deduce that $\mathcal{W}(\boldsymbol{\lambda})$ satisfies the

[1] W is an operator defined in the subspace of interest $\mathcal{R}$. In other words, we can write its matrix elements only for states $|\psi_n\rangle \in \mathcal{R}$. In contrast, $\mathcal{W}$ is defined in the whole Hilbert space. However, matrix elements $\langle \psi_l(\boldsymbol{\lambda}) | \mathcal{W} | \psi_s(0)\rangle$, where $|\psi_l\rangle$ or $|\psi_s\rangle$ do not belong to $\mathcal{R}$, are zero.

differential equation

$$\partial_{\boldsymbol{\lambda}}\mathcal{W}(\boldsymbol{\lambda}) = [\partial_{\boldsymbol{\lambda}}P, P]\mathcal{W}(\boldsymbol{\lambda}), \text{ with } \mathcal{W}(\mathbf{0}) = P(\mathbf{0}). \tag{3.27}$$

Looking at this differential equation and comparing it to $\partial_{\boldsymbol{\lambda}}U_A(\boldsymbol{\lambda}) = [\partial_{\lambda}P, P]U_A(\boldsymbol{\lambda})$, one might think that $\mathcal{W}(\boldsymbol{\lambda})$ and $U_A(\boldsymbol{\lambda})$ should be the same operator. However, since the initial conditions for $\mathcal{W}(\boldsymbol{\lambda})$ and $U_A(\boldsymbol{\lambda})$ are different, this is not the case. To find an expression for $\mathcal{W}(\boldsymbol{\lambda})$, let us first note that the infinite product

$$V(\boldsymbol{\lambda}) = \lim_{\Delta\boldsymbol{\lambda}\to 0} P(\boldsymbol{\lambda})P(\boldsymbol{\lambda}-\Delta\boldsymbol{\lambda})P(\boldsymbol{\lambda}-2\Delta\boldsymbol{\lambda})\ldots P(\Delta\boldsymbol{\lambda})P(\mathbf{0}) \equiv \prod_{\boldsymbol{\lambda}'}^{\boldsymbol{\lambda}\leftarrow\mathbf{0}} P(\boldsymbol{\lambda}') \tag{3.28}$$

satisfies the same initial condition as $\mathcal{W}(\boldsymbol{\lambda})$, i.e. $V(\mathbf{0}) = P(\mathbf{0})$. To prove that it also satisfies Eq. (3.27), we first take the derivative of $V(\boldsymbol{\lambda})$ to find

$$\partial_{\boldsymbol{\lambda}}V = \lim_{\boldsymbol{\Delta}\to\mathbf{0}} \frac{V(\boldsymbol{\lambda}+\boldsymbol{\Delta}) - V(\boldsymbol{\lambda})}{\boldsymbol{\Delta}} = \lim_{\boldsymbol{\Delta}\to\mathbf{0}} \frac{P(\boldsymbol{\lambda}+\boldsymbol{\Delta}) - P(\boldsymbol{\lambda})}{\boldsymbol{\Delta}} V(\boldsymbol{\lambda}) = [\partial_{\boldsymbol{\lambda}}P(\boldsymbol{\lambda})]V(\boldsymbol{\lambda}). \tag{3.29}$$

Using $P(\boldsymbol{\lambda})V(\boldsymbol{\lambda}) = V(\boldsymbol{\lambda})$ along with the relation $P(\boldsymbol{\lambda})[\partial_{\boldsymbol{\lambda}}P(\boldsymbol{\lambda})]P(\boldsymbol{\lambda}) = 0$ (which we have already met before), we find that

$$\begin{aligned} &\partial_{\boldsymbol{\lambda}}V = [\partial_{\boldsymbol{\lambda}}P, P]V, \\ &V(\mathbf{0}) = P(\mathbf{0}). \end{aligned} \tag{3.30}$$

Since $\mathcal{W}(\boldsymbol{\lambda})$ and $V(\boldsymbol{\lambda})$ satisfy the same ordinary differential equation and initial condition, they are the same operator. Thus we conclude that

$$\mathcal{W}(\boldsymbol{\lambda}) = \prod_{\boldsymbol{\lambda}'}^{\boldsymbol{\lambda}\leftarrow\mathbf{0}} P(\boldsymbol{\lambda}'). \tag{3.31}$$

Finally, since the matrix $W(\boldsymbol{\lambda})$ is obtained by restricting $\mathcal{W}(\boldsymbol{\lambda})$ to the subspace $\mathcal{R}$ of states, we deduce that the matrix elements of Eq. (3.31) between states in $\mathcal{R}$ give $W(\boldsymbol{\lambda})$.

Summing up, in this section we have first derived the parallel transport equation for the adiabatic evolution of a system through a path in parameter space, and defined the operator form of the Berry connection $\boldsymbol{\mathcal{A}}_s(\boldsymbol{\lambda})$ in this context. We have also derived an alternative expression for the Berry connection in terms of coefficients of the expansion, in a fixed basis, of a state in $\mathcal{R}$. Then, we have defined the operator $W(\boldsymbol{\lambda})$, whose spectrum in the subspace $\mathcal{R}$ is gauge invariant for closed paths in parameter space. Last, we showed how $\mathcal{W}(\boldsymbol{\lambda})$ can be written in terms of the projectors $P(\boldsymbol{\lambda})$.

Before moving on, let us show how the concepts of adiabatic transport apply to a particularly useful example: a spin-1/2 system under the influence of a magnetic field.

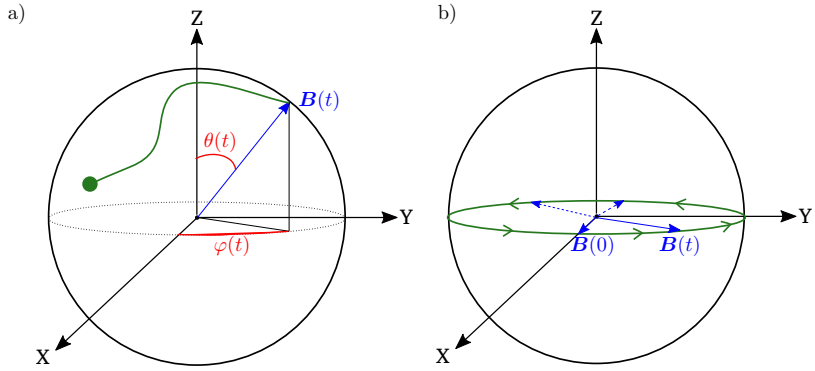

Figure 3.3: (a) general description of the magnetic field of constant magnitude involved in the problem (blue), a general path that the field can follow over the surface of the sphere (green) and the parametrization of the path in terms of the polar angle θ and azimutal angle φ (red). (b) The particular path $(\theta(t), \varphi(t)) \in \{(\pi/2, 2\pi t) \mid t \in [0, 1]\}$ studied in the text.

3.1.2 Example: Spin-1/2 in a magnetic field

Let us consider a magnetic field $\boldsymbol{B}(t)$ of constant magnitude $|\boldsymbol{B}(t)| = B_0$, whose direction rotates adiabatically with time. This means that, if we draw $\boldsymbol{B}(t)$, it traces out a continuous path over the surface of a sphere of radius B_0. We can write:

$$\boldsymbol{B}(t) = B_0 \hat{B}(t). \tag{3.32}$$

in terms of a unit vector $\hat{B}(t)$.

Let us write this vector in polar coordinates, which will be useful when specifying paths in the parameter space of the problem [e.g. as indicated in Fig. **3.3**(a)]:

$$\boldsymbol{B}(t) = B_0(\sin\theta(t)\cos\varphi(t), \sin\theta(t)\sin\varphi(t), \cos\theta(t)). \tag{3.33}$$

The dynamics of a spin-1/2 particle under the influence of this magnetic field can be described by a Zeeman-like Hamiltonian:

$$H(t) = -\mu \boldsymbol{B}(t) \cdot \boldsymbol{\sigma}, \tag{3.34}$$

where only the spin contributes to the energy. Here $\boldsymbol{\sigma} = (\sigma_x, \sigma_y, \sigma_z)$ is the vector of Pauli matrices. Note that the Hamiltonian of any gapped two-level system can be written in this form, modulo an overall energy shift. Therefore, the following discussion will be applicable to any two-level system, regardless of its physical origin.

Looking at the Hamiltonian (3.34), we see that we can consider the direction $\hat{B}(t)$ of the magnetic field as the parameter determining a family of parametric Hamiltonians.

That is, according to the notation adopted in this section, we can write $\boldsymbol{\lambda} = \hat{B}$. From Eq. (3.33), we see that our parameter space has dimension two: we need only specify θ and ϕ in order to uniquely determine $\hat{B}$. Thus, our parameter space is the two-dimensional sphere S^2, with coordinates

$$\mathcal{M} = S^2 = \{(\theta, \varphi) : \theta \in (0, \pi), \varphi \in (0, 2\pi)\}. \tag{3.35}$$

We take the subspace of interest at time t to be the low-energy eigenspace of the Hamiltonian $H(t)$. The projection operator onto this subspace can be written as

$$P(t) = 1/2(\mathbb{1} - \hat{B}(t) \cdot \boldsymbol{\sigma}), \tag{3.36}$$

where $\mathbb{1}$ is the 2×2 identity matrix. This can be seen by considering a frame that rotates together with the field and has the z-axis pointing along $\hat{B}(t)$. In such a frame, the Hamiltonian takes the simple form $H(\boldsymbol{\lambda}) = -\mu B_0 \sigma_z$. Note that we can equivalently, write the projector in terms of the value of $\boldsymbol{\lambda}$ reached at time t: $P(t) = 1/2(\mathbb{1} - \boldsymbol{\lambda} \cdot \boldsymbol{\sigma})$.

Now that we have the projector, we want to calculate the adiabatic evolution operator $U_A(\boldsymbol{\lambda})$ for a particular path in parameter space. We will do so in two steps. First, we will compute the Berry connection $\boldsymbol{\mathcal{A}}_s$. Second, we will solve Eq. (3.13). Starting with the first step, we apply our definition of Berry connection to find

$$\begin{aligned}
\mathcal{A}_s^{(i)}(\boldsymbol{\lambda}) &= [\partial_{\lambda_i} P(\boldsymbol{\lambda}), P(\boldsymbol{\lambda})] \\
&= [-1/2\sigma_i, 1/2(\mathbb{1} - \sum_j \lambda_j \sigma_j)] \\
&= \frac{1}{4} \sum_j \lambda_j [\sigma_i, \sigma_j] \\
&= \frac{i}{2} \sum_{jk} \epsilon_{ijk} \lambda_j \sigma_k.
\end{aligned} \tag{3.37}$$

Here, ϵ_{ijk} is the Levi-Civita symbol, and the indices i, j and k in the sums run over the three Cartesian directions. In the derivation, we have made use of the commutation relation $[\sigma_i, \sigma_j] = 2i \sum_k \epsilon_{ijk} \sigma_k$ satisfied by Pauli matrices. Then, by substitution into Eq. (3.13), we see that the dynamics of the adiabatic evolution operator is governed by

$$\dot{U}_A(\boldsymbol{\lambda}) = \dot{\boldsymbol{\lambda}} \cdot \boldsymbol{\mathcal{A}_s}(\boldsymbol{\lambda}) U_A(\boldsymbol{\lambda}) = \frac{i}{2} \sum_{ijk} \epsilon_{ijk} \dot{\lambda}_i \lambda_j \sigma_k U_A(\boldsymbol{\lambda}). \tag{3.38}$$

For the sake of clarity, we will write this once explicitly in cartesian components:

$$\dot{U}_A(\boldsymbol{\lambda}) = \frac{i}{2}\dot{\boldsymbol{\lambda}} \cdot (\boldsymbol{\lambda} \times \boldsymbol{\sigma})\, U_A(\boldsymbol{\lambda}) \tag{3.39}$$

$$= \frac{i}{2}[\dot{\lambda}_x(\lambda_y\sigma_z - \lambda_z\sigma_y) + \dot{\lambda}_y(\lambda_z\sigma_x - \lambda_x\sigma_z) + \dot{\lambda}_z(\lambda_x\sigma_y - \lambda_y\sigma_x)]U_A(\boldsymbol{\lambda}). \tag{3.40}$$

The next step is to integrate this expression to write $U_A(t)$ as a path ordered exponential. To go further, we can consider a particular path $(\theta(t), \varphi(t))$ in parameter space. Consider the following curve:

$$(\theta(t), \varphi(t)) = (\pi/2, 2\pi t), \quad t \in [0, 1], \tag{3.41}$$

which corresponds to starting with $\boldsymbol{B}(0)$ pointing along the positive x-axis, rotating its tip once around the equator, and returning to the initial point. We sketch this in Fig. **3.3**(b). Writing this path in terms of the vector $\boldsymbol{\lambda}(t)$, we have

$$\boldsymbol{\lambda}(t) = (\cos 2\pi t, \sin 2\pi t, 0). \tag{3.42}$$

Taking a time derivative yields

$$\dot{\boldsymbol{\lambda}}(t) = 2\pi(-\sin 2\pi t, \cos 2\pi t, 0). \tag{3.43}$$

Consequently, Eq. (3.38) becomes

$$\dot{U}_A(\boldsymbol{\lambda}) = -i\pi\sigma_z U_A. \tag{3.44}$$

Now, we can solve this equation, obtaining the adiabatic evolution operator:

$$U_A(t) = \exp\{-i\pi t\sigma_z\} = \cos(\pi t)\mathbb{1} - i\sin(\pi t)\sigma_z. \tag{3.45}$$

Let us show how $U_A(t)$ acts on the initial state $|\psi(0)\rangle = |-\rangle_x$ belonging to the subspace defined by the image of the projector $P(0)$,

$$|\psi(0)\rangle = |-\rangle_x = \frac{1}{\sqrt{2}}\begin{bmatrix}1\\-1\end{bmatrix}. \tag{3.46}$$

Acting with the adiabatic evolution operator, we find that the state at t is

$$|\psi(t)\rangle = U_A(t)\,|\psi(0)\rangle = \frac{1}{\sqrt{2}}\begin{bmatrix}\cos(\pi t) - i\sin(\pi t)\\ -\cos(\pi t) - i\sin(\pi t)\end{bmatrix}, \tag{3.47}$$

which can be written in the basis of $\{|+\rangle_x, |-\rangle_x\}$ as

$$|\psi(t)\rangle = \cos(\pi t)\,|-\rangle_x - i\sin(\pi t)\,|+\rangle_x. \tag{3.48}$$

Notice that, although at $t = 1$ we reach the initial point in parameter space, the state acquires an adiabatic (Berry) phase $|\psi(1)\rangle = -|\psi(0)\rangle$. In conclusion, when we adiabatically evolve over a closed loop in parameter space, the final state may not be the same as the initial state.

Eq. (3.48) can be interpreted in two equivalent ways. First, we may take the perspective where we view the initial state as

$$|\psi(0)\rangle = a_-(0)\,|-\rangle_x + a_+(0)\,|+\rangle_x\,, \tag{3.49}$$

with $a_+(0) = 0$ and $a_-(0) = 1$. Comparing Eq. (3.48) to Eq. (3.49), we conclude that $U_A(t)$ has evolved the coefficients of the expansion in this way:

$$\begin{aligned} a_+(0) = 0 \to a_+(t) &= -i\sin(\pi t), \\ a_-(0) = 1 \to a_-(t) &= \cos(\pi t). \end{aligned} \tag{3.50}$$

We will refer to this view of adiabatic evolution as the **active** convention: the expansion coefficients of the state evolve, but the basis stays fixed.

To motivate the second point of view, let us return to Eq. (3.48). By looking carefully at it, one might worry that the evolution is non-adiabatic, since $|\psi(t)\rangle$ has a component proportional to $|+\rangle_x$ and hence seems to be outside the image of the projector of interest. To understand this, recall that $P(t)$ in Eq. (3.36) is not the projector into $|+\rangle_x$, but into the state of lower energy of $H(t)$, i.e. into $|-\rangle_{\hat{B}(t)}$. At the same time, the expression for $|\psi(t)\rangle$ in Eq. (3.48) coincides with the expansion of $|-\rangle_{\hat{B}(t)}$:

$$|\psi(t)\rangle = |-\rangle_{\hat{B}(t)}\,, \tag{3.51}$$

and so we see that the state $|\psi(t)\rangle$ belongs to the image of $P(t)$. In other words, when an initial state $|\psi(0)\rangle$ is evolved adiabatically, the state $|\psi(t)\rangle$ at time t may have a component out of the image of a projector $P(t')$ for other times t', but it will not have any component out of the image of $P(t)$. This way of understanding the evolution, which consists in including the time-dependence in the basis states rather than in the coefficients, is called the **passive** convention. Applying this convention is equivalent to working with a frame that rotates together with the field, keeping the positive sense of the z-axis pointing towards the direction of $\boldsymbol{B}(t)$.

Let us summarize both conventions explained here and mentioned previously in the text: in the active convention the coefficients of the expansion of the initial state are time-dependent, while in the passive convention the basis states taking part in the expansion are time-dependent. It is important to realize that both points of view are equivalent.

In this example, we have worked with a two-level system in which the subspace of interest is spanned by a single state. Nevertheless, the formalism of adiabatic transport is also applicable to the case in which the dimension of the image of the projectors is

larger than one. In that case, there would be at least one additional eigenstate $|\psi_n(t)\rangle$ of $H(t)$ in the image of $P(t)$. The reason for including such a state may be, for example, that it shares degeneracy with the lower state $|-\rangle_{\hat{B}(t)}$ considered originally, at some point in parameter space. This occurs frequently when the states of interest are Bloch eigenstates, as we will see below.

3.1.3 Parametrization of Bloch's Hamiltonian

In the previous section, we have studied the adiabatic transport of quantum states when the system is driven over a path in parameter space. However, the parameter space was treated in general terms. On the other hand, our main focus is on the adiabatic transport in the context of electrons in solids. We thus introduce here the parameter space of this problem and how a family of parametric Hamiltonians arises naturally.

As we explained in Sec. 2.2, Bloch's theorem allows us to label each eigenstate of the single-particle Hamiltonian H of a solid by a pair of quantum numbers $(n, \boldsymbol{k})$, where n is a band-index and $\boldsymbol{k}$ is the crystal momentum belonging to the first Brillouin zone (BZ). The time-independent Schrödinger equation takes the form

$$H\psi_{n\boldsymbol{k}}(\boldsymbol{r}) = E_{n\boldsymbol{k}}\psi_{n\boldsymbol{k}}(\boldsymbol{r}). \tag{3.52}$$

Since every eigenfunction can be written as $\psi_{n\boldsymbol{k}}(\boldsymbol{r}) = e^{i\boldsymbol{k}\cdot\boldsymbol{r}}u_{n\boldsymbol{k}}(\boldsymbol{r})$, where $u_{n\boldsymbol{k}}(\boldsymbol{r})$ is function with the periodicity of the lattice, we can rewrite Eq. (3.52) as an equation for the periodic parts:

$$H(\boldsymbol{k})u_{n\boldsymbol{k}}(\boldsymbol{r}) = E_{n\boldsymbol{k}}u_{n\boldsymbol{k}}(\boldsymbol{r}) \tag{3.53}$$

where we have introduced the operator representation of the Bloch Hamiltonian,

$$H(\boldsymbol{k}) = e^{-i\boldsymbol{k}\cdot\boldsymbol{r}}He^{i\boldsymbol{k}\cdot\boldsymbol{r}}. \tag{3.54}$$

Often it will be convenient to work with the matrix elements of the Bloch Hamiltonian projected into some fixed basis of tight-binding orbitals. Letting $|u_{n\boldsymbol{k}}\rangle$ denote the column vector we obtain by expanding $u_{n\boldsymbol{k}}(\boldsymbol{r})$ in a fixed tight-binding basis, we can write

$$H(\boldsymbol{k})\,|u_{n\boldsymbol{k}}\rangle = E_{n\boldsymbol{k}}\,|u_{n\boldsymbol{k}}\rangle\,, \tag{3.55}$$

in the tight-binding approximation, where $H(\boldsymbol{k})$ should be understood as a matrix. In this chapter, we will always use the ket notation to denote Bloch functions expanded in the space of tight-binding basis vectors to avoid confusion. Eqs. (3.53) and (3.55) were derived by noting that states are indexed by their crystal momentum $\boldsymbol{k}$ and separating the Hamiltonian into blocks of different $\boldsymbol{k}$. However, we can equally well consider the Bloch Hamiltonian $H(\boldsymbol{k})$ as a **function** of $\boldsymbol{k}$. The set

$$\{H(\boldsymbol{k}),\ \boldsymbol{k} \in \text{Brillouin zone}\} \tag{3.56}$$

then forms the sort of family of parametric Hamiltonians considered in the quantum adiabatic theorem. Indeed, $\boldsymbol{k}$ plays the role of the vector of parameters $\boldsymbol{\lambda}$ of the previous section and the BZ is the parameter space of the problem.

3.2 Berry phase and polarization

In the following section, we will adopt a more practical point of view to show how the adiabatic variation of $\boldsymbol{k}$ is related to the response of the real-space distribution of charge to an electric field (i.e. the polarization). For that, we will restrict ourselves to one-dimension and we will closely follow the approach of Refs. [87,88]. Let us start with the Bloch Hamiltonian in Eq. (3.53) for a 1D crystal with periodic potential $V(x+a) = V(x)$:

$$H(k)u_{nk}(x) = \left[\frac{1}{2m}(p+k)^2 + V(x)\right]u_{nk}(x) = E_{nk}u_{nk}(x). \tag{3.57}$$

We define our projectors by means of eigenstates $|\psi_{nk}\rangle$ of the Hamiltonian:

$$P(k) = \sum_{n=1}^{N} |\psi_{nk}\rangle\langle\psi_{nk}| = \sum_{n=1}^{N} \int u^*_{nk}(x)u_{nk}(x')e^{ik(x'-x)}\,|x'\rangle\langle x|\,dxdx', \tag{3.58}$$

Now, let us assume that $P(k)$ is the projector onto the N "occupied" bands of an insulating crystal, and that there is a spectral gap of magnitude $\Delta > 0$ separating these bands from others in the spectrum. Consider the effect of a small uniform electric field,

$$E = -\frac{\partial}{\partial t}(-E_0 t) = -\frac{\partial A(t)}{\partial t}. \tag{3.59}$$

The vector potential $A(t)$ appears in the Hamiltonian through the minimal-coupling:

$$H(k,t) = \frac{1}{2m}[p + k - qA(t)]^2 + V(x) \equiv \frac{1}{2m}[p + k(t)]^2 + V(x) = H(k(t)), \tag{3.60}$$

where $k(t) = k + qE_0 t$, and q is the charge of the electron (we work in units where $c = 1$). Thus, the problem of an electron moving under the influence of a constant electric field maps to a problem of evolution within a parametric family of Hamiltonians. For instance, $|qE_0|^{-1}$ plays the role of τ from the previous lecture; if we take $|qE_0| << \Delta$, we can apply the adiabatic theorem.

We find then that for an initial state $\psi_{nk}(x) = e^{ik\cdot x}u_{nk}(x)$, the final state under adiabatic evolution is

$$\psi_{nk(t)}(x) = e^{ik\cdot x}W_{mn}(t)u_{mk(t)}(x), \tag{3.61}$$

with $W_{nm}(t) = \mathcal{P}e^{i\int_0^t A_{nm}(t')\mathrm{d}t'}$ the matrix elements of the operator $\mathcal{W}$, and $A_{nm} = i\int u_{nk}(x)\partial_k u_{mk}(x)\,\mathrm{d}x$. We see that the Berry phase captures the evolution of the wave

functions in the presence of an electric field[2].

We can go further and relate $W(t)$ to the position operator. To do so, let us consider our system to have length L, with periodic boundary conditions. The average position is related to the following expectation value:

$$\langle \mathfrak{P} \rangle = \langle \Psi_0 | e^{2\pi i \hat{X}/L} | \Psi_0 \rangle \equiv \langle \Psi_0 | \mathfrak{P} | \Psi_0 \rangle \,, \tag{3.62}$$

Here $|\Psi_0\rangle$ is the Slater determinant ground state for an insulator in which every $|\psi_{nk}\rangle$ is occupied, and $\hat{X}$ is the position operator. In second quantization, we can write $|\psi_{nk}\rangle = c_{nk}^\dagger |0\rangle$, where

$$\begin{aligned} c_{nk}^\dagger &= \int_0^L \mathrm{d}x \, \psi_{nk}(x) c_x^\dagger, \\ \{c_x, c_{x'}^\dagger\} &= \delta(x - x'), \\ \langle \psi_{nk} | \psi_{mk'} \rangle &= \delta_{nm} \delta_{kk'}. \end{aligned} \tag{3.63}$$

In this language, the position operator $\hat{X}$ can be written as

$$\hat{X} = \int_0^L \mathrm{d}x \, x c_x^\dagger c_x. \tag{3.64}$$

Taking this expression into account and applying the anticommutation relations in Eq. (3.63), it follows that:

$$\mathfrak{P} c_x \mathfrak{P}^{-1} = e^{-2\pi i x/L} c_x, \tag{3.65}$$

and hence

$$\mathfrak{P} c_{nk} \mathfrak{P}^{-1} = \int_0^L \mathrm{d}x \, \psi_{nk}^*(x) e^{-2\pi i x/L} c_x \equiv \tilde{c}_{nk}. \tag{3.66}$$

Using this and applying the fact that the Slater determinant ground state can be written

[2]Note that, as we have considered the adiabatic evolution U_A derived from Eq. (3.13), we have neglected the dynamical phase that can be acquired by the wave functions. See Ref. [82] for more details.

as $|\Psi_0\rangle = \prod_{nk} c^\dagger_{nk} |0\rangle$:

$$\begin{aligned}
\langle \mathfrak{P} \rangle &= \langle 0 | \prod_{nk} c_{nk} \mathfrak{P} \prod_{mk'} c^\dagger_{mk'} | 0 \rangle \\
&= \langle 0 | \prod_{nk} c_{nk} \prod_{mk'} \tilde{c}^\dagger_{mk'} | 0 \rangle \\
&= \det\Big(\langle \psi_{nk} | \tilde{\psi}_{mk'} \rangle \Big) \\
&= \det\left(\int_0^L \mathrm{d}x \, \psi^*_{nk}(x) \tilde{\psi}_{mk'}(x) \right) \\
&= \det\left(\int_0^L \mathrm{d}x \, u^*_{nk} e^{-ik\cdot x} u_{mk'} e^{i(k'+2\pi/L)\cdot x} \right).
\end{aligned} \tag{3.67}$$

The determinant appears owing to the application of Wick's theorem. By considering a lattice translation, we see $\tilde{\psi}_{mk'}$ is a Bloch-wave with crystal momentum $k'+2\pi/L$. Then, these overlaps vanish unless $k' = k - 2\pi/L$ due to conservation of crystal momentum:

$$\langle \mathfrak{P} \rangle = \prod_k \det\left[\int_0^L \mathrm{d}x \, u^*_{nk} u_{m(k-2\pi/L)} \right] = \det[W(2\pi)], \tag{3.68}$$

where we have considered the limit $L \to \infty$ and identified W by comparing this expression to Eq. (3.31), together with the property $\det(A)\det(B) = \det(AB)$. Therefore, the gauge invariant determinant of W along a closed path in the BZ is related to the mean center of charge in the unit cell. This connection between the determinant of W and the position operator suggests that there may be a deep connection between the geometry of adiabatic evolution and localization of electrons in solids.

In order to make this relation more clear, we explore it in terms of a physical quantity: the polarization density. Let us show that $\log(\langle \mathfrak{P} \rangle)$ is indeed the physical polarization density P_e of the crystal, defined by Maxwell's equations to satisfy:

$$\dot{P}_e = J_{bound} = q \, \langle v \rangle \, . \tag{3.69}$$

In order to show this, we will act with $\mathfrak{P}$ on $|\Psi_0\rangle$:

$$\begin{aligned}
\mathfrak{P} \, |\Psi_0\rangle &= e^{i\gamma} \left[|\Psi_0\rangle + i \frac{2\pi}{L} \sum_{j \neq 0} |\Psi_j\rangle \, \langle \Psi_j | X | \Psi_0 \rangle + \dots \right] = \\
&= e^{i\gamma} \left[|\Psi_0\rangle + 2\pi \sum_{j \neq 0} |\Psi_j\rangle \, \frac{\langle \Psi_j | v | \Psi_0 \rangle}{E_j - E_0} + \dots \right],
\end{aligned} \tag{3.70}$$

where we used $\langle \Psi_j | v | \Psi_0 \rangle = i/L \, \langle \Psi_j | [H, X] | \Psi_0 \rangle = i/L (E_j - E_0) \, \langle \Psi_j | X | \Psi_0 \rangle$. Here

$\gamma = \mathrm{Im}\log\langle\Psi_0|\mathfrak{P}|\Psi_0\rangle$ is the adiabatic (Berry) phase. Note that this shows that $\mathfrak{P}\,|\Psi_0\rangle$ is parametrically related (via perturbation theory) to the constant electric field state treated before. Let us now assume we have a time-dependent perturbation that varies adiabatically. We can then look at the change in $\langle\mathfrak{P}\rangle$ to lowest order in perturbation theory. We have that:

$$\frac{\mathrm{d}}{\mathrm{d}t}\mathrm{Im}\log\langle\mathfrak{P}\rangle = \frac{\mathrm{d}\gamma}{\mathrm{d}t} = \mathrm{Im}\frac{1}{\langle\Psi_0|\mathfrak{P}|\Psi_0\rangle}\Big(\langle\dot{\Psi}_0|\mathfrak{P}|\Psi_0\rangle + \langle\Psi_0|\mathfrak{P}|\dot{\Psi}_0\rangle\Big). \tag{3.71}$$

In the adiabatic limit, $\langle\dot{\psi_0}|\psi_0\rangle = 0$ from the parallel transport equation (3.17), so:

$$\frac{\mathrm{d}}{\mathrm{d}t}\mathrm{Im}\log\langle\mathfrak{P}\rangle = 2\pi\sum_{j\neq 0}\frac{1}{E_j - E_0}\Big(\langle\Psi_j|v|\Psi_0\rangle\,\langle\dot{\Psi}_0|\Psi_j\rangle + \langle\Psi_j|\dot{\Psi}_0\rangle\,\langle\Psi_0|v|\Psi_j\rangle\Big). \tag{3.72}$$

But the right-hand side is precisely $\langle v\rangle$ expanded to first order in perturbation theory, multiplied by 2π. This shows that the Berry phase $\mathrm{Im}\log\det W$ is, up to a multiplicative factor of $q/2\pi$, the physical polarization density. This connection between Berry phase and electronic position can be made even more precise through the exploration of Wannier functions and hybrid Wannier functions, as we will now show.

3.3 Wannier functions and charge localization

While Bloch's theorem tells us that the eigenstates of periodic Hamiltonians are delocalized, we know that electronic systems are built out of localized functions coming from atomic orbitals. How do we recover these functions? Motivated by this issue, we will introduce Wannier and hybrid Wannier functions and show how the Berry phase and holonomy are connected to charge localization.

To begin, let us take a projector P where $\mathrm{Im}(P)$ is spanned by the Bloch states $\{\psi_{n\boldsymbol{k}}(\boldsymbol{r})\}$ for all $\boldsymbol{k}$ in the Brillouin zone and $n = 1, \cdots, N_{occ}$, which satisfy the boundary conditions

$$\psi_{n(\boldsymbol{k}+\boldsymbol{G})}(\boldsymbol{r}) = \psi_{n\boldsymbol{k}}(\boldsymbol{r}), \tag{3.73}$$

for all $\boldsymbol{G}$ in the reciprocal lattice. Furthermore, let us assume there exists some periodic gauge transformation $U(\boldsymbol{k}) \in U(N)$ such that the functions $\tilde{\psi}_{n\boldsymbol{k}}(\boldsymbol{r}) = \sum_{m=1}^{N} U_{nm}\psi_{m\boldsymbol{k}}(\boldsymbol{r})$ are analytic in $\boldsymbol{k}$ (and therefore differentiable in $\boldsymbol{k}$ to any order). Then, we can form **Wannier functions** via the following expressions:

$$W_{n\boldsymbol{R}}(\boldsymbol{r}) = \frac{1}{\sqrt{\mathcal{N}}}\sum_{\boldsymbol{k}} e^{-i\boldsymbol{k}\cdot\boldsymbol{R}}\tilde{\psi}_{n\boldsymbol{k}}(\boldsymbol{r}) \approx \frac{V}{\sqrt{\mathcal{N}}(2\pi)^3}\int \mathrm{d}\boldsymbol{k}\, e^{-i\boldsymbol{k}\cdot\boldsymbol{R}}\tilde{\psi}_{n\boldsymbol{k}}(\boldsymbol{r}), \tag{3.74a}$$

$$\tilde{\psi}_{n\boldsymbol{k}}(\boldsymbol{r}) = \frac{1}{\sqrt{\mathcal{N}}}\sum_{\boldsymbol{R}} W_{n\boldsymbol{R}}(\boldsymbol{r})e^{i\boldsymbol{k}\cdot\boldsymbol{R}}. \tag{3.74b}$$

where $\boldsymbol{R}$ denotes vectors belonging to the Bravais lattice, $\mathcal{N}$ the number of unit cells in the system, and V is the volume. From Eq. (3.74b), we see that:

$$\left|\partial_{k_i}^n\ \tilde{\psi}_{n\boldsymbol{k}}(\boldsymbol{r})\right| = \left|\frac{1}{\sqrt{\mathcal{N}}}\sum_{\boldsymbol{R}}(iR_i)^n\ W_{n\boldsymbol{R}}(\boldsymbol{r})e^{i\boldsymbol{k}\cdot\boldsymbol{R}}\right| \leq \frac{1}{\sqrt{\mathcal{N}}}\sum_{\boldsymbol{R}}|R_i^n\ W_{n\boldsymbol{R}}(\boldsymbol{r})|, \tag{3.75}$$

which shows that if $W_{n\boldsymbol{R}}(\boldsymbol{r})$ decays faster than any power of $(\boldsymbol{r}-\boldsymbol{R})$, $\tilde{\psi}_{n\boldsymbol{k}}(\boldsymbol{r})$ will be smooth in $\boldsymbol{k}$ to any order. The localization of Wannier functions is thus a necessary condition for obtaining smooth functions $\tilde{\psi}_{n\boldsymbol{k}}(\boldsymbol{r})$ upon taking the Fourier transform. It is possible to show [89, 90] a converse to this as well: as long as $\tilde{\psi}_{n\boldsymbol{k}}(\boldsymbol{r})$ is an analytic function of $\boldsymbol{k}$, then the Wannier functions $W_{n\boldsymbol{R}}(\boldsymbol{r})$ will decay exponentially as $|\boldsymbol{r}-\boldsymbol{R}| \to \infty$. As we will see later in the text, this relation between the existence of a gauge that allows us to construct smooth functions in reciprocal space and the localization of Wannier functions is one of the cornerstones of the framework of topology in band structures [59, 91, 92].

Exponentially localized Wannier functions satisfy a variety of nice properties, such as

Property 1: $\langle W_{n\boldsymbol{R}}|W_{m\boldsymbol{R}'}\rangle = \delta_{nm}\delta_{\boldsymbol{R}\boldsymbol{R}'}$.

Property 2: $\sum_{n=1}^{N_{occ}}\sum_{\boldsymbol{k}}|\tilde{\psi}_{n\boldsymbol{k}}\rangle\langle\tilde{\psi}_{n\boldsymbol{k}}| = \sum_{n=1}^{N_{occ}}\sum_{\boldsymbol{R}}|W_{n\boldsymbol{R}}\rangle\langle W_{n\boldsymbol{R}}|$.

Property 3: $W_{n(\boldsymbol{R}+\boldsymbol{R}')}(\boldsymbol{r}) = W_{n\boldsymbol{R}}(\boldsymbol{r}-\boldsymbol{R}')$.

The first property means that Wannier functions form an orthonormal set; in the second property, we see that they span the same subspace of the Hilbert space as the band eigenstates from which they are constructed via (3.74a); finally, the third point means that the Wannier functions are distributed periodically through the lattice, so that it is enough to work with the Wannier functions in one unit cell (with one fixed $\boldsymbol{R}$). On the whole, localized Wannier functions form a complete basis that turns out to be convenient to build a quantitative position space picture of the occupied subset of states in a crystal. In this spirit, Wannier functions are good candidates to study phenomena that are more intuitively understood in position space; particularly, charge localization and pumping. As an example of this, let us reinterpret our expression Eq. (3.68) for $\langle\mathfrak{P}\rangle$ in the 1D case in terms of Wannier functions. Applying (3.22), we get:

$$\begin{aligned}\operatorname{Im}\log\langle\mathfrak{P}\rangle &= \operatorname{Im}\log(\det W)\\ &= \operatorname{tr}\oint \mathrm{d}k\, A(k)\\ &= i\sum_{n=1}^{N_{occ}}\int_0^{2\pi}\mathrm{d}k\int_{cell}\mathrm{d}x\, u_{nk}^*(x)\partial_k u_{nk}(x),\end{aligned} \tag{3.76}$$

where N_{occ} is the number of states in $\mathrm{Im}[P(\boldsymbol{k})]$. Working in the convention where

$$\tilde{u}_{nk}(x) = \sqrt{\mathcal{N}} e^{-ik\cdot x}\ \tilde{\psi}_{nk}(x) = \sum_R e^{ik\cdot(R-x)}\ W_{nR}(x). \tag{3.77}$$

(in this convention the Bloch functions $\tilde{u}_{n\boldsymbol{k}}$ are normalized to one within a single unit cell) and integrating over the whole space rather than over the unit cell, Eq. (3.76) becomes (recall we work in units where the lattice constant is equal to one):

$$\begin{aligned}
\mathrm{Im}\log\langle\mathfrak{P}\rangle &= \frac{i}{\mathcal{N}}\sum_{m=1}^{N_{occ}}\int \mathrm{d}x \int_0^{2\pi}\mathrm{d}k \sum_{RR'} e^{-ik\cdot(R-x)}\ W^*_{mR}(x)\partial_k\left[e^{ik\cdot(R'-x)}W_{mR'}(x)\right] + 2\pi n \\
&= \frac{2\pi}{\mathcal{N}}\sum_{m=1}^{N_{occ}}\sum_R \int \mathrm{d}x\,(x-R)W^*_{mR}(x)W_{mR}(x) + 2\pi n \\
&= \frac{2\pi}{\mathcal{N}}\sum_{m=1}^{N_{occ}}\sum_R \int \mathrm{d}x\, x\ W^*_{m0}(x)W_{m0}(x) + 2\pi n \\
&= 2\pi\sum_{m=1}^{N_{occ}}\langle W_{m0}|x|W_{m0}\rangle + 2\pi n,
\end{aligned} \tag{3.78}$$

thus, we see that writing $q/(2\pi)\mathrm{Im}\log\langle\mathfrak{P}\rangle$ in terms of Wannier functions leads us to a precise real-space interpretation of the polarization density: it is the displacement of the average charge center from the origin of the unit cell. Here, n is an integer given by the winding number $2\pi n = i\oint \mathrm{tr}\left[U^\dagger(k)\partial_k U(k)\right]\mathrm{d}k$, of the unitary transformation that converts from the original basis u_{nk} to the smooth basis $\tilde{u}_{nk}$, and shows that the Berry phase is only defined $\mod 2\pi$. Eq. (3.78) re-expresses the 2π gauge ambiguity of the Berry phase as an ambiguity of the charge center by an integer number of unit cells.

Until now, we have related the trace of the Berry phase to the average many-body position, but is it possible to get a grasp on the position of a single particle? Using our knowledge of adiabatic transport, we can go further and relate the position operator to the Berry phase, without the need for the trace over occupied bands. Before we tackle this problem, let us define a kind of functions that will turn out to be useful for this task: the **hybrid Wannier functions**. These functions are related to the smooth states $\tilde{\psi}_{n\boldsymbol{k}}(\boldsymbol{r})$ via the following expression:

$$W_{n\boldsymbol{R}_\perp}(\boldsymbol{r},\boldsymbol{k}_\parallel) = \frac{1}{\sqrt{\mathcal{N}_\perp}}\sum_{\boldsymbol{k}_\perp} e^{-i\boldsymbol{k}_\perp\cdot\boldsymbol{R}_\perp}\ \tilde{\psi}_{n\boldsymbol{k}}(\boldsymbol{r}). \tag{3.79}$$

Whereas Wannier functions are localized in all directions, hybrid Wannier functions are localized along the direction denoted by $\perp$ and delocalized in $\parallel$. This property manifests itself in Eq. (3.79) in the fact that the Fourier transform is taken only along the direction

$\perp$.

Let us now take a state $|f\rangle = \sum_{n\boldsymbol{k}} f_{n\boldsymbol{k}} |\psi_{n\boldsymbol{k}}\rangle \in \mathrm{Im}(P)$ and look at the action of the projected position operator $P\boldsymbol{x}P$ on it. Taking matrix elements in the basis of Bloch functions, we have

$$\begin{aligned}
\langle \psi_{n\boldsymbol{k'}} | P x_i P | f \rangle &= \sum_{m=1}^{N_{occ}} \sum_{\boldsymbol{k}} \langle \psi_{n\boldsymbol{k'}} | x_i | \psi_{m\boldsymbol{k}} \rangle \, f_{m\boldsymbol{k}} \\
&= \sum_{m=1}^{N_{occ}} \sum_{\boldsymbol{k}} f_{m\boldsymbol{k}} \int \mathrm{d}\boldsymbol{x} \, x_i \psi^*_{n\boldsymbol{k'}}(\boldsymbol{x}) \psi_{m\boldsymbol{k}}(\boldsymbol{x}) \\
&= \frac{1}{\mathcal{N}} \sum_{m=1}^{N_{occ}} \sum_{\boldsymbol{k}} \int \mathrm{d}\boldsymbol{x} \, f_{m\boldsymbol{k}} u^*_{n\boldsymbol{k'}}(\boldsymbol{x}) u_{m\boldsymbol{k}}(\boldsymbol{x}) e^{i(\boldsymbol{k}-\boldsymbol{k'})\cdot\boldsymbol{x}} \; x_i \\
&= \frac{1}{\mathcal{N}} \sum_{m=1}^{N_{occ}} \sum_{\boldsymbol{k}} \int \mathrm{d}\boldsymbol{x} \, f_{m\boldsymbol{k}} u^*_{n\boldsymbol{k'}}(\boldsymbol{x}) u_{m\boldsymbol{k}}(\boldsymbol{x}) (-i) \partial_{k_i} \left[e^{i(\boldsymbol{k}-\boldsymbol{k'})\cdot\boldsymbol{x}} \right] \\
&= i \partial_{k'_i} f_{n\boldsymbol{k'}} + i \frac{1}{N} \sum_{m=1}^{N_{occ}} \sum_{\boldsymbol{k}} f_{m\boldsymbol{k}} \int \mathrm{d}\boldsymbol{x} \, [u^*_{n\boldsymbol{k'}}(\boldsymbol{x}) \partial_{k_i} u_{m\boldsymbol{k}}(\boldsymbol{x})] e^{i(\boldsymbol{k}-\boldsymbol{k'})\cdot\boldsymbol{x}}.
\end{aligned} \tag{3.80}$$

Unless otherwise noted, we will use the convention that repeated indices are summed over from this point forward. Finally, we can rewrite the integral over $\boldsymbol{x}$ in the last term as an integral over a single unit cell, using

$$\begin{aligned}
\int \mathrm{d}\boldsymbol{x} \, [u^*_{n\boldsymbol{k'}}(\boldsymbol{x}) \partial_{k_i} u_{m\boldsymbol{k}}(\boldsymbol{x})] e^{i(\boldsymbol{k}-\boldsymbol{k'})\cdot\boldsymbol{x}} &= \sum_{\boldsymbol{R}} \int_{\text{cell}} \mathrm{d}\boldsymbol{x} \, [u^*_{n\boldsymbol{k'}}(\boldsymbol{x}+\boldsymbol{R}) \partial_{k_i} u_{m\boldsymbol{k}}(\boldsymbol{x}+\boldsymbol{R})] e^{i(\boldsymbol{k}-\boldsymbol{k'})\cdot(\boldsymbol{x}+\boldsymbol{R})} \\
&= \sum_{\boldsymbol{R}} e^{i(\boldsymbol{k}-\boldsymbol{k'})\cdot\boldsymbol{R}} \int_{\text{cell}} \mathrm{d}\boldsymbol{x} \, [u^*_{n\boldsymbol{k'}}(\boldsymbol{x}) \partial_{k_i} u_{m\boldsymbol{k}}(\boldsymbol{x})] e^{i(\boldsymbol{k}-\boldsymbol{k'})\cdot\boldsymbol{x}} \\
&= -i \delta_{\boldsymbol{k}\boldsymbol{k'}} A^i_{nm}(\boldsymbol{k})
\end{aligned} \tag{3.81}$$

where A^i_{nm} are the matrix elements of the Berry (adiabatic) connection in the k_i direction between occupied bands n and m. Putting this all together, we find

$$\langle \psi_{n\boldsymbol{k'}} | P x_i P | f \rangle = i \partial_{k'_i} f_{n\boldsymbol{k'}} + A^i_{nm}(\boldsymbol{k'}) f_{m\boldsymbol{k'}}. \tag{3.82}$$

We see that $-iP\boldsymbol{x}P$ acts as the adiabatic covariant derivative that appears in our parallel transport equation (3.20). We can go further and also look for eigenstates of $Px_\perp P$, which corresponds to looking for states satisfying

$$Px_\perp P \, |\psi\rangle = \varphi \, |\psi\rangle \, . \tag{3.83}$$

Let us take a trial solution of the form

$$|\psi\rangle = e^{-ik_\perp \varphi} W_{mn}(k_\perp) f_{n0} \, |\psi_{m\boldsymbol{k}}\rangle \,, \tag{3.84}$$

and check if it satisfies Eq. (3.83). Here, $k_\perp$ is the component of $\boldsymbol{k}$ along the direction denoted by $\perp$. The matrix $W_{nm}(k_\perp)$ is the familiar holonomy matrix, given in terms of Eq. (3.23), with the path given by a straight line from $\boldsymbol{k}_0 = \mathbf{0}$ to $k_\perp/(2\pi)\mathbf{G}_\perp$, with $\mathbf{G}_\perp$ the reciprocal lattice vector in the $\perp$ direction. Since $|\varphi\rangle \in \mathrm{Im}(P)$, the coefficients in Eq. (3.84) should satisfy Eq. (3.82), thus substituting $|\varphi\rangle$ in Eq. (3.83) yields:

$$\left[\delta_{m\ell}\partial_{k_\perp} - iA^\perp_{\ell m}(k_\perp)\right]\left[e^{-ik_\perp\varphi} W_{mn}(k_\perp) f_{n0}\right] = -i\varphi e^{-ik_\perp\varphi} W_{\ell n}(k_\perp) f_{n0}, \tag{3.85}$$

We know from the properties of W that the coefficients $W_{mn}(k_\perp)f_{n0}$ satisfy the parallel transport equation in Eq. (3.20):

$$\left[\delta_{\ell m}\partial_{k_\perp} - iA^\perp_{\ell m}(k_\perp)\right] W_{mn}(k_\perp) f_{n0} = 0, \tag{3.86}$$

which allows us to arrive at the right hand side on Eq. (3.85) and make sure that the equality holds. We have therefore shown that any function that can be expanded as Eq. (3.84) is a good candidate to be an eigenfunction of the projected position operator. However, we must still ensure that our choice of boundary conditions in Eq. (3.73) is preserved, i.e. that

$$e^{-i2\pi\varphi} W_{mn}(2\pi) f_{n0} = f_{m0}. \tag{3.87}$$

Thus we must choose the vector formed by the coefficients $\{f_{n0}\}$ to be an eigenvector of $W(2\pi)$ with eigenvalue $e^{2\pi i\varphi}$. In conclusion,

> The spectrum of Px_iP matches the spectrum of $\dfrac{1}{2\pi}\mathrm{Im}\log W_{mn}(\boldsymbol{k}_0 \to \boldsymbol{k}_0 + \mathbf{G}_i)$.

Note that we now have a more precise information about the real-space properties of a single electron, as we have shown how to extract information about the spectrum of the single-particle (projected) position operator from the holonomy W. However, we know that the eigenfunctions of an operator can also contain useful information about it. This fact motivates us to go on to calculate also the eigenfunctions of Px_iP.

Note first that our choice of $\mathbf{k_0} = \mathbf{0}$ as the intial point for our coefficients f_{n0} was arbitrary. Let us denote $W_{\boldsymbol{k}_0}(\boldsymbol{G}_\perp)$ the adiabatic evolution from $\boldsymbol{k} = \boldsymbol{k}_0$ to $\boldsymbol{k} = \boldsymbol{k}_0 + \mathbf{G}_\perp$. Let $Q(\boldsymbol{k}_0)$ denote the matrix containing in each column an eigenvector of $W_{\boldsymbol{k}_0}(\boldsymbol{G}_\perp)$, so that $W^{\mathbf{k_0}}_{nm}(\boldsymbol{G}_\perp)Q_{mj}(\boldsymbol{k}_0) = e^{i2\pi\varphi_j}Q_{nj}(\boldsymbol{k}_0)$. Since $W^{\mathbf{k_0}}_{nm}$ drives the evolution of $Q_{nj}(\boldsymbol{k}_0)$, we deduce that:

$$Q_{nj}(\boldsymbol{k}_0 + \frac{k_\perp \mathbf{G}_\perp}{2\pi}) = W^{\mathbf{k_0}}_{nm}(\frac{k_\perp \mathbf{G}_\perp}{2\pi}) Q_{mj}(\boldsymbol{k}_0). \tag{3.88}$$

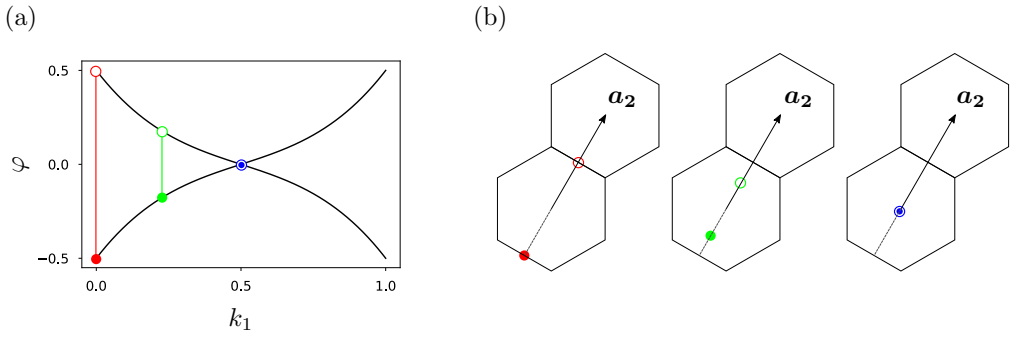

Figure 3.4: Eigenvalues of the holonomy $W^{k_1,k_2=0}(\mathbf{G}_2)$ for a set of 2 bands in a honeycomb lattice model [93, 94]. (a) Spectrum as a function of k_1, where vertical lines indicate different choices of k_1; two eigenvalues correspond to each choice, denoted by the solid circle and ring. (b) Interpretation of eigenvalues in terms of hybrid Wannier centers.

This implies that $e^{-ik_\perp\varphi_j}Q_{nj}(k_\perp)$ is periodic in $k_\perp$, and so satisfies Eq. (3.87). As a consequence, the following function is an eigenfunction of $Px_\perp P$ with eigenvalue $\varphi_j+R_\perp$:

$$W_{jR_\perp}(\boldsymbol{r},\boldsymbol{k}_\parallel) = \int \sum_{n=1}^{N_{occ}} \mathrm{d}k_\perp\, e^{-ik_\perp(\varphi_j+R_\perp)}Q_{nj}(\boldsymbol{k})\psi_{n\boldsymbol{k}}(\boldsymbol{r}). \tag{3.89}$$

Notice that the form of this function coincides with the expression of a hybrid Wannier function introduced in Eq. (3.79). Furthermore, since an eigenstate of $Px_\perp P$ is maximally localized in the $x_\perp$-direction, and we saw in Eq. (3.75) that this requires smoothness of derivatives with respect to $k_\perp$, we conclude that $Q(\boldsymbol{k})$ is constructed to ensure that derivatives of $\sum_n Q_{nj}(\boldsymbol{k})\psi_{n\boldsymbol{k}}(\boldsymbol{r})$ are smooth[3] with respect to $k_\perp$. In conclusion,

> Eigenfunctions of $Px_\perp P$ are hybrid Wannier functions localized maximally in the $x_\perp$-direction, whose charge centers coincide with the eigenvalues of $Px_\perp P$.

Consider the example of Fig. **3.4**, where we show the holonomy and hybrid Wannier function centers for two bands in two dimensions. In (a) we show the eigenvalues of the holonomy matrix $W^{k_1,k_2=0}(\mathbf{G}_2)$ – the holonomy along the $\mathbf{G}_2$ direction as a function of k_1. In (b) we show the location in position space of the corresponding centers of hybrid Wannier functions. These functions are maximally localized in the direction of the primitive lattice vector $\boldsymbol{a}_2$. When $k_1 = 0$, both centers are located a distance $\boldsymbol{a}_2/2$ from the center of the hexagon, corresponding to the eigenvalues $\phi/2\pi = \pm 0.5$ of

[3]The Berry connection cancels any discontinuity arising from degeneracies among states in $\mathrm{Im}(P)$.

the holonomy. As we start increasing k_1, the centers move towards the center of the hexagonal unit cell; at this point, there is a net electrical polarization in the unit cell. Finally, when $k_1/2\pi = 1/2$, both charge centers meet at the center of the hexagon.

To conclude, we have now seen how the Berry phase and holonomy encode information about charge localization in real space. First we have shown that the determinant of the adiabatic evolution operator gives the average charge center in a unit cell; then, we have gone further and we have derived the relation between the spectrum of the holonomy and the (single particle's) projected position operator; finally, we have concluded that the eigenfunctions of the projected position operator in a certain direction are hybrid Wannier functions maximally localized in that direction and interpreted the eigenvalues of the projected position operator as charge centers of hybrid Wannier functions. We will conclude this section with an example: the Rice-Mele chain.

3.3.1 The Rice-Mele chain

We consider a 1D inversion symmetric crystal, with lattice vector $\boldsymbol{a} = a\hat{x}$. Our basis will be formed by s and p_x-like functions localized on each lattice site, as drawn in Fig. **3.5**. While we will investigate the symmetry properties of $\mathcal{W}$ systematically in Sec. 3.4.1, we will show here that inversion symmetry has a profound effect on the Berry phase. If U_I is a unitary representation of inversion, then the following properties hold:

Property 1: $U_I P U_I^{-1} = P$,

Property 2: $U_I P x P U_I^{-1} = -PxP$.

The second property follows from the fact that the position operator x is odd under inversion. This property implies that eigenvalues of PxP come in pairs $\pm a\varphi/(2\pi) + \nu a$ ($\nu \in \mathbb{Z}$ appears due to the lattice ambiguity), where φ relates to the eigenvalue of the holonomy matrix $W(2\pi)$ via Eq. (3.87). Consequently, only eigenvalues $\varphi \in \{0, \pi\}$ – which correspond to hybrid Wannier functions at the center and borders of the unit cell, respectively – can be unpaired. In particular, it follows for a single band that:

$$\det W(2\pi) = \pm 1 \Rightarrow \langle W_{n0}|x|W_{n0}\rangle = \begin{cases} 0 \\ a/2 \end{cases} \mod a. \tag{3.90}$$

In other words, inversion symmetry quantizes the polarization. This can also be understood in a simple qualitative form: in the case of a single band, there is only one charge center in the unit cell. In 1D there are only two sites on which this charge center could sit without breaking inversion symmetry: $x = 0$ and $x = a/2$, i.e. those corresponding to Eq. (3.90).

Let us see this in action in our inversion symmetric chain, whose band structure contains two bands instead of one. As we mentioned, we take as basis states $\varphi_s(x - R)$ and $\varphi_p(x - R)$ sitting at the origin of the unit cell (see Fig. **3.5**), where:

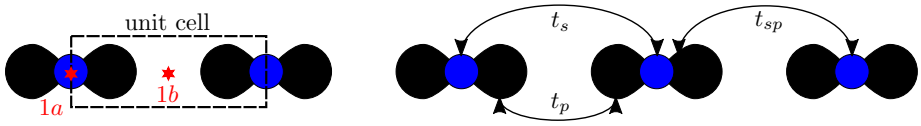

Figure 3.5: Schematic representation of the Rice-Mele model, where the basis formed by s (blue spheres) and p_x-orbitals (black) is shown. The choice of unit cell is indicated with dashed lines.

$$\begin{aligned}\varphi_s(x-R) &= \langle x|sR\rangle\,,\\ \varphi_p(x-R) &= \langle x|pR\rangle\,.\end{aligned} \tag{3.91}$$

Let $c^\dagger_{sR}$ and $c^\dagger_{pR}$ be the creator operators for states $|sR\rangle$ and $|pR\rangle$, respectively, so that

$$\begin{aligned}|sR\rangle &= c^\dagger_{sR}\,|0\rangle\,,\\ |pR\rangle &= c^\dagger_{pR}\,|0\rangle\,.\end{aligned} \tag{3.92}$$

We consider the following nearest-neighbor tight-binding Hamiltonian to investigate the topological properties of the chain's band structure:

$$\begin{aligned}H =& \sum_R \epsilon(c^\dagger_{sR}c_{sR} - c^\dagger_{pR}c_{pR})\\ &+ \sum_R \frac{1}{2}\left[t_{sp}\left(c^\dagger_{sR}c_{pR+1} - c^\dagger_{sR}c_{pR-1}\right) + t^*_{sp}(c^\dagger_{pR+1}c_{sR} - c^\dagger_{pR-1}c_{sR})\right]\\ &+ \sum_R \sum_{\sigma=s,p} t_\sigma(c^\dagger_{\sigma R}c_{\sigma R+1} + c^\dagger_{\sigma R+1}c_{\sigma R}).\end{aligned} \tag{3.93}$$

Note that this Hamiltonian is invariant under inversion symmetry[4]. This feature will allow us to investigate the interplay between inversion and topology. Moreover, we can take the Fourier transform $c_{\sigma k} = N^{-1/2}\sum_R e^{-ik\cdot R}c_{\sigma R}$ of the annihilation operators, which allows us to write the Hamiltonian in reciprocal space as

$$H = \sum_k \begin{bmatrix}c^\dagger_{sk} & c^\dagger_{pk}\end{bmatrix} H(k) \begin{bmatrix}c_{sk}\\ c_{pk}\end{bmatrix}, \tag{3.94}$$

with

$$H(k) = \epsilon\sigma_z + t^{(1)}_{sp}\sigma_y \sin k + (t_s - t_p)\sigma_z \cos k + (t_s + t_p)\mathbb{1}\cos k + t^{(2)}_{sp}\sigma_x \sin k. \tag{3.95}$$

[4]This is not the most general inversion-symmetric Hamiltonian that can be written with hoppings to nearest-neighbors. In particular, there is no symmetry forcing the on-site energies of both orbital species to be equal. However, there is not need to consider such a generalization as this simple model is enough to capture the physics we want to discuss.

For simplicity, we will take $t_s = -t_p = t/2$, as this eliminates terms proportional to the identity matrix. From the parity and distribution of orbitals in the lattice, it follows that the action of inversion on $H(k)$ can be described by the matrix σ_z:

$$\sigma_z H(k)\sigma_z = H(-k). \tag{3.96}$$

In addition to inversion, we can impose time-reversal symmetry. For spinless systems (or systems in which spin-orbit coupling can be neglected), time-reversal acts in position space as complex conjugation, i.e. $\mathcal{T} = \mathcal{K}$. Then, it has the following effect on annihilation operators of Bloch states:

$$\mathcal{T} c_{\sigma k} \mathcal{T} = \mathcal{N}^{-1/2} \sum_R e^{ik\cdot R} c_{\sigma R} = c_{\sigma,-k}, \tag{3.97}$$

with the corresponding action on creation operators. This means that time-reversal symmetry imposes the condition $H(k) = H^*(-k)$ on the Hamiltonian, which requires $t_{sp}^{(2)} = 0$ to be satisfied. The spectrum of $H(k)$ with time-reversal and inversion symmetry is finally given by:

$$E_k = \pm\sqrt{\left(\epsilon + t\cos k\right)^2 + [t_{sp}^{(1)}]^2 \sin^2 k} \tag{3.98}$$

In the simple case that $t_{sp}^{(1)} \equiv t$, the model has two gapped "flat-band" limits:

Limit 1: $t = t_{sp}^{(1)} = 0 \quad \Rightarrow E_k = \pm|\epsilon|$.

Limit 2: $\epsilon = 0,\ t = t_{sp}^{(1)} \Rightarrow E_k = \pm|t|$.

Since bands look very similar in both limits, we might think that both band structures are identical. This will turn out to be a naive statement as we now look into each limit in more detail.

Limit 1: trivial phase

The Hamiltonian adopts the following form in this limit:

$$H(k) = |\epsilon|\sigma_z, \tag{3.99}$$

whose eigenfunctions and corresponding periodic parts are:

$$\begin{aligned} \psi_{k\pm}(x) &= \frac{1}{\sqrt{\mathcal{N}}} \sum_R e^{ik\cdot R} \varphi_{(s,p)R}(x) \equiv \varphi_{(s,p)k}(x), \\ u_{k\pm}(x) &= \sqrt{\mathcal{N}} e^{-ik\cdot x} \varphi_{(s,p)k}(x). \end{aligned} \tag{3.100}$$

Here, we have denoted by $-$ the lower band, which contains the Bloch waves $\varphi_{pk}(x)$ constructed from p-orbitals. On the other hand, the eigenfunctions on the upper band

are indicated by + and coincide with the Bloch waves constructed as Fourier transforms of the s-orbitals.

After a bit of algebra, it can be shown that the Berry connection $A_s(k)$ for the state built-up from s-orbitals is

$$\begin{aligned} A_s(k) &= i \int_{cell} \mathrm{d}x\, u^*_{k+}(x) \partial_k u_{k+}(x) \\ &= \mathcal{N} \int_{cell} \mathrm{d}x\, e^{ikx} \varphi^*_{sk}(x) \partial_k \left[e^{-ikx} \varphi_{sk}(x) \right] \\ &= \int_{cell} \sum_{RR'} \mathrm{d}x\, (x-R) e^{ik(R-R')} \varphi^*_{sR'}(x) \varphi_{sR}(x). \end{aligned} \tag{3.101}$$

The corresponding Berry phase γ_s is obtained by integrating over the BZ:

$$\begin{aligned} \gamma_s &= \int_0^{2\pi} \mathrm{d}k\, A_s(k) \\ &= \int_0^{2\pi} \mathrm{d}k \int_{cell} \mathrm{d}x \sum_{RR'} (x-R) e^{ik(R-R')} \varphi^*_{sR'}(x) \varphi_{sR}(x) \\ &= \sum_R \int_{cell} \mathrm{d}x\, (x-R) \varphi^*_{sR}(x) \varphi_{sR}(x) \\ &= \int \mathrm{d}x\, x \varphi^*_{s0}(x) \varphi_{s0}(x) \\ &= 0. \end{aligned} \tag{3.102}$$

We could have anticipated this result: as $\psi_{k+}(x) = \varphi_{sk}(x)$, the Fourier transform in Eq. (3.74a) yields the Wannier function $W_{R+}(x) = \varphi_{sR}(x)$ for the upper band. Moreover, since Wannier functions coincide with hybrid Wannier functions in 1D, the Berry phase coincides with the charge center of $\varphi_{sR}(x)$, which sits at the origin of the unit cell, i.e. at $x = 0$.

Note also that we could have simplified our lives by working in the strict tight-binding limit in which orbitals are taken to be Dirac's deltas: $\varphi_{sR}(r) \propto \delta(r-R)$ and $\varphi_{pR}(r) \propto \delta'(r-R)$, where $\delta(r)$ and $\delta'(r)$ are even and odd under inversion, respectively; in that case, we would have:

$$u_{k\sigma}(x) = e^{-ikx} \sum_R e^{ikR} \varphi_{\sigma R}(x) = \sum_R \varphi_{\sigma R}(x), \text{ independent of } k. \tag{3.103}$$

This means that, in the strict tight-binding limit, the Berry connection can be evaluated by using only the Bloch coefficients of the eigenstates (which in this case are unity). We did not have to be so drastic as to assume our basis orbitals were delta functions to get this result; more generally, we can define the **tight-binding limit** to be the case

where $\langle\varphi_{\sigma R}|r|\varphi_{\sigma R'}\rangle \propto \delta_{RR'}$. In this case, the Berry phase can be evaluated entirely in terms of the Bloch coefficients. However, when the position operator has off-diagonal terms in the basis of orbitals, derivatives of Bloch functions constructed from these orbitals also contribute to the calculation of the Berry connection, so it is not enough to consider only the coefficients and their derivatives. This result is general, rather than a particular feature of the Rice-Mele chain.

Limit 2: topological phase

Even though the bands are flat also in this limit, the Hamiltonian of the system does depend on k:

$$H(k) = t(\cos k\sigma_z + \sin k\sigma_y), \tag{3.104}$$

and the periodic parts of its eigenstates are the following:

$$\begin{aligned} \psi_{k+}(x) &= \begin{bmatrix}\cos k/2 & i\sin k/2\end{bmatrix}\begin{bmatrix}\varphi_{sk}(x)\\ \varphi_{pk}(x)\end{bmatrix}, \\ \psi_{k-}(x) &= \begin{bmatrix}\sin k/2 & -i\cos k/2\end{bmatrix}\begin{bmatrix}\varphi_{sk}(x)\\ \varphi_{pk}(x)\end{bmatrix}. \end{aligned} \tag{3.105}$$

Despite being normalized and orthogonal between them, the states in Eq. (3.105) are not suitable for our adiabatic transport formalism, as they do not obey periodic-boundary conditions in reciprocal space [95]. For instance, it is easy to check that $\psi_{2\pi+}(x) = -\psi_{0+}(x)$ (the same holds for the other eigenstate). This pathology can be fixed by including a factor $\exp(ik/2)$ in the expressions for the eigenstates. The states constructed this way carry on being eigenstates of the Hamiltonian and they satisfy periodic-boundary conditions. Their periodic parts are the following:

$$\begin{aligned} u_{k+}(x) &= e^{ik/2}\sqrt{\mathcal{N}}e^{-ikx}\begin{bmatrix}\cos k/2 & i\sin k/2\end{bmatrix}\begin{bmatrix}\varphi_{sk}(x)\\ \varphi_{pk}(x)\end{bmatrix}, \\ u_{k-}(x) &= e^{ik/2}\sqrt{\mathcal{N}}e^{-ikx}\begin{bmatrix}\sin k/2 & -i\cos k/2\end{bmatrix}\begin{bmatrix}\varphi_{sk}(x)\\ \varphi_{pk}(x)\end{bmatrix}. \end{aligned} \tag{3.106}$$

We can now go on to repeat the calculation of the Berry phase γ_+ for the states on the upper band. We assume that we are working in the tight-binding limit and begin by computing the Berry connection $A_+(k)$ for the column vector $|u_{k+}\rangle$ of expansion coefficients:

$$A_+(k) = i\langle u_{k+}|\partial_k u_{k+}\rangle = i\begin{bmatrix}\cos k/2 & -i\sin k/2\end{bmatrix}\begin{bmatrix}-1/2 & \sin k/2\\ i/2 & \cos k/2\end{bmatrix} - 1/2 = -1/2. \tag{3.107}$$

Then, combining this with our expression for the Berry phase γ_+, we can show that in

the tight-binding limit:

$$\gamma_+ = \int_0^{2\pi} \mathrm{d}k\, A_+(k) = -\pi \tag{3.108}$$

and thus the center of charge for the corresponding Wannier function is $\gamma_+ a/(2\pi)$ mod $a = a/2$, where we have restored a as lattice constant. The Wannier centers are pinned at $a/2$ because symmetry quantizes the polarization, as we will see later.

Note that the actual eigenvalues of the Hamiltonian did not enter the calculation of Berry phases, but only the eigenstates did. These points out that the topology of bands is encoded in the states, rather than in the shape of bands. As a consequence, the topology of our bands (their Berry phases) can not change without modifying the states, which requires closing the gap between lower and upper bands. For instance, let us imagine we begun with the system in the flat-band limit 2 and we started tuning slowly the hopping parameters in our Hamiltonian. The bands would probably stop being flat, but the Berry phase would stay pinned at $a/2$ as long as the gap between both bands does not close. In this sense, we say that the Berry phase is robust under adiabatic variations of the parameters that control the dynamics of the system.

Diagnosing topology with inversion

Quantizing the Berry phase is not the only role that inversion symmetry could play in the Rice-Mele chain. Let us show how inversion could also be used to diagnose the topological phase without calculating the Berry phase. This analysis will allow us to get a flavor of the interplay between symmetries and topology, even though this aspect will be investigated in more detail in Secs. 3.4.1 and chapter 5.

First, recall the action of inversion on the Bloch states constructed from s and p_x-like orbitals is the following:

$$\begin{aligned} U_I\,|\varphi_{s,k}\rangle &= |\varphi_{s,-k}\rangle\,, \\ U_I\,|\varphi_{p,k}\rangle &= -\,|\varphi_{p,-k}\rangle\,. \end{aligned} \tag{3.109}$$

It follows from this action, together with Eqs. (3.100) and (3.105), that the eigenstates of the Hamiltonian transform in the following way:

Limit 1:

$$\begin{aligned} U_I\psi_{\Gamma\pm}(x) &= \pm\psi_{\Gamma\pm}(x), \\ U_I\psi_{X\pm}(x) &= \pm\psi_{X\pm}(x). \end{aligned} \tag{3.110}$$

Limit 2:

$$\begin{aligned} U_I\psi_{\Gamma\pm}(x) &= \pm\psi_{\Gamma\pm}(x), \\ U_I\psi_{X\pm}(x) &= \mp\psi_{X\pm}(x). \end{aligned} \tag{3.111}$$

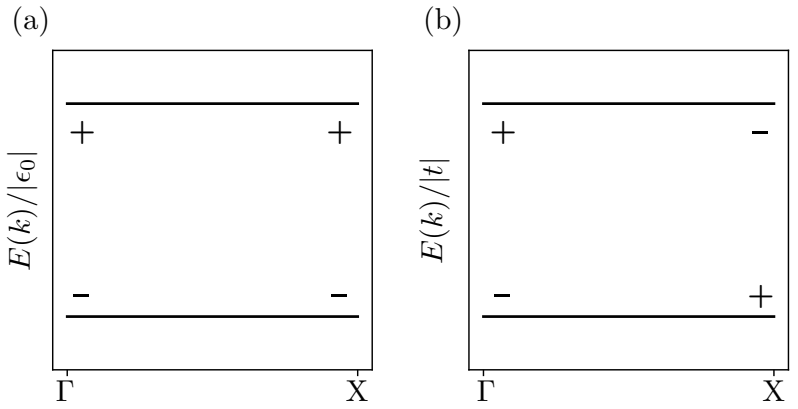

Figure 3.6: Flat bands of the Rice-Mele Hamiltonian in the two limits discussed in the text, with the inversion eigenvalues at Γ and X labeled. (a) Limit 1. (b) Limit 2.

These expressions show how bands in the Rice-Mele model inherit their symmetry properties from s and p_x-like states sitting in real space. The flat bands obtained in both limits and the inversion eigenvalues of the corresponding eigenstates at Γ and X are illustrated in Fig. **3.6**.

Note that all the combinations of inversion eigenvalues that a band can have at Γ and X (in 1D) are shown in Fig. **3.6**. We deduce that bands whose inversion eigenvalues are identical at both high-symmetry points have Berry phase $\gamma = 0$ [Fig. **3.6**(a)], whereas the Berry phase is $\gamma = \pi$ for bands with different inversion eigenvalues [Fig. **3.6**(b)]. This criterion allows us to determine the Berry phase of the bands by looking at their inversion eigenvalues, without calculating any integral.

Let us interpret this result in terms of *elementary band representations*, even if this discussion might look a bit premature until we reach chapter 5. Consulting the *Bilbao Crystallographic Server* [96–98], we find that the inversion eigenvalue distribution in limit-I matches what we would expect from orbitals at the 1a Wyckoff position transforming in the $A_g + A_u$ (s and p-orbitals) representation of inversion. We denote this as the $(A_g \uparrow G)_{1a} \oplus (A_u \uparrow G)_{1a}$ band representation – corresponding to s (A_g) and p (A_u) orbitals at the origin of the unit cell (the 1a position). Similarly, the inversion eigenvalues in limit-II match what we would expect for s and p orbitals at the 1b Wyckoff position, which we denote as the $(A_g \uparrow G)_{1b} \oplus (A_u \uparrow G)_{1b}$ band representation corresponding to s (A_g) and p (A_u) orbitals half a lattice constant away from the origin of the unit cell (the 1b position). In fact, it can be demonstrated that the Wannier states

constructed by applying Eq. (3.74a) coincide with those mentioned above[5].

The fact that bands in limit-I and limit-II have different Berry phases and symmetry properties makes these limits distinguishable, i.e. we can say that they belong to distinct phases. A particularly interesting property of bands in the second phase is that the charge centers of the corresponding Wannier functions sit away from the position occupied by the original s and p-orbitals. This fact motivates us to refer to the phase in limit-II as an **obstructed atomic limit**.

There are two aspects of the transition between limit-I and limit-II that deserve a discussion. First, note that such a transition is accompanied by the displacement of the charge centers from the atomic 1a position to position 1b, half a unit cell away; this generates a dipole moment of $ea/2$. Second, this transition can not be achieved without either closing the gap between upper and lower bands or breaking inversion symmetry; a transition that gives up any of these two constrains is said to be *non-adiabatic*. However, it would be possible to drive the transition without closing the gap if we gave up inversion – adding a term $t'\sigma_x \cos k$ with $t' \in \mathbb{R}$ (to preserve time-reversal symmetry) would do the job. It is in this spirit that these phases are said to be *protected by inversion*.

We conclude this section by mentioning that we will come back to the Rice-Mele chain later in the text, as we will use it as the starting point to model the quantum Hall effect (QHE) in topological (lattice) insulators.

3.4 Wilson loops of topological bands

In this section, we will define the Wilson loop and show how symmetries may constrain its spectrum. Then, we will learn that Wilson loop windings can be interpreted as an obstruction to constructing maximally localized Wannier functions and give an alternative interpretation in terms of the Chern number and gauge discontinuity. We will finish the section by exploring the obstruction in two models: the Thouless pump and the Kane-Mele model.

3.4.1 Wilson Loops and Symmetries

In previous sections, we have seen how adiabatic transport of Bloch functions reveals interesting information about the localization properties of (hybrid) Wannier states. In addition, we have seen in a particular model (Rice-Mele) that spatial symmetries like inversion can place constraints on the eigenvalues of the holonomy $\mathcal{W}$, and hence on the position of charge centers. We will now explore this relation in more generality.

For the remainder of these notes, we will work with Bloch functions as if they were obtained from a tight-binding model. Our starting point is thus a set of orthogonal tight-

[5] All bands in 1D could be induced from Wannier functions, if we only focus on their symmetry eigenvalues. This follows from the point that Wannier functions are the eigenfunctions of the projected position operator. We will demonstrate in Sec. 3.4.2 that this does not hold in higher dimensions.

binding orbitals $\varphi_{\sigma \boldsymbol{R}}(\boldsymbol{r})$, where σ denotes a collection of quantum numbers describing degrees of freedom within the unit cell, such as position within the unit cell, orbital type, or spin. The Bloch functions $\chi_{\sigma \boldsymbol{k}}(\boldsymbol{r})$ corresponding to these orbitals can be constructed via the following Fourier transform:

$$\chi_{\sigma \boldsymbol{k}}(\boldsymbol{r}) = \frac{1}{\sqrt{\mathcal{N}}} \sum_{\boldsymbol{R}} e^{i\boldsymbol{k}\cdot(\boldsymbol{R}+\boldsymbol{r}_\sigma)} \varphi_{\sigma \boldsymbol{R}}(\boldsymbol{r}). \tag{3.112}$$

The eigenfunctions $\psi_{n\boldsymbol{k}}(\boldsymbol{r})$ of the Hamiltonian can then be expanded as linear combinations of these Bloch waves as

$$\psi_{n\boldsymbol{k}}(\boldsymbol{r}) = \sum_{\sigma} u^{\sigma}_{n\boldsymbol{k}} \chi_{\sigma \boldsymbol{k}}(\boldsymbol{r}) = \frac{1}{\sqrt{\mathcal{N}}} \sum_{\sigma \boldsymbol{R}} u^{\sigma}_{n\boldsymbol{k}} e^{i\boldsymbol{k}\cdot(\boldsymbol{R}+\boldsymbol{r}_\sigma)} \varphi_{\sigma \boldsymbol{R}}(\boldsymbol{r}). \tag{3.113}$$

Finally, the periodic part $u_{n\boldsymbol{k}}(\boldsymbol{r})$ of the eigenfunctions reads:

$$u_{n\boldsymbol{k}}(\boldsymbol{r}) = \sum_{\sigma \boldsymbol{R}} u^{\sigma}_{n\boldsymbol{k}} \varphi_{\sigma \boldsymbol{R}}(\boldsymbol{r}) e^{-i\boldsymbol{k}\cdot(\boldsymbol{r}-\boldsymbol{R}-\boldsymbol{r}_\sigma)}. \tag{3.114}$$

The periodicity of the eigenstates $\psi_{n\boldsymbol{k}}(\boldsymbol{r})$ as $\boldsymbol{k} \to \boldsymbol{k} + \boldsymbol{G}$ implies that

$$u^{\sigma}_{n\boldsymbol{k}+\boldsymbol{G}} = e^{-i\boldsymbol{G}\cdot\boldsymbol{r}_\sigma} \delta_{\sigma\sigma'} u^{\sigma'}_{n\boldsymbol{k}} \equiv [V^{-1}(\boldsymbol{G})]_{\sigma\sigma'} u^{\sigma'}_{n\boldsymbol{k}}. \tag{3.115}$$

In principle, the Berry connections computed from $u^{\sigma}_{n\boldsymbol{k}}$ and $u_{n\boldsymbol{k}}(\boldsymbol{r})$ generally differ outside the tight-binding limit. In spite of this, both connections obey the same symmetry constraints, because $u^{\sigma}_{n\boldsymbol{k}}$ and $u_{n\boldsymbol{k}}(\boldsymbol{r})$ transform under isomorphic representations of the crystal symmetry group. The geometry of adiabatic transport of the $u^{\sigma}_{n\boldsymbol{k}}$ is itself interesting, since they are eigenstates of the parametric family of matrix Hamiltonians

$$h_{\sigma\sigma'}(\boldsymbol{k}) = \int \mathrm{d}^d r \, \varphi^*_{\sigma \boldsymbol{k}}(\boldsymbol{r}) H(\boldsymbol{k}) \varphi_{\sigma' \boldsymbol{k}}(\boldsymbol{r}), \tag{3.116}$$

where we have (re)-introduced $\varphi_{\sigma \boldsymbol{k}}(\boldsymbol{r}) = N^{-1/2} \sum_{\boldsymbol{R}} \varphi_{\sigma \boldsymbol{R}}(\boldsymbol{r}) e^{-i\boldsymbol{k}\cdot(\boldsymbol{r}-\boldsymbol{R}-\boldsymbol{r}_\sigma)}$. In matrix notation, the Schrödinger equation for $u^{\sigma}_{n\boldsymbol{k}}$ becomes

$$h(\boldsymbol{k}) \begin{bmatrix} u^1_{n\boldsymbol{k}} \\ u^2_{n\boldsymbol{k}} \\ \vdots \end{bmatrix} = E_{n\boldsymbol{k}} \begin{bmatrix} u^1_{n\boldsymbol{k}} \\ u^2_{n\boldsymbol{k}} \\ \vdots \end{bmatrix}. \tag{3.117}$$

For the rest of these notes we will focus on the parallel transport of the projectors $[P(\boldsymbol{k})]_{\sigma\sigma'} = \sum_{n=1}^{N} u^{\sigma *}_{n\boldsymbol{k}} u^{\sigma'}_{n\boldsymbol{k}}$. We will denote $|u_{n\boldsymbol{k}}\rangle$ the column vector of coefficients $u^{\sigma}_{n\boldsymbol{k}}$, so that $P(\boldsymbol{k}) = \sum_{n=1}^{N} |u_{n\boldsymbol{k}}\rangle\langle u_{n\boldsymbol{k}}|$. Let us consider the holonomy matrix $W_{\mathcal{C}}$ along a

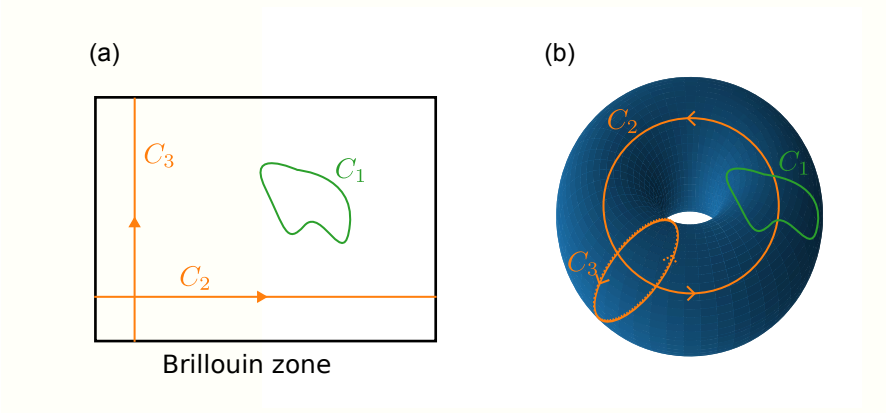

Figure 3.7: Different types of paths that could be considered in a 2D BZ. The path C_1 in green is contractible, while the C_2 and C_3 in orange are non-contractible. (a) The non-contractible paths cross the boundaries of the BZ, whereas the C_1 is contained entirely within the boundaries of the BZ. (b) The BZ becomes a torus when we glue the borders based on the periodicity of the boundaries. The topology of the torus impedes shrinking the non-contractible paths to a point.

smooth contour $\mathcal{C}$ in the BZ given by

$$W_{\mathcal{C}}^{nm} = \langle u_{n\boldsymbol{k}_f} | \mathcal{W}_{\mathcal{C}} | u_{m\mathbf{k_0}} \rangle = \langle u_{n\boldsymbol{k}_f} | \prod_{\boldsymbol{k}}^{\mathcal{C}} P(\boldsymbol{k}) | u_{m\mathbf{k_0}} \rangle , \tag{3.118}$$

where $\mathcal{C}$ starts at $\boldsymbol{k_0}$ and ends at $\boldsymbol{k_f}$. By construction, each projector is invariant under a $U(N)$-valued gauge transformations $U(\boldsymbol{k})$ at each $\boldsymbol{k}$,

$$U(\boldsymbol{k})P(\boldsymbol{k})U^{\dagger}(\boldsymbol{k}) = P(\boldsymbol{k}). \tag{3.119}$$

As such, by defining $|u'_{n\boldsymbol{k}}\rangle = U_{nm}(\boldsymbol{k}) |u_{m\boldsymbol{k}}\rangle$, the holonomy matrix $W_{\mathcal{C}}$ transforms into $W'_{\mathcal{C}}$ in the following way:

$$W'_{\mathcal{C}} = U^{\dagger}(\boldsymbol{k_f}) W_{\mathcal{C}} U(\boldsymbol{k_0}), \tag{3.120}$$

thus, like all adiabatic transport, the spectrum of $W_{\mathcal{C}}$ is gauge invariant only when $\mathcal{C}$ is a closed curve. The holonomy $\mathcal{W}_{\mathcal{C}}$ for a closed loop $\mathcal{C}$ is referred to as **Wilson Loop**.

For simple (i.e. contractible) closed curves like C_1 in Fig. **3.7**, this is the end of the story. However, recall that the Brillouin zone is topologically a d-dimensional torus due to the imposed periodic-boundary conditions, which allows us to draw non-contractible cycles like C_2 and C_3 in Fig. **3.7**. Such curves cross the boundary of the BZ and thus can not shrink to a point. The simplest non contractible curves we can think of are linear and wind only once [see Fig. **3.8**(a)]. They are given analytically by

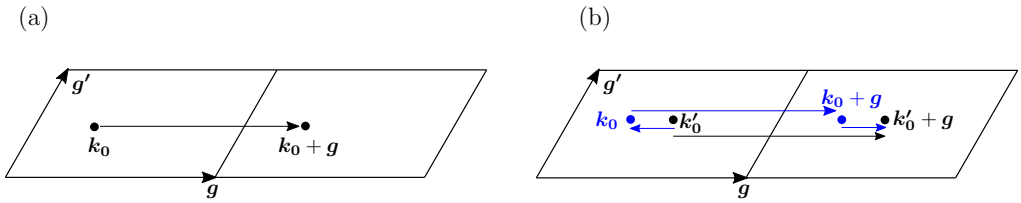

Figure 3.8: Paths in the BZ for a Wilson loop. (a) The simplest nontrivial closed path given in Eq. (3.121), winding once and parallel to a primitive reciprocal lattice vector $\boldsymbol{g}$. (b) A simple nontrivial path $\boldsymbol{k'_0} \to \boldsymbol{k'_0} + \boldsymbol{g}$ with basepoint $\boldsymbol{k'_0}$, and an alternative path with basepoint at $\boldsymbol{k_0}$.

$$\mathcal{C}_{\boldsymbol{g}} = \{\boldsymbol{k_0} + \boldsymbol{g}\ t \mid t \in [0,1]\}, \tag{3.121}$$

where $\boldsymbol{g}$ denotes a primitive reciprocal-lattice vector. Recall also from Sec. 3.3 that eigenvalues of $\mathcal{W}_{\mathcal{C}_{\boldsymbol{g}}}$ give the charge centers of hybrid Wannier functions that are exponentially localized in the direct-lattice direction that is not orthogonal to $\boldsymbol{g}$. When considering the Wilson loop along a closed curve, we need to make sure that the constrain in Eq. (3.115) set by our periodic-boundary gauge is satisfied:

$$W^{nm}_{\mathcal{C}_{\boldsymbol{g}}} = \langle u_{n\boldsymbol{k}+\boldsymbol{g}} | \mathcal{W}_{\mathcal{C}_{\boldsymbol{g}}} | u_{m\boldsymbol{k}} \rangle = \langle u_{n\boldsymbol{k}} | V(\boldsymbol{g}) \mathcal{W}_{\mathcal{C}_{\boldsymbol{g}}} | u_{m\boldsymbol{k}} \rangle\,. \tag{3.122}$$

This means that the parallel transport along the closed and non contractible cycle $\mathcal{C}_{\boldsymbol{g}}$ is described by the Wilson loop:

$$\mathcal{W}_{\boldsymbol{g},\boldsymbol{k_0}} = V(\boldsymbol{g}) \prod_{\boldsymbol{k}}^{\boldsymbol{k_0}+\boldsymbol{g} \leftarrow \boldsymbol{k_0}} P(\boldsymbol{k}), \tag{3.123}$$

whose nonzero eigenvalues are gauge invariant and correspond in the tight-binding limit to the centers of hybrid Wannier functions localized in the $\boldsymbol{r} \cdot \hat{\boldsymbol{g}}$ direction.

What is the role of the basepoint $\boldsymbol{k_0}$? Consider the paths $\boldsymbol{k'_0} \to \boldsymbol{k'_0} + \boldsymbol{g}$ and $\boldsymbol{k_0} \to \boldsymbol{k_0} + \boldsymbol{g}$ [see Fig. **3.8**(b)], whose basepoints are shifted in the $\hat{\boldsymbol{g}}$-direction. Writing the Wilson loop $W^{mn}_{\boldsymbol{g},\boldsymbol{k'_0}}$ as a product of projectors and applying the unitary property of $V(\boldsymbol{g})$ leads to:

$$W^{mn}_{\boldsymbol{g},\boldsymbol{k'_0}} = W^{ml}_{\boldsymbol{k'_0}+\boldsymbol{g}\leftarrow\boldsymbol{k_0}+\boldsymbol{g}}\, W^{lp}_{\boldsymbol{g},\boldsymbol{k_0}} W^{pn}_{\boldsymbol{k_0}\leftarrow\boldsymbol{k'_0}} = [W^{\dagger}_{\boldsymbol{k_0}\leftarrow\boldsymbol{k'_0}}]^{ml}\, W^{lp}_{\boldsymbol{g},\boldsymbol{k_0}}\, W^{pn}_{\boldsymbol{k_0}\leftarrow\boldsymbol{k'_0}}. \tag{3.124}$$

which is a similarity relation where the holonomy matrix $W_{\boldsymbol{k_0}\leftarrow\boldsymbol{k'_0}}$ plays the role of a unitary gauge transformation. This demonstrates that Wilson loops $W_{\boldsymbol{g}}$ starting from basepoints that differ in the $\hat{\boldsymbol{g}}$ direction share the same spectrum, although they generally have different matrix elements. The choice of the basepoint is therefore irrelevant for

the calculation of hybrid Wannier centers.

Note however that in 2 and 3 dimensions the Wilson loop $W_{\boldsymbol{g}}$ will still depend on the components of the basepoint that are perpendicular to $\hat{\boldsymbol{g}}$. Let us for instance consider that we decompose the basepoint $\boldsymbol{k}$ into two components $\boldsymbol{k}_{\parallel}$ and $\boldsymbol{k}_{\perp}$ that are respectively parallel and perpendicular to $\hat{\boldsymbol{g}}$, so that $\boldsymbol{k} = (\boldsymbol{k}_{\parallel}, \boldsymbol{k}_{\perp})$; we can then omit $\boldsymbol{k}_{\parallel}$ as it is physically irrelevant, but the Wilson loop matrix still depends on $\boldsymbol{k}_{\perp}$, i.e. $W_{\boldsymbol{g},\boldsymbol{k}} = W_{\boldsymbol{g}}(\boldsymbol{k}_{\perp})$.

We will now focus on the action of space group symmetries. A space group symmetry operation $h = \{R|\boldsymbol{v}\}$ acts on the vector of coefficients $u^{\sigma}_{n\boldsymbol{k}}$ as

$$u^{\sigma}_{n\boldsymbol{k}} \to U^{\sigma\sigma'}(R) u^{\sigma'}_{n(R\boldsymbol{k})} e^{-i(R\boldsymbol{k})\cdot\boldsymbol{v}} \equiv S^{\sigma\sigma'}_{\boldsymbol{k}} u^{\sigma'}_{n(R\boldsymbol{k})}. \tag{3.125}$$

Here, $U(R)$ is the matrix of R in the representation that describes the transformation of the degrees of freedom denoted by σ (orbital angular momentum, spin and site within the unit cell). Let us focus on two important cases: inversion and time-reversal symmetry.

Inversion symmetry:

Let us study in general terms the transformation under inversion symmetry of the Wilson loop operator $\mathcal{W}_{\boldsymbol{g}}(\boldsymbol{k}_{\perp})$. According to Eq. (3.125), under inversion the projector $P(\boldsymbol{k})$ transforms as

$$U_I P(\boldsymbol{k}) U_I^{\dagger} = P(-\boldsymbol{k}). \tag{3.126}$$

Writing out the Wilson loop operator as a product of projectors:

$$U_I \mathcal{W}_{\boldsymbol{g}}(\boldsymbol{k}_{\perp}) U_I^{\dagger} = \lim_{\delta\to 0} U_I V(\boldsymbol{g}) P(\boldsymbol{g}, \boldsymbol{k}_{\perp}) P(\boldsymbol{g}-\boldsymbol{\delta}, \boldsymbol{k}_{\perp}) \dots P(\boldsymbol{0}) U_I^{\dagger}. \tag{3.127}$$

Having in mind that U_I is unitary, we insert the identity $U_I^{\dagger} U_I$ between $V(\boldsymbol{g})$ and $P(\boldsymbol{g}, \boldsymbol{k}_{\perp})$:

$$U_I \mathcal{W}_{\boldsymbol{g}}(\boldsymbol{k}_{\perp}) U_I^{\dagger} = \lim_{\delta\to 0} U_I V(\boldsymbol{g}) U_I^{\dagger} P(-\boldsymbol{g}, -\boldsymbol{k}_{\perp}) P(-\boldsymbol{g}+\boldsymbol{\delta}, -\boldsymbol{k}_{\perp}) \dots P(0). \tag{3.128}$$

where we have applied Eq. (3.126). We need to work out the relation between U_I and $V(\boldsymbol{g})$. On the one hand

$$P(\boldsymbol{g}, \boldsymbol{k}_{\perp}) = V^{\dagger}(\boldsymbol{g}) P(\boldsymbol{0}, \boldsymbol{k}_{\perp}) V(\boldsymbol{g}) = V^{\dagger}(\boldsymbol{g}) U_I P(\boldsymbol{0}, -\boldsymbol{k}_{\perp}) U_I^{\dagger} V(\boldsymbol{g}); \tag{3.129}$$

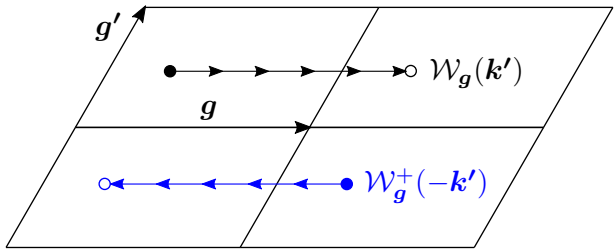

Figure 3.9: In black, the graphical discretization of the Wilson loop $\mathcal{W}_{\boldsymbol{g}}(\boldsymbol{k'})$ applied in the derivation of the effect of inversion and time-reversal on it. In blue, the Wilson loop $\mathcal{W}^{\dagger}_{\boldsymbol{g}}(-\boldsymbol{k'})$ to which it is related by these symmetries.

on the other hand

$$P(\boldsymbol{g},\boldsymbol{k}_\perp) = U_I P(-\boldsymbol{g},-\boldsymbol{k}_\perp)U_I^\dagger = U_I V(\boldsymbol{g})P(\boldsymbol{0},-\boldsymbol{k}_\perp)V^\dagger(\boldsymbol{g})U_I^\dagger. \tag{3.130}$$

Then, Eqs. (3.129) and (3.130) to be consistent, we must have:

$$U_I V(\boldsymbol{g})U_I^\dagger = V^\dagger(\boldsymbol{g}) = V(-\boldsymbol{g}). \tag{3.131}$$

Applying this back in Eq. (3.128) yields:

$$\begin{aligned} U_I \mathcal{W}_{\boldsymbol{g}}(\boldsymbol{k}_\perp)U_I^\dagger &= \lim_{\boldsymbol{\delta}\to\boldsymbol{0}} V(-\boldsymbol{g})P(-\boldsymbol{g},-\boldsymbol{k}_\perp)P(-\boldsymbol{g}+\boldsymbol{\delta},-\boldsymbol{k}_\perp)\dots P(\boldsymbol{0}) \\ &= W^\dagger_{\boldsymbol{g}}(-\boldsymbol{k}_\perp). \end{aligned} \tag{3.132}$$

In conclusion, inversion relates $\mathcal{W}_{\boldsymbol{g}}(\boldsymbol{k}_\perp)$ and $\mathcal{W}^{\dagger}_{\boldsymbol{g}}(-\boldsymbol{k}_\perp)$ via a similarity relation (see Fig. **3.9**) and hence forces them to share the same spectrum. This constrain becomes particularly restrictive for inversion-invariant momenta[6] $\boldsymbol{k}_\perp \equiv -\boldsymbol{k}_\perp$, as it implies that the spectrum of $\mathcal{W}_{\boldsymbol{g}}(\boldsymbol{k}_\perp)$ is real. We illustrate in Fig. **3.10**(a) the shape of the Wilson loop spectra constrained by inversion.

Time-reversal symmetry:

We could expect the influence of time-reversal symmetry $\mathcal{T}$ on the Wilson loop to be similar to that of inversion, because both symmetries map $\boldsymbol{k}$ to $-\boldsymbol{k}$. Nevertheless, unlike inversion, time-reversal symmetry is an antiunitary operation that acts on the coefficients as the complex-conjugate operation (spinless case). Let us consider its action on the Wilson loop:

[6]The symbol $\equiv$ denotes equivalence module a reciprocal lattice vector.

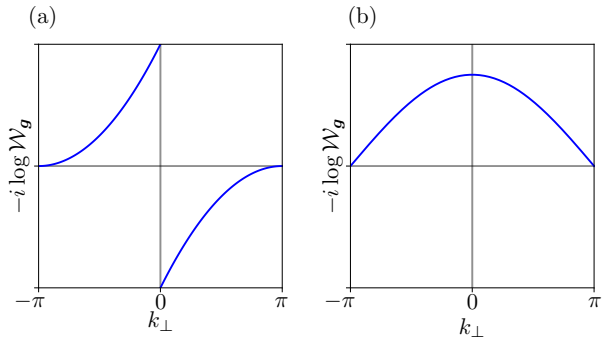

Figure 3.10: Example Wilson loop spectra of spinless systems with (a) inversion symmetry (b) time-reversal symmetry.

$$\begin{aligned}\mathcal{T}\mathcal{W}_{\boldsymbol{g}}(\boldsymbol{k}_\perp)\mathcal{T}^{-1} &= \mathcal{T}V(\boldsymbol{g})P(\boldsymbol{g},\boldsymbol{k}_\perp)P(\boldsymbol{g}-\boldsymbol{\delta},\boldsymbol{k}_\perp)\dots P(\boldsymbol{0})\mathcal{T}^{-1} \\ &= V(-\boldsymbol{g})\mathcal{T}P(-\boldsymbol{g},-\boldsymbol{k}_\perp)P(-\boldsymbol{g}+\boldsymbol{\delta},-\boldsymbol{k}_\perp)\dots P(\boldsymbol{0}) \\ &= \mathcal{W}_{-\boldsymbol{g}}(-\boldsymbol{k}_\perp).\end{aligned} \tag{3.133}$$

If $\mathcal{T}$ was unitary, this equation would be a similarity relation imposing the same constrains as inversion. It instead forces the spectra of $\mathcal{W}_{\boldsymbol{g}}(\boldsymbol{k}_\perp)$ and $\mathcal{W}_{-\boldsymbol{g}}(-\boldsymbol{k}_\perp)$ to be related by complex conjugation. Fig. **3.10**(b) sketches the shape of a Wilson loop constrained by time-reversal symmetry.

For spinful particles, the constrain becomes particularly interesting at inversion-invariant momenta[7], as it forces each eigenstate of $W_{\boldsymbol{g}}(\boldsymbol{k}_\perp)$ to be doubly-degenerate (Kramers degeneracy). Let us emphasize that this is not the case of inversion, whose effect is to form pairs of complex-conjugate eigenvalues (unless they are real).

A similar analysis can be carried out for any symmetry operation [99], which may be helpful to investigate the constraints that symmetries place on Wilson loop spectra in more complicated space groups. Nevertheless, we will only make use of time reversal and inversion symmetry in what follows.

To contextualize these results, let us return to the 1D Rice-Mele chain. According to our analysis, inversion symmetry forces eigenvalues of $\mathcal{W}_g$ to be real or come in complex conjugate pairs. Since there exists a single occupied band, the nonzero eigenvalue λ of $\mathcal{W}_g$ should be real, and so it must be either 1 or -1; equivalently: $(2i\pi)^{-1}\log\lambda = 0, 1/2$.

[7]Inversion-invariant points, which satisfy $-\boldsymbol{k} \equiv \boldsymbol{k}$, are often referred to as time-reversal invariant momenta (TRIM). We will adopt this naming from now on.

Now, we have a wider picture of how inversion symmetry quantizes hybrid Wannier centers in 1D. In systems defined in more dimensions, we do not have this quantization for generic $\boldsymbol{k}_\perp$, because $\boldsymbol{k}_\perp \not\equiv -\boldsymbol{k}_\perp$ in general. However, we gain something amazing: the possibility for finding **topologically distinct** spectra for $\mathcal{W}_g(\boldsymbol{k}_\perp)$ as a function of $\boldsymbol{k}_\perp$.

Let us briefly comment on the consequence that the constrain set by time-reversal symmetry has on the topology, which could serve to motivate the discussion in the next section. As we illustrate in Fig. **3.10**(b), time-reversal symmetry forces the spectrum of the Wilson loop $\mathcal{W}_g(\boldsymbol{k}_\perp)$ to be symmetric with respect to the $\boldsymbol{k}_\perp = 0$ axis. Owing to this fact, the curve corresponding to a single eigenvalue can not wind as $\boldsymbol{k}_\perp$ goes through the whole BZ. Indeed, having an odd number of eigenvalues which wind requires breaking TR symmetry.

3.4.2 Wilson Loop Winding and Wannier Obstruction

To further motivate this discussion, let us recall that in 1D, the notions of Wannier and hybrid Wannier functions coincide. Thus, in the tight-binding limit in 1D, the **Wannier centers** coincide with $(2\pi i)^{-1}$ times the logarithm of eigenvalues of the Wilson loop $\mathcal{W}_g$ (mod a). In higher dimensions, this is not generically the case even in the tight-binding limit, because projected position operators along different directions need not commute,

$$[Px_iP, Px_jP] \neq 0. \tag{3.134}$$

In such cases, it is not possible to simultaneously diagonalize all the projected position operators. In other words, generally it is not possible to find functions that are simultaneous eigenstates of projected positions along multiple directions. To see how this can happen, let us take a trial state $|f\rangle = \sum_{n,\boldsymbol{k}} f_{n\boldsymbol{k}} |\psi_{n\boldsymbol{k}}\rangle$ belonging to $\mathrm{Im}(P)$. From Eq. (3.82), we have

$$\begin{aligned}[Px_iP, Px_jP]\,|f\rangle &= \sum_{\boldsymbol{k},mnl} \Big(i\partial_i A^j_{nm} - i\partial_j A^i_{nm} + A^i_{nl}A^j_{lm} - A^j_{nl}A^i_{lm}\Big) f_{m\boldsymbol{k}} \,|\psi_{n\boldsymbol{k}}\rangle \\ &= i \sum_{\boldsymbol{k},mn} \Omega^{ij}_{nm}(\boldsymbol{k}) \,|\psi_{n\boldsymbol{k}}\rangle \, f_{m\boldsymbol{k}},\end{aligned} \tag{3.135}$$

where

$$\Omega^{ij}_{nm}(\boldsymbol{k}) = \partial_i A^j_{nm}(\boldsymbol{k}) - \partial_j A^i_{nm}(\boldsymbol{k}) - i[A^i(\boldsymbol{k}), A^j(\boldsymbol{k})]_{nm} \tag{3.136}$$

is the **Berry-curvature** tensor. We read in Eq. (3.135) that the Berry curvature tensor must vanish for all $\boldsymbol{k}$ for there to exist a basis in which Px_iP and Px_jP are simultaneously diagonal. This means that, in general, hybrid Wannier functions – eigenstates of a single Px_iP – will not coincide with maximally localized Wannier functions – orbitals designed to be as localized as possible in all directions. Thus, we must take care to

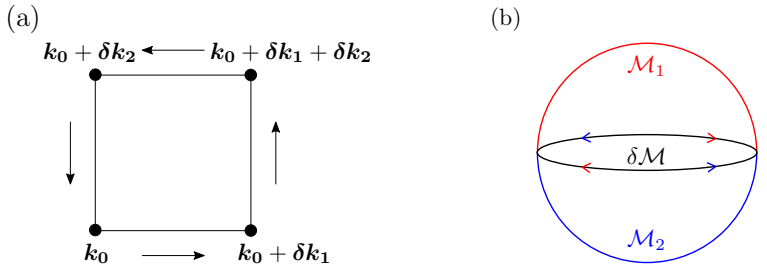

Figure 3.11: (a) Path considered in the statement of Ambrose-Singer theorem in Eq. (3.137). (b) Sphere $\mathcal{M} = \mathcal{M}_1 \cup \mathcal{M}_2$ considered as closed manifold for the definition of the (first) Chern number.

distinguish between hybrid Wannier centers and Wannier centers. This distinction will turn out to be particularly important because, while unique hybrid Wannier functions exist for any gapped projector, Wannier functions are not unique and may not even be exponentially localizable (while respecting symmetries). Eq. (3.135) suggests a deep relation between topology and the possibility for finding hybrid Wannier functions that are exponentially localized in different directions. We will devote the remaining of the section to unveiling this relation.

We begin by exploring how the Wilson loop contains information about the Berry curvature tensor. This relation between the holonomy of the connection and its curvature is given by the **Ambrose-Singer** theorem. We consider a parallelogram in the Brillouin zone with sides of infinitesimal length [see Fig. **3.11**(a)]; according to Ambrose-Singer theorem, the leading order term in the Taylor series of the Wilson loop along the boundary of the parallelogram is related to the Berry curvature via

$$i\Omega^{12}_{nm}(k_0)\delta k_1 \delta k_2 = \log W_4 W_3 W_2 W_1 + \mathcal{O}\big(\delta k^3\big). \tag{3.137}$$

Let us neglect the $\mathcal{O}\big(\delta k^3\big)$ terms and take the trace on both sides of the equation:

$$i \operatorname{tr} \Omega^{12}_{nm}(k_0)\delta k_1 \delta k_2 = \log \det\{W_4 W_3 W_2 W_1\} + \mathcal{O}\big(\delta k^3\big). \tag{3.138}$$

Here, we have applied the property $\operatorname{tr} \log W = \log \det W$. There are two reasons for taking the trace: On the one hand, it will lead to the definition of an important topological invariant, namely the Chern number. On the other hand, it will be helpful to get over the issue of non-commutativity of the matrices W_i on the right-hand side, specially when going beyond infinitesimal parallelograms.

We first focus on the left-hand side of Eq. (3.138). Due to the cyclic property $\operatorname{tr}(AB) = \operatorname{tr}(BA)$, the commutator in Eq. (3.136) does not contribute to the trace. This simplification reduces the trace of the Berry curvature to the curl of the Berry connection, so that we are left with an integral which gives the flux of $\boldsymbol{\nabla} \times \boldsymbol{A}(\boldsymbol{k})$ through

our parallelogram. Furthermore, we can add up a series of infinitesimal Wilson loops to create a path that encloses a finite region $\mathcal{M}$ of the BZ, like in Fig. **3.12**(b):

$$\begin{aligned}\frac{1}{2\pi}\int_M \operatorname{tr}\bigl(\Omega^{12}\bigr)\,\mathrm{d}k_1\,\mathrm{d}k_2 &= \frac{1}{2\pi}\int_M \left(\partial_{k_1}\operatorname{tr}A_2 - \partial_{k_2}\operatorname{tr}A_1\right)\mathrm{d}k_1\,\mathrm{d}k_2 \\ &= \frac{1}{2\pi}\oint_{\partial M}\operatorname{tr}\boldsymbol{A}\cdot\mathrm{d}\boldsymbol{l}\,,\end{aligned} \tag{3.139}$$

where subscripts of the Berry connection denote directions in reciprocal space. Here, we have used Stokes theorem[8] to turn the integral giving the flux of the Berry curvature $\boldsymbol{\Omega}(\boldsymbol{k})$ through $\mathcal{M}$ into the line integral of the Berry curvature $\boldsymbol{A}(\boldsymbol{k})$ along its boundary ∂M. If $\mathcal{M}$ is a closed manifold (such as a plane "bounded" by reciprocal lattice vectors $\boldsymbol{g}_1$ and $\boldsymbol{g}_2$ in the 2D Brillouin zone), this integral vanishes modulo gauge discontinuities in $\operatorname{tr}\boldsymbol{A}(\boldsymbol{k})$.

As an example of this statement, we consider $\mathcal{M}$ to be the sphere of Fig. **3.11**(b). We denote $\mathcal{M}_1$ and $\mathcal{M}_2$ the upper and lower patches of this sphere, respectively. The wave functions defined on $\mathcal{M}_1$ and $\mathcal{M}_2$ must match at the equator, up to a unitary gauge transformation $U(\boldsymbol{k})$:

$$|\psi^{\mathcal{M}_2}_{n\boldsymbol{k}}\rangle = U_{nm}(\boldsymbol{k})\,|\psi^{\mathcal{M}_1}_{m\boldsymbol{k}}\rangle\,. \tag{3.140}$$

This implies that, at the equator, the Berry connections $\boldsymbol{A}_1(\boldsymbol{k})$ and $\boldsymbol{A}_2(\boldsymbol{k})$ are related via

$$\boldsymbol{A}_2 = U^\dagger \boldsymbol{A}_1 U + iU^\dagger \boldsymbol{\nabla} U, \tag{3.141}$$

and their traces by

$$\operatorname{tr}\boldsymbol{A}_2 = \operatorname{tr}\boldsymbol{A}_1 + i\operatorname{tr}\bigl(U^\dagger\boldsymbol{\nabla}U\bigr) = \operatorname{tr}\boldsymbol{A}_1 - \boldsymbol{\nabla}\varphi, \tag{3.142}$$

where we have defined $\varphi = \operatorname{Im}\log\det U$ as the sum of the phase of the eigenvalues of U. Note that the traces of both the connections would be the same if there was not any gauge discontinuity at the equator between the wave functions of $\mathcal{M}_1$ and $\mathcal{M}_2$. We finally find that the integral of the Berry curvature over the sphere is

$$\begin{aligned}\frac{1}{2\pi}\int_M \operatorname{tr}(\Omega)\,\mathrm{d}^2k &= \frac{1}{2\pi}\int_{M_1}\operatorname{tr}(\Omega)\,\mathrm{d}^2k + \frac{1}{2\pi}\int_{M_2}\operatorname{tr}(\Omega)\,\mathrm{d}^2k \\ &= \frac{1}{2\pi}\int_{\partial M}\operatorname{tr}(\boldsymbol{A}_1)\cdot\mathrm{d}\boldsymbol{l} - \frac{1}{2\pi}\int_{\partial M}\operatorname{tr}(\boldsymbol{A}_2)\cdot\mathrm{d}\boldsymbol{l} \\ &= \frac{1}{2\pi}\int_{\partial M}\boldsymbol{\nabla}\varphi\cdot\mathrm{d}\boldsymbol{l}\,.\end{aligned} \tag{3.143}$$

[8] When the subspace of interest contains more than one band, Ambrose-Singer theorem might not be equivalent to Stokes's theorem [76].

It is now clear that the integral in Eq. (3.139) vanishes for closed regions if there is not any discontinuity in the gauge. Moreover, the fact that the gauge $U(\boldsymbol{k})$ must be periodic in the reciprocal lattice constrains this integral to be an integer number ν. This integer is known as the first **Chern number**:

$$\frac{1}{2\pi}\int_M \mathrm{tr}(\Omega)\cdot \mathrm{d}^2k = \nu \in \mathbb{Z}. \tag{3.144}$$

The Chern number is a topological invariant of states defined on the closed manifold $\mathcal{M}$. The only way to change the value it takes is to close the gap between the manifold of states in the image of our projectors and the rest of states.

We have figured out how the Chern number arises from the flux of the Berry curvature through a closed surface by working out the left-hand side of Ambrose-Singer theorem. We now focus on the right-hand side to relate the Chern number to the Wilson loop spectrum.

Let us consider the 2D plane $\{(k_1\boldsymbol{g}_1, k_2\boldsymbol{g}_2) \mid k_1, k_2 \in [0,1]\}$ in the BZ and Wilson loops $\mathcal{W}_{\boldsymbol{g}_2}(k_1)$ and $\mathcal{W}_{\boldsymbol{g}_2}(k_1+\Delta k)$ (see Fig. **3.12**). There are two practical problems to apply Ambrose-Singer theorem in Eq. (3.137) to this path: First, the length of the boundary is not infinitesimal; we can overcome this problem by dividing the region in infinitesimal parallelograms. Second, the right-hand side of the equation would involve a product of matrices W_i that is hard to simplify owing to the fact that these matrices do not commute; the determinant in Eq. (3.138) solves this problem. All in all, this equation applied to the aforementioned 2D plane reads:

$$\begin{aligned} i\int_M \mathrm{tr}(\Omega)\,\mathrm{d}^2k + \mathcal{O}(\Delta k^2) &= \log\det\Big(\square\square\ldots\square\Big) \\ &= \log\det\left[W_{\boldsymbol{g}_2}(k_1+\delta k_1)W^\dagger_{\boldsymbol{g}_2}(k_1)\right], \end{aligned} \tag{3.145}$$

where M is the region between the two loops, and $\square\square\ldots\square$ schematically represents dividing region M into Wilson loops evaluated on plaquettes, as shown in Fig. **3.12**(b). Note that we have gotten rid of all horizontal segments in this figure thanks to the determinant. In the limit $\delta k \to 0$ the change in $\log\det(W_{\boldsymbol{g}_2})$ is dominated by $\mathrm{tr}(\Omega)$:

$$\partial_{k_1}\log\det W_{\boldsymbol{g}_2}(k_1) = i\int \mathrm{d}k_2\,\Omega^{12}(\boldsymbol{k}), \tag{3.146}$$

and so

$$\frac{1}{2\pi i}\int \mathrm{d}k_1\,\partial_{k_1}\log\det W_{g_2}(k_1) = \nu. \tag{3.147}$$

The integral in this expression is the number of times the sum of hybrid Wannier centers winds across the entire unit cell and ν is the Chern number – we will explore this interpretation in more detail in the following section. This expression gives as an alternative

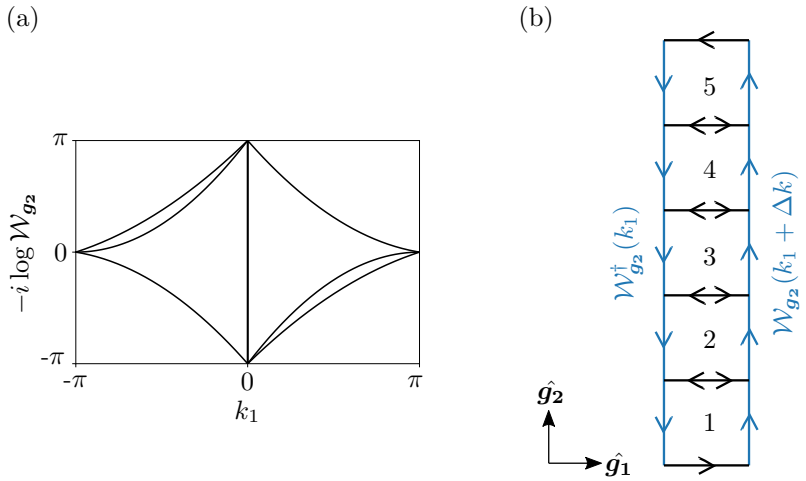

Figure 3.12: (a) Wilson loop spectrum for a system with Chern number $\nu = 1$. (b) In blue, Wilson loops along $\boldsymbol{g_2}$ at k_1 and $k_1 + \delta k_1$. Taking the logarithm of the determinant in Eq. (3.145) allows us to close the path in the border of the BZ and apply Stokes theorem. It also makes the contribution of the black segments vanish.

to Eq. (3.144) for calculating the Chern number of a group of bands. For example, in the case sketched in Fig. **3.12**(a), we have two centers winding upwards while only one winds downwards, so the Chern number is $\nu = 2 - 1 = 1$.

The Chern number defines classes of insulating Hamiltonians which cannot be deformed into each other without closing a gap, since

i) $\int \mathrm{tr}\,\Omega\, \mathrm{d}^2k$, being an integer, cannot change under small perturbations of the Hamiltonian.

ii) Periodicity of both the hybrid Wannier centers and the Brillouin zone implies that eigenvalues of the Wilson loop cannot smoothly unwind.

This means that projectors with different values of ν are **topologically distinct**. In terms of bands, two sets of bands with different values for the Chern number can not be deformed one into the other without closing the gap with other bands. In this spirit, the Chern number is robust against deformations that do not close gap.

Whereas we mentioned in the case of the Rice-Mele chain that the eigenvalue of the Wilson loop could be changed without closing the gap if we give up inversion symmetry, here we have not considered such a possibility. The reason for not considering it is that symmetries do not play any role in the robustness of the Chern number's value. Indeed, we have not considered any symmetry when defining the Chern number from Ambrose-Singer theorem nor deriving an interpretation for it.

A part from the interpretation as pumping of hybrid Wannier centers, the Chern number admits another interpretation in terms of an obstruction to charge localization. Recall the way we originally defined the Chern number for the sphere above: we showed that $\boldsymbol{A}_1(\boldsymbol{k})$ and $\boldsymbol{A}_2(\boldsymbol{k})$ (the Berry connections in either patch of the sphere) are related by a gauge transformation at the intersection of the two patches, and the Chern number is indeed the nontrivial winding number of this gauge. But the unitary matrix of the gauge transformation $U(\boldsymbol{k})$ cannot wind if it is globally defined. Thus, the Chern number can only be nonzero when there fails to exist a global smooth gauge choice for the wavefunctions. In particular, there fails to exist a smooth gauge $U(\boldsymbol{k})$ which would allows us to construct Bloch waves $\tilde{\psi}_{n\boldsymbol{k}}(\boldsymbol{r})$ satisfying Eq. (3.75), i.e. a gauge leading to exponentially localized Wannier functions. In conclusion, **a non-zero value for the Chern number is a Wannier obstruction.**

We have intepreted the Chern number in two ways: as the pumping of hybrid Wannier centers and as the obstruction to constructing exponentially localized Wannier functions out of our bands. Both interpretations can be connected by noting that if an eigenvalue $e^{i\theta_n}$ of the Wilson loop winds ν times, then the hybrid Wannier functions $|W_{n\boldsymbol{R_2}}(\boldsymbol{k_1})\rangle$ and $|W_{n\boldsymbol{R_2}}(\boldsymbol{k_1}+\boldsymbol{g_1})\rangle$ have centers of charge which differ by ν unit cells. As a consequence of this lack of periodicity in $\boldsymbol{k}_1$, hybrid Wannier functions can not be Fourier transformed to get exponentially localized Wannier functions.

In the following section, we will present an example of a "Chern insulator" that will help us to internalize the interpretation of the Chern number as winding of hybrid Wannier centers, namely the *Thouless pump*.

3.4.3 The Thouless pump

In this section, we will present a model for a topological insulator with a non-vanishing Chern number. Although we will introduce it as an extension of the Rice-Mele model, it can be understood as a 2D system with broken time-reversal (TR) symmetry.

Recall our simplified tight-binding Hamiltonian for the Rice-Mele chain,

$$h(k_1) = (\epsilon + t\cos k_1)\sigma_z + t\sin k_1 \sigma_y, \tag{3.148}$$

where we have renamed $k \to k_1$. We showed in Sec. 3.3.1 that when $t < \epsilon$, the eigenvalue of the Wilson loop for the valence band is 1, while for $t > \epsilon$ it is -1. Let us imagine that ϵ and t depend on a periodic parameter denoted k_2, which goes from $-\pi \to \pi$ and is odd under inversion and TR symmetry. We can then rewrite the Hamiltonian as $h(k_1, k_2)$. If we can ensure that inversion symmetry is preserved and that $h(k_1, 0)$ has $W_{g_1} = 1$ while $h(k_1, \pi)$ has $W_{g_1} = -1$, then we will have a model which, at a minimum, pumps the (hybrid) Wannier centers from $R_1 = 0$ to $R_1 = 1$ as a function of k_2; such a model would have[9] $\nu = -1$. Note that this requires breaking TR symmetry, since this

[9] Assuming $\mathbf{g_1}$ and $\boldsymbol{g}_2$ form a right-handed coordinate system

symmetry forces the Wilson loop matrices $W_{g_1}(k_2)$ and $W_{g_1}(-k_2)$ to be isospectral[10]. To satisfy these requirements, we can take

$$h(k_1, k_2) = a[(1 + \cos k_1 + \cos k_2)\sigma_z + \sin k_1 \sigma_y + \sin k_2 \sigma_x], \tag{3.149}$$

which at $k_2 = 0$ and $k_2 = \pi$ becomes

$$\begin{aligned} h(k_1, 0) &= a[(2 + \cos k_1)\sigma_z + \sin k_1 \sigma_y], \\ h(k_1, \pi) &= a[\cos k_1 \sigma_z + \sin k_1 \sigma_y]. \end{aligned} \tag{3.150}$$

We see that as a function of k_2, the Hamiltonian $h(k_1, k_2)$ interpolates between a 1D inversion symmetric chain (Rice-Mele chain) Hamiltonian with valence band inversion (σ_z) eigenvalues[11] $(--)$ at $k_2 = 0$ and one with valence band inversion eigenvalues $(-+)$ at $k_2 = \pi$. In terms of the eigenvalue of the Wilson loop for the valence band, this implies that

$$\begin{aligned} W_1(k_2 = 0) &= +1, \\ W_1(k_2 = \pi) &= -1. \end{aligned} \tag{3.151}$$

Thus, $\mathrm{Im} \log W_{g_1}(k_2)$ has the spectrum shown in Fig. **3.13**, which corresponds to the Chern number $\nu = -1$. According to our discussion, this indicates that there is an obstruction to constructing exponentially localized Wannier functions, and a topological distinction between projectors.

Note that the σ_x term in $h(k_1, k_2)$ plays two important roles. First, it ensures the existence of a gap for all k_1 and k_2. Second, as we mentioned, it breaks TR symmetry and allows $W_{g_1}(k_2)$ and $W_{g_1}(-k_2)$ to have different spectra, thus allowing for the winding in the Wilson loop spectrum.

Two comments about this model are in order:

1. While inversion symmetry simplifies the analysis by pinning $W_1(0, \pi)$ to ± 1, it is not necessary to define the Chern number. The winding of the Wilson loop spectrum – and hence the Chern number – is robust to inversion symmetry breaking.

2. Recall from Sec. 3.2 that a small electric field applied in the $\boldsymbol{R}_2$ direction will adiabatically shift k_2. From Fig. **3.13** , we see that this will adiabatically shift the hybrid Wannier centers in the $\boldsymbol{R}_1$ direction, generating a current. Therefore, ν governs the quantization of the **Hall conductance**.

We have seen that when $\det(W)$ winds, i.e. when $\nu \neq 0$, there is an obstruction to constructing exponentially localized Wannier functions, and hence also a topological

[10] We can also prove the bulk-boundary correspondence: the spectrum of PxP can be deformed to the spectrum of a surface potential $\theta(x - x_0)$ [100, 101].

[11] The first sign corresponds to the high-symmetry point Γ, while the second sign to X.

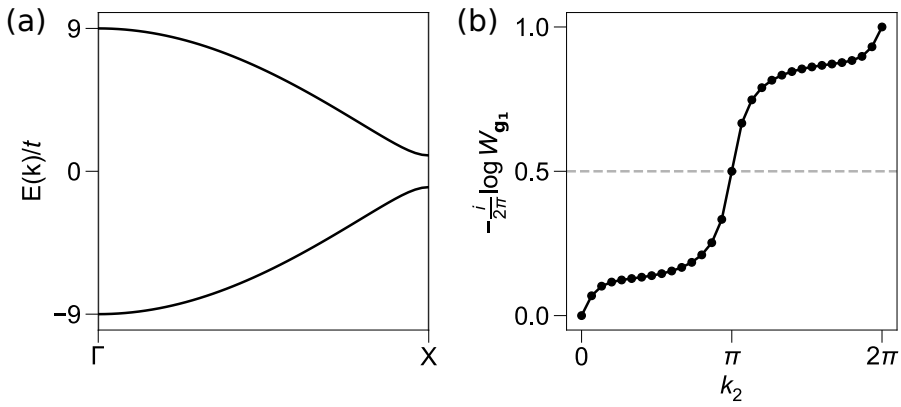

Figure 3.13: Wilson loop eigenvalue of the valence band in the model for the Thouless pump. Notice that, as it was explained in detail in Sec. 3.4.1, inversion symmetry requires the spectrum to be antisymmetric about $k_2 = 0$.

distinction between projectors. In the presence of additional symmetries, we can generalize this significantly by looking at the entire spectrum of the Wilson loop rather than just its determinant. As we saw earlier, symmetries may protect degeneracies in the Wilson loop spectrum and when this happens, individual Wilson loop eigenvalues may wind, even if the determinant of the Wilson loop is trivial ($\nu = 0$). Then, adiabatic deformations that preserve symmetries cannot deform the spectrum of W to a spectrum consistent with any atomic limit. These **topological-crystalline phases** include concepts such as mirror Chern insulators (Wilson loop eigenvalue crossings protected by mirror symmetry eigenvalues) and TR-invariant topological insulators (Wilson crossings protected by Kramers theorem). To conclude, we will examine the simplest example of the latter, by means of the **Kane-Mele** model.

A note about inversion and the role of k_2 is in order before we go on. Whereas we claimed in Sec. 3.3.1 that the phases of the Rice-Mele chain are protected by inversion, we have driven here the system through a transition between both phases without closing neither breaking inversion. The key to solve this paradox is to realize that the Hamiltonian for the Thouless pump in Eq. (3.149) does not correspond to at 1D chain, but to the 2D system shown in Fig. **3.14**. Indeed, even though k_2 was introduced as the interpolation parameter corresponding to the term proportional to σ_x and $\epsilon(k_2)$, the constrains set by inversion to these prevents us from interpreting them as hopping parameters anymore. The Hamiltonian in Eq. (3.149) for the Thouless pump corresponds to a 2D arrangement of s and p-orbitals at the origin of a lattice of space group $P\bar{1}$, with the following on-site parameters $\epsilon_\alpha = \langle\alpha(\mathbf{0})|H|\alpha(\mathbf{0})\rangle$ and nearest-neighbor hopping parameters $t_{\alpha\beta}(\boldsymbol{R}) = \langle\alpha(\boldsymbol{R})|H|\beta(\mathbf{0})\rangle$ $(\alpha, \beta = s, p)$:

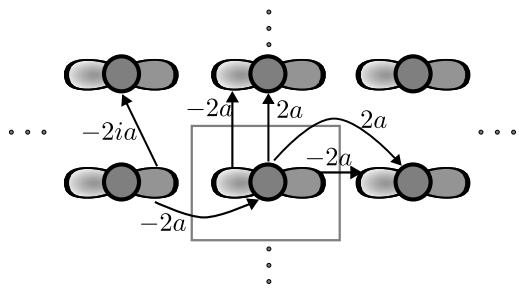

Figure 3.14: 2-dimensional lattice representation for the Thouless pump, with the minimal (symmetry independent) intercell hopping parameters. Cicles (lobes) denote s (p_x) orbitals. The rectangle is the primitive unit cell.

$$\begin{array}{lll} \epsilon_s = a, & t_{ss}(\boldsymbol{R}) = 2a, & t_{sp}(1,0) = -2a, \\ \epsilon_p = -a, & t_{pp}(\boldsymbol{R}) = -2a, & t_{sp}(0,1) = -2ia. \end{array}$$

Here $\boldsymbol{R}$ is a vector connecting an orbital to any of its nearest neighbors and $a \in \mathbb{R}$. Note that the responsible for breaking TR symmetry is the hopping between s and p-orbitals along the direction $[0,1]$, as it is given by a complex number.

3.4.4 Kane-Mele model

Let us consider the lattice of p_z orbitals sitting on a honeycomb structure, whose symmetry group is the layer group p6/mmm – isomorphic to space group 191 when we forget about translations in the z-direction. We choose $a = 1$ as lattice constant and the following basis vectors for the Bravais lattice:

$$\begin{aligned} \boldsymbol{e}_1 &= \frac{1}{2}(\sqrt{3}, -1), \\ \boldsymbol{e}_2 &= \frac{1}{2}(\sqrt{3}, 1). \end{aligned} \tag{3.152}$$

In this basis, the positions of the honeycomb lattice sites are given (within the unit cell) by

$$\begin{aligned} \boldsymbol{q}_A &= \frac{1}{3}\boldsymbol{e}_1 + \frac{1}{3}\boldsymbol{e}_2, \\ \boldsymbol{q}_B &= \frac{2}{3}\boldsymbol{e}_1 + \frac{2}{3}\boldsymbol{e}_2. \end{aligned} \tag{3.153}$$

Although we distinguish the sites in the unit cell by A and B as if they belonged to two different types of sites, they do not form completely independent sublattices. In fact, some symmetries of the space group (like the 6-fold rotation) map the sites A into B, and viceversa.

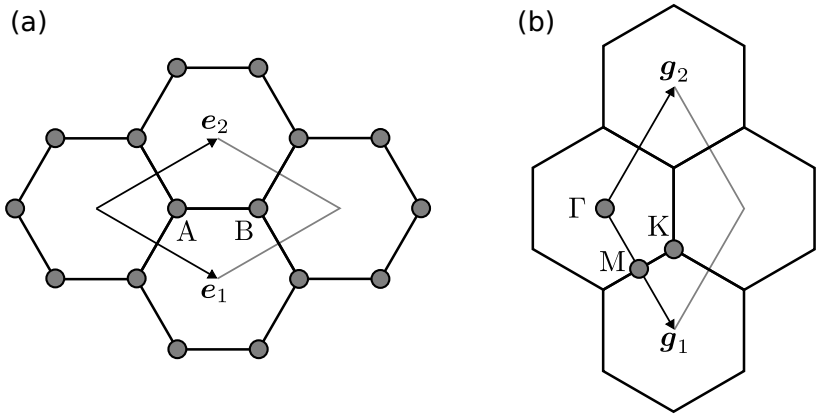

Figure 3.15: (a) Choice of unit cell for the honeycomb lattice. Circles denote sites where p_z orbitals sit. (b) Reciprocal lattice and Brillouin zone corresponding to that choice. The circles correspond to maximal $\boldsymbol{k}$-points.

A basis for the reciprocal lattice corresponding to the choice in Eq. (3.152) is

$$\begin{aligned} \boldsymbol{g}_1 &= 2\pi(1/\sqrt{3}, -1), \\ \boldsymbol{g}_2 &= 2\pi(1/\sqrt{3}, 1). \end{aligned} \tag{3.154}$$

The Bravais lattice and reciprocal lattice described here are shown in Fig. **3.15**. We would like to write a tight-binding Hamiltonian to investigate the band structure of the honeycomb lattice and its topology. This Hamiltonian should be consistent with the symmetries of the group $p6/mmm$. We begin by defining our tight-binding basis orbitals as

$$\varphi_{\boldsymbol{R},\alpha,s}(\boldsymbol{r}) = \varphi(\boldsymbol{r} - \boldsymbol{R} - \boldsymbol{q}_\alpha)|s\rangle, \tag{3.155}$$

where $\boldsymbol{R}$ is the vector of the lattice that denotes the unit cell, $\alpha \in \{A, B\}$ denotes the "type of the site" (often called sublattice), and $|s\rangle$ the spin state $s =\uparrow, \downarrow$. We can write down the spin-independent nearest-neighbor Hamiltonian for these orbitals as:

$$H = t \sum_{\boldsymbol{R},s} \left[c^\dagger_{\boldsymbol{R},B,s} c_{\boldsymbol{R},A,s} + c^\dagger_{\boldsymbol{R}-\boldsymbol{e}_2,B,s} c_{\boldsymbol{R},A,s} + c^\dagger_{\boldsymbol{R}-\boldsymbol{e}_1,B,s} c_{\boldsymbol{R},A,s} \right] + h.c. \tag{3.156}$$

Note that the spin-up and spin-down channels remain uncoupled in this Hamiltonian. In other words, the Hamiltonian is block-diagonal in the spin degree of freedom. Furthermore, both spin subspaces have in correspondence the same Hamiltonian.

Fourier transforming the creation and annihilation operators through the relation

$$c^\dagger_{\boldsymbol{k},\alpha,s} = \sum_{\boldsymbol{R}} e^{i\boldsymbol{k}\cdot(\boldsymbol{R}+\boldsymbol{q}_\alpha)} c^\dagger_{\boldsymbol{R},\alpha,s} \tag{3.157}$$

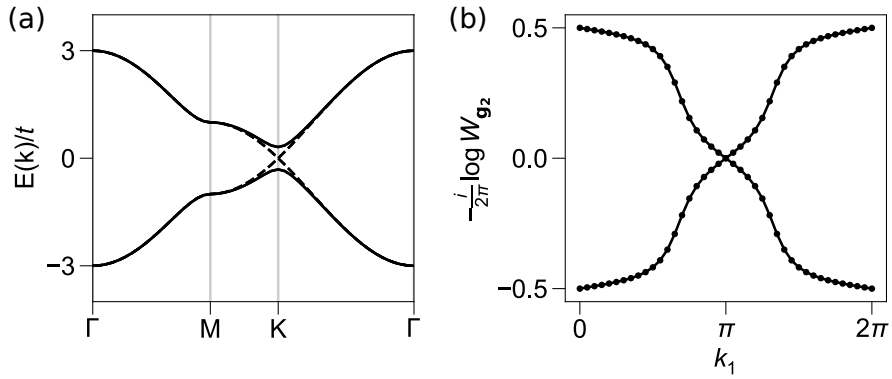

Figure 3.16: (a) Bands corresponding to the Kane-Mele model for the honeycomb lattice. Dashed lines correspond to the Hamiltonian without SOC in Eq. (3.156), while solid lines show the band structure with SOC ($\lambda/t = 0.06$) (b) Eigenvalues of $W_{\boldsymbol{g}_2}(k_1)$ for the band structure with SOC ($\lambda/t = 0.06$).

yields the following matrix expression for the Hamiltonian:

$$H(\boldsymbol{k}) = \begin{bmatrix} 0 & Q(\boldsymbol{k}) \\ Q^\dagger(\boldsymbol{k}) & 0 \end{bmatrix} \otimes s_0, \tag{3.158}$$

where s_0 is the 2×2 identity matrix in the space of spins and $Q(\boldsymbol{k}) = t\left[e^{i2\pi(k_1+k_2)/3} + e^{i2\pi(-2k_1+k_2)/3} + e^{i2\pi(-2k_2+k_1)/3}\right]$. Here k_1 and k_2 are components of $\boldsymbol{k}$ along the directions of $\boldsymbol{g_1}$ and $\boldsymbol{g_2}$, correspondingly, so that $\boldsymbol{k} = k_1\boldsymbol{g}_1 + k_2\boldsymbol{g}_2$. Fig. **3.16**(a) shows the spectrum of $H(\boldsymbol{k})$ along lines connecting the high-symmetry points $\Gamma = (0,0)$, $M = (1/2,0)$ and $K = (2/3,1/3)$ in the Brillouin zone (given in reduced coordinates). At these points, the Hamiltonian reduces to

$$H(\Gamma) = 3t\sigma_x \otimes s_0, \tag{3.159}$$

$$H(M) = (t/2\sigma_x - \sqrt{3}/2\ t\sigma_y) \otimes s_0, \tag{3.160}$$

$$H(K) = 0. \tag{3.161}$$

We have introduced the Pauli matrices $\boldsymbol{\sigma}$ which act in the basis of A, B sublattice states. As it can be seen in Fig. **3.16**(a) and Eqs. (3.159)-(3.161), the Hamiltonian is gapped at Γ and M, while $H(K)$ [and its time-reversed partner $H(K')$] has a linearly-dispersing fourfold-degenerate Dirac point at $E = 0$

Inversion symmetry is represented as $\sigma_x \propto h(\Gamma)$ at the Γ point. Let us illustrate the derivation of the matrix for inversion at $M = (1/2,0)$. We denote $|\chi_A(\boldsymbol{k})\rangle, |\chi_B(\boldsymbol{k})\rangle$ the Bloch states obtained by Fourier-transforming the basis orbital states at A and B

lattice sites, respectively. The action of inversion on these states at M is the following:

$$I\left|\chi_A(M)\right\rangle = \left|\chi_B(-M)\right\rangle = e^{-i\boldsymbol{g}_1\cdot\boldsymbol{q}_B}\left|\chi_B(M)\right\rangle, \tag{3.162}$$

$$I\left|\chi_B(M)\right\rangle = \left|\chi_A(-M)\right\rangle = e^{-i\boldsymbol{g}_1\cdot\boldsymbol{q}_A}\left|\chi_A(M)\right\rangle. \tag{3.163}$$

$$\tag{3.164}$$

Accordingly, the matrix for inversion in this basis is:

$$I(M) = \begin{bmatrix} 0 & e^{-i\boldsymbol{g}_1\cdot\boldsymbol{q}_A} \\ e^{-i\boldsymbol{g}_1\cdot\boldsymbol{q}_B} & 0 \end{bmatrix} = -\sigma_x/2 + \sqrt{3}/2\sigma_y. \tag{3.165}$$

which is proportional to $H(M)$ and thus commutes with it. After simultaneously diagonalizing $H(M)$ and $I(M)$, we conclude that the lowest bands at Γ have inversion eigenvalues $(-,-)$, whereas at M they have inversion eigenvalues $(+,+)$[12]. Based on these inversion eigenvalues and TR symmetry, we can determine[13] the eigenvalues of the Wilson loop matrix $\mathcal{W}_{\boldsymbol{g}_2}(k_1)$ at $k_1 = 0$ and $k_1 = \pi$:

$$\begin{aligned} W_{\boldsymbol{g}_2}(0) &= -\sigma_0, \\ W_{\boldsymbol{g}_2}(\pi) &= \sigma_0, \end{aligned} \tag{3.166}$$

where the degeneracy is due to $T^2 = -1$ (or in this case, simply spin conservation).

If we could gap the Dirac points at K, K' while preserving TR symmetry, in such a way that the lower two bands form an isolated set, the Wilson loop spectrum of this set would be the one shown in Fig. **3.16**(b): each hybrid Wannier function center would wind, leading to a Wannier obstruction. However, in this case we could sacrifice TR symmetry to form non-winding hybrid Wannier functions that do not transform locally under TR symmetry. Hence this phase is protected by TR symmetry. Also, since crossings in the spectrum of $W_{\boldsymbol{g}_2}(k_1)$ are protected only at Γ and M, the Wilson loop can generically either wind once or not at all, meaning that we can characterize the phases by a $\mathbb{Z}_2$ **invariant**.

We need to show that we can open such a gap at K, K', without breaking TR symmetry. As Kane and Mele showed [2], this requires spin-orbit coupling, which can be included via the following term:

$$H_{so} = -i\lambda \sum_{<<\boldsymbol{R}\boldsymbol{R}'>>} s_z^{\sigma\sigma'} \nu_{\boldsymbol{R}\boldsymbol{R}'} \left(c^\dagger_{A\boldsymbol{R}\sigma} c_{A\boldsymbol{R}'\sigma'} + c^\dagger_{B\boldsymbol{R}\sigma} c_{B\boldsymbol{R}'\sigma'} \right). \tag{3.167}$$

Here s_z is the $z-$directed Pauli matrix in the basis of spin states, $\nu_{RR'} = (\boldsymbol{d}_1 \times \boldsymbol{d}_2)_z/|\boldsymbol{d}_1 \times \boldsymbol{d}_2|$, where $\boldsymbol{d}_1$ and $\boldsymbol{d}_2$ are the nearest-neighbor vectors along the bonds that

[12] It has been assumed that $t > 0$. If $t < 0$ was considered, bands would be switched and the analysis would be analogous.

[13] The proof falls out of the range of these notes, but it can be found in Refs. [94, 102].

the electron should traverse to go from the site in $\boldsymbol{R}'$ to the site in $\boldsymbol{R}$. In particular, at the K points, we have:

$$H(K) = \begin{bmatrix} s_z & 0 \\ 0 & -s_z \end{bmatrix}, \tag{3.168}$$

thus, the desired gap is opened by adding the spin-orbit term. This opening of the gap is shown in Fig. **3.16**(a), where $\lambda/t = 0.06$ has been considered for the case with SOC. Fig. **3.16**(b) shows the winding of Wilson loops corresponding to the two lower bands in the case with SOC.

Let us conclude with a note about the role of inversion symmetry. Even though inversion symmetry allowed us to deduce the $\mathbb{Z}_2$ invariant characterizing this phase, it is not necessary for protecting the topology: the Wannier obstruction needs only TR symmetry. Without inversion symmetry, however, we need to do more work to deduce that the Kane-Mele model is topologically nontrivial.

4 Group Theory and band structures

In the previous section we gained insight into the topology of band structures, from the particular perspective of adiabatic transport. We showed that their topological properties are encoded in the spectra of Wilson loops, which can serve to diagnose and classify the actual topological phase of a set of bands. Indeed, Berry phases and Wilson loops were the essential components in the toolkit used to diagnose topology in the early years of the research on topological phases of matter. Furthermore, Wilson loops provide us with an elegant framework to interpret non-trivial topology in terms of obstruction of charge localization.

Even though the topology of simple models can be investigated successfully by looking into Wilson loops' spectra, this approach turns out to be inefficient to study the topology of bands in real materials. The main drawback of this approach consists in the elevated numerical cost of the calculation of Wilson loops. This calculation is done by applying the expression in Eq. (3.31) for the Wilson loop as a product of projectors, which requires computing first the eigenstates of $H(\boldsymbol{k})$ in a fine grid of the path [103]. The number of products of eigenstates involved in these computation grows rapidly with the number of connected bands and the number of $\boldsymbol{k}$-points in the grid, so the computation demands usually a big amount of memory.

Another drawback comes from the rich variety of non-trivial loops that could be defined in reciprocal space (for dimensions greater than one). Every loop might lead to a Wilson loop with a unique spectrum and not all Wilson loops might be insightful to investigate the topology. We hence need to decide which Wilson loop is worth the numerical effort of its calculation. This pick requires generally having some intuition about the nature of the problem even before we start with the probe.

The formalism called topological quantum chemistry [25,26], which emerged in 2017, set a new viewpoint to investigate the topology of bands. According to it, the topological phase hosted by a set of bands can be diagnosed by studying the symmetry properties of

its Bloch states at $\boldsymbol{k}$-points of maximal symmetry of the BZ. This method requires thus the calculation of the eigenstates of $H(\boldsymbol{k})$ only for a few $\boldsymbol{k}$-vectors, in contrast to the Wilson loop based approach. Moreover, the numerical cost of the calculation of Bloch states' symmetry properties (irreducible representations) grows linearly with the number of bands, whereas the cost of the product of two projectors grows as the square of the number of bands. Besides being numerically cheaper, the TQC formalism accounts for the interplay between topology and the symmetries of the lattice in general terms.

It is due to its capacity to get over the limitations the Wilson loop based approach suffers from that TQC has become one of the standard frameworks for the diagnosis of topology in band structures. In fact, this method has been applied for a systematic search of topological insulators in the Inorganic Crystal Structure Database [30, 72, 104], which unveiled that twelve percent of the discovered inorganic materials are topological insulators. Not only whole sets of valence bands have been classified with the TQC framework, but also the smaller disconnected groups of bands [104] – those lying above the Fermi level, for instance. These TQC based investigations proved that topological insulators and bands are not as uncommon and scarce as it was though.

This chapter is devoted to presenting the TQC formalism, which has been widely used in the works that form this manuscript and the collaborations held during this thesis. We will begin by introducing the group theory concepts that form the basis of the TQC framework, namely reducible and irreducible representations (irrep) of finite groups, and their application to band structures of periodic crystals. These concepts have also been applied to construct models compatible with the symmetry of certain lattices and are vital to understand our contribution to the search of topological materials: the software *IrRep*.

4.1 Reducible and irreducible representations of finite groups

A comment on the notation and perspective adopted for this section is in order before we begin. Since group theory has been applied in this thesis mainly in the context of quantum mechanics, we adjust the notation, definitions and examples given in this chapter to this field. However, group theory is widely applied in many different fields of physics, as its applicability is not restricted to quantum mechanical problems.

We say that a transformation is a **symmetry** of a system if it leaves invariant the equations of motion associated to it. Most of the symmetries can usually be spotted following geometrical considerations. This is indeed the case of crystal symmetries, which are on the focus of TQC.

A set of symmetries forms a **group** if its elements satisfy certain properties under an internal composition rule, namely the composition must be associative and the set must contain the inverse for every element, in addition to the neutral element. A group is

said to be finite if its number of elements is finite, and the number of elements of a finite group is called **order** of the group. The groups of symmetries which leave molecules invariant, also known as **point groups**, are an example of a family of finite groups. Moreover, some groups are continuous (Lie groups), whereas the groups we will focus on throught this work are discrete. The reason for this is that we are interested in the application of group theory to crystals, whose symmetry groups are finite.

Although the properties of finite groups can be studied at an abstract level, the discussion becomes more interesting when we consider their representations in certain space. Let us consider the Hilbert space $\mathcal{H}_N$ of dimension N which is spanned by the states $\{|\psi_1\rangle, \ldots, |\psi_N\rangle\}$. We say that the representation G of dimension N of the group G is defined in $\mathcal{H}_N$ if a $N \times N$ matrix $D(g)$ can be put in correspondence to every element $g \in G$, in such a way that these matrices obey the group composition law[1]:

$$\forall g_1, g_2 \in G,\ D(g_1 g_2) = D(g_1) D(g_2). \tag{4.1}$$

The space $\mathcal{H}_N$ and states $|\psi_i\rangle$ are then said to be the space and basis states of the representation D, respectively. Note that the dimension of the representation coincides with the dimension of the space it is defined in. The matrices of the representation describe the action of the group on its basis states, *i.e.* how the states in the basis transform under the action of the group:

$$g\,|\psi_i\rangle = D_{ji}(g)\,|\psi_j\rangle\,, \tag{4.2}$$

where $g \in G$. Once the matrices of the representation are settled, the transformation of a generic state $|\psi\rangle = \sum_{i=1}^{N} c_i\,|\psi_i\rangle$ is determined:

$$g\,|\psi\rangle = \sum_{i=1}^{N} c_i g\,|\psi_i\rangle = \sum_{j,i=1}^{N} D_{ji}(g) c_i\,|\psi_j\rangle\,. \tag{4.3}$$

Analogously as in the adiabatic transport of a spin-1/2 under a magnetic field [Sec. 3.1.2], this equation can be implemented in two ways: On the one hand, we can consider that symmetries act on the coefficients c_i, which transform as column-vectors with the matrix $D(g)$:

$$c'_j = \sum_{i=1}^{N} D_{ji}(g) c_i. \tag{4.4}$$

On the other hand, it can be considered that symmetries act on the basis states as in Eq. (4.2):

[1] The formal definition for a representation of a group is not restricted to Hilbert spaces. Representations can indeed be defined in many other vector spaces, like the euclidean $\mathbb{R}^3$-space.

$$|\psi_i'\rangle = \sum_{i=1}^{N} D_{ji}(g)\,|\psi_j\rangle\,. \tag{4.5}$$

Both implementations lead to Eq. (4.3) and are hence equivalent. In the following of the manuscript, we will stick to the transfromation in Eq. (4.5).

Let $\mathcal{H}_M$ be a subspace of $\mathcal{H}_N$ of dimension M, where $M < N$. $\mathcal{H}_M$ is said to be an invariant subspace if all states belonging to it fall back in H_M under the action of the elements in G, i.e. if it is closed under G:

$$\forall g \in G \text{ and } \forall\,|\phi\rangle \in \mathcal{H}_M,\ g\,|\phi\rangle \in \mathcal{H}_M. \tag{4.6}$$

If a non-trivial invariant subspace $\mathcal{H}_M$ of $\mathcal{H}_N$ exists, the representation D defined in $\mathcal{H}_N$ is **reducible**; otherwise, if the space in which a representation is defined can not be divided into smaller invariant non-trivial subspaces, the representation is **irreducible**.

The matrices of a reducible representation show a characteristic shape when the basis states are chosen and sorted in a particular way. Let us choose as the first M states those states $|\psi_1\rangle, \ldots, |\psi_M\rangle$ which span the invariant subspace $\mathcal{H}_M$ – these states are said to be **adapted to the symmetry** of the representation D_M defined in $\mathcal{H}_M$. The rest of states in the basis are the states $|\phi_1\rangle, \ldots, |\phi_{N-M}\rangle$ which belong to $\mathcal{H}_{N-M}$, *i.e.* the subspace orthogonal to $\mathcal{H}_M$. It follows from the invariance of $\mathcal{H}_N$ and the orthogonality between this subspace and $\mathcal{H}_{N-M}$ that all matrix elements $\langle\phi_j|g|\psi_i\rangle = 0$, for $\forall g \in G$. It then stems from the unitarity[2] of the representation D that $\langle\psi_i|g|\phi_j\rangle = 0$ for $\forall g \in G$, which means that $\mathcal{H}_{N-M}$ is also an invariant subspace. As a consequence, the matrices $D(g)$ are block-diagonal with this choice of the basis:

$$D(g) = \begin{bmatrix} D_M(g) & & \\ & & \\ & D_{N-M}(g) & \end{bmatrix}. \tag{4.7}$$

The block corresponding to $\mathcal{H}_M$ is indeed the matrix of the representation $D_M(g)$ defined in this subspace, while the other block correspond to the representation defined in the invariant subspace $\mathcal{H}_{N-M}$.

Let us consider as an example the point group C_{4v} and the Hilbert space formed by the p-orbitals $|p_x\rangle$, $|p_y\rangle$ and $|p_z\rangle$. The group C_{4v} contains eight symmetry operations [see Fig. **4.1**(a)]. In particular, it contains the 4-fold (counter-clockwise) rotation C_4^+ and the mirror reflection $M_{1\bar{1}}$, which maps the space coordinate x to y and x to y. The

[2] All the representations we work with are unitary, as we require the conservation of the states' norm.

action of these symmetries on the p-orbitals is given by:

$$\begin{aligned} C_4^+ |p_x\rangle &= |p_y\rangle & M_{1\bar{1}} |p_x\rangle &= |p_y\rangle\,, \\ C_4^+ |p_y\rangle &= -|p_x\rangle & M_{1\bar{1}} |p_y\rangle &= |p_x\rangle\,, \\ C_4^+ |p_z\rangle &= |p_z\rangle & M_{1\bar{1}} |p_z\rangle &= |p_z\rangle\,. \end{aligned}$$

This action is illustrated in Fig. **4.1**(b). Note that the p_x and p_y-orbitals remain in the xy-plane as these symmetries act on them. The subspace spanned by these orbitals is thus invariant under the group[3] C_{4v}. Its orthogonal subspace, which is spanned by the p_z-orbital, is also invariant. Indeed, the matrices of the representation D corresponding to these symmetries and basis states have the block-diagonal shape of Eq. (4.7):

$$D(C_4^+) = \left[\begin{array}{cc|c} 0 & -1 & 0 \\ 1 & 0 & 0 \\ \hline 0 & 0 & 1 \end{array}\right], \qquad D(M_{1\bar{1}}) = \left[\begin{array}{cc|c} 0 & 1 & 0 \\ 1 & 0 & 0 \\ \hline 0 & 0 & 1 \end{array}\right]. \tag{4.8}$$

The 2×2 blocks here are the matrices of the representation E defined in the subspace spanned by p_x and p_y-orbitals, wheareas the element in the lower-right corner corresponds to the unidimensional representation A_1 of the p_z-orbital. Both of these representations are irreducible because the corresponding Hilbert spaces can not be split into smaller invariant subspaces. We then say that the representation D is decomposed into the irreps E and A_1 as:

$$D = E \oplus A_1. \tag{4.9}$$

Coming back to the general discussion, the space of a reducible representation D might in general be split in several invariant subspaces which can not be further divided into smaller invariant subspaces. Each of this small subspaces hosts then an irrep D_i of dimension d_i of the group. Furthermore, different subspaces might have in correspondence the same irrep. The number of times an irrep D_i takes part in this decomposition is called the **multiplicity** of that irrep, and we denote it m_i. Once we determine the multiplicity of all irreps, we can write:

$$D = \bigoplus_i m_i D_i(d_i). \tag{4.10}$$

This expression is the decomposition of a reducible representation of a group into irreps and plays a vital role in this thesis. The matrices of D will be diagonal by blocks after the decomposition, such that neither of the blocks can be divided into smaller blocks.

[3] The rest of symmetries of C_{4v} also satisfy this property, since they can be obtained through the composition of C_4^+ and $M_{1\bar{1}}$. These symmetries form a (non-unique) set of generators of C_{4v}.

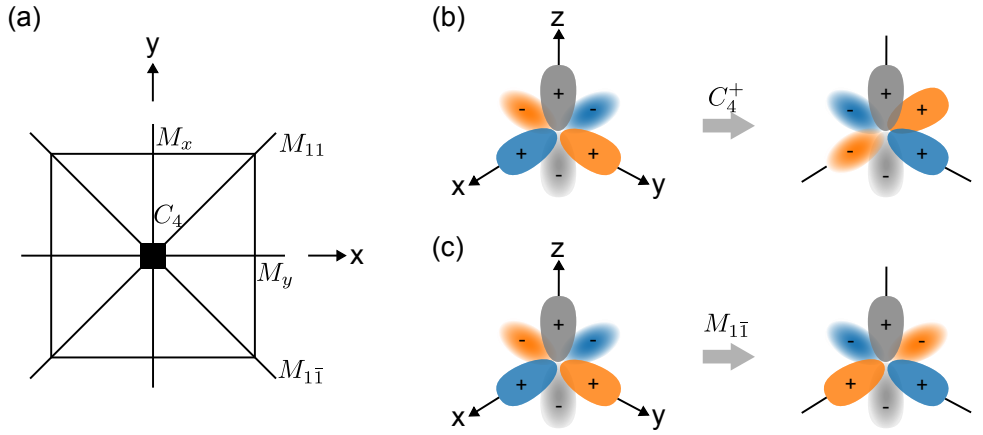

Figure 4.1: (a) Symmetry operations of the point group C_{4v}. Solid lines indicate mirror planes. The black square denotes the 4-fold and 2-fold rotations with respect to the z-axis (perperdicular to the plane). (b) and (c) show the action of C_4^+ and $M_{1\bar{1}}$ on the basis of p-orbitals, respectively.

The diagonal of D will contain m_i identical $d_i \times d_i$ blocks corresponding to the irrep D_i:

$$D(g) = \begin{bmatrix} \ddots & & & \\ & D_i & & \\ & & D_i & \\ & m_i \text{ blocks} & & D_i \\ & & & \ddots \end{bmatrix}. \tag{4.11}$$

In practice, the reducible representation D and irreps D_i are known from the beginning, and the problem of the decomposition consists in determining the multiplicity m_i of each irrep. This determination might be straightforward for the simple cases where the dimension of D is small or we possess a clear picture of its Hilbert space – like in the example of the group C_{4v} given above. However, an efficient method to solve the problem is in order for more complicated scenarios, like the application in numerical approaches. Such a systematic approach can be derived based on the orthogonality properties and is based on the application of the following formula to determine the multiplicity of each irrep in the decomposition:

$$m_i = \frac{1}{||G||} \sum_{g \in G} \chi^*(g) \chi_i(g). \tag{4.12}$$

$||G||$ stands here for the order of the group G, while χ and χ_i stand for the characters of the representations D and D_i, respectively. The **character** of a representation is the set of traces corresponding to its matrices. $\chi(g)$ and $\chi_i(g)$ are thus the traces for g.

4.2 Wigner's theorem: the form of the Hamiltonian

We have shown that the matrices of symmetries corresponding to reducible representations become diagonal by blocks when the representation is decomposed into irreps and the basis of states is chosen wisely. This provides us with interesting information about the symmetry properties of the basis states which span our Hilbert space. Nevertheless, since crystal symmetries are not related to physical observables, we might wonder if they have any relationship with measurable quantities like the energy levels of the system.

We will now unveil the way in which crystal symmetries set constrains on the energy spectrum of the system. In particular, we will demonstrate that the decomposition of a reducible representation into irreps determines the degeneracy of the energy levels and allows us to classify the states corresponding to each energy level. It should not however be surprising to discover such a relationship, since we have already shown that symmetries allow us to split the Hilbert space into independent subspaces.

As we mentioned before, a transformation g is a symmetry of a system if it leaves the Schrödinger equation invariant. This invariance condition can be recast as the commutativity between the Hamiltonian $\hat{H}$ of the system and the operator T_g corresponding to the symmetry[4]:

$$\hat{H}T_g = T_g\hat{H}. \tag{4.13}$$

Let us consider that the basis we choose for the Hilbert space of the problem transforms as the representation D of the symmetry group G. The invariance Eq. (4.13) of the Hamiltonian can the be expressed in matrix form:

$$HD(g) = D(g)H. \tag{4.14}$$

In conclusion, once a basis of states spanning the Hilbert space is chosen, the invariance of the Hamiltonian with respect to the symmetry transformations of a group is equivalent to the commutativity between the matrices of Hamiltonian and the representation of the group.

We now explain, in terms of representations, the constrains set by symmetries on the matrix elements of the Hamiltonian. Let us for that consider that $D(g)$ has the quasidiagonal form corresponding to its decomposition into irreps. There are two types of matrix elements of H: those between states which transform as different irreps, those involving states of equivalent irreps. For the sake of simplicity, let us restrict ourselves

[4]We will denote the Hamiltonian operator as $\hat{H}$ and keep H to denote its matrix form when there is a risk of mixing them up.

to the case in which only two irreps take part in the decomposition of $D(g)$, namely the irreps D_1 and D_2 – note that there is no loss of generality in this assumption, as the problem can be considered the restriction of the Hilbert space to the union of subspaces corresponding to these two irreps. The matrices of $D(g)$ have the aformentioned quasidiagonal shape:

$$D(g) = \left[\begin{array}{c|c} D_1(g) & \\ \hline & D_2(g) \end{array}\right], \tag{4.15}$$

whereas the matrix of the Hamiltonian has the following form, in the analogous block based structure:

$$H = \left[\begin{array}{c|c} H_{11} & H_{12} \\ \hline H_{12}^\dagger & H_{22} \end{array}\right], \tag{4.16}$$

where H_{11}, H_{22} and H_{12} are blocks of size $d_1 \times d_1$, $d_2 \times d_2$ and $d_1 \times d_2$, respectively (with d_i the dimension of the irrep D_i). Then, by virtue of Eq. (4.14):

$$\left[\begin{array}{c|c} H_{11} & H_{12} \\ \hline H_{12}^\dagger & H_{22} \end{array}\right] = \left[\begin{array}{c|c} D_1^\dagger(g) H_{11} D_1(g) & D_1^\dagger(g) H_{12} D_2(g) \\ \hline D_2^\dagger(g) H_{12}^\dagger D_1(g) & D_2^\dagger(g) H_{22} D_2(g) \end{array}\right]. \tag{4.17}$$

According to Schur's second lemma [105], a matrix M satisfying $D_1 M = M D_2$ should vanish if D_1 and D_2 are non-equivalent irreps. Therefore, the off-diagonal block H_{12} vanishes and Eq. (4.17) reduces to:

$$\left[\begin{array}{c|c} H_{11} & \\ \hline & H_{22} \end{array}\right] = \left[\begin{array}{c|c} D_1^\dagger(g) H_{11} D_1(g) & \\ \hline & D_2^\dagger(g) H_{22} D_2(g) \end{array}\right]. \tag{4.18}$$

Moreover, Schur's first lemma [105] states that any matrix which commutes with all the matrices of an irrep must be proportional to the identity matrix, thus

$$\begin{aligned} H_{11} &= E_1 \mathbb{1}_{d_1}, \\ H_{22} &= E_2 \mathbb{1}_{d_2}. \end{aligned} \tag{4.19}$$

where $\mathbb{1}_{d_i}$ is the identity matrix of dimension d_i. Three important results stem from this: First of all, the eigenstates and energy levels of the Hamiltonian can be labeled by irreps of the symmetry group. Second, the degeneracy of the energy level corresponding to every irrep (of multiplicity one) is equal to the dimension of the irrep. Thirdly, the matrix of the Hamiltonian is diagonal by blocks.

There is a third possibility in Eq. (4.17), namely that D_1 and D_2 are equivalent irreps. This corresponds to the case where there is an irrep of multiplicity greater than one in the decomposition of D. Based again on Schur's first lemma, every block in

Eq. (4.16) must be proportional to the identity matrix:

$$H = \left[\begin{array}{c|c} h_{11}\mathbb{1}_{d_1} & h_{12}\mathbb{1}_{d_1} \\ \hline h_{12}^*\mathbb{1}_{d_1} & h_{22}\mathbb{1}_{d_1} \end{array}\right], \tag{4.20}$$

where $h_{11}, h_{22} \in \mathbb{R}$ and $h_{12} \in \mathbb{C}$. Let us consider as basis the sets of symmetry-adapted states $\{|\psi_1\rangle, |\psi_2\rangle, \ldots, |\psi_{d_1}\rangle\}$ and $\{|\phi_1\rangle, |\phi_2\rangle, \ldots, |\phi_{d_1}\rangle\}$, which do not mix between them under any symmetry, *i.e.* each set is closed under the group. If we sort these states as

$$\{|\phi_1\rangle, |\psi_1\rangle, |\phi_2\rangle, |\psi_2\rangle \ldots, |\phi_{d_1}\rangle, |\psi_{d_1}\rangle\}, \tag{4.21}$$

the matrix for H takes the following quasidiagonal structure:

$$H = \left[\begin{array}{cc|cc|c} h_{11} & h_{12} & & & \\ h_{12}^* & h_{22} & & & \\ \hline & & h_{11} & h_{12} & \\ & & h_{12}^* & h_{22} & \\ \hline & & & & \ddots \end{array}\right], \tag{4.22}$$

where the same block repeats itself d_1-times along the diagonal of the matrix. As a consequence, an irrep of multiplicity m_i and dimension d_i has in correspondence m_i energy levels (different, in principle) of degeneracy d_i. However, calculating the energy levels of such an irrep requires further diagonalization of the corresponding $m_i \times m_i$-block.

Even if Eqs. (4.22) and (4.11) might look similar, in general it is not possible to achive the block diagonal form in both the matrices of the representation and the matrix of H. The reason for this is that these quasidiagonal forms require sorting differently the states in the basis. In other words, the ordering that leads to Eq. (4.22) does not turn the matrices of the representation into block-diagonal form.

All in all, we have shown that the decomposition into irreps of the symmetry representation D defined in the Hilbert space determines the form of the Hamiltonian, which is quasidiagonal for certain choice of the basis states. Every irrep of dimension d_i and

multiplicity m_i will hence have in correspondence d_i identical blocks of shape $m_i \times m_i$:

$$H = \begin{bmatrix} \ddots & & & & \\ & H_i & & & \\ & & H_i & & \\ & d_i \text{ blocks} & & H_i & \\ & \text{of shape } m_i \times m_i & & & \ddots \end{bmatrix}. \tag{4.23}$$

This result is known as **Wigner's theorem** and it turns out to be a powerful tool to deal with analytical models for systems. The key considerations that follow immediately from this block-diagonal form are the following: First, every energy level has in correspondence an irrep, which describes the transformation of the corresponding states under the symmetry group. This irrep can be used as a label of the energy level. Second, every irrep D_i of dimension d_i and multiplicity m_i in the decomposition of the representation D has in correspondence m_i energy levels of degeneracy d_i.

We must mention that the dimension of the irrep determines the minimum degeneracy of the corresponding energy level, *i.e.* the degeneracy we would observe if the Hamiltonian was the most general one compatible with the symmetry of the group. In practical terms, however, we often find degeneracies greater than the dimensions of irreps involved in it. This is called **accidental degeneracy**, as it does not stem from the constrains set by symmetries, and it might be caused by different reasons.

On the one hand, accidental degeneracies are common when working with simplified models for systems. Usually, the number of parameters included in such models is kept simple enough to explore clearly a certain aspect of the system. When choosing the parameters to be included, those responsible for the absence of accidental degeneracy might be left out. This is indeed common when constructing tight-binding models for crystals: the most general Hamiltonian compatible with the symmetries of the lattice would not suffer from accidental degeneracies, but it might require including a big number of hoppings. Since working with that many tunneling amplitudes is impossible, only hoppings to certain (relatively) close neighbors are considered, based on the fact that the capacity of an electron to hop between two atoms decreases with the distance between these atoms. Accidental degeneracies in the band structure arise often as the price to be paid for this simplification. As the root of the problem suggests, the way to get rid of these degeneracies is to include additional hoppings, *e.g.* to further neighbors.

On the other hand, accidental degeneracies might be the consequence of a particular choice for the parameters. For example, a certain choice of values of hopping parameters might lead to band-touching points. As soon as the values differ slightly from that particular choice, accidental degeneracies vanish. This scenario is often dubbed **fine-**

tuning.

It is worth mentioning that, even though all accidental degeneracies might be gapped out by including in the model additional parameters and choosing them carefully, getting rid of some of them might be hard. For instance, it is sometimes complicated to get rid of band crossings between bands of different irreps.

4.3 Group theory for periodic crystals

The group theory concepts introduced in the previous chapters are directly applicable to point groups, which are symmetry groups of molecules, for example. The application of these concepts to symmetry groups of periodic crystals is, nevertheless, not straightforward. Let us for instance think about the size of the Hamiltonian. On the one hand, the Hilbert space of a molecule is relatively small. For example, a molecule formed by four atoms, each with a single orbital, has in correspondence a Hilbert space of dimension four and a 4×4 Hamiltonian matrix. On the other hand, a crystal formed as a periodic arrangement of N such atoms has a Hilbert space of dimension N. This number tends to be of the order of Avogadro's number, *i.e.* $N \sim 10^{23}$. Writing down such a $N \times N$ Hamiltonian, and applying Wigner's theorem to it, are clearly an unrealistic goals.

Another immediate problem is that, whereas point groups contain a finite number of symmetries, the group of a periodic crystal is not finite. This is due to the fact that it includes all translation by vectors of the Bravais lattice, which account for the periodicity of the crystal pattern.

Since periodic crystals are indeed the main focus of our work, we will devote this section to a detailed explanation of how the theory of representations and Wigner's theorem are applied to these systems.

4.3.1 Space groups and translation subgroups

The symmetry group of an ideal crystal, also known as the **space group** of the crystal, is formed by the transformations that leave the crystal pattern invariant. In other words, every transformation in this group maps any point of the crystal to an equivalent point.

Let G denote a space group. A general symmetry $g \in G$ can be written as a point group symmetry R followed by a translation $\boldsymbol{v}$: $g = \boldsymbol{v}R$. Through this text, we will use the more convenient **Seitz notation** [106], according to which the space group operation g can be denoted as $g = \{R|\boldsymbol{v}\}$.

The main characteristic of the symmetry of a periodic crystal is that its crystal pattern repeats itself periodically. In other words, crystals have discrete translational symmetry. As we mentioned in Sec. 2.2, this translation symmetry is described by the Bravais lattice formed by the vectors that leave the crystal invariant. A vector $\boldsymbol{t}$ of the Bravais lattice can be written in terms of the primitive lattice vectors $\boldsymbol{a}_1$, $\boldsymbol{a}_2$ and $\boldsymbol{a}_3$ of

the lattice:

$$\boldsymbol{t} = n_1\boldsymbol{a}_1 + n_2\boldsymbol{a}_2 + n_3\boldsymbol{a}_3. \tag{4.24}$$

where $n_1, n_2, n_3 \in \mathbb{Z}$. Since the combination of two lattice vectors is always another lattice vectors, the translations by vectors of the lattice form a group that is indeed the **translation subgroup** T of the space group G, *i.e.* $T \subset G$.

The space group G can be written as a coset decomposition with respect to its translation subgroup T as:

$$G = T \cup g_1T \cup \cdots \cup g_nT. \tag{4.25}$$

The elements $g_1, g_2, \ldots, g_n$ are referred to as the coset representatives of the decomposition. It should be mentioned that the set of coset representatives is finite and non-unique, as the composition of a coset representative and any translation of T yields an equally valid set. There exist two different types of space groups, depending on the possible choices of coset representatives: if the coset representative can be chosen to be point group symmetries, the space group is said to be **symmorphic**. In contrast, if every valid choice of representatives involves at least a symmetry whose translational part does not vanish, the space group is **non-symmorphic**. Such a representative could be a screw rotation or a glide reflection, and could be written as $g_i = \{R_i|\boldsymbol{v}_i\}$, where $\boldsymbol{v}_i$ does not belong to the Bravais lattice. $Pm\bar{3}m$, $Fm\bar{3}m$ and $Pmm2$ are examples of symmorphic space groups, while $Pbam$, $P4/mbm$ and $P4_2/mbc$ are non-symmorphic groups.

Non-symmorphic symmetries can protect band crossings which lead to exotic nodal lines. In fact, while working on this thesis, I took part in a collaboration which showed that glide reflections are able to protect coplanar-elliptical nodal lines in some non-symmorphic space groups [107, 108]. We will look into this work in more detail in Sec. 6.3.2.

Let us for now know focus on the translation subgroup. When two or more translations are applied in a row, the order in which they are considered is clearly non-relevant. In other words, the subgroup of translations is an abelian group. A particularly interesting property of abelian groups is that all their irreducible representations are one-dimensional – this property follows from the fact that the matrices of their representations should also commute. A basis state $|\phi\rangle$ of an irrep τ of T satisfies then:

$$\hat{\boldsymbol{t}}\,|\phi\rangle = \tau(\boldsymbol{t})\,|\phi\rangle\,, \tag{4.26}$$

where $\hat{\boldsymbol{t}}$ is the operator corresponding to the translation by the vector $\boldsymbol{t}$ of the Bravais lattice and $\tau(\boldsymbol{t})$ is a unimodular complex number. The basis states of the irreps of T are therefore eigenstates of translations. Since τ is one-dimensional, the elements corresponding to the generators $\boldsymbol{a}_1, \boldsymbol{a}_2$ and $\boldsymbol{a}_3$ of T can be written as $\tau(\boldsymbol{a}_i) = \exp(i\theta_i)$. A generic translation $\boldsymbol{t} = n_1\boldsymbol{a}_1 + n_2\boldsymbol{a}_2 + n_3\boldsymbol{a}_3 \in T$ is then represented by the following

expression:

$$\tau(\boldsymbol{t}) = \tau(\boldsymbol{a}_1)^{n_1}\tau(\boldsymbol{a}_2)^{n_2}\tau(\boldsymbol{a}_3)^{n_3} = e^{i\theta_1 n_1}e^{i\theta_2 n_2}e^{i\theta_3 n_3}, \tag{4.27}$$

Therefore, τ is determined by the triplet $(\theta_1, \theta_2, \theta_3)$. We can achieve a more convenient expression by saving these numbers in a vector defined as:

$$\boldsymbol{k} = \theta_1\boldsymbol{g}_1 + \theta_2\boldsymbol{g}_2 + \theta_3\boldsymbol{g}_3, \tag{4.28}$$

where the vectors $\boldsymbol{g}_j$ satisfy $\boldsymbol{g}_j \cdot \boldsymbol{a}_i = 2\pi\delta_{ij}$ – notice that this is the definition for the primitive vectors of the reciprocal lattice. Then, Eq. (4.27) can be written as:

$$\tau(\boldsymbol{t}) = e^{i\boldsymbol{k}\cdot\boldsymbol{t}}. \tag{4.29}$$

We have hence reached an alternative derivation of Bloch's theorem, which is given from a group theory perspective. Each irrep of the translation subgroup of an space group can be labeled by a vector $\boldsymbol{k}$ in the BZ and its basis state $|\psi_{\boldsymbol{k}}\rangle$ is the Bloch state corresponding to $\boldsymbol{k}$. Moreover, the matrix element of a translation $\boldsymbol{t} \in T$ for this state is the well-known phase in Eq. (2.11) obtained when acting on a Bloch state with this translation:

$$\hat{\boldsymbol{t}}\,|\psi_{\boldsymbol{k}}\rangle = e^{i\boldsymbol{k}\cdot\boldsymbol{t}}\,|\psi_{\boldsymbol{k}}\rangle\,. \tag{4.30}$$

The reason why the irreps of T are interesting is the following: as we mentioned in Sec. 4.2, the Hamiltonian of a system commutes with the operators of its symmetry transformations. Especially the Hamiltonian of a periodic crystal commutes with all $\hat{\boldsymbol{t}} \in T$. This allows us to choose Bloch waves as the basis for the Hilbert space of the problem, which turns the matrix H of the Hamiltonian into diagonal by blocks, so that each block $H(\boldsymbol{k})$ corresponds to a $\boldsymbol{k}$ in the BZ. We can then study independently the spectrum and eigenstates of each $H(\boldsymbol{k})$. In particular, we could apply Wigner's theorem to each $H(\boldsymbol{k})$, but this requires identifying first the symmetry group of $H(\boldsymbol{k})$.

4.3.2 Star and little group of a vector $\boldsymbol{k}$

We know that the symmetry group of the Hamiltonian H is the space group G, but we are now interested in the symmetry group of $H(\boldsymbol{k})$. We will identify this group and discuss the transformation properties of the vector $\boldsymbol{k}$.

For the remaining of the discussion about the application of group theory to periodic crystals, we adopt the aforementioned basis of the Hilbert space $\mathcal{H}$. This choice corresponds to dividing $\mathcal{H}$ in subspaces $\mathcal{H}_{\boldsymbol{k}}$ which are invariant under the translation subgroup:

$$\mathcal{H} = \mathcal{H}_{\boldsymbol{k}_1} \oplus \mathcal{H}_{\boldsymbol{k}_2} \oplus \cdots \oplus \mathcal{H}_{\boldsymbol{k}_\mathcal{N}}, \tag{4.31}$$

where $\mathcal{N}$ is the number of vectors in the BZ. This expression stands for the fact that a representation of G defined in $\mathcal{H}$ subduces a reducible representation of the translation

subgroup. Whereas $\mathcal{H}$ is closed under G, a subspace $\mathcal{H}_{\boldsymbol{k}}$ is not, in general. Such a subspace is closed under a subgroup $G_{\boldsymbol{k}} \subset G$ which contains the symmetry operations that leave the vector $\boldsymbol{k}$ invariant (up to translations by vectors of the reciprocal lattice):

$$G_{\boldsymbol{k}} = \{\{R|\boldsymbol{v}\} \in G \mid \ R\boldsymbol{k} = \boldsymbol{k} + \boldsymbol{G}\}, \tag{4.32}$$

where $\boldsymbol{G}$ is a vector of the reciprocal lattice[5]. This group is called **little group** of $\boldsymbol{k}$, and plays an important role in the application of Wigner's theorem to band structures of crystals, since it is also the symmetry group of $H(\boldsymbol{k})$.

Now, let us look into the actual transformation of a Bloch state $|\psi_{\boldsymbol{k}}\rangle \in \mathcal{H}_{\boldsymbol{k}}$ under the space group. We define for that $|\psi'\rangle = g\,|\psi_{\boldsymbol{k}}\rangle$, where $g = \{R|\boldsymbol{v}\} \in G$. In order to identify this new state, let us act on it with a translation $\hat{\boldsymbol{t}} \in T$:

$$\begin{aligned}\hat{\boldsymbol{t}}\,|\psi'\rangle &= \{E|\boldsymbol{t}\}\{R|\boldsymbol{v}\}\,|\psi_{\boldsymbol{k}}\rangle = \{R|\boldsymbol{v}\}\{E|R^{-1}\boldsymbol{t}\}\,|\psi_{\boldsymbol{k}}\rangle = \exp\big(i\boldsymbol{k}\cdot R^{-1}\boldsymbol{t}\big)\,|\psi'\rangle \\ &= \exp(iR\boldsymbol{k}\cdot\boldsymbol{t})\,|\psi'\rangle\,.\end{aligned} \tag{4.33}$$

Here E denotes the identity element. We have therefore obtained that the transformation of a Bloch state $|\psi_{\boldsymbol{k}}\rangle$ under a symmetry operation is described entirely by the action of the symmetry's rotational part on the vector $\boldsymbol{k}$ of the state:

$$\{R|\boldsymbol{v}\}\,|\psi_{\boldsymbol{k}}\rangle = |\psi_{R\boldsymbol{k}}\rangle\,. \tag{4.34}$$

The **star of** $\boldsymbol{k}$ is defined as the set of vectors in the BZ related to it by the symmetries of the space group:

$$\mathrm{star}(\boldsymbol{k}) = \{R\boldsymbol{k} \in \mathrm{BZ} \mid \forall\{R|\boldsymbol{v}\} \in G\}. \tag{4.35}$$

Even thought the space group contains an infinite number of elements, the number of vectors in the star of $\boldsymbol{k}$ is finite. In fact, this number can not be greater than the number of coset representatives in the decomposition in Eq. (4.25) of G with respect to T. It can be shown that the little groups of all vectors in $\mathrm{star}(\boldsymbol{k})$ are isomorphic, so they have equivalent irreps. Furthermore, the matrices $H(\boldsymbol{k})$ and $H(R\boldsymbol{k})$ are connected by a similarity relation, which means that they have the same spectrum. In other words, the energy levels of bands are identical for all $\boldsymbol{k} \in \mathrm{star}(\boldsymbol{k})$.

4.3.3 Irreducible representations of the little group of $\boldsymbol{k}$

Before we apply Wigner's theorem to periodic crystals, let us comment on the derivation of the irreps of the little group $G_{\boldsymbol{k}}$. The issue in this derivation is that $G_{\boldsymbol{k}}$ is not a finite

[5]The reason for defining the equivalence modulo a vector $\boldsymbol{G}$ of the reciprocal lattice is that $\boldsymbol{k}$ and $\boldsymbol{k}+\boldsymbol{G}$ have in correspondence the same irrep of the translation subgroup, thus also the same Bloch state.

group. The idea behind the way to tackle the problem is to set a relationship between the irreps of $G_{\boldsymbol{k}}$ and certain point group.

Since the little group $G_{\boldsymbol{k}}$ is a subgroup of the space group G which also includes all translations by vectors of the Bravais lattice, it can also be decomposed in cosets with respect to the same translational subgroup T:

$$G_{\boldsymbol{k}} = T + g_1^{\boldsymbol{k}} T + \cdots + g_m^{\boldsymbol{k}} T. \tag{4.36}$$

This decomposition might involve only some of the coset representatives in the decomposition in Eq. (4.25) of the space group. For symmorphic space groups, the representatives here form a point group $\bar{G}_{\boldsymbol{k}}$ dubbed **little cogroup** of $\boldsymbol{k}$. The action of every element $g \in G_{\boldsymbol{k}}$ can then be obtained by applying a symmetry $R \in \bar{G}_{\boldsymbol{k}}$, followed by a translation $\boldsymbol{t} \in T$, so that $g = \{R|\boldsymbol{t}\}$. The representation $D_{\boldsymbol{k}}$ for such a symmetry is the following, with the choice of basis for $\mathcal{H}_{\boldsymbol{k}}$ adopted above in Eq. (4.31):

$$D_{\boldsymbol{k}}(\{R|\boldsymbol{t}\}) = \exp(i\boldsymbol{k}\cdot\boldsymbol{t})\bar{D}_{\boldsymbol{k}}(R), \tag{4.37}$$

where $\bar{D}_{\boldsymbol{k}}$ is the matrix for the representation of $\bar{G}_{\boldsymbol{k}}$. Especially, if $\bar{D}_{\boldsymbol{k}}$ is chosen to be an irrep of $\bar{G}_{\boldsymbol{k}}$, then $D_{\boldsymbol{k}}$ is also an irrep of $G_{\boldsymbol{k}}$. In conclusion, the irreps of a little group are in one to one correspondence to the irreps of its little cogroup, for symmorphic space groups.

If the space group is non-symmorphic, the coset representatives in Eq. (4.36) do not form a point group, as the second powers of glide reflections and certain powers of screw rotations give rise to translations belonging to T. In this case, the little cogroup is formed by the rotational parts of the coset representatives. Deriving the irreps of the little group from those of the little cogroup is not as straightforward as for symmorphic groups, especially for vectors $\boldsymbol{k}$ lying on the surface of the BZ. It is nevertheless possible to follow a procedure based on a similar idea to derive the irreps of the little group [105, 109].

In practical terms, we will not have to construct the irreps of little groups. They can be found in the *Bilbao Crystallographic Server* [96]. We can then decompose the representatation $D_{\boldsymbol{k}}$ of $G_{\boldsymbol{k}}$ in terms of these irreps as:

$$D_{\boldsymbol{k}} = \bigoplus_i m_i^{\boldsymbol{k}} D_i^{\boldsymbol{k}}, \tag{4.38}$$

where $D_i^{\boldsymbol{k}}$ is an irrep of $G_{\boldsymbol{k}}$ with multiplicity $m_i^{\boldsymbol{k}}$. The multiplicity of each irrep can be calculated by applying the magic formula in Eq. (4.12), where the sum is in practice taken only for the coset representatives in Eq. (4.36):

$$m_i^{\boldsymbol{k}} = \frac{1}{||\bar{G}_{\boldsymbol{k}}||} \sum_{j=1}^{M} [\chi^{\boldsymbol{k}}(g_j^{\boldsymbol{k}})]^* \chi_i^{\boldsymbol{k}}(g_j^{\boldsymbol{k}}). \tag{4.39}$$

Here, $\chi^{\boldsymbol{k}}$ and $\chi_i^{\boldsymbol{k}}$ denote the traces of $D_{\boldsymbol{k}}$ and $D_i^{\boldsymbol{k}}$, while M is the number of coset representatives in Eq. (4.36).

According to Wigner's theorem, the matrix $H(\boldsymbol{k})$ of the Hamiltonian will be diagonal by blocks in the basis of states adapted to the symmetry of the irreps of $G_{\boldsymbol{k}}$. Each irrep $D_i^{\boldsymbol{k}}$ of dimension $d_i^{\boldsymbol{k}}$ will then have in correspondence $d_i^{\boldsymbol{k}}$ identical blocks of size $m_i^{\boldsymbol{k}} \times m_i^{\boldsymbol{k}}$. It follows from this block-diagonal structure that each irrep is related to $m_i^{\boldsymbol{k}}$ different (modulo accidental degeneracy) energy levels of degeneracy $d_i^{\boldsymbol{k}}$. Note that this allows us to identify each eigenvalue of $H(\boldsymbol{k})$ by the irrep it corresponds to.

Let us point out how narrowing the choice of the basis of the Hilbert space led to the block diagonal structure of $H(\boldsymbol{k})$. This procedure was performed in two steps. First, we divided the Hilbert space $\mathcal{H}$ into subspaces $\mathcal{H}_{\boldsymbol{k}}$ that are invariant under the translation subgroup: $\mathcal{H} = \mathcal{H}_{\boldsymbol{k}_1} \oplus \mathcal{H}_{\boldsymbol{k}_2} \oplus \ldots \mathcal{H}_{\boldsymbol{k}_\mathcal{N}}$, where $\mathcal{N}$ is the number of vectors in the BZ. Each of these subspaces is spanned by Bloch states, which are basis states of irreps of the translation subgroup. With this split of the Hilbert space and choice of basis, the matrix $H(\boldsymbol{k})$ becomes diagonal by blocks and each block corresponds to a $\mathcal{H}_{\boldsymbol{k}}$ [see Fig. **4.2**a]. Second, we realized that each of these blocks subduces a representation of the little group $G_{\boldsymbol{k}}$ that is (generally) reducible. Therefore, choosing for each $\mathcal{H}_{\boldsymbol{k}}$ a basis of Bloch states that are also adapted to the symmetries of the irreps of $G_{\boldsymbol{k}}$ splits each block into smaller blocks [see Fig. **4.2**(b)].

Notice that, even if an eigenstate $|\psi_{\boldsymbol{k}}\rangle$ of $H_{\boldsymbol{k}}$ is also an eigenstate of the Hamiltonian H of the whole crystal, it does not transform as an irrep of the space group, but as an irrep of $G_{\boldsymbol{k}}$. Nevertheless, it is possible to choose the eigenstates of $\mathcal{H}$ to transform as irreps of the space group, by building them up as linear combinations of the states $|\psi_{\boldsymbol{k}}\rangle, |\psi_{g\boldsymbol{k}}\rangle, \ldots$ in the star of $\boldsymbol{k}$ – the fact that these states are degenerate, which follows from the similarity relation connecting the Hamiltonians of the vectors in the same star, allows us to make this choice. This property is not exclusive to single-electron Hamiltonians of crystals in reciprocal space; it is indeed a characteristic of any Hamiltonian that can be written as the sum of smaller Hamiltonians acting on disconnected subspaces of the Hilbert space.

4.4 Spinful particles and double groups

We have not mentioned the spin degree of freedom so far. In fact, the group theory concepts introduced until now are valid regardless of whether the particles are spinful or spinless. Explaining how spin enters the theory of symmetry representations might however be worth it, as the main focus of our work in on electrons, which are spinful particles. This aspect is indeed vital to include spin-orbit coupling effects in tight-binding models, like in Sec. 10.5.

Spinful and spinless particles have different transformation properties and the representations we work with must account for these differences. In order to illustrate this

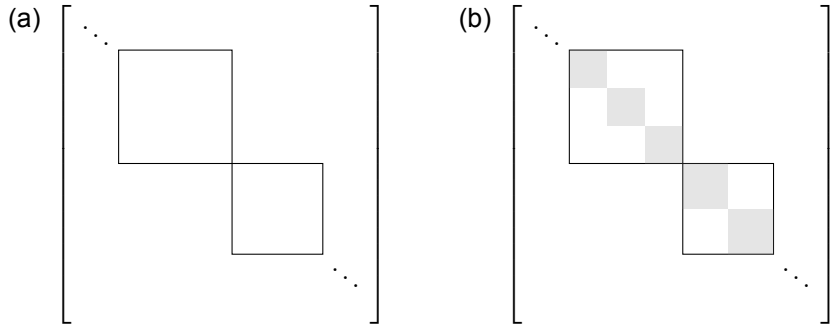

Figure 4.2: Block-diagonal form of the matrix H of a crystal. (a) Form obtained when the Bloch states are chosen for the basis of the Hilbert space $\mathcal{H}$. Each block corresponds to a subspace $\mathcal{H}_{\boldsymbol{k}}$ of a definite $\boldsymbol{k}$. (b) When the states adapted to the symmetry of the irreps of $G_{\boldsymbol{k}}$ are chosen as basis for each $\mathcal{H}_{\boldsymbol{k}}$, the block corresponding to each of these subspace generally divides into smaller blocks (grey squares), according to Wigner's theorem.

point, let us come back to the example of the point group C_{4v} and consider an electron on a p_x-orbital, denoted as $|p_x\rangle$. This state acquires a π-phase under the two-fold rotation C_{2z} with respect to the z-axis. So after applying this rotation twice in a row:

$$C_{2z}^2 \, |p_x\rangle = (-1)^2 \, |p_x\rangle = |p_x\rangle \, . \tag{4.40}$$

Even if this transformation might look reasonable for vectors, it contradicts the fact that fermions (like the electron) acquire a π-phase under 2π-rotations. The root of the problem is that the state $|p_x\rangle$ describes only the particle's space degrees of freedom. To account efficiently for the spin, we need to include it as a degree of freedom in our basis of the Hilbert space. A state in this basis could then be denoted as $|\psi_{i\sigma}\rangle$, where i describes the space degrees of freedom, while σ stands for the spin. Such a state transforms as follows under a symmetry operation $g = \{R|\boldsymbol{v}\}$:

$$g \, |\psi_{i\sigma}\rangle = \sum_{\sigma' j} D_{ji}(g) S_{\sigma'\sigma}(R) \, |\psi_{j\sigma'}\rangle \, . \tag{4.41}$$

Here, D is the matrix of the representation that describes how space degrees of freedom transform, whereas S is the representation as which the spin transforms, often called **spin representation**. We can thus consider that the transformation of the spinful basis states is described by the product representation $\bar{D} = D \times S$, whose matrices are constructed as the Kroenecker product between the matrices of D and S. Such "spinful representations" are often dubbed **double-valued representations**.

Let us come back to the example of the p_x-orbital above. The matrix of C_{2z} in the spin representation is:

$$S(C_{2z}) = \exp(i\sigma_z \pi/2) = i\sigma_z, \tag{4.42}$$

where σ_z is the third Pauli matrix. The transformation of the spinful p_x-orbital under a 2π-rotation over the z-axis is then:

$$C_{2z}^2 \left|p_{x\sigma}\right\rangle = (-1)^2 i^2 \left|p_{x\sigma}\right\rangle = -\left|p_{x\sigma}\right\rangle, \tag{4.43}$$

so we get the correct transformation.

Notice that now a rotation C_θ by an angle θ differs from $C_{\theta+2\pi}$. Strictly speaking, double-valued representations are not representations of the symmetry groups we have considered so far, but of groups that are twice as large as them due to the fact that 2π-rotations should be distinguished from the identity for spinful particles. These enlarged groups are known as **double groups**.

For systems with weak SOC, the electron could be considered a spinless particle and the symmetry analysis could be restricted to single-valued representations. The study of the symmetry properties of phonons [110] and photons [111] could also be performed in terms of single-valued representations. However, the dependence of the Hamiltonian on the spin can not be neglected for some systems. This is the case for materials containing heavy elements with strong spin-orbit coupling. Indeed, this effect turns out to be vital to understand or reproduce some insulating phases [2, 3] . Moreover, considering electrons as spinful particles has also lead to the prediction of high-degeneracy crossings of bands [112].

4.5 Time-reversal symmetry in group theory

Everything we have explained so far in this chapter has been based on groups containing crystal symmetries. Unlike these symmetries, time reversal (TR) is an antiunitary transformation that has profound effects on the band structure of crystals. In fact, it is responsible of the Kramers degeneracy of bands and it can protect topological phases [11]. Here, we will comment on the implementation of TR symmetry in group theory.

TR symmetry enters the theory of symmetry representation as an anti-unitary transformation which reverses the spin. Regarding the crystal structure, it reverses locally the direction of magnetic moments. Apart from leaving the array of ions invariant, any symmetry in the space group must also leave now the magnetic moments unaltered.

Let us denote by θ the operator of TR and by G the space group corresponding to a certain arrangement of ions, without considering the magnetic moments – the kind of space groups considered so far, also known as **Fedorov groups** or type-I Shubnikov groups. If the crystal is not magnetically ordered, the combination of unitary crystal

symmetries and TR forms antiunitary symmetries which leave the ions' positions invariant. After considering TR symmetry, the space group M of the system is twice as large as G:

$$M = G + \theta G. \tag{4.44}$$

This kind of space groups are called **grey groups** or type-II Shubnikov groups.

When the crystal shows certain magnetic ordering, only some of the transformations in Eq. (4.44) leave invariant at the same time the arrangement of ions and the magnetic moments. For example, it might happen that the two-fold rotation C_{2z} does not belong to the space group, while θC_{2z} does. These space groups corresponding to magnetically ordered crystals are known as **black and white** groups (they include both type-III and IV Shubnikov groups). All in all, there exist 1651 magnetic space groups.

Motivated by the fact that we have considered only magnetically non-ordered crystals in this work, we will concentrate our discussion on how the theory of representations is modified to include TR symmetry in grey groups. Let us choose as our starting point the irreducible representation Δ of the space group group G defined in the Hilbert space of dimension N spanned by the states $|\psi_i\rangle$. Then, for every $g \in G$:

$$g\,|\psi_i\rangle = \sum_{j=1}^{N} \Delta_{ji}(g)\,|\psi_j\rangle\,. \tag{4.45}$$

We shall write this equation for short in the following form:

$$g\,|\psi\rangle = \Delta(g)\,|\psi\rangle\,, \tag{4.46}$$

where $|\psi\rangle$ denotes the basis formed by the states $|\psi_i\rangle$. Under TR symmetry, these states turn into the states $|\phi_i\rangle$, which we also denote for short as $|\phi\rangle$:

$$|\phi\rangle = \theta\,|\psi\rangle\,. \tag{4.47}$$

It can be shown that the transformations $g \in G$ leave also the subspace of $|\phi\rangle$ invariant. In addition, the transformations $\tilde{g} \in \theta G$ map the states $|\psi\rangle$ into $|\phi\rangle$, and the states $|\phi\rangle$ into $|\psi\rangle$. The space $\mathcal{H}_{2N}$ formed as the union of the spaces spanned by all these states is hence invariant under the grey group $M = G + \theta G$. The action of M on the states $|\psi, \phi\rangle \in \mathcal{H}_{2N}$ is described by the following matrices [109]:

$$\begin{aligned} D\Delta(g) &= \begin{bmatrix} \Delta(g) & 0 \\ 0 & \Delta^*(\theta^{-1} g \theta) \end{bmatrix} \quad \forall g \in G, \\ D\Delta(\tilde{g}) &= \begin{bmatrix} 0 & \Delta(\tilde{g}\theta) \\ \Delta^*(\theta^{-1}\tilde{g}) & 0 \end{bmatrix} \quad \forall \tilde{g} \in \theta G. \end{aligned} \tag{4.48}$$

These set of matrices forms the **corepresentation** $D\Delta$ of M constructed from the irrep

Δ of G. A corepresentation is the analogous to a representation within the context of magnetic groups containing antiunitary symmetries. The reason why it is not called simply "representation" is that its matrices do not obey the multiplication law in Eq. (4.1) rigorously for all pairs of symmetries in M.

If the space H_{2N} admits a split into non-trivial invariant subspaces, the corepresentation $D\Delta$ will be reducible. In other words, the corepresentation is reducible if there exists a change of basis in $\mathcal{H}_{2N}$ for which both matrices in Eq. (4.48) turn into block diagonal, for every pair of unitary and antiunitary operations in M. Otherwise, it will be irreducible.

It turns out that whether $D\Delta$ is reducible or irreducible depends on the irrep Δ of G it was derived from. We can distinguish between three types of representations: type 1 (real), -1 (pseudoreal) and 0 (complex). If Δ is a type 1 single-valued or type -1 doble-valued irrep of G, the space $\mathcal{H}_{2N}$ can be divided into two invariant subspaces of dimension N, so the corepresentation $D\Delta$ is reducible. In the rest of cases, the corepresentation induced from Δ is irreducible, thus it will have in correspondence an energy level of degeneracy $2N$, upon application of Wigner's theorem.

In practical terms, the irreps of unitary groups G and their corresponding classification as type 1, -1 or 0 irreps can be found in the literature [96,109]. This information allows us to predict the degeneracy of the corresponding energy levels upon inclusion of TR symmetry. Moreover, the irreducible corepresentations of magnetic point groups and (little groups of) magnetic space groups have been recently included in the *Bilbao Crystallographic Server* [34,72].

5 Topological quantum chemistry

In Sec. 3, we learnt that topological properties of bands are encoded in their wave functions. We also proved the existence of a relationship between symmetries and topology, which manifested itself as constrains set by symmetries on the spectrum of Wilson loops. Moreover, the description of the way in which representations of little groups of vectors $\boldsymbol{k}$ are related to wave functions of bands was given in Sec. 4. However, we have not set yet a general relationship between symmetries and topology valid for all space groups. In this section, we will marry the concepts explored in both Secs. 3 and 4 by introducing the formalism named topological quantum chemistry. This theory provides us with an efficient recipe to diagnose the topology of a set of bands from its little group irreps, besides giving us a deep insight into how bands inherit their symmetry properties from localized states in real space.

Since it was published in 2017 [25–27], TQC has become a widely used formalism to investigate the topology of band structures. On the one hand, its combination with *ab initio* techniques forms a powerful method to diagnose topology in actual materials; this method has been recently applied to search for topological phases in big material-databases [30, 72, 104]. On the other hand, TQC turned out to be a useful tool for identifying space groups and crystals which might host particular topological phases, and for engineering models to look into these phases [94, 113, 114].

The original works by J. Zak [31–33] set in the 1980s the ground for the development of the actual TQC formalism. In this works, J. Zak explored how Wannier functions sitting in real space induce bands in reciprocal space; in particular, he described the way in which these bands inherit their little group representations from the transformation properties of Wannier functions. Bands induced from exponentially localized (in real space) Wannier functions are said to have an *atomic limit*; equivalently, in the language used in Sec. 3, a set of bands has an atomic limit if it is possible to construct via Eq. (3.74) exponentially localized Wannier functions that respect the space group. J.

Zak further realized that space groups might host a rich variety of atomic limits, which stems from the existence of many special positions in the unit cell and types of Wannier functions.

The formalism was complemented later by B. Bradlyn *et al.* to deal with the topology of bands [25–27]. This extension is rooted in the idea that trivial bands have an atomic limit; notice that this concept is in accordance with our discussion about Wannier obstruction discussed in Sec. 3.4.2. Moreover, elementary band representations were defined in these works as building blocks of atomic limits. The process of checking if a set of bands has an atomic limit is then equivalent to determining if it can be expressed as an integer combination of EBRs. This task was further simplified as the authors derived and tabulated the EBRs for all single and double-valued space groups, together with the corresponding irreps of little groups.

This chapter is divided into two sections. First, we will introduce the concept of band representations of a space group, and we will derive expressions for their matrices in both real and reciprocal space. The conditions to be satisfied by a representation corresponding to a set of bands will also be described in detail. Then, a rule to diagnose topological sets of bands from the symmetry representations of their little groups will be described, besides a general classification of topological states that could be detected with this criterion.

5.1 Band representations

A real-space defined representation of the space group G requires a basis that is closed under all its symmetries. We will construct such a basis starting from a handful of Wannier functions and this basis will then be enlarged as symmetries take the states out of it.

Let us consider as our starting point a set of Wannier functions $|W_{i\boldsymbol{q}}(\boldsymbol{0})\rangle$ sitting at the position $\boldsymbol{q}$. The index $i = 1, \ldots, \dim(\rho)$ labels the orbital degrees of freedom of the Wannier function, while the vector $\boldsymbol{r} = 0$ indicates the cell the site belongs to. We choose these functions to transform as the irrep ρ of its site-symmetry group $G_{\boldsymbol{q}}$:

$$g\,|W_{i\boldsymbol{q}}(\boldsymbol{0})\rangle = \sum_{j=1}^{\dim(\rho)} \rho_{ji}(g)\,|W_{j\boldsymbol{q}}(\boldsymbol{0})\rangle\,, \tag{5.1}$$

where $g \in G_{\boldsymbol{q}}$ [see App. B].

We now consider a symmetry $g_\alpha \in G$ which takes the site $\boldsymbol{q}$ to $\boldsymbol{q}_\alpha = g\boldsymbol{q}$ within the same unit cell. This transformation maps the Wannier functions at $\boldsymbol{q}$ to states sitting at $\boldsymbol{q}_\alpha$:

$$g_\alpha\,|W_{i\boldsymbol{q}}(\boldsymbol{0})\rangle = |W_{i\boldsymbol{q}_\alpha}(\boldsymbol{0})\rangle\,. \tag{5.2}$$

Our initial basis is hence open under such symmetry operations. In order to achieve a

basis closed under the whole space group, we include in our basis the Wannier functions sitting on the n sites of the Wyckoff position which belong to the same cell as $\boldsymbol{q}$.

Furthermore, the elements in the translation subgroup T of G take these states to other cells. This forces us to extend the basis with states related to the already included ones by vectors of the Bravais lattice:

$$\hat{\boldsymbol{t}}\,|W_{i\boldsymbol{q}}(\boldsymbol{0})\rangle = |W_{i\boldsymbol{q}}(\boldsymbol{t})\rangle\,. \tag{5.3}$$

On the whole, the real-space basis we consider is formed by $N \times \dim(\rho) \times n$ states $|W_{i\boldsymbol{q}_\alpha}(\boldsymbol{t})\rangle$. This basis is already closed under the space group G, since any element of this group can be generated as $\{E|\boldsymbol{t}\}g_\alpha g$. This corresponds to writing G through the following coset decompostion:

$$G = (G_{\boldsymbol{q}} \cup g_1 G_{\boldsymbol{q}} \cup \cdots \cup g_n G_{\boldsymbol{q}})T. \tag{5.4}$$

Let us derive the transformation of the basis states under an arbitrary element $h = \{R|\boldsymbol{v}\} \in G$:

$$h\,|W_{i\boldsymbol{q}_\alpha}(\boldsymbol{t})\rangle = h\{E|\boldsymbol{t}\}\,|W_{i\boldsymbol{q}_\alpha}(\boldsymbol{0})\rangle = \{E|R\boldsymbol{t}\}hg_\alpha\,|W_{i\boldsymbol{q}}(\boldsymbol{0})\rangle\,. \tag{5.5}$$

Based on Eq. (5.4), we can write $hg_\alpha = \{E|\boldsymbol{t}_{\beta\alpha}\}g_\beta g$, where $g \in G_{\boldsymbol{q}}$ and $\boldsymbol{t}_{\beta\alpha} = h\boldsymbol{q}_\alpha - \boldsymbol{q}_\beta$. Notice that the vector $t_{\beta\alpha}$ accounts for the fact that h might move the site $\boldsymbol{q}_\alpha$ to the site $\boldsymbol{q}_\beta$ belonging to a different unit cell. Then,

$$\begin{aligned} h\,|W_{i\boldsymbol{q}_\alpha}(\boldsymbol{t})\rangle &= \{E|R\boldsymbol{t}\}\{E|\boldsymbol{t}_{\beta\alpha}\}g_\beta g\,|W_{i\boldsymbol{q}}(\boldsymbol{0})\rangle \\ &= \sum_{j=1}^{\dim(\rho)} \rho_{ji}(g)\,\big|W_{j\boldsymbol{q}_\beta}(R\boldsymbol{t}+\boldsymbol{t}_{\beta\alpha})\big\rangle\,. \end{aligned} \tag{5.6}$$

Writing this expression in matrix form yields the representation as which the chosen set of Wannier functions transforms. This representation of the space group G is said to be induced from the irrep ρ of the site-symmetry group of the Wyckoff position, and is dubbed **band representation**. We will often denote this band representation

$$\rho_G = (\rho \uparrow G)_{WP}, \tag{5.7}$$

where the subscript WP stands for the actual Wyckoff position from which it was induced. For example, $(A_1 \uparrow G)_{2c}$ would indicate the band representation of G induced from Wannier functions which sit at the sites of Wyckoff position 2c and transforms as the irrep A_1 of their site-symmetry groups.

5.2 Band representations in reciprocal space

Since the real-space expression of Eq. (5.6) is rarely used in practice, we will skip the step of writing it to derive its reciprocal space form. To this end, we consider the change to a basis of Bloch states constructed via the Fourier transform of the Wannier functions:

$$|W_{i\boldsymbol{q}_\alpha}(\boldsymbol{k})\rangle = N^{-1/2}\sum_{\boldsymbol{t}} \exp(i\boldsymbol{k}\cdot\boldsymbol{t})\,|W_{i\boldsymbol{q}_\alpha}(\boldsymbol{t})\rangle\,. \tag{5.8}$$

where $\boldsymbol{k}$ is chosen as a vector of the BZ. It follows from Eq. (5.6) that the action of a symmetry $h=\{R|\boldsymbol{t}\}\in G$ on these Bloch states is:

$$h\,|W_{i\boldsymbol{q}_\alpha}(\boldsymbol{k})\rangle = \exp[i(R\boldsymbol{k})\cdot\boldsymbol{t}_{\beta\alpha}]\sum_{j=1}^{\dim(\rho)}\rho_{ji}(g)\,\big|W_{j\boldsymbol{q}_\beta}(R\boldsymbol{k})\big\rangle\,. \tag{5.9}$$

In reciprocal space, every matrix of the band representation is formed by $\mathcal{N}\times\mathcal{N}$ blocks of dimension $n\times\dim(\rho)$:

$$\rho^{R\boldsymbol{k},\boldsymbol{k}}_{j\boldsymbol{q}_\beta,i\boldsymbol{q}_\alpha}(h) = \exp[i(R\boldsymbol{k})\cdot\boldsymbol{t}_{\beta\alpha}]\rho_{ji}(g). \tag{5.10}$$

This is the expression for the matrix elements of the band representation in reciprocal space. Even though each of these blocks should have in correspondence a pair of vectors $(R\boldsymbol{k},\boldsymbol{k})$, we will omit the label $R\boldsymbol{k}$, as we will focus for each $\boldsymbol{k}$ on the symmetries of its little group $G_{\boldsymbol{k}}$.

Let us now concentrate on a particular $\boldsymbol{k}$ point of the BZ. The matrices $\rho^{\boldsymbol{k}}$ in Eq. (5.10) form a representation of the little group $G_{\boldsymbol{k}}$, which we $\rho_G\downarrow G_{\boldsymbol{k}}$. This representation is generally reducible and can thus be decomposed in terms of irreps $D^{\boldsymbol{k}}_i$ of $G_{\boldsymbol{k}}$ via (4.38):

$$\rho_G\downarrow G_{\boldsymbol{k}} = \bigoplus_i m^{\boldsymbol{k}}_i D^{\boldsymbol{k}}_i. \tag{5.11}$$

Recall that, while $\rho_G\downarrow G_{\boldsymbol{k}}$ describes the transformation of Bloch states defined in Eq. (5.8), the eigenstates $|\psi_{n\boldsymbol{k}}\rangle$ of the Hamiltonian $H(\boldsymbol{k})$ transform as irreps of $G_{\boldsymbol{k}}$. According to our discussion in Sec. 4.3.3, the degeneracy of each energy level at $\boldsymbol{k}$ is related to the dimension of an irrep in Eq. (5.11) and the symmetry properties of the corresponding eigenstates are described by the matrices of the irreps themselves. At the same time, as the derivation of the band representation above reveals, these irreps are inherited from the transformation properties of the Wannier functions in real space. All in all, we conclude that the irreps of little groups of a set of bands with an atomic limit are inherited from the real-space transformation properties of the Wannier functions they originate from.

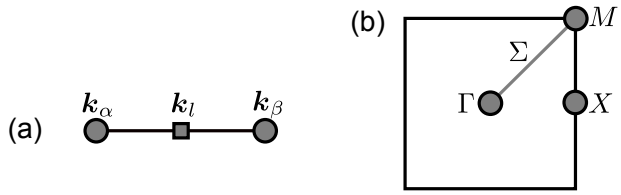

Figure 5.1: (a) Illustration of the vectors $\boldsymbol{k}_\alpha$, $\boldsymbol{k}_\beta$ and (the intermediate vector) $\boldsymbol{k}_l$ considered in the text. (b) BZ corresponding to the wallpaper group of $P4mm$. Γ, X and M are the maximal $\boldsymbol{k}$-points. Σ denotes the vectors in the line connecting Γ to M and its irreps are determined by the irreps at maximal $\boldsymbol{k}$-points.

5.3 Compatibility relations

At this point, we might wonder if any arbitrary combination of irreps of little groups yields a band structure. It turns out that these irreps must satisfy some compatibility relations. These relations can be interpreted as the constrains set by symmetries on the connectivity of the bands or little group irreps.

We consider two points $\boldsymbol{k}_\alpha$ and $\boldsymbol{k}_\beta$ with non-trivial little groups $G_{\boldsymbol{k}_\alpha}$ and $G_{\boldsymbol{k}_\beta}$, respectively. Let us pick a vector $\boldsymbol{k}_l$ belonging to a line of lower symmetry which connects these vectors [see Fig. **5.1**a]. The little group $G_{\boldsymbol{k}_l}$ is a subgroup of both $G_{\boldsymbol{k}_\alpha}$ and $G_{\boldsymbol{k}_\beta}$, *i.e.* $G_{\boldsymbol{k}_l} \subset G_{\boldsymbol{k}_\alpha}, G_{\boldsymbol{k}_\beta}$. Therefore, for the band structure to be consistent, the representations of $G_{\boldsymbol{k}_\alpha}$ and $G_{\boldsymbol{k}_\beta}$ corresponding to the blocks $\rho^{\boldsymbol{k}_\alpha}$ and $\rho^{\boldsymbol{k}_\beta}$ must both subduce the same representation of $G_{\boldsymbol{k}_l}$:

$$(\rho_G \downarrow G_{\boldsymbol{k}_\alpha}) \downarrow G_{\boldsymbol{k}_l} = (\rho_G \downarrow G_{\boldsymbol{k}_\beta}) \downarrow G_{\boldsymbol{k}_l}. \tag{5.12}$$

This consistency relation reveals that the irreps of little groups corresponding to a set of bands are not independent. It turns out that the irreps in a finite number of $\boldsymbol{k}$-points determine the irreps in the rest of the BZ. These primal points are the **maximal $\boldsymbol{k}$-points** of the BZ (see App. B). Therefore, to characterize a set of bands it is enough to determine the irreps of little groups at the maximal $\boldsymbol{k}$-points; the irreps in the rest of symmetry-lines, planes and points can be then be obtained by applying the compatibility relations for the space group. These compatibility relations can be found in tables [96]. See Fig. **5.1**b for an example.

It is important to realize that, whereas the connectivity of the irreps of little groups is determined by the compatibility relations, the actual energy levels are not constrained. In other words, how energy energy levels labeled by irreps are sorted from smaller to larger energy is not specified by any symmetry consideration. This in fact depends on the system's microscopic details.

Let us suppose we wish to determine if a set of bands, whose states transform as the representation ρ of the space group, satisfies the compatibility relations. Let $\boldsymbol{k}_j$ be

a maximal $\boldsymbol{k}$-vector and $m^i_{\boldsymbol{k}_j}$ the multiplicity of the i$^{\text{th}}$ irrep of its little group $G_{\boldsymbol{k}_j}$ in the decomposition of the representation of our set of bands. These multiplicities can be represented as a data vector B

$$B = (m^1_{\boldsymbol{k}_1}, m^2_{\boldsymbol{k}_1}, \cdots, m^{N_1}_{\boldsymbol{k}_1}, m^1_{\boldsymbol{k}_2}, \cdots)^T, \tag{5.13}$$

whose size N is equal to the total number of irreps in all maximal $\boldsymbol{k}$-points. We will now follow a description based on Ref. [115]. Furthermore, let us denote $\boldsymbol{k}_\alpha$ and $\boldsymbol{k}_\beta$ two maximal $\boldsymbol{k}$-vectors. The representations of the little groups $G_{\boldsymbol{k}_\alpha}$ and $G_{\boldsymbol{k}_\beta}$ subduced by ρ could be decomposed as:

$$\rho \downarrow G_{\boldsymbol{k}_\alpha} = \sum_{i=1}^{N_\alpha} m^i_{\boldsymbol{k}_\alpha} \rho^i_{\boldsymbol{k}_\alpha}, \tag{5.14}$$

$$\rho \downarrow G_{\boldsymbol{k}_\beta} = \sum_{i=1}^{N_\beta} m^i_{\boldsymbol{k}_\beta} \rho^i_{\boldsymbol{k}_\beta}. \tag{5.15}$$

where $\rho^i_{\boldsymbol{k}_\alpha}$ and $\rho^i_{\boldsymbol{k}_\beta}$ are irreps of the little groups of $\boldsymbol{k}_\alpha$ and $\boldsymbol{k}_\beta$, respectively. Let $\boldsymbol{k}_l$ be a vector in a line connecting $\boldsymbol{k}_\alpha$ and $\boldsymbol{k}_\beta$. Every irrep in Eqs. (5.14) and (5.15) subduces a representation of $G_{\boldsymbol{k}_l}$ that is generally reducible:

$$\rho^i_{\boldsymbol{k}_\alpha} \downarrow G_{\boldsymbol{k}_l} = \sum_{j=1}^{N_{\boldsymbol{k}_l}} c^{ij}_{\boldsymbol{k}_\alpha, \boldsymbol{k}_l} \rho^j_{\boldsymbol{k}_l}, \tag{5.16}$$

$$\rho^i_{\boldsymbol{k}_\beta} \downarrow G_{\boldsymbol{k}_l} = \sum_{i=1}^{N_\beta} c^{ij}_{\boldsymbol{k}_\beta, \boldsymbol{k}_l} \rho^j_{\boldsymbol{k}_l}. \tag{5.17}$$

The integers c here are the multiplicities of the decomposition. We have not denoted them m because they are not related to the decomposition of our initial set of bands B, unlike the multiplicities in Eqs. (5.14) and (5.15). The data vector B will respect the compatibility relations along $\boldsymbol{k}_l$ if the expressions we obtain by applying Eqs. (5.16) and (5.17) in Eqs. (5.14) and (5.15) match:

$$\sum_{j=1}^{N_{\boldsymbol{k}_l}} m^i_{\boldsymbol{k}_\alpha} c^{ij}_{\boldsymbol{k}_\alpha, \boldsymbol{k}_l} = \sum_{j=1}^{N_{\boldsymbol{k}_l}} m^i_{\boldsymbol{k}_\beta} c^{ij}_{\boldsymbol{k}_\beta, \boldsymbol{k}_l}. \tag{5.18}$$

It is convenient to construct a matrix $C^{\boldsymbol{k}_\alpha, \boldsymbol{k}_\beta, \boldsymbol{k}_l}_{comp}$ with the multiplicities c. Every column of this matrix has in correspondence an irrep of $G_{\boldsymbol{k}_l}$, while every row is related to an irrep of a maximal $\boldsymbol{k}$ vector. Indeed, the element in the j^{th} column corresponding to $\rho^i_{\boldsymbol{k}_\alpha}$ contains the integer $c^{ij}_{\boldsymbol{k}_\alpha, \boldsymbol{k}_l}$, whereas the element corresponding to $\rho^i_{\boldsymbol{k}_\beta}$ contains $-c^{ij}_{\boldsymbol{k}_\beta, \boldsymbol{k}_l}$. The compatibility relations in Eq. (5.18) can then be written efficiently as:

$$B \cdot C^{\boldsymbol{k}_\alpha, \boldsymbol{k}_\beta, \boldsymbol{k}_l}_{comp} = 0. \tag{5.19}$$

Furthermore, we can construct the matrix C_{comp} by stacking along the directions of columns the matrices $C_{comp}^{\boldsymbol{k}_\alpha,\boldsymbol{k}_\beta,\boldsymbol{k}_l}$ for all paths $\boldsymbol{k}_l$ connecting all pairs of maximal vectors $\boldsymbol{k}_\alpha$ and $\boldsymbol{k}_\beta$. Our initial set of bands respects then all compatibility relations if its data vector B satisfies:

$$B \cdot C_{comp} = 0. \tag{5.20}$$

The convenience of this method resides in the fact that the matrix C_{comp} depends only on the space group, rather than on the particular set of bands we are investigating. Therefore, once this matrix has been constructed, checking if a particular isolated set of bands satisfies the compatibility relations reduces to calculating the product in Eq. (5.20).

5.4 Composite and elementary band representations

The composition of band representations consists in the stacking of the corresponding bands in the band structure of the Hamiltonian. A representation is said to be a **composite band representation** if it can be written as the sum of two smaller band representations. In contrast, band representations which are not composite are called **elementary band representations**. It turns out that only irreps of site-symmetry groups of sites in maximal WPs induce EBRs[1]. Therefore, whereas the number of band representations of a space group is infinite, the number of EBRs is finite. Indeed, the EBRs of all space groups were computed in Ref. [25] and a catalogue of them is can be found in the *Bilbao Crystallographic Server* [96].

EBRs of a space group can thus be interpreted as the basic building-blocks of bands representations; in other words, EBRs form a basis for the space of bands connected to atomic limits of a space group. Any band representation ρ_G of a space group G can be decomposed in terms of its EBRs:

$$\rho_G = \bigoplus_i C_i \, \rho_G^i, \tag{5.21}$$

where ρ_G^i denotes an EBR of G.

An EBR is said to be **decomposable** if its bands can be separated into two or more disconnected sets which respect the compatibility relations independently. As an example illustrate the concept of decomposable EBR, let us choose the band structure studied in Ref. [94]. We consider the EBR $(A_1 \uparrow G)_{3c}$ of the wallpaper group of $P6mm$ (hexagonal lattice). The irreps at maximal $\boldsymbol{k}$-points of this EBR can be distributed into two sets: $\{\Gamma_1, M_1, K_1\}$ and $\{\Gamma_5, M_3 \oplus M_4, K_3\}$. These irreps can be connected such that each set satisfies the compatibility relations independently. As a consequence, the EBR

[1] This is the reason why considered for Wannier functions transforming as irreps of the site-symmetry group as starting point for the derivation of band representations. Band representations can be induced from both reducible or irreducible representations, but only the later lead to EBRs.

can be split into two separated groups of bands, each hosting the irreps of one of this sets.

Notice that, if an EBR is decomposable, at least one of the set of bands it splits into is not a band representation. Therefore, there exist set of bands which do not have an atomic limit.

5.5 Topological bands in TQC

By construction, band representations have in correspondence bands originated from exponentially localized Wannier functions, that is, bands connected to an atomic limit. In contrast, bands whose states do not transform as band representations are not adiabatically connected to any atomic limit and are therefore **topological bands**. According to this criterion, whether a set of bands is topological might be checked by decomposing its representation in terms of EBRs, like in Eq. (5.21). If any of the coefficients C_i is negative or fractional, the bands are topological.

Two types of topological bands can be distinguished immediately by looking at the coefficients:

- If any of the coefficients in a fractional number, the bands host a **stable topological phase**.
- If the coefficients which are not positive integer are negative integers, the bands are **fragile topological** [93, 116]. Fragile bands could be made trivial upon stacking with certain trivial set of bands.

A more detailed classification of topological bands can be found in Ref. [117].

Let us come back to the example given in the previous section. We mentioned that the EBR $(A_1 \uparrow G)_{3c}$ of the wallpaper group $P6mm$ can be divided into two sets of separated bands with irreps $\{\Gamma_1, M_1, K_1\}$ and $\{\Gamma_5, M_3 \oplus M_4, K_3\}$ at maximal $\boldsymbol{k}$-points. It turns out that the first of these sets of irreps corresponds to the EBR $(A_1 \uparrow G)_{1a}$. The second set of irreps can consequently be written in terms of the EBRs of the group as $(A_1 \uparrow G)_{3c} \ominus (A_1 \uparrow G)_{1a}$, and corresponds therefore to a set of fragile bands.

It must be mentioned that, having a set of irreps that coincides with those of a band representation is necessary but not enough for the set of bands to be trivial. Such a set of bands might still have non-trivial topology that is invisible to crystal symmetries [118]. Furthermore, in some space groups two sets of bands with identical irreps could be topologically different, even if these irreps coincide with those of an atomic limit. Analyzing the spectrum of Wilson loops operators is often the way to unveil topology in such cases. The power of TQC resides in the opposite case: if the irreps of a set of bands do not match with the irreps of any band representation, the set of bands is topological.

5.6 Diagnosing topology from little group irreps

In this section, we will put forward a way to calculate the coefficients of decomposition in Eq. (5.21) once the irreps at maximal $\boldsymbol{k}$-points have been calculated. The description given here follows the discussion in Ref. [115].

Let us suppose we wish to determine the decomposition in terms of EBRs of a set of bands whose irreps at maximal $\boldsymbol{k}$-points are represented by the data vector B [see Eq. 5.13]. Moreover, we consider the matrix EBR, whose element EBR_{ji} contains the multiplicity of the j^{th} irrep in the decomposition of the i^{th} EBR into irreps of the maximal $\boldsymbol{k}$-points. Note that EBR is generally a rectangular matrix of N rows and N_{EBR} columns, where N_{EBR} is the number of EBRs in the space group.

The representation of our set of bands can be written as a linear combination of EBRs:

$$EBR \cdot X = B, \tag{5.22}$$

where X is the vector of coefficients of the decomposition. The Smith decomposition of the matrix EBR allows us to simplify this set of diophantine equations and to identify a way to check the constrains set by symmetries on B. According to this decomposition, the matrix EBR is related to a diagonal matrix Δ of the same size via the equation:

$$EBR = L^{-1} \cdot \Delta \cdot R^{-1}, \tag{5.23}$$

where L and R are unimodular $N_{EBR} \times N_{EBR}$ and $N \times N$ matrices, respectively. Note that these matrices depend only on the EBRs of the space group and are independent of B – the same matrices take part in the decomposition of any set of bands. Δ is called the *Smith normal form* of the matrix EBR. In some space groups, some EBRs can be written in terms of other EBRs with integer coefficients, even though they are fundamentaly different EBRs. In other words, some EBRs might have in correspondence the same set of irreps. The rank of EBR might thus be smaller than the number of EBRs, i.e. $\text{rank}(EBR) < N_{EBR}$. As a consequence, the number of non-zero elements in the diagonal of Δ is equal to $\text{rank}(EBR)$. The matrix Δ has hence the following structure:

$$\begin{aligned} &\Delta_{ii} = 0 \quad \text{if } i > \text{rank}(EBR), \\ &\Delta_{ij} = 0 \quad \text{otherwise.} \end{aligned} \tag{5.24}$$

By substituting Eq. (5.23) in Eq. (5.22), we reach:

$$\Delta \cdot Y = C, \tag{5.25}$$

where $Y = R^{-1} \cdot X$ and $C = L \cdot B$. Solving this set of equations is generally simpler than Eq. (5.22).

It should be mention that, when $rank(EBR) < N$, the solution is not unique. In other words, when some of the EBRs share the same set of irreps, the decomposition of a set of bands in terms of EBRs is not unique.

6 *IrRep*: irreducible representations of *ab initio* band structures

Density Functional Theory is the state-of-the-art approach to calculate band structures of materials. Its numerical implementation provides us with a systematic method to calculate the energy levels and wave functions of the single-electron Hamiltonian $H(\boldsymbol{k})$ of a crystal. The keys of the success of DFT are its (relatively) low numerical cost and availability of softwares to implement it. Accordingly, DFT postulated soon itself as a candidate to become the standard method for the calculation of bands whose topology would later be classified with TQC.

An immediate obstacle for the combined action of DFT and TQC is that, while TQC diagnoses the topology of bands from their irreps, DFT codes lack generally of the possibility to calculate these irreps. To fix this problem, we have developed the code *IrRep*, which calculates the irreps of *ab initio* band structures. This contribution bridges the gap between the theoretical foundation and practical implementation of TQC.

IrRep is a robust, open source Python that interfaces directly with 3 of the most widely used DFT softwares: the Vienna Ab initio Simulation Package (VASP) [60], Abinit [61,62] and Quantum Espresso (QE) [63]. *IrRep* can also read input files in Wannier90 (W90) [64] format (`.win`, `.eig`, `_UNK`), prepared by interfaces like pw2wannier90. This allows *IrRep* to be used with any code that has a W90 interface, such as SIESTA [119]. Furthermore, *IrRep* has been structured in a user friendly format allowing the implementation of routines to interface with any other plane-wave based code.

Although similar codes have recently been developed for VASP [78] and QE [79], *IrRep* is the only code that does not restrict the user to a single DFT program. Moreover, our code follows the same notation as the popular Bilbao Crystallographic Server (BCS) [96] to identify the irreps, which avoids confusion coming from the lack of an official standard notation, especially for spin-orbit coupled systems. Tables of irreps are

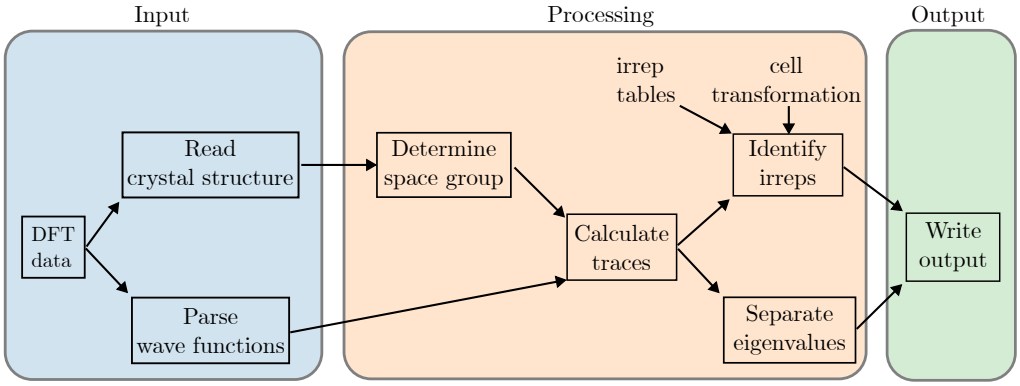

Figure 6.1: Schematic illustration of *IrRep*'s workflow, showing its the three main parts: input, processing and output. The running process flows from left to right. The small text-boxes indicate stages of the process, while the text without boxes correspond to auxiliary data and calculations for a particular stage.

encapsulated within the code package, so that *IrRep* can assign irreps to wave functions without extra input from the user. The output is written in a form that is compatible with the *CheckTopologicalMat* tool of the BCS [30, 104]. As additional functionality, *IrRep* can separate bands by eigenvalues of certain symmetry operator and calculates the $\mathbb{Z}_2$ and $\mathbb{Z}_4$ topological indices of time-reversal symmetric band structures [2]. The code evolved from the routines written for Ref. [120] to determine the eigenvalues of screw rotations. At a testing level, the code was used in Refs. [121–125] for topological quantum chemistry, and in Refs. [126, 127] to analyze the dipole selection rules for optical matrix elements. In Sec. 6.1 we will go through the workflow of the code, explaining in detail every stage of it. Sec. 6.2 will be devoted to several examples, illustrating the capabilities of *IrRep* code for the analysis of symmetry and topology.

6.1 Workflow of *IrRep* code

We introduce in this section the workflow of the *IrRep* code and describe its main functionalities and the particularities of the interface to each DFT software. The running process can be divided into three main parts (see Fig. **6.1**): (i) parsing of the DFT data given as **input** to *IrRep*; (ii) **processing** of the data to obtain the desired information; (iii) writing this information as **output**. Each of this part can further be split in stages, which will be explained thoroughly in the following.

6.1.1 Reading DFT data and input parameters

To keep the interaction with the user simple, *IrRep* reads as much needed information as possible from the DFT code's output files. Only parameters determining the user-defined task should be given in the command line (CLI) in the format

```
irrep -<keyword1>=<value1> -<keyword2>=<value2> ...
```

Alternatively, parameters may be set in YAML or JSON format in an input file passed to *IrRep* via the parameter `config`, as we show in the following lines:

```
irrep -config=input_filename.yml
```

The most important input parameters and their default values are described in Tab. **6.1**. This information can be accessed by calling to *IrRep*'s help interface in the CLI:

```
irrep --help
```

Depending on the DFT code used to calculate wave functions, a different interface should be chosen to parse the corresponding DFT output files (see Tab. **6.2**). The interfaces are selected with the keyword `code`; currently, it includes interfaces to VASP [60], Abinit [61, 62] and QE [63]. It can also read the input files for W90 [64], which allows *IrRep* to be used with the multiple codes that support the Wannier90 interface.

Once keywords are set in the CLI, the code parses the DFT data files passed as input (see Tab. **6.2**). In essence, the lattice vectors, positions of atoms and the energies and wavefunctions of electronic states are read in this way (see Sec. 6.1.3 for details). The step of reading the DFT data is naturally different for each DFT software, since each of them saves its output in a particular fashion – each DFT code might use a different data structure, different units, etc. This is why every DFT software has its own interface in *IrRep*. Nevertheless, once the information is parsed, it is stored in an object of class `Bandstructure` which is independent of the *ab initio* code used. Thus, if an interface to a new *ab initio* code is needed, one has to simply implement another constructor for the `Bandstructure` class.

Although most keywords are self-explanatory, the meaning of the keywords `refUC` and `shiftUC` requires some elaboration. The expectation values of symmetry operations depend on the choice of unit cell for the crystal. Whereas *IrRep* calculates the traces of symmetries for the unit cell parsed from DFT data, the user might be interested in obtaining them for a different unit-cell choice. If that is the case, the user can specify through `refUC` and `shiftUC` the transformation from the DFT cell to the cell of interest and *IrRep* will accordingly compute the traces of symmetry operations for both settings.

Let $\{\boldsymbol{a}_1, \boldsymbol{a}_2, \boldsymbol{a}_3\}$ denote the basis vectors of the cell adopted for the DFT calculation and $\{\boldsymbol{c}_1, \boldsymbol{c}_2, \boldsymbol{c}_3\}$ those of the setting the user is interested in. `refUC` is used to provide *IrRep* with the 3×3 matrix M relating both bases of vectors, according to the following expression

$$(\boldsymbol{c}_1\ \boldsymbol{c}_2\ \boldsymbol{c}_3)^T = M(\boldsymbol{a}_1\ \boldsymbol{a}_2\ \boldsymbol{a}_3)^T \tag{6.1}$$

Keyword	Function	Default
`code`	DFT code: *vasp*, *espresso*, *abinit*, *wannier90*	*vasp*
`fWAV`	VASP wave functions' file	WAVECAR
`fPOS`	VASP crystal structure's file	POSCAR
`fWFK`	Abinit wave functions' file	Mandatory if `code=abinit`
`prefix`	Variable `prefix` in QE calculation or `seedname` in W90	Mandatory if `code=espresso` or `code=wannier90`
`IBstart`	First band to be considered	First band in DFT calculation
`IBend`	Last band to be considered	Last band in DFT calculation
`spinor`	Whether wave functions are spinors or not	`False` (mandatory for `vasp`)
`Ecut`	Plane wave cutoff (in eV). Usually, a value around 50 eV yields accurate results	Cutoff used for the DFT calculation
`kpoints`	Indices of $\boldsymbol{k}$-points at which irreps must be computed	All k-points
`kpnames`	Labels of $\boldsymbol{k}$-points at which irreps must be computed	`None`, not needed to calculate traces but mandatory to assing irreps to them
`refUC`	Transformation of basis vectors	3×3 identity matrix
`shiftUC`	Shift of origin	$(0, 0, 0)$
`onlysym`	Stop after finding symmetries	`False`
`isymsep`	Indeces of symmetries to separate eigenstates	`None`
`ZAK`	Calculate Zak phases	`False`
`WCC`	Calculate wannier charge centers	`False`
`EF`	Fermi energy to shift energy levels	0.0 eV
`degenThresh`	Threshold used to decide if bands are degenerate	10^{-4} eV
`config`	Path of YML or JSON file with input parameters	`None`, read input parameters from CLI
`searchcell`	Check if the transformation leads to the conventional cell	`False`

Table 6.1: Principal keywords to fix running options with *IrRep* and their function. If no value is set for parameters that are `None` by default, they and the functions corresponding to them will be ignored. Boolean parameters work as flags (for example, `spinor` is set to `True` by passing `-spinor` to the command `irrep` in the CLI.)

interface	`-code=`	files
VASP	`vasp`	`POSCAR` and `WAVECAR`
Abinit	`abinit`	`*_WFK`
QE	`espresso`	`*.save/data_file_schema.xml` and `*.save/wfc*.dat`
Wannier90	`wannier90`	`*.win`, `*.eig`, `UNK*`

Table 6.2: Files read by *IrRep* depending on the chosen interface.

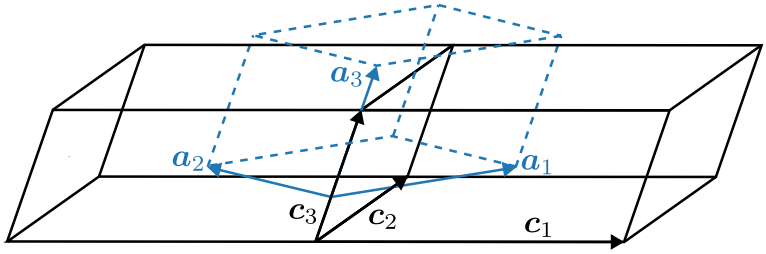

Figure 6.2: The two choices considered for the unit cell of the C-centered monoclinic structure. Conventional (primitive) basis vectors are indicated in black (blue). The conventional unit cell is marked by solid black lines, while the primitive cell is dashed blue.

Similarly, `shiftUC` describes the shift (p_1, p_2, p_3) of the DFT unit cell's origin $\boldsymbol{O}_{DFT}$ with respect to the origin of the user's cell $\boldsymbol{O}_c$:

$$\boldsymbol{O}_{DFT} = \boldsymbol{O}_c + (p_1\ p_2\ p_3) \cdot (\boldsymbol{c}_1\ \boldsymbol{c}_2\ \boldsymbol{c}_3)^T \tag{6.2}$$

In order to illustrate the use of these keywords, we work out the example of the C-centered monoclinic structure. Let us suppose the DFT cell is defined by the vectors $\{\boldsymbol{c}_1, \boldsymbol{c}_2, \boldsymbol{c}_3\}$ in Fig. 6.2, but the user wants the traces in the cell delimited by $\{\boldsymbol{a}_1, \boldsymbol{a}_2, \boldsymbol{a}_3\}$. The relation between both bases is the following:

$$\begin{aligned}
\boldsymbol{c}_1 &= \boldsymbol{a}_1 + \boldsymbol{a}_2, \\
\boldsymbol{c}_2 &= -\boldsymbol{a}_1 + \boldsymbol{a}_2, \\
\boldsymbol{c}_3 &= \boldsymbol{a}_3.
\end{aligned}$$

Notice also that the origins of both cells are related by the shift $0.3\boldsymbol{c}_3$. Then, the keywords `refUC` and `shiftUC` should be used with arguments

```
-refUC=1,1,0,-1,1,0,0,0,1 -shiftUC=0,0,0.3
```

When a basis transformation is applied, the lattice vectors of both and symmetry operations will be printed for both settings. For instance, the following lines illustrate the symmetry operations (only identity and inversion) printed by the code for the example of a crystal in the C-centered structured worked out above:

```
Space group C2/m (# 12) has 4 symmetry operations

###  1
rotation : |  1   0   0 |     rotation : |  1   0   0 |
           |  0   1   0 |       (refUC)  |  0   1   0 |
           |  0   0   1 |                |  0   0   1 |
translation          :  [   0.0000   0.0000   0.0000 ]
translation (refUC) :  [   0.0000   0.0000   0.0000 ]
axis: [0. 0. 1.] ; angle =  0 , inversion : False

###  3
rotation : | -1   0   0 |     rotation : | -1   0   0 |
           |  0  -1   0 |       (refUC)  |  0  -1   0 |
           |  0   0  -1 |                |  0   0  -1 |
translation          :  [   0.0000   0.0000   0.0000 ]
translation (refUC) :  [   0.0000   0.0000   0.6000 ]
axis: [0. 0. 1.] ; angle =  0 , inversion : True
```

Let us comment on the role played by the cell transformation when the user wants to identify the irreps of little groups. This identification in performed by calculating the traces of symmetry operations and matching them to the characters of irreps read from a set of reference tables included in the code. This reference characters are defined for a particular choice of unit cell, dubbed **conventional cell**. Therefore, *IrRep* must get to know the transformation to the conventional cell in order to assign little-group irreps to bands.

The transformation to the conventional cell can be passed to *IrRep* via the input parameters `refUC` and `shiftUC`. Alternatively, *IrRep* will take the charge of determining the transformation automatically if the user sets the parameter `-searchcell`, instead of `refUC` and `shiftUC`.

6.1.2 Determination of the space group

The next step after parsing DFT data files is to determine the space group. Basis vectors and atomic positions are for that passed to the Python library *spglib* [128], whose routine `get_symmetry_dataset` gives the space group's number and symbol. This function also returns the coset representatives of the decomposition of the space group with respect to the translation subgroup [see Eq. (4.25)]. At this point, if the flag `onlysym` in Tab. **6.1** was set, *IrRep* prints the crystal structure and aforementioned coset representatives and then stops. This utility can be useful for VASP even before running the DFT calculation to make sure that the configuration described in POSCAR really matches the assumed space group.

6.1.3 Reading wave functions

In VASP, Abinit and QE, eigenstates $|\psi_{n\boldsymbol{k}}\rangle$ of $H(\boldsymbol{k})$ are expanded in a basis of plane waves $|\boldsymbol{k}+\boldsymbol{G}\rangle$:

$$|\psi_{n\boldsymbol{k}}\rangle = \sum_{\boldsymbol{G}} C_{n\boldsymbol{k}}(\boldsymbol{G})\,|\boldsymbol{k}+\boldsymbol{G}\rangle\,, \tag{6.3}$$

where the sum runs over all the reciprocal lattice vectors $\boldsymbol{G}$ whose energy is smaller than a cutoff, i.e. $\hbar^2(\boldsymbol{k}+\boldsymbol{G})^2/2m_e < E_{\text{cut}}$. The cutoff coincides with the value indicated by the user if a value for `Ecut` in Tab. **6.1** was set in the CLI; otherwise, it will be the cutoff used in the DFT calculation. After testing the code with different systems, we have noticed that usually a value $E_{\text{cut}} \sim 50$ eV yields accurate results, since the most dominant coefficients in Eq. (6.3) correspond to short $\boldsymbol{G}$. After the application of the cutoff, the eigenstates $|\psi_{n\boldsymbol{k}}\rangle$ are normalized.

If the DFT calculation ran with PAW pseudopotentials [129–131], the expansion Eq. (6.3) gives the smooth pseudo-wavefunctions $|\tilde{\psi}_{n\boldsymbol{k}}\rangle$, which are related to the all-electron wavefunctions $|\psi_{n\boldsymbol{k}}\rangle$ by a linear transformation $|\psi_{n\boldsymbol{k}}\rangle = \mathcal{T}\,|\tilde{\Psi}_{n\boldsymbol{k}}\rangle$. Since $|\tilde{\psi}_{n\boldsymbol{k}}\rangle$ and $|\psi_{n\boldsymbol{k}}\rangle$ transform under symmetry operations in the same way, *IrRep* works with the pseudo-wavefuncions.

In the Wannier90 input files (`UNK*`) the wavefunctions are written on a real-space grid. In that case we perform a fast Fourier transform (FFT) to obtain the coefficients $C_{n\boldsymbol{k}}(\boldsymbol{G})$ of Eq. (6.3).

6.1.4 Calculation of traces

Inequivalent irreps have different characters. In this sense, the character is a feature that identifies unambiguously the irrep. Therefore, the identification of irreps of bands is preceded in *IrRep* by the calculation of the traces of symmetry operations.

We will now describe the calculation of the expectation value of symmetries in the little group of $\boldsymbol{k}$. Since the transformation of $|\psi_{n\boldsymbol{k}}\rangle$ under translations is trivial, we need only iterate through the coset representatives $g_i^{\boldsymbol{k}}$ in Eq. (4.36). Let us consider a coset representative $g = \{R|\boldsymbol{v}\} \in G_{\boldsymbol{k}}$; the calculation of the expectation value $\langle\psi_{n\boldsymbol{k}}|g|\psi_{n\boldsymbol{k}}\rangle$ depends on whether the DFT calculation was performed on scalar or spinor wave functions:

(i) **Scalar wavefunctions**:

$$\langle\psi_{n\boldsymbol{k}}|g|\psi_{n\boldsymbol{k}}\rangle = \sum_{\boldsymbol{G}\boldsymbol{G}'} C^*_{n\boldsymbol{k}}(\boldsymbol{G}')C_{n\boldsymbol{k}}(\boldsymbol{G})\,\langle\boldsymbol{k}+\boldsymbol{G}'|g|\boldsymbol{k}+\boldsymbol{G}\rangle\,. \tag{6.4}$$

From the transformation property of plane-waves,

$$g\,|\boldsymbol{k}+\boldsymbol{G}\rangle = e^{-i(R\boldsymbol{k}+R\boldsymbol{G})\cdot\boldsymbol{v}}\,|R\boldsymbol{k}+R\boldsymbol{G}\rangle\,, \tag{6.5}$$

together with their orthogonality property,

$$\langle \boldsymbol{k}+\boldsymbol{G}'|\boldsymbol{k}+\boldsymbol{G}\rangle = \delta_{\boldsymbol{G}',\boldsymbol{k}-\boldsymbol{k}'+\boldsymbol{G}}, \tag{6.6}$$

it follows that Eq. (6.4) is reduced to:

$$\langle \psi_{n\boldsymbol{k}}|g|\psi_{n\boldsymbol{k}}\rangle = \sum_{\boldsymbol{G}} C^*_{n\boldsymbol{k}}(R\boldsymbol{k}-\boldsymbol{k}+R\boldsymbol{G})C_{n\boldsymbol{k}}(\boldsymbol{G}) \tag{6.7}$$

(ii) For **spinor wavefunctions** $|\psi_{n\boldsymbol{k}}\rangle = (\,|\psi^{\uparrow}_{n\boldsymbol{k}}\rangle\ |\psi^{\downarrow}_{n\boldsymbol{k}}\rangle)^T$ the expected value involves summing over spin indices:

$$\langle \psi_{n\boldsymbol{k}}|g|\psi_{n\boldsymbol{k}}\rangle = \sum_{\sigma\sigma'} S_{\sigma\sigma'}(R)\,\langle \psi^{\sigma}_{n\boldsymbol{k}}|g|\psi^{\sigma'}_{n\boldsymbol{k}}\rangle\,, \tag{6.8}$$

where $\langle \psi^{\sigma}_{n\boldsymbol{k}}|g|\psi^{\sigma'}_{n\boldsymbol{k}}\rangle$ is computed by means of Eq. (6.7) and $S(R)$ is an SU(2) matrix corresponding to R.

Once the expectation value is computed, *IrRep* adds the values obtained for degenerate eigenstates (flag `degenThresh` in Tab. **6.1**). Each of these sums is the trace $\chi^{\boldsymbol{k}}(g)$ of a matrix $D_{\boldsymbol{k}}(g)$ belonging to the representation $D_{\boldsymbol{k}}$ defined in the subspace of degenerate eigenstates.

6.1.5 Identification of irreducible representations

The code identifies the representation $D_{\boldsymbol{k}}$ corresponding to each set of degenerate states by means of the magic formula in Eq. (4.12):

$$m^{\boldsymbol{k}}_i = \frac{1}{||\bar{G}_{\boldsymbol{k}}||}\sum_{j=1}^{M}[\chi^{\boldsymbol{k}}(g^{\boldsymbol{k}}_j)]^*\chi^{\boldsymbol{k}}_i(g^{\boldsymbol{k}}_j). \tag{6.9}$$

The characters $\chi^{\boldsymbol{k}}_i$ of irreps of $G_{\boldsymbol{k}}$ in this formula were obtained from the BCS [96] and are provided with the *IrRep* module. As it is indicated in Fig. **6.1**, *IrRep* will both retrieve the characters of irreps and transform the character $\chi^{\boldsymbol{k}}$ to the conventional cell before applying the magic formula.

Notice that the representation $D_{\boldsymbol{k}}$ might in general if the degeneracy of the corresponding states is accidental. In that case, the multiplicities of at least two irreps will be different from zero.

At this point, *IrRep* will print the non-vanishing multiplicities obtained with the magic formula for each set of degenerate states, together with the character of $D_{\boldsymbol{k}}$. If traces of symmetry operations in the conventional cell differ from those in DFT cell, they will be printed for both settings.

By default, the procedure is performed for all the bands calculated by the DFT code. Nevertheless, the user can set values for `IBstart` and `IBend` in order to consider only bands in the range [`IBstart`,`IBend`]. This can be used to noticeably shorten the calculation time. Moreover, for the selected set of bands, the smallest direct and indirect gaps with respect to higher bands will be printed. For centrosymmetric crystals, the number of inversion-eigenvalue inversions (band inversions) and the $\mathbb{Z}_2$ index [8, 18] will also be calculated and written. In Sec. 6.2.1, we show an example of the output generated by *IrRep* where all these features are represented.

6.1.6 Separation by symmetry eigenvalues

When writing the traces or the multiplicities of irreps, the code can separate the states by their eigenvalues with respect to a certain symmetry operation. The index of the symmetry must be specified via the keyword `isymsep` for that (see Tab. **6.1**). The energies will also be written in a file according to this separation. This data turns out to be useful if the DFT calculation was done for an ordered set of $\boldsymbol{k}$-points following a certain path in the BZ, as it allows for the study to the role of symmetries in the protection of band crossings [120].

IrRep also contains routines to calculate the Zak phase and Wannier charge centers of a given set of bands (see keys ZAK and WCC in Tab. **6.1**). These functionalities work stably only for calculations employing norm-conserving pseudopotentials, and `Ecut` should not be specified in the command line – the DFT cutoff will be used. With the PAW method, due to the lack of consideration of the all-electron wavefunction, the results for symmetry separation and ZAK phase might be unreliable.

6.1.7 Writing the output

Finally, *IrRep* will return its output to the user. The output will be written in the CLI and it can be captured in plain text format. The output will also be printed in a JSON format file called `irrep-output.json` from which it can be easily parsed by downstream codes.

Furthermore, *IrRep* also writes a file `trace.txt`, which can be passed directly to the program *CheckTopologicalMat* of BCS [30, 104], in order to get information about (physical) elementary band representations and symmetry-based indicators [25, 28, 29] to diagnose the band topology. Owing to this feature, the combination between *IrRep* and this BCS software forms a powerful toolkit for the diagnosis and classification of topological bands in crystals.

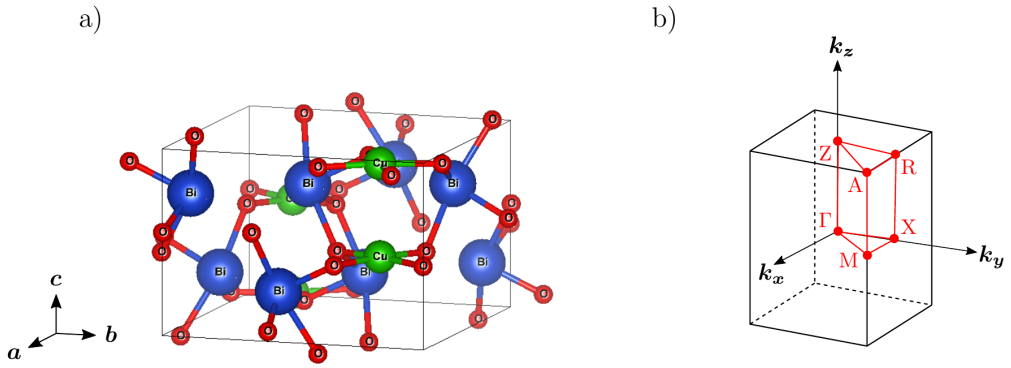

Figure 6.3: Crystal structure of $CuBi_2O_4$. (a) Unit cell, with Cu, Bi and O atoms in green, blue and red, respectively. (b) BZ and irreducible BZ (red), with high-symmetry points.

6.2 Example materials

In this section, we present the application of *IrRep* to two material examples, with different symmetries and topology, and analyzed by different DFT codes. With these examples, we cover the main functionalities of the code and also the subtlety related to the transformation between primitive and conventional cells. Input files to generate the DFT data and input files that may be used to run *IrRep* for these examples can be found in the Github repository of the code [132].

6.2.1 Irreducible representations in $CuBi_2O_4$

First, we show the application of *IrRep* to $CuBi_2O_4$. This material has been observed in a tetragonal paramagnetic crystal structure characterized by the non-symmorphic space group P4/ncc (No. 130) [133, 134]. Its crystal structure and BZ are shown in Fig. **6.3**.

An interesting aspect of $CuBi_2O_4$ is found in reciprocal space: the little group of point A=$(1/2, 1/2, 1/2)$, in the corner of the BZ, has only one (double-valued) IR. The dimension of this irrep is 8, which leads to an unusually large 8-fold degeneracy of the energy levels. This feature makes $CuBi_2O_4$ promising for the realization of high-degeneracy unconventional fermions [112, 135]. Moreover, due to the fact that the number of electrons in the unit cell is not a multiple of 8, this IR forces $CuBi_2O_4$ to be a filling-enforced semimetal.

We have calculated the band structure of $CuBi_2O_4$ with Abinit, both treating spin trivially (scalar calculation) and including spin-orbit corrections (spinor calculation). A plane-wave cutoff of 500 eV and cold smearing [136] were used in the calculation. The BZ was sampled with a grid of $5 \times 5 \times 7$. Lattice parameters and atomic positions were

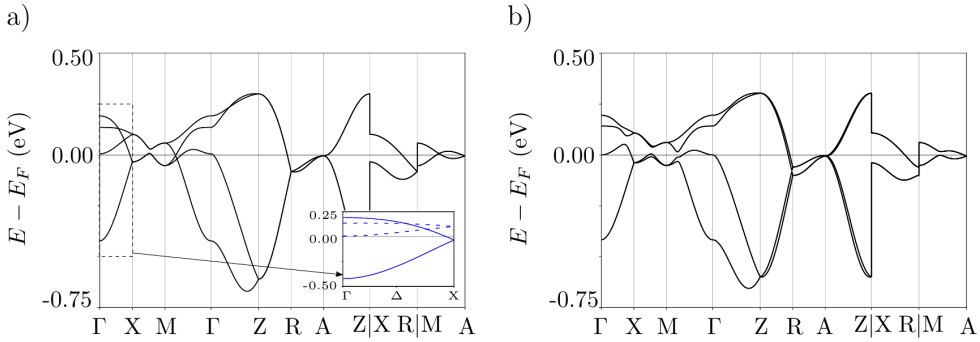

Figure 6.4: Band structure of $CuBi_2O_4$ (a) without SOC included. Inset: bands in line Δ (connecting Γ to X) separated according to the eigenvalue of symmetry $\{m_x|1/2, 0, 1/2\}$ in the little group: solid (dashed) corresponds to eigenvalue -1 $(+1)$. (b) Band structure of $CuBi_2O_4$ with SOC included.

Γ	X	M	Z	R	A
$\Gamma_4^+ \oplus \Gamma_2^+ \oplus \Gamma_4^- \oplus \Gamma_2^-$	$X_2 \oplus X_1$	$M_4 \oplus M_3$	$2Z_1$	R_1R_2	A_3A_4
$2\bar{\Gamma}_6 \oplus 2\bar{\Gamma}_8$	$2\bar{X}_3\bar{X}_4$	$2\bar{M}_5$	$2\bar{Z}_5\bar{Z}_7$	$\bar{R}_4\bar{R}_4 \oplus \bar{R}_3\bar{R}_3$	$\bar{A}_5\bar{A}_5$

Table 6.3: Irreps at maximal $\boldsymbol{k}$-points of the partially-filled set of bands of $CuBi_2O_4$. In the second (third) row, irreps of the calculation without (with) SOC included are listed.

taken from the topological quantum chemistry database of materials [25, 30, 104]. The exchange-correlation term was approximated through General Gradient Approximation, in the Perdew Burke Ernzerhof [137] parametrization and PAW pseudopotentials were taken from Pseudo Dojo database [138, 139]. *Ab initio* band structures are shown in Fig. **6.4**. Output files of *IrRep* are available in the `examples` folder of *IrRep*'s official Github repository [132].

In the rest of the analysis, we focus on the partially-filled isolated set of bands cut by the Fermi level. Irreps of wave functions at maximal $\boldsymbol{k}$-points can be calculated by running the following lines (case without SOC):

```
irrep -code=abinit -kpnames=GM,X,M,Z,R,A
      -Ecut=100 -fWFK=CuBi2O4-spinor_WFK
      -IBstart=289 -IBend=296 -EF=auto
```

The set of irreps obtained in this way are written in Tab. **6.3**. The following lines illustrate part of the output for the point R$= (0, 1/2, 1/2)$ – even though the little group of R contains many coset representatives, only two of them (represented by indices 1 and 6) are shown here for brevity.

```
k-point   5 : [0.   0.5 0.5] (in DFT cell)
              [0.   0.5 0.5] (after cell trasformation)

number of states : 8

Energy |   degeneracy   |  irreps   | sym. operations
       |                |           |          1        6
-0.10  |        4       | -R4(2.0)  |   4.0+0.0j    0.0+0.0j
-0.06  |        4       | -R3(2.0)  |   4.0+0.0j    0.0+0.0j
inversion is # 9
number of inversions-odd Kramers pairs :  2
Gap with upper bands :  2.02
```

As we explained in Sec. 5, analyzing these set of irreps within the framework of TQC could allow us to gain deep insight into the chemistry of the bands and the system. The irreps in Tab. **6.3** are consistent with the EBR induced from Wannier functions sitting in Wyckoff position 4c: $(B \uparrow G)_{4c}$ in the case without SOC, $({}^1\bar{\mathrm{E}}_2^2\bar{\mathrm{E}}_2 \uparrow G)_{4c}$ with SOC. These bands are hence induced from Wannier functions transforming under the site-symmetry group as a combination of $\mathrm{d}_{x^2-y^2}$ and d_{xy} orbitals.

Let us illustrate also the separation of bands in terms of the eigenvalues of a particular symmetry operation. Notice that the little group of every $\boldsymbol{k}$-point in the line Δ (which connects Γ to X) contains the glide symmetry $g_x = \{m_x|1/2, 0, 1/2\}$. As a result, wave functions of bands in this line can be chosen to be eigenstates of g_x and can thus be distinguished by their eigenvalue under this symmetry. *IrRep* can separate bands in terms of this eigenvalue by running it with the option `isymsep`= 14, which is the index corresponding to g_x:

```
irrep -code=abinit -Ecut=100 -fWFK=CuBi2O4-scalar_WFK
    -IBstart=145 -IBend=148 -isymsep=13
```

The index of g_x can be derived beforehand by running the option `onlysym` (see Tab. **6.1**). The result is shown in the inset of Fig. **6.4**(a), where bands with eigenvalue -1 $(+1)$ of g_x are indicated in solid (dashed). We conclude from this result that the crossings between dashed and solid bands are protected by g_x and thus cannot be gapped out without breaking this symmetry. Such criteria can be used to systematically study symmetry protected band crossings [120].

6.2.2 Bismuth: high order topological insulator

In this example, we will present the calculation of $\mathbb{Z}_2$ and $\mathbb{Z}_4$ indices with *IrRep*. For that, we will work with a particularly interesting and well-known material: bismuth.

In the presence of only time-reversal symmetry (TRS), an insulator can belong to either the trivial or the topological phase. The system cannot undergo a transition from one phase to the other if the gap is not closed or TRS is not broken in the process. In

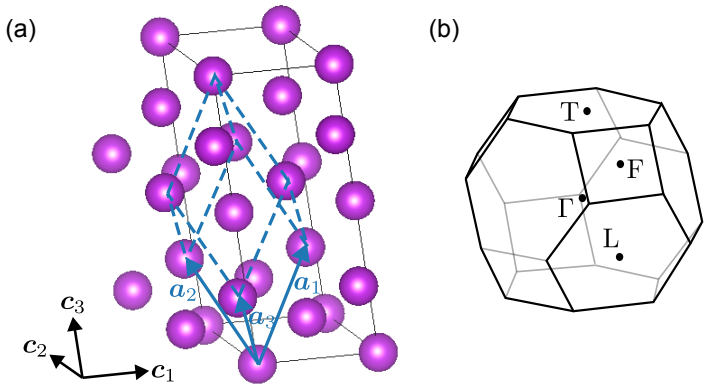

Figure 6.5: a) Crystal structure of Bi in space group R$\bar{3}m$. Black lines delimit the conventional unit cell, whose basis vectors are $\{\boldsymbol{c}_i\}_{i=1,2,3}$. Blue lines delimit the primitive unit cell used in the DFT calculation. b) Brillouin zone corresponding to the primitive cell and TRIM (one from each star of $\boldsymbol{k}$-points).

this spirit, the topology of the system can be characterized by a $\mathbb{Z}_2$ invariant [2, 3, 8], which is -1 (+1) in the topological (trivial) phase. With inversion, the $\mathbb{Z}_2$ invariant can be calculated by multiplying the inversion eigenvalues of Kramers pairs of occupied bands at all time-reversal invariant momenta (TRIM) [18]. In the topological case, we say that the system has a band-inversion.

Crystal symmetries may enrich the topology of time-reversal invariant insulators, giving access to new phases, some of which can not be detected by the $\mathbb{Z}_2$ index. This is the case for bismuth in space group R$\bar{3}m$: the $\mathbb{Z}_2$ index has value +1, which means that the ground state corresponding to the occupied bands in Bi is a trivial insulator as per its $\mathbb{Z}_2$ index, according to the discussion above. However, in Ref. [24] it was shown that the ground state belongs to a higher-order topological phase, characterized by a $\mathbb{Z}_4$ index equal to 2. Here, we will reproduce with *IrRep* this analysis.

The bands of Bi calculated with VASP for the primitive unit cell are shown in Fig. **6.6**a. The calculation included spin-orbit corrections and was performed with a cutoff of 520 eV for the plane-wave basis, together with a Gaussian smearing. The BZ was sampled with a grid of $7 \times 7 \times 7$ $\boldsymbol{k}$-points. We used PBE prescription as an approximation for the exchange-correlation term and PAW pseudopotentials [137]. Fig **6.6**b shows the bands separated by eigenvalues of the three-fold rotation C_{3z} using *IrRep*'s option `isymsep`.

Space group R$\bar{3}m$ (No. 166) belongs to the rhombohedral family, in which conventional and primitive unit cells do not match [see Fig. **6.5**a]. Consequently, *IrRep* will need the transformation to the conventional cell in order to identify the irreps of energy levels. Even though we could let the code calculate `refUC` and `shiftUC` automat-

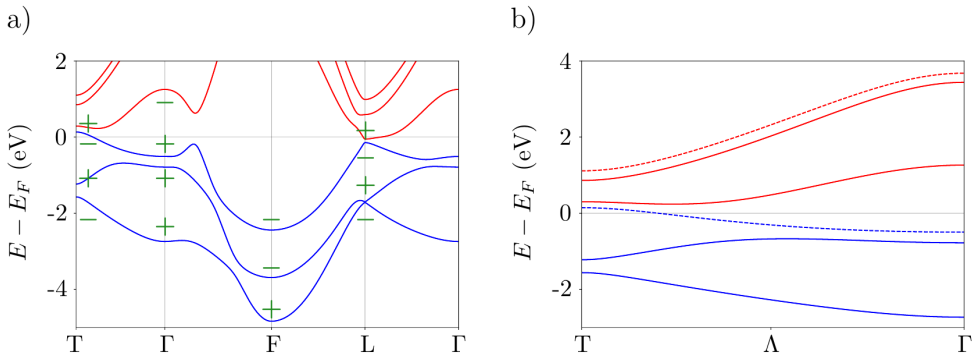

Figure 6.6: Band structure of Bi in space group R$\bar{3}m$. Since blue and red bands do not touch, we will ignore the electron-hole pockets and speak of occupied (blue) and unoccupied (red) bands. (a) Inversion eigenvalues at TRIM are indicated in green. (b) Bands along C_{3z}-invariant line Λ, which connects T to Γ; solid and dashed bands have C_{3z} eigenvalues -1 and $\exp(\pm i\pi/3)$, respectively.

ically, we will set them manually to illustrate them on a practical example. The relation between the basis vectors of the primitive (DFT) and conventional cells [expressed by Eq. (6.1)] is the following form:

$$(\boldsymbol{c}_1, \boldsymbol{c}_2, \boldsymbol{c}_3)^T = \begin{bmatrix} 1 & -1 & 0 \\ 0 & 1 & -1 \\ 1 & 1 & 1 \end{bmatrix} (\boldsymbol{a}_1, \boldsymbol{a}_2, \boldsymbol{a}_3)^T. \tag{6.10}$$

Accordingly, we pass this information to *IrRep* by specifying the parameter `-refUC=1,-1,0,0,1,-1,1,1,1` in the CLI. There is no need to specify `shiftUC`, as the origins of both unit cells sit at the same position. The following lines show how *IrRep* prints a description of symmetry operations, in particular the 3-fold rotation $\{C_{3z}|\mathbf{0}\}$, in the settings before and after applying the transformation of the unit cell:

```
### 2

rotation : |  0   0   1 |     rotation : |  0  -1   0 |
           |  1   0   0 |      (refUC)   |  1  -1   0 |
           |  0   1   0 |                |  0   0   1 |

spinor rot.          : | 0.500-0.866j -0.000-0.000j |
                       | 0.000-0.000j  0.500+0.866j |
spinor rot. (refUC)  : | 0.500-0.866j -0.000-0.000j |
                       | 0.000-0.000j  0.500+0.866j |

translation          :  [   0.0000   0.0000   0.0000 ]
```

```
translation (refUC) :  [   0.0000   0.0000   0.0000 ]

axis: [0. 0. 1.] ; angle = 2/3 pi, inversion : False
```

To make sure that the transformation is correct, one has to check whether matrices and translation vectors after the change of basis match with those in the table file of the corresponding space group. Alternatively, they can be compared to matrices and translations in the GENPOS application of the BCS [97].

The next step is to calculate the irreps of occupied bands at maximal $\boldsymbol{k}$-points (Tab. **6.4**). For that, we call *IrRep* with the keywords written in the following lines:

```
irrep -spinor -code=vasp -kpnames=T,GM,F,L -Ecut=50 -EF=auto
      -refUC=1,-1,0,0,1,-1,1,1,1 -IBstart=5 -IBend=10
```

T	Γ	F	L
$\bar{\mathrm{T}}_9 \oplus \bar{\mathrm{T}}_8 \oplus \bar{\mathrm{T}}_6\bar{\mathrm{T}}_7$	$2\bar{\Gamma}_8 \oplus \bar{\Gamma}_4\bar{\Gamma}_5$	$\bar{\mathrm{F}}_3\bar{\mathrm{F}}_4 \oplus \bar{\mathrm{F}}_5\bar{\mathrm{F}}_6 \oplus \bar{\mathrm{F}}_5\bar{\mathrm{F}}_6$	$\bar{\mathrm{L}}_5\bar{\mathrm{L}}_6 \oplus \bar{\mathrm{L}}_3\bar{\mathrm{L}}_4 \oplus \bar{\mathrm{L}}_5\bar{\mathrm{L}}_6$

Table 6.4: Irreps at maximal $\boldsymbol{k}$-points calculated with *IrRep* for the last 6 occupied bands of Bi. In each $\boldsymbol{k}$-point, irreps are written from left to right in ascending energy order, e.g., $\bar{\mathrm{T}}_6\bar{\mathrm{T}}_7$ is higher in energy than $\bar{\mathrm{T}}_8$.

With the knowledge of the IRs and their inversion eigenvalues [see Fig. **6.6**(a)], we conclude that the total number of Kramers pairs with -1 inversion eigenvalues in the occupied bands is even, thus the $\mathbb{Z}_2$ index is $z_2 = +1$. However, there are two band inversions between Γ and T that the $\mathbb{Z}_2$ invariant cannot detect, as they involve a pair of inversion-odd eigenvalues which cancel each other upon considering the product of such eigenvalues. Indeed, this double band-inversion leads to the $\mathbb{Z}_4$ invariant $z_4 = 2$, since the number of Kramers pairs of -1 inversion eigenvalues is equal to 2 mod 4. This means that Bi is a higher-order topological insulator (HOTI) [24]. The value of the $\mathbb{Z}_4$ index and number of -1 inversion eigenvalues are, by default, calculated and printed by *IrRep*; in the following line, we show the way in which they are printed by the code, together with information about the direct and general gaps:[1]

```
Number of inversions-odd Kramers pairs IN THE LISTED KPOINTS: 6  Z4=2
Minimal direct gap: 0.08857033154551353  eV
Indirect  gap: -0.1886089499035215  eV
```

6.3 Publications using *IrRep*

Currently, the article where we published *IrRep* has been cited in another 9 articles [140–148]. However, it might have been used without been cited in other works, as the

[1] Here the gap refers only to the maximal $\boldsymbol{k}$-points included in the calculation. In general, the real gap might be smaller (and even might close) at some arbitrary point away from high-symmetry points.

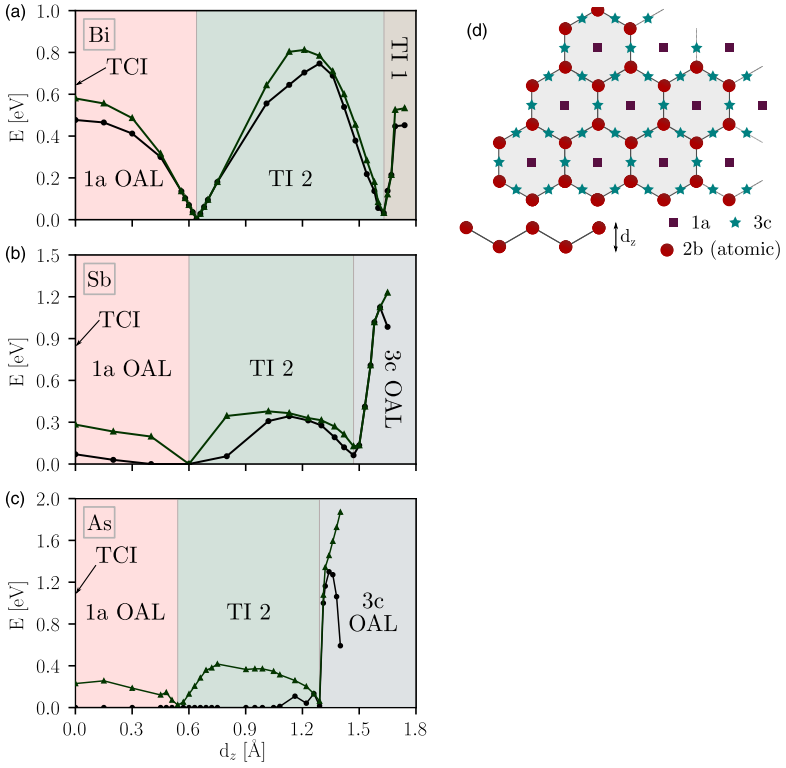

Figure 6.7: Evolution of the bulk gap in terms of buckling parameter for (a) bismuthene, (b) antimonene and (c) arsenene. (d) Buckled-hexagonal crystal structure considered for the monolayers. Source: [121].

code was made available for use before its article was published. In this section, we will comment on the use of *IrRep* in some of the collaborations we have hold while we were working on this thesis.

6.3.1 Fractional corner charges in spin-orbit coupled crystals, by F. Schindler *et al.* [121]

This work was developed in collaboration with the group of Titus Neupert, from the University of Zurich. All corner charge distributions that might be hosted by 2D spinful crystals in any point group are identified in project. The correspondence between every corner charge configuration and the topology of the bulk is also established, based on Wilson loop invariants and symmetry-based indicators of topology [28]. In addition, formulas for the calculation of corner charges from symmetry eigenvalues of Bloch wave functions are provided in the text. These framework is then tested on buckled arsenic

and antimony monolayers.

IrRep enters this work in the numerical analysis of bismuth, antimony and arsenic monolayers. These materials share a hexagonal crystal structure similar to graphene's honeycomb lattice, but the two ions in the primitive unit cell are at different height (buckled), as it is shown in Fig. **6.7**(d). The single-particle bulk-electronic structure and Bloch states at maximal $\boldsymbol{k}$-points of these compounds were obtained via *VASP* [60], within the DFT framework. As the buckling parameter is varied by means of in-plane strain, the materials undergo phase transitions accompanied by the closing and reopening of the bulk gap. *IrRep* was then used to calculate the irreps and symmetry eigenvalues of valence bands in each of the gapped phase. The knowledge about irreps was used to identify each topological phase, according to the criterion introduced in Sec. 5.5 and Eq. (5.21). The eigenvalues of symmetry operations served as data to calculate the corner charges for the crystals in symmetry-respecting open geometries.

6.3.2 Novel family of topological semimetals with butterflylike nodal lines, by X. Zhou *et al.* [107]

This article is the result of a collaboration held with the group of Nicholas Kioussis, from the California State University.

A specific family of semimetals hosting exotic nodal lines is identified in this work. The nodal lines of this materials consist on concentric intersecting coplanar ellipses (CICE), and are a manifestation of symmetry-protected crossings of bands happening in certain planes of the BZ. Moreover, the space groups of crystals that might realize these nodal lines are determined by identifying the symmetries required to protect the corresponding band crossings. Regarding the practical realization of CICEs, a model exhibiting such nodal structures is provided in the text. In addition, ZrX_2 (X=P,As), Tl_2GeTe_5, CYB_2 and Al_2Y_3 are proposed as candidates to host these nodal lines.

As it is natural, *IrRep* was used in the analysis of the material candidates. The band structures and Bloch states at maximal $\boldsymbol{k}$-points were obtained via DFT first-principle calculations for these materials. As Fig. **6.8**(b) and (e) show for $ZrAs_2$ and Tl_2GeTe_5, these band structures seem to display the band crossings which give raise to the CICE. We used *IrRep* to rule out the possibility for having small gaps and corroborate that the bands do cross each other. For that, we first determined with *IrRep* the irreps at the maximal $\boldsymbol{k}$-points connected by the symmetry lines where the crossings take place. We then determined by subduction the irreps of bands at the symmetry lines. Two bands can cross each other at a point $\boldsymbol{k}$ of the line only if their wave functions transform as different irreps of the little group of $\boldsymbol{k}$.

This criterion follows from Wigner's theorem [introduced in Secs. 4.2 and 4.3.3]: If both bands had in correspondence the same irrep, the block(s) $H(\boldsymbol{k})$ of the Hamiltonian corresponding to this irrep would contain off-diagonal elements for a (general) basis of states adapted to the symmetry of the irrep. The presence of these off-diagonal

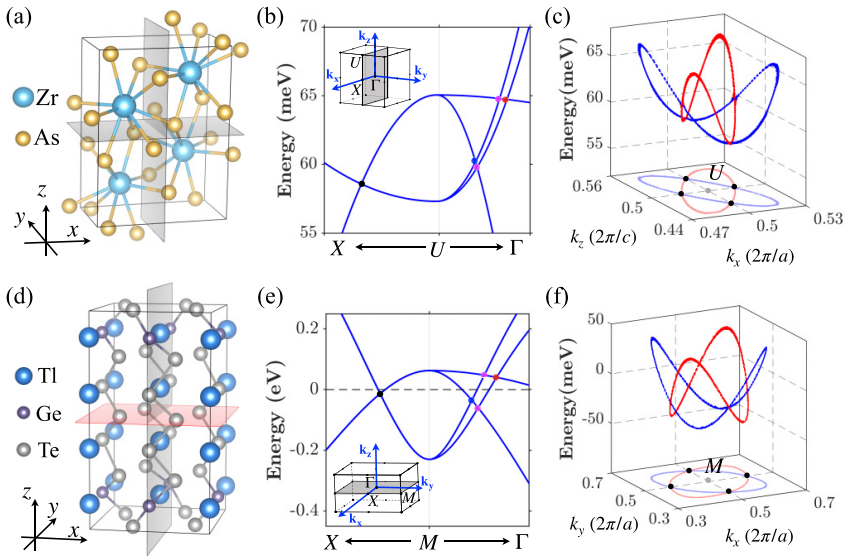

Figure 6.8: Evolution of the bulk gap in terms of buckling parameter for (a) bismuthene, (b) antimonene and (c) arsenene. (d) Buckled-hexagonal crystal structure considered for the monolayers. Source: [107].

components forces the eigenvalues of $H(\boldsymbol{k})$ to be different[2].

6.3.3 Prediction of double-Weyl points in the iron-based superconductor $CaKFe_4As_4$, by N. Heinsdorf *et. al.*

This work was developed in collaboration with the groups of Roser Valentí (Goethe University, in Frankfurt), Rafael M. Fernandes (University of Minnesota) and Cristian D. Batista (University of Tennessee Knoxville).

This work puts forward the possibility for realizing double Weyl points in $CaKFe_4As_4$, based on a methodological approach which consists of the combination of symmetry analysis of bands, *ab initio* calculations and low-energy modeling. In fact, depending on the relative magnitudes of the magnetic field, crystal potential and SOC, Weyl points with different charges could arise in the band structure.

The work begins with an *ab initio* based analysis of the suitability of $CaKFe_4As_4$ to double-Weyl points. In particular, the effect of SOC on the degeneracies of bands is studied in terms of symmetry representations. Fig. **6.9**(a)-(b) show schematically the effect of SOC observed in the *ab initio* simulations. The role of *IrRep* in this work is the

[2]Whether such off-diagonal terms are present of not is a matter of the microscopic parameters of the Hamiltonian. Their absence requires fine-tuning of these parameters, which is unrealistic within the DFT framework and in actual materials

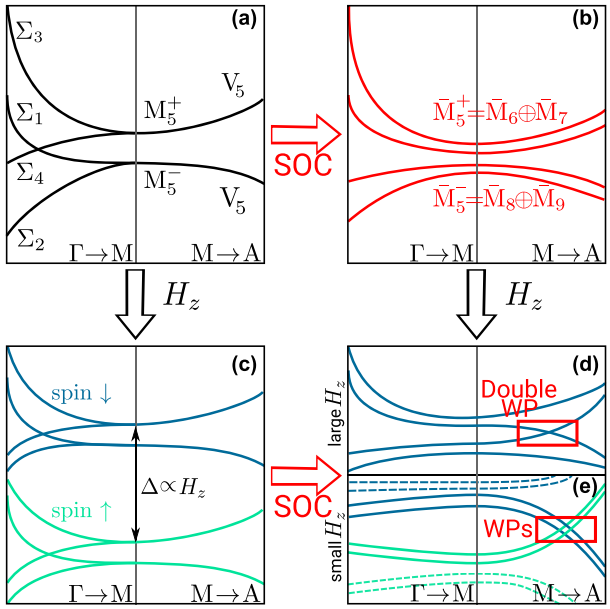

Figure 6.9: Evolution of the bulk gap in terms of buckling parameter for (a) bismuthene, (b) antimonene and (c) arsenene. (d) Buckled-hexagonal crystal structure considered for the monolayers. Source: [107].

calculation of irreps of bands on the $\boldsymbol{k}$-points Γ, M $(\pi, \pi, 0)$ and A (π, π, π) of the BZ, both with and without SOC. This data was then interpreted in terms of the capacity of SOC to split bands.

6.4 Conclusion

IrRep is a Python code for the calculation of irreducible representations of DFT calculated bands at high-symmetry points. It is a powerful tool for the detection and classification of topological sets of bands and materials, applicable with calculations performed both with or without SOC and using unit cells that might be non-conventional. Its structure keeps the implementation of interfaces to plane-wave DFT codes simple; currently, it is compatible with VASP, Abinit, Quantum Espresso and any code that has an interface to Wannier90 (which covers most of the popular DFT codes). Additionally, routines for separating bands based on an eigenvalue of certain symmetry operation are included. *IrRep* can be freely downloaded from `https://github.com/stepan-tsirkin/irrep` and/or installed with `pip` and its official webpage can be found in `http://irrep.dipc.org/`; the repository also contains examples, including the analysis of $CuBi_2O_4$ that we have presented in this work to

illustrate the utility of the code.

Part II

Topology of strongly-correlated heavy-fermion insulators

7 Valence fluctations in heavy-fermion materials

Heavy-fermion materials, first discovered in 1965 [149], are widely known for displaying high density of states close to the Fermi level, and for their electrons behaving as slow particles. Since they often lie on the frontier between magnetic and non-magnetic systems, they have usually been considered as testbed to understand the interplay between magnetic and electronic phenomena in crystals. In particular, heavy-fermion systems became a typical platform for the study of Kondo physics, as they contain the ingredients present in Anderson's microscopic model for the formation of magnetic moments in crystals [150]. Moreover, they have attracted considerable attention as platforms to host spintronic applications or high-temperature superconductivity [39].

The interesting properties of heavy-fermion materials stem from their chemical composition. They contain rare-earth or actinide[1] elements, whose valence electrons populate spatially-localized f-orbitals. Electrons suffer from strong repulsive interactions in these orbitals, which influences many properties of heavy-fermion materials. The effect of interactions on the valence fluctuations of lanthanide ions is especially important, as this property turns out to be crucial for the understanding of the electronic features of the compounds. We will thus dedicate this chapter to describing valence fluctuations in heavy-fermion systems. This will help us to decide in which scenarios could TQC be applied to these materials.

The valence of a lanthinide element in a heavy-fermion compound can be defined as the number of electron in its $4f$-states. On the one hand, we could expect the valence to be stable, as the overlap of these orbitals with those of neighboring ions is small owing to their spatial confinement. On the other hand, the $4f$-shell tends to be close in energy to $5d$-states, which might facilitate transitions of electrons between these shells, and hence

[1] We will focus our discussion on actinide compounds, since the spatial localization is more considerable in $4f$-orbitals than in $5f$-states. This decision can be supported based on difficulties to actually work experimentally with actinides. Anyway, the possibility for actinide materials to display a behavior similar to that discussed in this chapter should not be discarded, in principle.

allow the valence to fluctuate.

The Anderson model [150] is suitable to capture valence fluctuations as it includes all these ingredients. The (minimal) Hamiltonian of the Anderson model can be written in the following form:

$$H = H_{5d-bands} + \sum_{ij,\sigma\sigma'} [V_{i\sigma,j\sigma'}\ d^{\dagger}_{i\sigma} f_{j\sigma'} + \text{h.c.}] + \sum_{i\sigma} E_{i\sigma} f^{\dagger}_{i\sigma} f_{i\sigma} + U \sum_{i} f^{\dagger}_{i\uparrow} f_{i\uparrow} f^{\dagger}_{i\downarrow} f_{i\downarrow}. \quad (7.1)$$

Here, $H_{5d-bands}$ is the independent-electron Hamiltonian for the $5d$-states. $f_{i\sigma}$ ($d_{i\sigma}$) is the operator which annihilates an electron from the $4f$ ($5d$)-orbital labeled by quantum numbers i and spin σ. The third term accounts for the on-site energy of the $4f$-states. V is the matrix describing the hybridization between $4f$ and $5d$-orbitals. Since off-site hoppings between $4f$-orbitals are not included, fluctuations in the valence can only take place through transitions mediated by V. The last term is the **Hubbard interaction**. It accounts for the on-site Coulomb repulsion between electrons by setting a energy penalty U for each $4f$-orbital containing two electrons. The decision for including electron interactions only for the $4f$-states is motivated by the fact that $5d$-orbitals are broader in space.

In order to gain a grasp on how Hubbard interactions can affect the valence, let us focus first on the case of a single impurity with a pair of spinful f-states. Although the Hubbard interaction term has been chosen to be diagonal in the orbital indices in this work, for this discussion it is convenient to consider that it has the form: $U \sum_{ij} f^{\dagger}_{i\uparrow} f_{i\uparrow} f^{\dagger}_{j\downarrow} f_{j\downarrow}$, *i.e.* it adds a penalty every time a pair of electrons is added to the $4f$-shell of a site. In the non-interacting limit ($U = 0$), there is not any restriction on the occupation of an arbitrary site, apart from Pauli's exclusion principle. This means that if we take a snapshot of the site at an arbitrary time, the probability for observing it with no electrons, a spin-up electron, a spin-down electron or two electrons, is identical. All these configurations contribute to the valence of the lanthanide ion. In the strongly interacting case with a large value for U, the configuration where the site hosts two electrons is energetically unfavorable, as it requires paying an energy penalty U. Therefore, only three out of the four possible states of the impurity contribute to the average occupation. The valence is hence constrained by strong-electron interactions.

Let us extend this discussion to the case we are interested in: a crystal containing a periodic arrangement of lanthanide ions. We will now describe qualitatively the evolution of both the chemical potential μ and valence of $4f$-orbitals, in terms of the number of electrons per unit cell n. For that, we denote n_f the average number of electrons (per cell) in the $4f$-orbitals, and we consider first the scenario without hybridization ($V = 0$) illustrated in Fig. **7.1**. Assuming that E_f is above the bottom of the $5d$-bands, μ increases progressively as these states get filled. Meanwhile, $4f$-states remain empty ($n_f = 0$).

When the number n reaches a certain critical value n_{c1}, electrons begin to populate

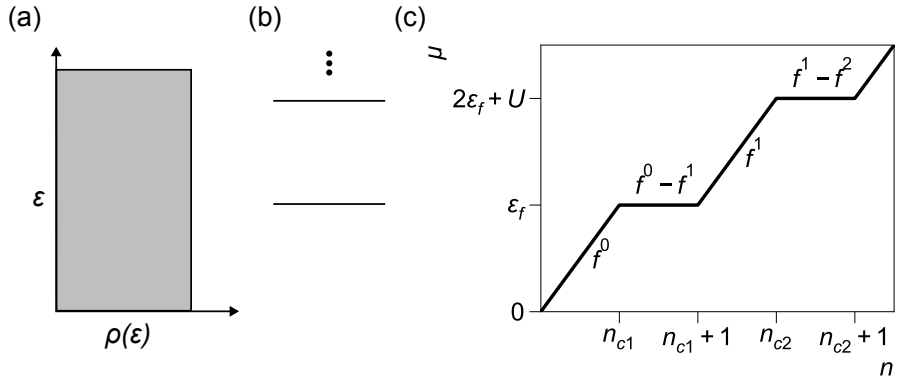

Figure 7.1: Schematic representation of valence fluctuations, for the case without hybridization ($V = 0$). (a) DOS of bands induced from $5d$-orbitals, kept featureless for the sake of simplicity. (b) Energy levels of $4f$-orbitals, at $E_f, 2E_f+U, \ldots$ (c) Evolution of the chemical potential μ as the number of electrons per unit cell n is increased. Plateaus correspond to mixed-valence states, whereas the lines where μ increases correspond to integral-valence configurations.

$4f$-states, while the chemical potential is pinned to $\mu = E_f$ – the system is on the $f^0 - f^1$ plateau in Fig. **7.1**(c). Some of the lanthanide ions host an electron in the $4f$-states and the rest are empty, thus the ionic configuration lies between f^0 and f^1. In other words, the average valence n_f takes a non-integer value $n_f \in (0, 1)$. This is the **mixed-valence** case.

Once all ions contain an electron in the $4f$-states, the mean valence reaches an integer value ($n_f = 1$). If we keep on injecting electrons into the lattice, they will again populate $5d$-states, while the mean valence will be pinned at $n_f = 1$. In this stage, the system is said to be in an **integral-valence** configuration. Increasing n further, the system will undergo other mixed and integer-valence configurations.

The effect of strong interactions should be emphasized. If the interaction strength U was small compared to the rest of parameters in Eq. (7.1), mixed-valence states would not be a mixture of ions in only two successive configurations. For example, the first plateau in Fig. **7.1**(c) would also involve ions in $f^2, f^3, \ldots$ configurations, rather than only f^0 and f^1.

At this point, we could classify lanthanide compounds as mixed or integral-valence materials. However, an important ingredient is missing in the discussion above: the hybridization between $5d$ and $4f$-orbitals. As a result of this coupling, the plateaus' corners in Fig. **7.1**(c) become rounded, and the difference between mixed and integral-valence configurations is not sharp anymore. Therefore, the system can lie either deep in the mixed-valence regime, deep in an integral-valence regime or belong to the **nearly-**

integral valence region. In this last case, the average valence is neither exactly an integer nor takes a value midway between two integral numbers.

Notice that the occupation and average valence are not the same. The occupation of the $4f$-orbitals is a dynamical quantity; indeed, it fluctuates between two valence states, and at particular time, it might differ from site to site. It is in this sense that the valence is said to fluctuate in some heavy-fermion materials. The average valence, in contrast, is the mean value of the occupation of $4f$-states taken for the whole lattice. Unlike the occupation, it can take non-integer values. It must be mentioned that, in this work, we only consider homogeneous systems, *i.e.* crystals where the average occupation respects the symmetries of the space group.

Once the mechanism behind valence fluctuation is understood, we can focus on the electronic properties. As we mentioned, valence electrons populate $4f$ and $5d$-states in lanthanide elements, which are usually close in energy. This feature tends to manifest itself in reciprocal space as the presence of $4f$ and $5d$-bands in the region around the chemical potential. The interplay between these bands, mediated by hybridization and SOC effects, could then lead to topological phases.

Before we tackle the analysis of topology in these materials, we have to build a more precise picture about the description of their electronic structure, in particular, about the applicability of TQC for their analysis. We will now explain separately the limits in which the electronic structures of mixed and integral-valence systems admit a description in terms of quasiparticles.

7.1 Mixed-valence materials

Many-mixed valence materials can be described in terms of quasiparticles. In order to convince ourselves about this statement, we will describe briefly the approach presented in Ref. [151].

We consider the Anderson model in Eq. 7.1, restricted to a model made up of a pair of spinful $5d$-orbitals and another pair of $4f$-states:

$$\begin{aligned} H = &\sum_{\boldsymbol{k},\sigma} \epsilon(\boldsymbol{k})\ c^\dagger_{\boldsymbol{k}\sigma} c_{\boldsymbol{k}\sigma} + \sum_{\boldsymbol{R},\sigma} E_f f^\dagger_{\boldsymbol{R},\sigma} f_{\boldsymbol{R},\sigma} - \sum_{\boldsymbol{k},\sigma} v(\boldsymbol{k})(c^\dagger_{\boldsymbol{k},\sigma} f_{\boldsymbol{k},\sigma} + \text{h.c.}) \\ &+ U \sum_{\boldsymbol{R}} f^\dagger_{\boldsymbol{R},\uparrow} f_{\boldsymbol{R},\uparrow} f^\dagger_{\boldsymbol{R},\downarrow} f_{\boldsymbol{R},\downarrow}. \end{aligned} \tag{7.2}$$

where $c^\dagger_{\boldsymbol{k},\sigma}$ creates a state on the $5d$-band, $f^\dagger_{\boldsymbol{R},\sigma}$ a particle in the $4f$-orbital of the cell $\boldsymbol{R}$, and $f^\dagger_{\boldsymbol{k},\sigma}$ a Bloch state corresponding to $4f$-orbitals. Although specific aspects of $\epsilon(\boldsymbol{k})$ and $v(\boldsymbol{k})$ are not considered here, we assume that the (flat) $4f$-bands cut through the dispersive $5d$-band, which is common to happen in heavy-fermion materials due to the tendency of $5d$-orbitals to induce bands with large dispersion [see Fig. **7.2**].

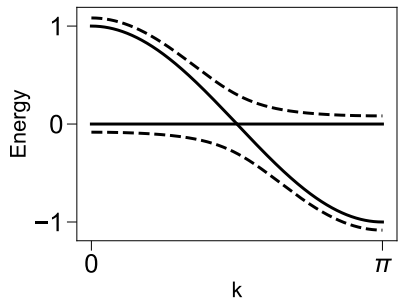

Figure 7.2: Band structure of the non-interacting part of the Anderson model in Eq. (7.2), with $\epsilon(k) = \cos k$. Solid lines correspond to the case without hybridization $[v(k) = 0]$, while dashed lines are the bands for $v(k) = 0.3$.

The eigenstates of the non-interacting part in Eq. (7.2) are given by:

$$E_{\pm}(\boldsymbol{k}) = \frac{E_f + \epsilon(\boldsymbol{k}) \pm \sqrt{[\epsilon(\boldsymbol{k}) - E_f]^2 + 4|v(\boldsymbol{k})|^2}}{2}. \tag{7.3}$$

Owing to the hybridization $v(\boldsymbol{k})$, the band structure splits into upper and lower bands separated by a gap, whose energy levels are $E_+(\boldsymbol{k})$ and $E_-(\boldsymbol{k})$, respectively. The creation operator for the states in the lower band is the following:

$$\psi^{\dagger}_{\sigma,\boldsymbol{k}} = \frac{1}{\sqrt{2}}[c^{\dagger}_{\boldsymbol{k},\sigma} + a_0(\boldsymbol{k}) f^{\dagger}_{\boldsymbol{k},\sigma}], \tag{7.4}$$

where

$$a_0(\boldsymbol{k}) = \frac{2v(\boldsymbol{k})}{E_f - \epsilon(\boldsymbol{k}) + \sqrt{[\epsilon(\boldsymbol{k}) - E_f]^2 + 4|v(\boldsymbol{k})|^2}}. \tag{7.5}$$

The many-body ground state of the system is then a Slater determinant of the states in the lower band:

$$\Psi^{\dagger}_0 = \prod_{\boldsymbol{k},\sigma} \psi^{\dagger}_{\boldsymbol{k},\sigma} = \prod_{\boldsymbol{k},\sigma} \frac{1}{\sqrt{2}}[c^{\dagger}_{\boldsymbol{k},\sigma} + a_0(\boldsymbol{k}) f^{\dagger}_{\boldsymbol{k},\sigma}]. \tag{7.6}$$

In order to unveil the nature of the ground state in the strongly interacting case, let us motivate the variational approach proposed in Ref. [151]. If we expanded $f^{\dagger}_{\boldsymbol{k},\sigma}$ in terms of the real-space creation operators, we would realize that $\Psi^{\dagger}_0$ contains ions in the f^2 configuration. At the same time, we know that the effect of a strong Hubbard interaction U is to get rid of these terms involving f^2 ions. We could then consider as *ansatz* for the variational method an operator obtained by applying the projector $\prod_{\boldsymbol{R}}(1 - n_{\boldsymbol{R},\uparrow} n_{\boldsymbol{R},\downarrow})$ to Eq. (7.6). Moreover, we could substitute $a_0(\boldsymbol{k})$ by a function $a(\boldsymbol{k})$, which plays the role of variational parameter. This substitution stands for the

redistribution of electrons when interactions are included. All in all, the variational operator considered for the ground state is:

$$\Psi^\dagger = \prod_{\boldsymbol{R}}(1 - n_{\boldsymbol{R},\uparrow}n_{\boldsymbol{R},\downarrow}) \prod_{\boldsymbol{k},\sigma} \frac{1}{\sqrt{2}}[c^\dagger_{\boldsymbol{k},\sigma} + a(\boldsymbol{k}) f^\dagger_{\boldsymbol{k},\sigma}]. \tag{7.7}$$

It turns out that the optimum $a(\boldsymbol{k})$ has the same expression as Eq. (7.5), but $v(\boldsymbol{k})$ and E_f should be substituted by renormalized expressions for hybridization and f-levels energy, respectively. This result suggests that many mixed-valence materials might be described in terms of quasiparticles, and the application of TQC to them might therefore be straightforward.

7.2 Kondo insulators

In order to explore the applicability of TQC out of the mixed-valence case, we will focus on the integral-valence case and look into its physics. We will comment on a renormalization group approach which simplifies the Anderson model Hamiltonian to an insightful expression, known as Kondo Hamiltonian. Then, we will identify the limit where the solution of this Hamiltonian admits a description in terms of quasiparticles.

We consider first the Anderson model for a single magnetic impurity, and we will later comment on the extension to case where lanthanide ions form a lattice. For a moment, let us neglect the presence of $5d$-electrons in the Anderson Hamiltonian, *i.e.* we neglect the first two terms in Eq. 7.1. There are then three energy levels in the model: when $E_f < 0$, $|f_\downarrow\rangle$ and $|f_\uparrow\rangle$ are the states with lowest energy $E = E_f$, followed by the empty and double-occupation states of energy $E = 2E_f + U$, respectively. Since at the integral-valence case all lanthanide ions are at half-filling [2], we expect valence fluctuations to be present in the low-energy limit of order $10K$ only virtually – the reason for considering this order of magnitude will be clear later on. This insight encourages us to integrate out valence fluctuations from the Anderson Hamiltonian in Eq. (7.1).

This renormalization group approach is dubbed **Schrieffer-Wolff transformation** [152]. In order to understand its essence, let us break it down into steps, as it is illustrated in Fig. **7.3**. Adopting the Anderson model as starting point already stands for getting rid of superfluous features shown in red. Once in the Anderson model, we first notice that processes involving two electrons in the impurity require an energy gain of the order U, which is usually $\sim 1,10$ eV for lanthanides [40]. We could therefore set an energy cutoff $D' < E_f + U$ and fold the key effects lying at frequencies $\omega > D'$ to the low-energy spectrum, so that they do not anymore take part on it explicitly. Similarly, since we are interested in the physics happening at a scale smaller than E_f, we can repeat this step by setting a new cutoff $D'' < E_f < D'$, which allows us to integrate out transitions to

[2] For simplicity, we will consider that each site contains only two f-orbitals.

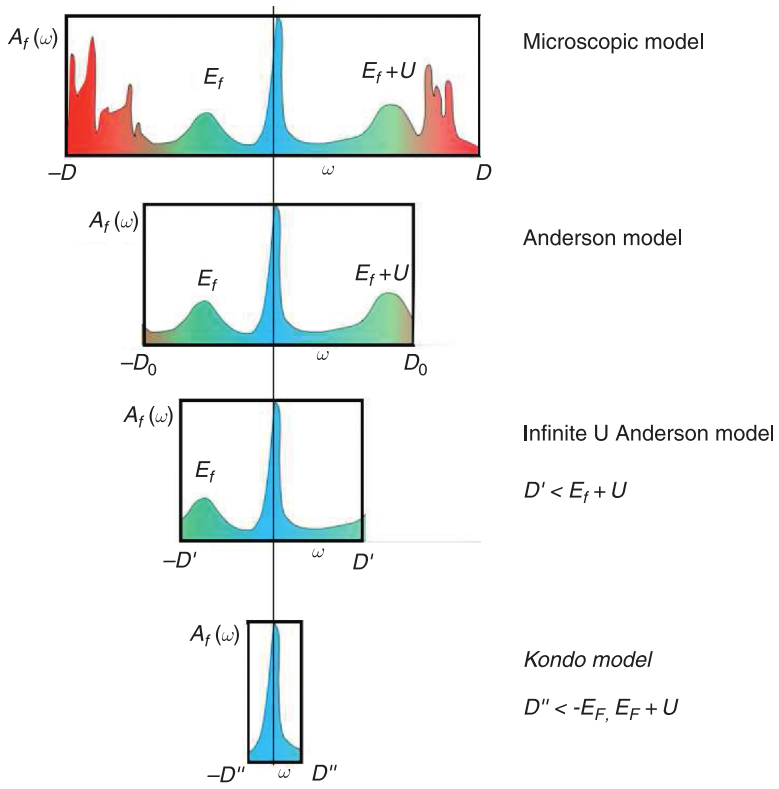

Figure 7.3: Renormalization group concept behind Schrieffer-Wolff transformation. Integrating out valence fluctuations in the Anderson model leads to the Kondo Hamiltonian, where they enter as virtual processes mediating spin-flips. Source: Ref. [38].

the empty configuration of the ion.

Let us describe the Schrieffer-Wolff transformation in more mathematical terms. For that, we consider a basis which allows us to write down the matrix of the Hamiltonian in the following block structure:

$$H = \begin{bmatrix} H_L & V \\ V^\dagger & H_H \end{bmatrix}, \tag{7.8}$$

where H_L is the block of elements between states where f-orbitals contain one electron, H_H is the block for doubly-occupied and empty configurations of the ion, and V is the hybridization matrix responsible for valence fluctuations. The renormalization follows by aiming a canonical transformation, driven by the matrix S, which decouples the low

and high-energy subspaces:

$$e^S H e^{-S} = \begin{bmatrix} \tilde{H}_L & \\ & \tilde{H}_H \end{bmatrix}. \tag{7.9}$$

The steps to integrate out doubly-occupied and empty configurations of f-orbitals are thus given at once im the Schrieffer-Wolff transformation. Expanding S in powers of the hybridization parameter v and neglecting terms $\mathcal{O}(v^3)$ – and higher-order terms – leads[3] to the following the following expression for the low-energy Hamiltonian $\tilde{H}_L$:

$$\tilde{H}_L = \sum_{\boldsymbol{k},\sigma} \epsilon_{\boldsymbol{k}}\, c^\dagger_{\boldsymbol{k}\sigma} c_{\boldsymbol{k}\sigma} + E_f\, f^\dagger_\sigma f_\sigma + \sum_{\boldsymbol{k}\boldsymbol{k}',\alpha\beta} J(\boldsymbol{k},\boldsymbol{k}') c^\dagger_{\boldsymbol{k}\alpha} c_{\boldsymbol{k}'\beta} \boldsymbol{\sigma}_{\alpha\beta} \cdot \boldsymbol{S}_f, \tag{7.10}$$

where $\boldsymbol{S}_f$ is the spin operator for the f-orbital. This expression is widely know as **Kondo Hamiltonian**. It describes the low-energy interplay between $5d$-electrons and electrons localized in $4f$-orbitals. According to it, $5d$-electrons suffer from scattering off the impurities and, as a result, both their crystal momentum might change and the spin of the $4f$-electron might flip.

Usually, the dependence on momentum of the coupling constant $J(\boldsymbol{k},\boldsymbol{k}')$ is neglected. The last term in Eq. (7.10) describes then a point like interplay between the impurity and the spin density of $5d$-orbitals which favors their ferromagnetic alignment ($J > 0$). The analysis of this scattering lead Jun Kondo to an explanation of the resistance minimum observed in many metals upon lowering of temperature [36]. It turns out that, at low temperature, the local moments of the f-orbital are screened by the $5d$-electrons and the electron fluid can be described as a Fermi liquid.

When an array of impurities is considered, like in the case of a heavy-fermion crystals, Kondo scattering turns into a coherent effect which conserves crystalline momenta. Consequently, as temperature is lowered, the resistivity reaches a maximum and drops then to zero with the typical behavior corresponding to Fermi liquids.

Nevertheless, in the lattice case, local moments tend to polarize the conduction sea, which gives raise to the RKKY interaction [38, 153]. This interaction interaction between localized spins favors the antiferromagnetic ordering, and therefore competes with the Kondo interaction. When the RKKY interaction dominates over the Kondo effect, the ground state of the lattice is antiferromagnetic. However, when the Kondo interaction is the dominant effect, the system might behave as a paramagnetic Fermi liquid. This later case, which we dub Kondo lattice, might be particularly suitable for hosting topological phases describable in terms of TQC.

In the case of a dominant Kondo interaction, two different regimes separated by a critical temperature T_K can be identified. For $T > T_K$, the system shows magnetic order, while local moments get screened by conduction electrons for $T < T_K$, yielding a ground state without magnetic ordering. T_K is called **Kondo temperature**, and it

[3] See Ref. [38] for rigorous expressions and a detailed derivation.

is usually of the order of ~ 10 K. Valence fluctuations involve changes in energy of the order of $U \sim 1,10$ eV and $E_f \sim 1$ eV, which are much larger than the energy scale of ~ 1 meV set by T_K for Kondo physics. Therefore, the Schrieffer-Wolff transformation should be interpreted as a renormalization procedure which allows integrating out the features of the Anderson's model that lie out of the energy range set by T_K.

It turns out that Kondo lattices might display a variety of behaviors [40]. Here, we are particularly interested in **Kondo insulators**. These Kondo lattices behave as metals with an array of localized magnetic moments at $T > T_K$. Upon cooling to $T < T_K$, they turn into insulators whose electronic structure can be described in terms of quasiparticle bands. As explained in Refs. [40, 49], the fact that Kondo insulators behave as Fermi liquids can be interpreted in the following way: In the strong-coupling limit, where Kondo interaction is the dominant term in Eq. (7.10) and the rest can be neglected, the ground state of the lattice corresponds to a spin singlet in each site, formed as the coupling of an electron in a f-orbital to a conduction electron. If we remove an electron from a site, we break the corresponding singlet. A small but finite hopping term in the non-interacting part of Eq. (7.10) would then allow the unpaired electron of the site to propagate through the crystal – a similar argument follows for particle-like excitations. Therefore, particle and hole excitations propagate through the Kondo lattice (at $T < T_K$) as quasiparticles.

8 Topological quantum chemistry for heavy-fermion insulators

The discovery of topological insulators was one of the most inspiring developments in condensed matter physics in the last decades. The first proposal by C. Kane and E. J. Mele for the realization of the quantum spin Hall effect in a two-dimensional lattice [2,3], and the later generalization by L. Fu *et al.* to three-dimensions [7, 18], stimulated an intense research on topological band structures and an extensive identification of topological materials. While initially the focus was on topological phases protected by time-reversal (TR) symmetry, the development of the topological quantum chemistry (TQC) formalism set a framework to study the interplay between crystal symmetries and topological phases. TQC provides a recipe to explain how bands in a crystal inherit their symmetry properties from exponentially-localized Wannier functions in real space. The combination of TQC and the symmetry-based indicators of topology [28,29] constitutes a powerful tool to investigate topological crystalline insulators. However, it remains largely unexplored to which extent could these formalisms be extended to describe topology in strongly-correlated electrons. In order to explore the possibilities of TQC beyond band topology in weakly-interacting systems, in the present work we apply TQC to a canonical class of correlated systems, namely heavy-fermion materials without magnetic order.

Heavy-fermion materials [154–158] are intermetallic compounds of rare earth metals and actinideswith localized f and dispersive d bands near the Fermi surface. A most discussed type of heavy-fermion material are Kondo insulators [154, 158], which undergo a transition into a paramagnetic phase when the temperature is lowered below a critical value. The corresponding paramagnetic insulator can be described in terms of highly renormalized f-electrons that hybridize with conduction electrons to form a filled band of quasiparticles. Importantly, while these materials are strongly interacting electron systems, their excitations and ground states can nevertheless be regarded as adiabatically

connected to noninteracting band insulators, as long as the phase sits far enough from the quantum-critical point [159,160]. Alternatively, if the mean occupation of the f-orbitals is not close from an integer value, the systems are classified as mixed valent. Even though both kinds of systems have been intensively analyzed during the last decades and preliminary research has been done on their topological properties [46,48–50,161], there is still a lack of a methodology for the general classification of topological phases in heavy fermion materials in the insulating state.

In this work, we present a TQC based analysis of the origin of topology in the quasiparticle band structure of non-magnetic heavy-fermion insulators. We identify three fundamental cases where the interplay between dispersive d-bands and heavy f-bands might lead to topological band structures. Our analysis is valid with and without spin-orbit corrections and general for all 230 space groups. This implementation of TQC allows for a rigorous classification of topological phases in these materials, as it considers all crystal symmetries of the space group on an equal footing. Furthermore, it is applicable to classify the topological phase of any disconnected set of bands, which might turn out to be useful to predict boundary states.

The first material we consider as testbed is the prototypical mixed-valence insulator SmB_6. By applying our formalism to it, we diagnose and classify the topology of its *ab initio* band structure (and discuss how effects of band renormalizations due to electron correlation may affect this classification). Although previous works predicted that SmB_6 could be a topological insulator protected by TR-symmetry [46,48–51] or a mirror-Chern insulator [162,163], we show that its band structure corresponds to a strong-topological insulator with $z_{4\pi m} = 3$ and $z_8 = 5$ indicators. This more precise classification is the result of accounting not only for inversion and TR-symmetry, but also the full crystal symmetries of the structure.

The structure of this chapter is the following: In Sec. 8.1, we discuss in terms of TQC how the hybridization between bands might produce topological valence bands in the band structure of heavy-fermion insulators. The origin of topology in the band structure of SmB_6 is then investigated in Sec. 8.2, and the actual topological phase is classified based on symmetry-indicators of topology. We finish the chapter by summarizing the results and commenting on our outlook for this contribution to the field of heavy-fermion insulators.

8.1 Types of hybridization-driven topological phases in heavy-fermion materials

A set of Wannier functions is said to be closed if the action of the space group on it does not transform any of them into a state that is not included in the set. A closed set of Wannier functions forms a basis for a representation of the space group called *band representation* [31–33]. If a set of bands transforms as a band representation (in reciprocal

space), it is said to have an *atomic limit*. Furthermore, a band representation whose atomic limit can not be broken down into smaller atomic limits is dubbed *elementary band representation* (EBR).

According to the formalism of topological quantum chemistry [25–27], if a set of band does not have and atomic limit, it is topological. Determining that a set of bands does not have an atomic limit is then sufficient to show that they are topological bands. This can be inferred from its little group irreducible representations (irreps) at maximal $\boldsymbol{k}$-points of the BZ: when this set of irreps can not be written as a linear combination of EBRs where the coefficients of all EBRs are positive integers of zero, the bands do not have an atomic limit, and are hence topological.

A remarkable feature of mixed valence and (magnetically non-ordered) Kondo insulators containing lanthanide elements is that the low energy part of their quasiparticle band structure is dominated by the presence of dispersive and heavy bands. Heavy bands transform as a band representation induced from localized $4f$-orbitals of the lanthanide element, while the band representation of dispersive bands is induced from spatially extended $5d$-orbitals of the same element. Another property of these materials is the fluctuating occupation of $4f$-orbitals, which is a consequence of electron-hopping transitions between these and $5d$-orbitals.

Moreover, in the case of topological heavy-fermion materials, the dispersive $5d$-bands are cut by the (almost) flat $4f$-bands. Due to the hybridization between orbitals, the irreps of the corresponding band representations redistribute among valence and conduction bands. Then, if the irreps belonging to valence bands can not be written as a linear combination of EBRs with positive-integer (or zero) coefficients, the material hosts a topological phase.

Although the hybridization can not be tuned arbitrarily in an actual material, it will be helpful to consider here that we can switch it on and off in order to gain insight of the interplay between dispersive and heavy bands. We consider as starting point the band structure without hybridization, where the bundle of heavy $4f$-bands intersects the set of dispersive $5d$-bands. Let us denote ρ_f and ρ_d the band representations induced from the $4f$ and $5d$-orbitals, respectively. In the absence of hybridization, even if these representations might share the same irreps, it is possible to relate every irrep to one of them

When the hybridization is considered, irreps of ρ_d and ρ_f redistribute among valence and conduction bands. Depending on manner they reorganize themselves, it is possible to distinguish between three cases of hydridization-driven topology in heavy-fermion insulators.

8.1.1 Combination of band representations

This case, illustrated in Figs.**8.1**(a) and (b), corresponds to insulators where the irreps of valence bands can not be identified as a set stemming exclusively from neither ρ_d nor

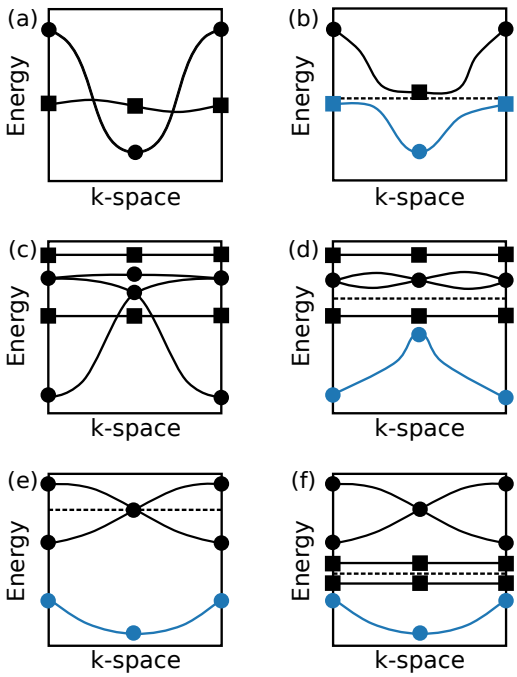

Figure 8.1: Schematic illustrations of the three types of mechanism to explain topological phases in non-magnetic heavy-fermion insulators. Bands in blue are topological. Circles (squares) indicate irreps which can be related to ρ_d (ρ_f) when the hybridization is unconsidered. (a) and (b) illustrate the case described in Sec. 8.1.1 with and without considering the hybridization, respectively. (c) and (d) sketch the case explained in Sec. 8.1.2, before and after including the hybridization in the analysis, respectively. (e) and (f) show an example for the case in introduced in Sec. 8.1.3, with and without considering the $4f$-bands in the discussion.

ρ_f. We say that the irreps of valence bands are combination of irreps which belonged to ρ_d and ρ_f before considering the hybridization.

Identifying this scenario is particularly simple if every irrep in can be related with either ρ_d or ρ_f, *i.e.* if these band representations have different irreps. This is the case for symmorphic crystals where lanthanide ions sit on inversion centers, like SmB_6. In such a material, irreps of ρ_d and ρ_f have opposite parity at inversion-invariant maximal $\boldsymbol{k}$-points.

8.1.2 Split of the band representation induced from $5d$-orbitals

The hybridization-driven transition might be different when the band representation ρ_d is decomposable, that is when it admits a separation into smaller disconnected sets of bands such that each subset satisfies independently the compatibility relations of the space group. The hybridization with heavy bands could then disconnect ρ_d, and a topological subset of bands coming out of the split could become part of the valence states. It is important to realize that, in group theory grounds, this case does not require the combination of irreps at maximal $\boldsymbol{k}$-points introduced in the previous case. See Figs. **8.1**(c) and (d) for an illustration of this case.

This type of transition might be particularly prone to yielding fragile topological phases. To understand this point, let us consider that the irreps of the $5d$-bands split by the hybridization coincides with the irreps of an EBR ρ. The separation of this set of dispersive bands can then be written as

$$\rho = \rho_c \oplus \rho_v, \tag{8.1}$$

where ρ_c and ρ_v are subsets which become part of the conduction and valence states, respectively. At least one of these subsets must be topological, since otherwise ρ would not be an EBR. In particular, if ρ_c has an atomic limit, then ρ_v is fragile topological as it can be written as $\rho_v = \rho \ominus \rho_d$, *i.e.* as a linear combination of EBRs with integer coefficients, where at least one of the coefficient is negative.

8.1.3 Topology induced by filling-matching

Let us suppose that ρ_d is decomposable and that the band structure would be metallic in the absence of $4f$-bands. This happens when the chemical potential cuts through a set of $5d$-bands, which are thus partially filled. Due to the contribution of the $4f$-shell to the total number of electrons, the chemical potential might move to the region between two disconnected sets of bands. The bands below the chemical potential might then host a topological phase.

Let us consider the example illustrated in Figs. **8.1**(e) and (f). The band representation of $5d$-bands is separated in two sets of bands. The lower set is two-fold degenerate and topological, while chemical potential cuts through the upper set of bands, as the

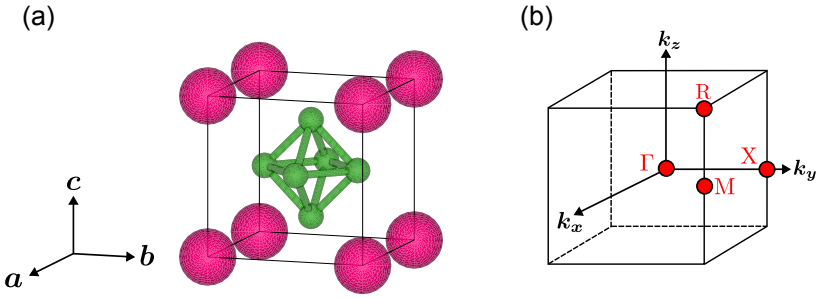

Figure 8.2: Crystal structure of SmB_6. a) Primitive unit cell. Sm atoms are shown in red (Wyckoff position 1a), while B atoms are shown in green. b) First BZ, where maximal $\boldsymbol{k}$-points are indicated in red.

contribution of the $5d$-shell to the number of electrons per unit cell is $N_d = 3$. Let us denote $\tilde{\rho}_d$ the representation of the lower topological set of bands. If the $4f$-shell contributes $N_f = 1$ electron per unit cell, the total number of electrons per primitive cell ($N_d + N_f = 4$) is even. The system might consequently be an insulator, such that the valence bands are formed by a set of states transforming as $\tilde{\rho}_d$ and some additional bands which do not trivialize this representation. As a result, the system is a topological insulator.

Notice that the hybridization between $4f$ and $5d$-orbitals is not vital for the system to be an insulator. The contribution of both shells to the number of electrons and the actual connectivity of the corresponding bands are in fact the responsible for leading to a topological insulating phase.

8.2 Topological band structure of SmB_6

In this chapter, we will investigate the band structure of SmB_6 in terms of TQC. SmB_6 crystallizes in a primitive cubic structure in the space group $Pm\bar{3}m$ (No. 221). The unit cell and BZ of the crystal are shown in Fig. **8.2**(a) and (b), respectively. This compound is a mixed-valence semiconductor predicted to be topologically non-trivial at $T < 30$ K by theoretical calculations and experiments [46, 48–50, 161]. We will begin by looking into the orbital character of the region around the Fermi level and by determining the topology of the valence bands by means of *ab initio* calculations. Then, we will work out the crystal-field split $5d$ and $4f$-orbitals suffer from, in order to determine the irreps of their band representations. The information obtained in these two steps will be used in the third step to investigate the origin of the topological phase in terms of TQC. Finally, we present a minimal tight-binding model which captures the topological phase obtained within the framework of DFT.

8.2.1 *Ab initio* band structure

The ground state electron density and band structure of SmB_6 have been calculated with self-consistently with VASP [164]. The details of the calculation can be found in appendix C.1. According to our DFT calculations, the average occupation of the $4f$-shell of Sm in the ground state is $n_f = 5.5$, which indicates that the valence of Sm fluctuates between $4f^5$ and $4f^6$ configurations. SmB_6 is, therefore, a mixed-valence insulator. This result is in good agreement with previous works [52,165–167]. The cause of this fluctuation is the proximity in energy of samarium's $4f$ and $5d$-shells, which allows electrons to hop between these orbitals. SmB_6 is thus a mixed-valence compound where $4f$-states play the role of localized orbitals, whereas $5d$-states act as overlapping orbitals.

The low-energy part of the band structure of SmB_6 is dominated by bands induced from samarium's $5d$ and $4f$-orbitals. Fig. **8.3**(c) shows the weight of Sm's $5d$-states on the bands. According to this data, the set of $5d$-bands are located well above the Fermi level. Nevertheless, one of these bands comes down to -2 eV in the line connecting Γ to X. Furthermore, the $4f$-orbitals induce heavy (quasi)bands which lie close to the Fermi level and cut through this $5d$-band [see Fig. **8.3**(d)].

Fig. **8.3**(a) shows the band structure of SmB_6 calculated with pseudopotentials which do not include $4f$-states as valence electrons, whereas the band structure in Fig. **8.3**(b) includes the bands induced from these localized orbitals. This data is compatible with the fact that the band going down from 2 eV to -2 eV between Γ and X is a $5d$-band. Moreover, it corroborates that the heavy bands in the region around the Fermi level are induced from $4f$-orbitals. The $5d$-band is split by the hybridization with $4f$-bands, such that the valence band looks to be formed out of the gluing of $5d$ and $4f$-bands. This fact suggests the origin of topology in SmB_6 is the hybridization-driven combination of band representations explained in Sec. 8.1.1.

The origin of the gap separating valence and conduction bands is more complicated. On the one hand, Fig. **8.3**(b) shows SmB_6 would be a metal if $4f$-bands were not present around the Fermi level, thus the hybridization between these and $5d$-states contributes to the material being an insulator. On the other hand, the highest valence and lowest conduction bands belong to the subset of $J = 5/2$ and $J = 7/2$-bands originated from the separation by SOC of the bundle of $4f$-bands. These subsets split further due to the crystal field and combine between them, yielding to the gap that separates them. Therefore, the reason for the DFT band structure of SmB_6 to be an insulator is the interplay between SOC, the crystal field felt by $4f$-states, and the hybridization between these and $5d$-states.

In order to determine if the valence bands are topological, we have calculated with the software *IrRep* [77] their irreps of little groups at maximal $\boldsymbol{k}$-points of the BZ, which are shown in Fig. **8.4**(a) and collected in Tab. **8.1**. It turns out that this set of irreps can not be written as a linear combination of EBRs with positive or zero integer coefficients.

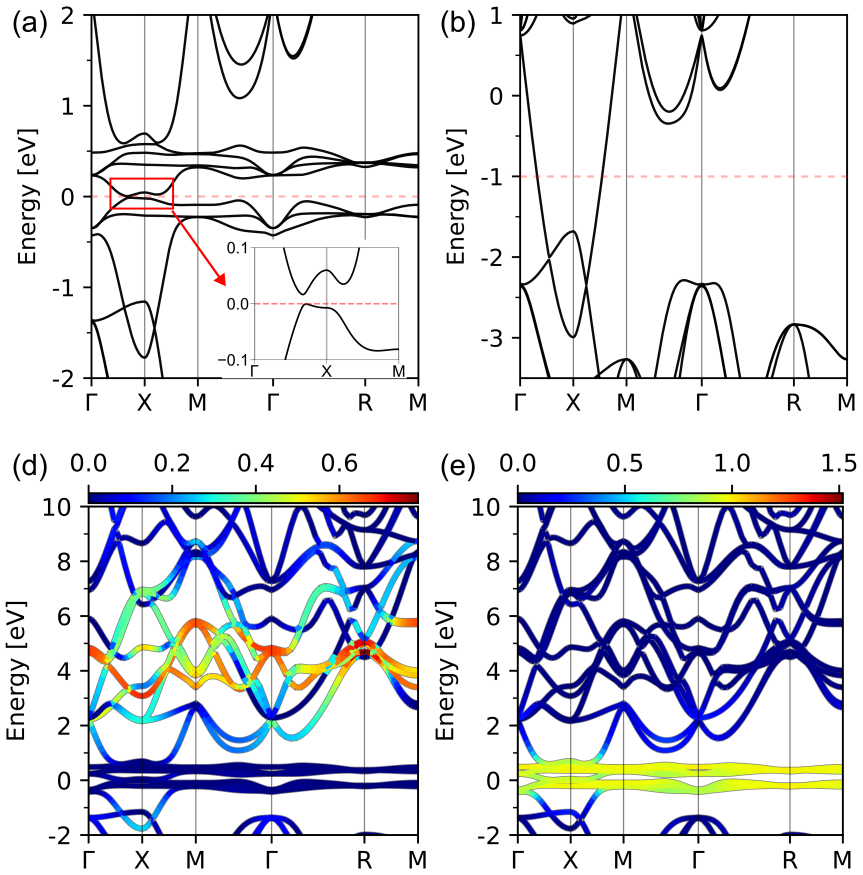

Figure 8.3: (a) and (b) show the band structure of SmB_6 around the Fermi level (red dashed line), with and without including the $4f$-states of Sm, respectively. The inset in (a) demonstrates that valence and conduction states are separated by a gap of the order of ~ 10 meV. (c) and (d) show the weight of samarium's d and f-orbitals in the bands, respectively. A dispersive d-band crosses the manifold of heavy f-bands in the line Γ-X-M.

Table 8.1: Irreps of bands in SmB_6 calculated with *IrRep* from *ab initio* bands. The irreps above (below) the horizontal line correspond to states in the conduction (valence) bands. Moreover, black and orange irreps belong to the band representation induced from $4f$-orbitals. The irreps in blue and orange are those which allow us to understand the non-trivial topology in terms of a band inversion [see Figs. **8.4**(a)-(b)].

Γ	X	M	R
Γ_{10}	$\bar{X}_9$	$\bar{M}_8$	$\bar{R}_{11}$
$\bar{\Gamma}_8$	$\bar{X}_8$	$\bar{M}_9$	$\bar{R}_9$
$\bar{\Gamma}_9$	$\bar{X}_9$	$\bar{M}_9$	
$\bar{\Gamma}_{11}$	$\bar{X}_8$	$\bar{M}_8$	
	$\bar{X}_9$		
Γ_{11}	X_9	M_8	R_{11}
$\bar{\Gamma}_9$	$\bar{X}_8$	$\bar{M}_9$	$\bar{R}_9$
	$\bar{X}_7$	$\bar{M}_8$	

As a result, the valence bands host a topological phase according to the formalism of TQC. Furthermore, we have computed the values for the symmetry-based indicators of topology [28, 29] via the software *CheckTopologicalMat* of the BCS [30, 104], which yields the weak indicators $(z_{2w,1}, z_{2w,2}, z_{2w,3}) = (1, 1, 1)$ and $z_{4\pi m} = 3$, also the strong indices $z_2 = 1$, $z_4 = 1$ and $z_8 = 5$. SmB_6 is therefore a strong-topological insulator, in accordance to our DFT calculations.

Our topological classification is compatible with previous works which predicted SmB_6 to be a strong-topological insulator [46–54]. Nonetheless, while previous classifications are based on the calculation of the weak $(z_{2w,1}, z_{2w,2}, z_{2w,3})$ and strong z_2 invariants [7, 8, 18], our diagnosis incorporates additional indicators which take indeed values that indicate non-trivial topology. We have therefore obtained a more rigorous classification as our analysis includes all crystal symmetries on an equal footing.

8.2.2 Band representations induced from $5d$ and $4f$-orbitals of samarium

To determine the irreps of little groups of maximal $\boldsymbol{k}$-points corresponding to the band representations of samarium's $5d$ and $4f$-states, we will work out the split these shells suffer owing to the crystal-field.

If samarium atoms were isolated from their environment, the $4f$ and $5d$-orbitals would be 10 and 14-fold degenerate, and they would transform as the irreducible representations $D_3^- \otimes D_{1/2}^+$ and $D_2^+ \otimes D_{1/2}^+$ of the symmetry group $O(3)$, respectively – D_J^p is an irrep of $O(3)$, where J and p are the parity, and $D_{1/2}^+$ is the spin-representation. However, in SmB_6, samarium sits at WP 1a whose coordinates are $(0, 0, 0)$. The symmetry group leaving this position invariant is lowered to $G_{1a} = m\bar{3}m$, thus $4f$ and $5d$-orbitals

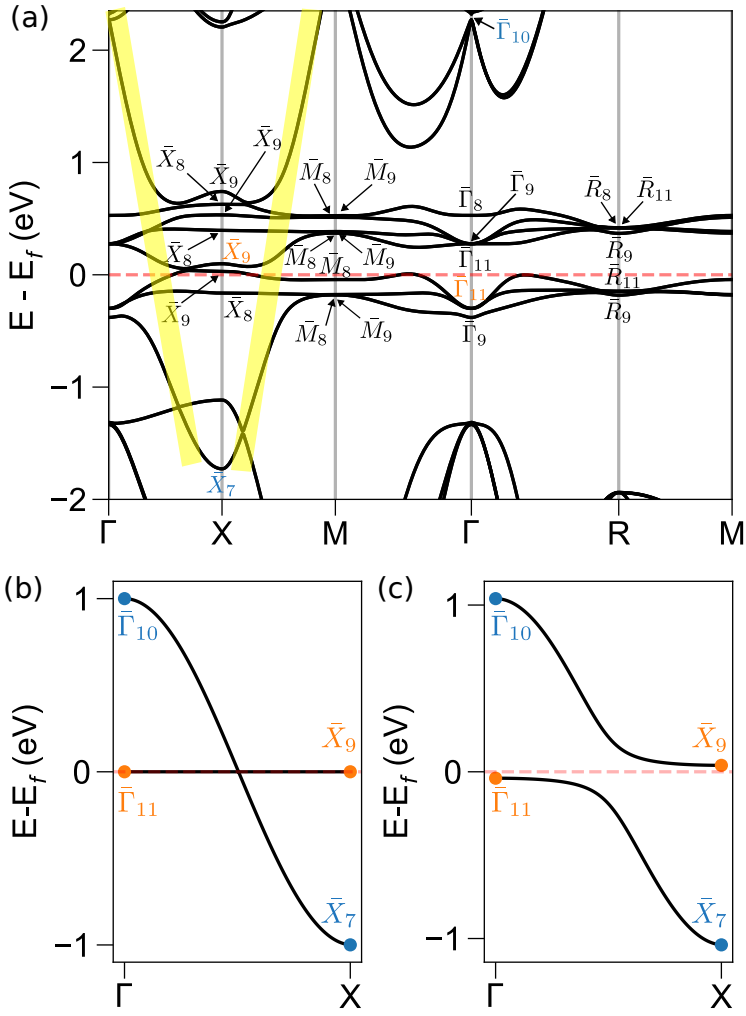

Figure 8.4: (a) Band structure of SmB_6 with the irreps of bands induced from $4f$-states of samarium. The $5d$-band which crosses the bundle of $4f$-bands is indicated in yellow. Irreps induced taking part in the band inversion are indicated in blue (induced from d-orbitals) and orange (f-orbitals). (b) Sketch to illustrate the position of $5d$ and $4rf$-bands before considering their hybridization. The irrep $\bar{X}_9$ (orange) comes from the $4f$-states, whereas $\bar{X}_7$ (blue) has its origin in the $5d$-states. (c) Sketch showing how the hybridization opens a gap between $4f$ and $5d$ bands. As a result of of the gap opening, the irrep $\bar{X}_9$ ($\bar{X}_7$) belongs to the conduction (valence) bands of the insulator. The Fermi energy is marked by the red-dashed line in all the three figures.

transform now as the representations of G_{1a} subduced by $D_3^- \otimes D_{1/2}^+$ and $D_2^+ \otimes D_{1/2}^+$, *i.e.* $(D_3^- \otimes D_{1/2}^+) \downarrow G_{1a}$ and $(D_2^+ \otimes D_{1/2}^+) \downarrow G_{1a}$, respectively.

Regarding $4f$-orbitals, their representation $(D_3^- \otimes D_{1/2}^+) \downarrow G_{1a}$ is reducible and can be decomposed as the direct sum of irreps of G_{1a}:

$$(D_3^- \otimes D_{1/2}^+) \downarrow G_{1a} = \bar{E}_{1u}(2) \oplus 2\bar{E}_{2u}(2) \oplus 2\bar{F}_u(4). \tag{8.2}$$

where the numbers between brackets indicate the dimensions of the irreps – degeneracy of the corresponding states. The 14-fold degenerate $4f$-shell is thus split into three groups of 2-fold degenarate and two groups of 4-fold degenerate states. Each of these set of degenerate states induces Bloch waves that transform as an EBR of $Pm\bar{3}m$. The irreps at maximal $\boldsymbol{k}$-points of these EBRs are the following:

$$(\bar{E}_{1u} \uparrow G)_{1a} : \{\bar{\Gamma}_8, \bar{R}_8, \bar{M}_9, \bar{X}_8\}, \tag{8.3a}$$
$$(\bar{E}_{2u} \uparrow G)_{1a} : \{\bar{\Gamma}_9, \bar{R}_9, \bar{M}_8, \bar{X}_9\}, \tag{8.3b}$$
$$(\bar{F}_u \uparrow G)_{1a} : \{\bar{\Gamma}_{11}, \bar{R}_{11}, \bar{M}_8 \oplus \bar{M}_9, \bar{X}_8 \oplus \bar{X}_9\}. \tag{8.3c}$$

These result further corroborates the fact that the heavy-bands around the Fermi level are $4f$-bands, since they have in correspondence these set of irreps as Fig. **8.4**(a).

Similarly, the representation $D_2^+ \otimes D_{1/2}^+$ corresponding to the $5d$-shell is also reducible:

$$(D_2^+ \otimes D_{1/2}^+) \downarrow G_{1a} = \bar{E}_{2g}(2) \oplus 2\bar{F}_g(4). \tag{8.4}$$

The 10-fold degeneracy is split into a group of 2-fold and two groups of 4-fold degenerate states. Each of the irreps of G_{1a} in Eq. 8.4 induces an EBR of $Pm\bar{3}m$ as the WP 1a is maximal. The irreps at maximal $\boldsymbol{k}$-points of these EBRs are the following:

$$(\bar{E}_{2g} \uparrow G)_{1a} : \{\bar{\Gamma}_7, \bar{R}_7, \bar{M}_6, \bar{X}_7\}, \tag{8.5a}$$
$$(\bar{F}_g \uparrow G)_{1a} : \{\bar{\Gamma}_{10}, \bar{R}_{10}, \bar{M}_6 \oplus \bar{M}_7, \bar{X}_6 \oplus \bar{X}_7\}. \tag{8.5b}$$

Since the space group is symmorphic and samarium sits at an inversion center, the irreps of band representations induced from this element inherit the parity of the orbital. For instance, the irreps of the band representation induced from $4f$-orbitals [Eqs. (8.3a)-(8.3c)] are odd under inversion, whereas those of the band representation induced from $5d$-orbitals [Eqs. (8.5a) and (8.5b)] are even. This allows us to relate each irrep to either of the band representations and facilitates the analysis of the origin of topology.

8.2.3 Origin of the topology of SmB_6 in terms of TQC

In order to gain deep insight into the origin of topology in SmB_6, we will now construct a simplified picture of the band structure which captures values for the symmetry-indicators of the phase. This simplification will facilitate us to interprete the topology

in terms of the TQC based perspective explained in Sec. 8.1.

The first simplification is based on the idea that unoccupied bands do not contribute to the topological classification of the insulator. This provides us with freedom to leave out of the discussion some conduction bands. In particular, even if the conduction bands of irreps $\{\bar{\Gamma}_8, \bar{X}_8, \bar{M}_9, \bar{R}_8\}$, $\{\bar{\Gamma}_9, \bar{X}_9, \bar{M}_8, \bar{R}_9\}$ and $\{\bar{\Gamma}_{11}, \bar{X}_8 \oplus \bar{X}_9, \bar{M}_8 \oplus \bar{M}_9, \bar{R}_{11}\}$ are crossed by the $5d$-band and hybridize with it, they do not play any significant role in the determination of symmetry-based indicators of the topology of valence bands. Their irreps coincide indeed with set of irreps of the band representation $(\bar{E}_{1u} \uparrow G)_{1a} \oplus (\bar{E}_{2u} \uparrow G)_{1a} \oplus (\bar{F}_u \uparrow G)_{1a}$. Therefore, we can leave these $4f$-bands out of the discussion.

Concerning valence bands, the set of irreps $\{\bar{\Gamma}_9, \bar{X}_9, \bar{M}_8, \bar{R}_9\}$ coincides with the irreps of the EBR $(E_{2u} \uparrow G)_{1a}$. Consequently, this set of irreps makes no contributions to the values of symmetry-indicators which classify the topological phase of valence electrons, and we hence get rid of them.

The set of $5d$-bands also admits a simplification. Fig. (**8.3**) shows that it is a single $5d$-band which is intersected by the bundle of heavy bands. In an scenario without hybridization, this band would have the irrep $\bar{X}_7$ indicated in blue in Fig. (**8.4**)(a) and would be connected to the irreps $\bar{\Gamma}_{10}$, $\bar{X}_6$ and $\bar{X}_7$ at X, and $\bar{M}_6$ and $\bar{M}_7$ at M. This fact motivates us to simplify the set of $5d$-bands by considering only the band with the mentioned irreps.

All at all, we are left with a simplified band structure containing the $4f$ and $5d$-bands whose irreps coincide with the set of irreps of the EBRs $(\bar{F}_u \uparrow G)_{1a}$ and $(\bar{F}_g \uparrow G)_{1a}$, respectively. It must be mentioned that this simplification does not imply that these bands stem from the orbitals which induce the aformentioned EBRs; generally, the four $4f$-bands ($5d$-bands) might be originated as a combination of many EBRs in Eq.(8.7) [Eq. (8.6)].

Without hybridization, one of the $5d$-band would go down when moving from Γ to X and the $4f$-bands would intersect it, as shown in Fig. **8.4**(b). The hybridization would then separate the bands, as depicted in Fig. **8.4**(c). See appendix C.2 for a discussion about the possibility for having crossing in other symmetry lines and planes. The lower band would then be a combination of both band representations, in the sense that it would contain at Γ an irrep originated from the $4f$-orbitals ($\bar{\Gamma}_{11}$), while its irrep $\bar{X}_7$ at X would stem from $5d$-orbitals. This supports the idea that the topology is produced by the hybridization-driven combination of band representations described in Sec. 8.1.1. Moreover, the irreps of the valence band would be $\{\bar{\Gamma}_{11}, \bar{X}_8 \oplus \bar{X}_9, \bar{M}_8 \oplus \bar{M}_9, \bar{R}_{11}\}$. This set of bands does not have an atomic limit and is hence topological. It has indeed in correspondence the same values for the symmetry-indicators of topology as the whole set of *ab initio* bands discussed in Sec. 8.2.1. Notice that exchanging $\bar{X}_7$ by $\bar{X}_9$ in the valence bands, which is equivalent to avoiding the inversion between $5d$ and $4f$-bands, trivializes the occupied states.

8.2.4 Tight-binding model for SmB_6

In this section, we present a minimal tight-binding model that captures the key topological aspects of the band structure of SmB_6. The model is based on the simplified band structure derived in the previous section. Besides providing a picture of the microscopic details of electron-hopping amplitudes, it will serve us to give a demonstration of the effectiveness of the TQC guided exploration of topological phases in heavy-fermion insulators.

We consider eight spinful Wannier functions sitting at WP 1a. Four of them transform as the irrep $\bar{F}_g$ under the action of the site-symmetry group $G_{1a} = m\bar{3}m$, while the rest transform as the irrep $\bar{F}_u$. The EBRs $(\bar{F}_g \uparrow G)_{1a}$ and $(\bar{F}_u \uparrow G)_{1a}$ induced from these contain the irreps present in the simplified band structure derived above.

In order to deal efficiently with the constrains set by symmetries on the parameters of the model, it is convenient to consider the decomposition of these spinful representations as the product of the spin representation $S = \bar{E}_{1g}$ and a spinless representation:

$$\bar{F}_g = E_g \otimes S, \tag{8.6}$$

$$\bar{F}_u = E_u \otimes S. \tag{8.7}$$

We denote the tight-binding basis states $|p_{\boldsymbol{R},i,\sigma}\rangle$, where $\boldsymbol{R}$ is the lattice vector of the unit cell, $p = g, u$ stands for the parity of the corresponding irrep, $i = 1, 2$ labels the state within the basis of the irrep E_p and σ is the spin-degree of freedom – for example, $|g_{\boldsymbol{R},2,\uparrow}\rangle$ is the basis state of $\bar{F}_g$ in the cell $\boldsymbol{R}$ constructed as the product of the second basis state of E_g and the $\uparrow$-spin state. The transformation of these states under a symmetry $h \in m\bar{3}m$ is described by the following expression:

$$h\,|p_{\boldsymbol{R},i,\sigma}\rangle = [E_p(h)]_{i'i}\; S_{\sigma'\sigma}(h)\,\left|p_{(h\boldsymbol{R}),i',\sigma'}\right\rangle, \tag{8.8}$$

where $E_p(g)$ is the matrix of h in the representation E_p. We will use greek letters to denote the degrees of freedom corresponding to the irreps, except for the parity. The matrix of h in Eq. (8.8) will be written accordingly as $V_{\alpha'\alpha} = [E_p(h)]_{i'i} S_{\sigma'\sigma}(h)$, with $\alpha = (i\sigma)$ and $\alpha' = (i'\sigma')$.

We now consider the matrix elements of the Hamiltonian in the basis of tight-binding states defined in real space. Let us denote these elements

$$H_{p\alpha,p'\alpha'}(\boldsymbol{R}) = \left\langle p_{\boldsymbol{R},\alpha}\middle|H\middle|p'_{\boldsymbol{0},\alpha'}\right\rangle, \tag{8.9}$$

Here, we only consider amplitudes for hoppings from the unit cell at the origin. Amplitudes involving other unit cells can be obtained from Eq. 8.9 through translations by vectors of the lattice. The fact that the Hamiltonian must be invariant under the symmetries of the space group, together with Eq. (8.8), leads to the following relation

between hopping amplitudes:

$$H_{p\beta,p'\beta'}(h\boldsymbol{R}) = V_{\beta\alpha}(h)H_{p\alpha,p'\alpha'}(\boldsymbol{R})V^{\dagger}_{\alpha'\beta'}(h). \tag{8.10}$$

For some symmetry operations, this relation could further set constrains on some matrix elements, reducing the number of independent parameters needed to account for them. Apart from the on-site energy ϵ_f of the f-states ($p = u$), we consider $f - f$ and $d - d$ hopping elements up to next-nearest neighbors (NNN):

$$\begin{aligned}
&\epsilon_f = \epsilon\ \mathbb{1},\\
&T_{11,p}(\boldsymbol{R^{NN}}) = t^{NN}_{11,p}\ \mathbb{1},\\
&T_{12}(\boldsymbol{R^{NN}}) = t^{NN}_{12}\ \mathbb{1},\\
&T_{11,p}(\boldsymbol{R^{NNN}}) = t^{NNN}_{11,p}\ \mathbb{1},\\
&T_{12}(1,1,0) = t^{NNN}_{12}\ \mathbb{1} + i\ \tilde{t}^{NNN}_{12}\sigma_z,
\end{aligned} \tag{8.11}$$

where ϵ, $t^{NN}_{11,p}$, t^{NN}_{12}, $t^{NNN}_{11,p}$, t^{NNN}_{12} and $\tilde{t}^{NNN}_{12}$ are real-valued scalar parameters governing the strength of the matrix elements, and p denotes the parity of the orbital.

We also include nearest-neighbor (NN) hybridization between f and d-states:

$$V_{11}(a\boldsymbol{u}) = i\ v\sigma_u. \tag{8.12}$$

Here, $\boldsymbol{u}$ is the unit vector along one cubic unit cell's principal axes and a is the lattice parameter. Eqs. (8.11) and (8.12) show only one of the matrices of each hopping amplitude. The rest of matrices can be generated by applying the transformation in Eq. (8.10) for the generators of $m\bar{3}m$.

Fig. **8.5** shows the tight-binding band structure of SmB_6 with the same ordering of irreps as the *ab initio* bands in Fig. **8.4**(a). The lower two connected bands correspond to a strong-topological insulator with the same $z_{4\pi m} = 3$ and $z_8 = 5$ as the DFT valence states. In conclusion, the tight-binding model presented here is able yield valence bands with the same values for the symmetry-based indicators of topology as those obtained via *ab initio* calculations. It also gives us a qualitative picture of the magnitude of hopping amplitudes in SmB_6.

8.3 Discussion and Conclusions

In this work, we have presented a TQC-based analysis of topological phases in non-magnetic heavy-fermion insulators. We have indeed described three cases where the interplay between $4f$ and $5d$-states in mixed-valence and Kondo insulators might lead to topological phases. Our approach is valid for crystals in any of the 230 space groups, both with and without spin-orbit corrections. In addition, since it accounts for the role

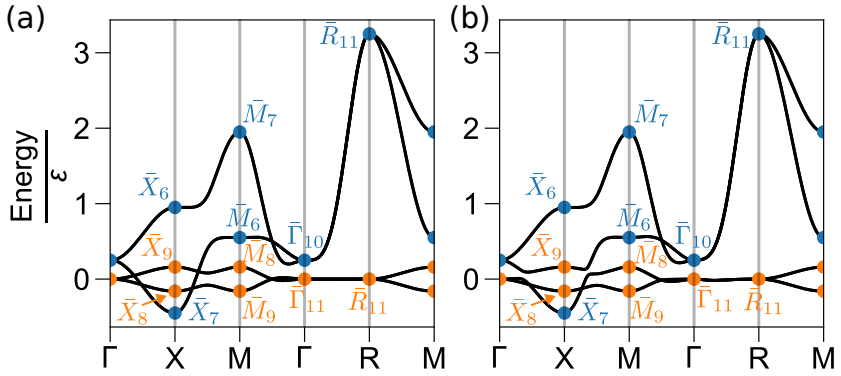

Figure 8.5: Tight-binding band structure of SmB_6 with $t^{NN}_{11,g}/\epsilon = -1/4$, $t^{NNN}_{11,g}/\epsilon = 1/16$, $t^{NNN}_{12,g}/\epsilon = 0.7/8$ and $t^{NNN}_{12,u}/\epsilon = -0.02$. The rest of hopping parameters are chosen to be zero. (a) Bands without hybridization between f and d-orbitals. (b) Bands with hybridization $v = 0.03$. Valence bands have the same irreps as the DFT bands, and hence the same values for the symmetry-based indicators of topology.

of all crystal symmetries, it allows for a detailed classification of topological phases which is not restricted to just a particular subset of symmetries of the system.

Owing to this strengthened capacity for diagnosing and classifying topological phases, our approach might motivate intensive search of topological phases in heavy-fermion systems. This search which might lead to the discovery of novel topological materials as well as to diagnosing as non-trivial some phases that had been previously classified as trivial.

We have tested our method on SmB_6. While state-of-the-art methods beyond DFT provide an accurate description of the electronic properties [52, 165], DFT calculations already capture the mixed-valence behavior of the system. Moreover, our approach suggests that SmB_6 hosts a strong-topological phase diagnosed by $z_4 = 1$, $z_{4\pi m} = 3$ and $z_8 = 5$ symmetry indicators, in addition to the well known weak and strong indicators for topological insulators [7,8,18]. We hence have achieved a more rigorous classification than previous theoretical studies which rely only on the weak and strong-invariants [46,52] or the mirror-Chern number [162]. The analysis was also performed with modified Becke-Johnson (MBJ) potential [168], which yields the same topological classification, although the separation between $J = 5/2$ and $J = 7/2$ manifolds of bands is bigger than that observed in Fig. 3(a). This suggests MBJ might be a good candidate to capture the separation between $J = 5/2$ and $J = 7/2$ manifolds, without the need for tuning artificially the strength of SOC [169]. Furthermore, we demonstrated that topology originates in SmB_6 as a result of the combination of irreps of $5d$ and $4f$-bands mediated by hybridization. We have in addition presented a tight-binding model for SmB_6 which captures both the symmetry-indicators of topology corresponding to the

material's valence bands, and the interplay between dispersive and heavy-bands which leads to the topology.

Due to the large multiplicity of f-shells, the number of heavy bands around the Fermi level is usually large in heavy-fermion materials. As a consequence, the hybridization between these and dispersive bands might open several gaps below and above the Fermi level. Surface states might arise to connect the sets of disconnected topologically inequivalent bulk-bands on the boundary of the crystal and many of these surface states might be accessible to experimental probes owing to their proximity to the Fermi level. Our TQC based analysis might turn out to be helpful for the prediction of such surface modes, since it makes possible to classify every isolated set of bands separately.

It remains unexplored to which extent holds the applicability of TQC to interacting phases that are not adiabatically connected to band-insulators [80], e.g. Mott insulators. We suggest however that the inclusion of magnetic elementary band correpresentations [34] could make our formalism applicable to magnetic topological heavy-fermion materials, as long as their electronic structure can be described in terms of quasiparticle bands.

Table 8.2: Irreps for the 32 representations $\tilde{\rho}(VB)$ that respect the compatibility relations and their symmetry-based indicators of topology. The remaining (not shown) 32 configurations are complementary to these, as they can be obtained by substracting the listed bands to the whole representation $(\bar{F}_g \uparrow Pm\bar{3}m)_{1a} \oplus (\bar{F}_u \uparrow Pm\bar{3}m)_{1a}$. Bands with an odd value of the $\mathbb{Z}_8$ indicator are strong topological.

Γ	R	X	M	$\mathbb{Z}_4$	$\mathbb{Z}_8$
$\bar{\Gamma}_{11}$	$\bar{R}_{10}$	$\bar{X}_6 \oplus \bar{X}_7$	$\bar{M}_6 \oplus \bar{M}_7$	0	6
$\bar{\Gamma}_{11}$	$\bar{R}_{10}$	$\bar{X}_6 \oplus \bar{X}_7$	$\bar{M}_6 \oplus \bar{M}_9$	2	5
$\bar{\Gamma}_{11}$	$\bar{R}_{10}$	$\bar{X}_6 \oplus \bar{X}_7$	$\bar{M}_8 \oplus \bar{M}_7$	2	1
$\bar{\Gamma}_{11}$	$\bar{R}_{10}$	$\bar{X}_6 \oplus \bar{X}_7$	$\bar{M}_8 \oplus \bar{M}_9$	0	0
$\bar{\Gamma}_{11}$	$\bar{R}_{10}$	$\bar{X}_6 \oplus \bar{X}_9$	$\bar{M}_6 \oplus \bar{M}_7$	1	1
$\bar{\Gamma}_{11}$	$\bar{R}_{10}$	$\bar{X}_6 \oplus \bar{X}_9$	$\bar{M}_6 \oplus \bar{M}_9$	3	0
$\bar{\Gamma}_{11}$	$\bar{R}_{10}$	$\bar{X}_6 \oplus \bar{X}_9$	$\bar{M}_8 \oplus \bar{M}_7$	3	4
$\bar{\Gamma}_{11}$	$\bar{R}_{10}$	$\bar{X}_6 \oplus \bar{X}_9$	$\bar{M}_8 \oplus \bar{M}_9$	1	3
$\bar{\Gamma}_{11}$	$\bar{R}_{10}$	$\bar{X}_8 \oplus \bar{X}_7$	$\bar{M}_6 \oplus \bar{M}_7$	1	5
$\bar{\Gamma}_{11}$	$\bar{R}_{10}$	$\bar{X}_8 \oplus \bar{X}_7$	$\bar{M}_6 \oplus \bar{M}_9$	3	4
$\bar{\Gamma}_{11}$	$\bar{R}_{10}$	$\bar{X}_8 \oplus \bar{X}_7$	$\bar{M}_8 \oplus \bar{M}_7$	3	0
$\bar{\Gamma}_{11}$	$\bar{R}_{10}$	$\bar{X}_8 \oplus \bar{X}_7$	$\bar{M}_8 \oplus \bar{M}_9$	1	7
$\bar{\Gamma}_{11}$	$\bar{R}_{10}$	$\bar{X}_8 \oplus \bar{X}_9$	$\bar{M}_6 \oplus \bar{M}_7$	2	0
$\bar{\Gamma}_{11}$	$\bar{R}_{10}$	$\bar{X}_8 \oplus \bar{X}_9$	$\bar{M}_6 \oplus \bar{M}_9$	0	7
$\bar{\Gamma}_{11}$	$\bar{R}_{10}$	$\bar{X}_8 \oplus \bar{X}_9$	$\bar{M}_8 \oplus \bar{M}_7$	0	3
$\bar{\Gamma}_{11}$	$\bar{R}_{10}$	$\bar{X}_8 \oplus \bar{X}_9$	$\bar{M}_8 \oplus \bar{M}_9$	2	2
$\bar{\Gamma}_{11}$	$\bar{R}_{11}$	$\bar{X}_6 \oplus \bar{X}_7$	$\bar{M}_6 \oplus \bar{M}_7$	2	4
$\bar{\Gamma}_{11}$	$\bar{R}_{11}$	$\bar{X}_6 \oplus \bar{X}_7$	$\bar{M}_6 \oplus \bar{M}_9$	0	3
$\bar{\Gamma}_{11}$	$\bar{R}_{11}$	$\bar{X}_6 \oplus \bar{X}_7$	$\bar{M}_8 \oplus \bar{M}_7$	0	7
$\bar{\Gamma}_{11}$	$\bar{R}_{11}$	$\bar{X}_6 \oplus \bar{X}_7$	$\bar{M}_8 \oplus \bar{M}_9$	2	6
$\bar{\Gamma}_{11}$	$\bar{R}_{11}$	$\bar{X}_6 \oplus \bar{X}_9$	$\bar{M}_6 \oplus \bar{M}_7$	3	7
$\bar{\Gamma}_{11}$	$\bar{R}_{11}$	$\bar{X}_6 \oplus \bar{X}_9$	$\bar{M}_6 \oplus \bar{M}_9$	1	6
$\bar{\Gamma}_{11}$	$\bar{R}_{11}$	$\bar{X}_6 \oplus \bar{X}_9$	$\bar{M}_8 \oplus \bar{M}_7$	1	2
$\bar{\Gamma}_{11}$	$\bar{R}_{11}$	$\bar{X}_6 \oplus \bar{X}_9$	$\bar{M}_8 \oplus \bar{M}_9$	3	1
$\bar{\Gamma}_{11}$	$\bar{R}_{11}$	$\bar{X}_8 \oplus \bar{X}_7$	$\bar{M}_6 \oplus \bar{M}_7$	3	3
$\bar{\Gamma}_{11}$	$\bar{R}_{11}$	$\bar{X}_8 \oplus \bar{X}_7$	$\bar{M}_6 \oplus \bar{M}_9$	1	2
$\bar{\Gamma}_{11}$	$\bar{R}_{11}$	$\bar{X}_8 \oplus \bar{X}_7$	$\bar{M}_8 \oplus \bar{M}_7$	1	6
$\bar{\Gamma}_{11}$	$\bar{R}_{11}$	$\bar{X}_8 \oplus \bar{X}_7$	$\bar{M}_8 \oplus \bar{M}_9$	3	5
$\bar{\Gamma}_{11}$	$\bar{R}_{11}$	$\bar{X}_8 \oplus \bar{X}_9$	$\bar{M}_6 \oplus \bar{M}_7$	0	6
$\bar{\Gamma}_{11}$	$\bar{R}_{11}$	$\bar{X}_8 \oplus \bar{X}_9$	$\bar{M}_6 \oplus \bar{M}_9$	2	5
$\bar{\Gamma}_{11}$	$\bar{R}_{11}$	$\bar{X}_8 \oplus \bar{X}_9$	$\bar{M}_8 \oplus \bar{M}_7$	2	1
$\bar{\Gamma}_{11}$	$\bar{R}_{11}$	$\bar{X}_8 \oplus \bar{X}_9$	$\bar{M}_8 \oplus \bar{M}_9$	0	0

Part III

Approach to interacting topological insulators through the analysis of single-particle Green's functions in terms of topological quantum chemistry

In this part, we will present our research towards the extension of TQC formalism to interacting systems. In particular, we show our work on an approach which consists in analyzing the spectra of single-particle Green's functions within the TQC framework, via the topological Hamiltonian.

The content of this part is organized according to the following structure: In chapter 9, the theoretical framework is introduced. The concepts of Green's functions, spectral function, topological Hamiltonian and cluster perturbation theory are explained there. Then, the Hubbard Diamond Chain and the analysis of its topological phases are presented in chapter 10. In particular, we report the results probing the weakly-relativistic phase diagram via the TQC based analysis of Green's functions, using as benchmark a classification obtained via state-of-the-art methods and many-body topological invariants. This analysis is followed by the study of the effect of SOC, and the interplay between this relativistic correction and strong interactions.

9 Single-particle Green's functions of many-body systems

In quantum mechanics, the Green's function of an independent particle system is defined as the propagator that describes the time-evolution of the wave function. Once the Green's function of the system is calculated by solving its equation of motion, it can be used to obtain an expression for the wave-function as a function of time, as long as its value is know for a previous time. This way of proceeding leads to the path-integral formulation of quantum mechanics [170]. In the context of many-particle physics, Green's functions are defined as quantum amplitudes for processes which consist in the propagation of a particle and/or hole excitation. If the propagation takes place in interacting media, the dynamics of the excitation will be influenced by interactions, and this influence will be captured by the Green's function. This motivates us to consider Green's functions as fundamental objects to investigate ways to classify topology in interacting systems.

9.1 Definition and basis transformation

The (retarded) single-particle Green's function is defined, for fermions[1], as:

$$G_{\nu,\nu'}(t,t') = -i\theta(t-t')\left\langle \{c_\nu(t), c^\dagger_{\nu'}(t')\} \right\rangle . \tag{9.1}$$

where $\theta(t-t')$ is the Heaviside function and $c^\dagger_\nu(t)$ is the operator in Heisenberg's picture which creates a particle at a state labeled by ν.

A variety of different single-particle Green's functions can be defined, like the advanced, the greater and the lesser Green's functions. Here, we stick to the retarded

[1] The definition for bosons is obtained by substituting the anticommutator by a commutator. Since we are interested in the application to electron systems, we restrict here to the case of fermions. Nevertheless, many definitions given through the text are easily generalized for bosons.

Green's function because they are the ones which express propagation forward in time and reduce to the propagators of independent-particles in the path-integral formulation of quantum mechanics. The expectation value $\langle\cdot\rangle$ denotes the thermal trace over the eigenstates of the Hamiltonian:

$$\langle A\rangle = \frac{\mathrm{tr}[\exp(-\beta H A)]}{\mathrm{tr}[\exp(-\beta H)]}, \tag{9.2}$$

where $\beta = (k_B T)^{-1}$ and H is considered within the grandcanonical ensemble. In the limit of zero-temperature, only the ground state contributes to the trace. Moreover, since time-dependent Hamiltonians are out of the focus of our work, the Green's functions we deal with do not depend on both t and t', but on their difference $t - t'$. We will hence simplify our notation by choosing $t' = 0$.

Notice that these Green's functions are many-body objects, as they describe the propagation of a single-particle governed by a many-body Hamiltonian which could include interactions between particles. Furthermore, the thermal trace involves many-body states, thus the propagation takes place in a many-body environment.

Let us now consider the basis transformation $\psi^\dagger(\nu) = \sum_\mu \langle\mu|\nu\rangle\, a^\dagger_\mu$. The expression relating the Green's function in both bases is:

$$G(\boldsymbol{r}, \boldsymbol{r}', t) = \sum_{\mu\mu'} \langle\nu|\mu\rangle\, G_{\mu\mu'}(t)\, \langle\mu'|\nu'\rangle\,. \tag{9.3}$$

In particular, let us illustrate the transformation from real to reciprocal space. We consider that the states in our real-space basis are Wannier functions created by the operators $c^\dagger_{\boldsymbol{R},\alpha}$, where $\boldsymbol{R}$ is a lattice vector denoting the cell the Wannier function belongs to, and α denotes the rest of degrees of freedom (like the spin, orbital type and site within the cell). The reciprocal-space states, which are created by operators $c^\dagger_{\boldsymbol{k},\alpha}$ are related to those in real-space through the following Fourier transform:

$$c^\dagger_{\boldsymbol{k},\alpha} = \frac{1}{\sqrt{\mathcal{N}}} \sum_{\boldsymbol{R}} e^{i\boldsymbol{k}\cdot\boldsymbol{R}}\, c^\dagger_{\boldsymbol{R},\alpha}, \tag{9.4a}$$

$$c^\dagger_{\boldsymbol{R},\alpha} = \frac{1}{\sqrt{\mathcal{N}}} \sum_{\boldsymbol{k}} e^{-i\boldsymbol{k}\cdot\boldsymbol{R}}\, c^\dagger_{\boldsymbol{k},\alpha}, \tag{9.4b}$$

where $\mathcal{N}$ is the number of unit cells in the lattice. According to Eq. (9.3), the relation between the Green's function's real and reciprocal space expressions is:

$$G_{\alpha\beta}(\boldsymbol{k}, t) = \mathcal{N}^{-1} \sum_{\boldsymbol{R}\boldsymbol{R}'} e^{i\boldsymbol{k}\cdot(\boldsymbol{R}-\boldsymbol{R}')} G_{\alpha\beta}(\boldsymbol{R}, \boldsymbol{R}', t). \tag{9.5}$$

The fact that the Green's function depends only on $\boldsymbol{k}$, instead of on $\boldsymbol{k}$ and $\boldsymbol{k}'$, follows from the invariance under translations by vectors of the Bravais lattice – $G_{\alpha\beta}(\boldsymbol{R}, \boldsymbol{R}', t)$

can not depend on $\boldsymbol{R}$ or $\boldsymbol{R}'$, but on their difference $\boldsymbol{R} - \boldsymbol{R}'$.

In addition, we can define the Fourier transform from time t to frequency ω, and *vice versa*, as:

$$G_{\nu,\nu'}(\omega) = \int_{-\infty}^{\infty} \mathrm{d}t\, e^{i(\omega+i\eta)t} G_{\nu,\nu'}(t), \tag{9.6a}$$

$$G_{\nu,\nu'}(t) = (2\pi)^{-1} \int_{-\infty}^{\infty} \mathrm{d}\omega\, e^{-i\omega t} G_{\nu,\nu'}(\omega), \tag{9.6b}$$

$$\tag{9.6c}$$

Here, η is a positive real number introduced *ad hoc* to ensure convergence of the integral. The limit $\eta \to 0^+$ is usually consider at the end of the calculations.

9.2 Single-particle Green's function

Let us consider the application of the Fourier transform to Green's function of independent electrons. For crystals where electron-electron interactions are negligible, the single-particle Green's function takes the following form in the basis of eigenstates of the Hamiltonian $H(\boldsymbol{k})$ [171]:

$$G^{(0)}_{n,n}(\boldsymbol{k}, t) = -i\theta(t) e^{-i\epsilon_n(\boldsymbol{k})t}, \tag{9.7}$$

where $\epsilon_n(\boldsymbol{k})$ is an eigenvalue of $H(\boldsymbol{k})$ and n is the band index. As t goes to infinity, this function keeps oscillating with an undamped amplitude, so the integral in Eq. (9.6a) would not converge without including the term $i\eta$. The Fourier transform from time to frequency reads:

$$G^{(0)}_{n,n}(\boldsymbol{k}, \omega) = \int_{-\infty}^{\infty} \mathrm{d}t\, e^{i(\omega+i\eta)t}(-i)\theta(t) e^{-i\epsilon_n(\boldsymbol{k})t} = \frac{1}{\omega + i\eta - \epsilon_n(\boldsymbol{k})}. \tag{9.8}$$

The poles of the independent-electron Green's function are located, in the frequency axis, at the values for ω which coincide with the eigenstates $\epsilon_n(\boldsymbol{k})$ of the Hamiltonian. They indeed sit slightly below the real-frequency axis for the retarded Green's function, due to the term $i\eta$ included to ensure convergence of the Fourier transformation.

This form of the Green's function is valid for systems which can be described in terms of independent particles. In the case of systems for which these independent particles are quasiparticles rather than the genuine constituents (*e.g.*, electrons), the expression for the single-particle Green's function is similar to Eq. (9.8), but the "renormalized" quasiparticle energy substituting the $\epsilon_n(\boldsymbol{k})$.

9.3 Lehmann representation

The Lehmann representation of the Green's function consists in expressing it in terms of the many-body eigenstates of the Hamiltonian. This representation will be useful to explore some properties of the Green's function, such as the hermiticity. It will also help us to interpret its poles.

We begin the derivation by writing the thermal trace in Eq. (9.1) explicitly for a general basis of states labeled by ν:

$$G_{\nu,\nu'}(t) = -i\mathcal{Z}^{-1}\theta(t)\sum_n e^{-\beta E_n}[\,\langle n|c_\nu(t)c^\dagger_{\nu'}|n\rangle + \langle n|c^\dagger_{\nu'}c_\nu(t)|n\rangle], \tag{9.9}$$

where E_n is the energy of the eigenstate $|n\rangle$ of the Hamiltonian. Let us include the completeness relation $\mathbb{1} = \sum_{n'}|n'\rangle\langle n'|$ between the creation and annihilation operators:

$$\begin{aligned} G_{\nu\nu'}(t) =& -i\mathcal{Z}^{-1}\theta(t)\sum_{n,n'} e^{-\beta E_n}[\,\langle n|c_\nu(t)|n'\rangle\ \langle n'|c^\dagger_{\nu'}|n\rangle + \langle n|c^\dagger_{\nu'}|n'\rangle\ \langle n'|c_\nu(t)|n\rangle] \\ =& -i\mathcal{Z}^{-1}\theta(t)\sum_{n,n'} e^{-\beta E_n}e^{-i(E_{n'}-E_n)t}\,\langle n|c_\nu|n'\rangle\ \langle n'|c^\dagger_{\nu'}|n\rangle \\ & -i\mathcal{Z}^{-1}\theta(t)\sum_{n,n'} e^{-\beta E_n}e^{-i(E_n-E_{n'})t}\,\langle n|c^\dagger_{\nu'}|n'\rangle\ \langle n'|c_\nu|n\rangle \end{aligned} \tag{9.10}$$

where we have used the expression $c_\nu(t) = \exp(iHt)c_\nu\exp(-iHt)$ for the time-dependence of the annihilation operator. By applying the Fourier transform in Eq. (9.6a):

$$G_{\nu\nu'}(\omega) = \mathcal{Z}^{-1}\sum_{n,n'} e^{-\beta E_n}\left[\frac{\langle n|c_\nu|n'\rangle\ \langle n'|c^\dagger_{\nu'}|n\rangle}{\omega+i\eta-(E_{n'}-E_n)} + \frac{\langle n|c^\dagger_{\nu'}|n'\rangle\ \langle n'|c_\nu|n\rangle}{\omega+i\eta-(E_n-E_{n'})}\right] \tag{9.11}$$

The first fraction in the sum describes the propagation of particle excitations, while the second term corresponds to hole excitations. Each of these fraction is a reminder of the independent-electron Greens function in Eq. (9.8). The fundamental difference is that, instead of having a single pole, the single-particle Green's function of an interacting system is a sum of a plethora of poles. Furthermore, the denominator of each pole can now be smaller than one, unlike in the independent-electron case. As we will show later, when introducing the spectral function, that the number in the denominator can be interpreted as its weight.

In order to reach further in the interpretation, let us consider the $T = 0$ limit, where

only the ground state $|\Psi_0\rangle$ (of energy E_0) contributes to the thermal trace[2]:

$$G_{\nu\nu'}(\omega) = \sum_n \left[\frac{\langle\Psi_0|c_\nu|n\rangle\ \langle n|c^\dagger_{\nu'}|\Psi_0\rangle}{\omega + i\eta - (E_n - E_0)} + \frac{\langle\Psi_0|c^\dagger_{\nu'}|n\rangle\ \langle n|c_\nu|\Psi_0\rangle}{\omega + i\eta - (E_0 - E_n)} \right] \tag{9.12}$$

We focus first on the particle contribution, for which the states $|n\rangle$ are eigenstates of H belonging to the subspace $\mathcal{H}_{N+1}$ of the Hilbert space, where N is the number of particles in the system. The pole of the non-interacting Green's function splits into a plethora of poles upon inclusion of interactions, each pole corresponding to an eigenstate of the Hamiltonian and having as weight the overlap of that eigenstate with the state generated by adding to (extracting from) the ground state a particle at the state labeled by ν' (ν). When the weight of a pole is zero, it does not contribute to the Green's function. This discussion is similarly applicable to the hole contribution, but the states $|n\rangle$ belong to the subspace $\mathcal{H}_{N-1}$ of the Fock space.

Concerning the location of poles, those corresponding to particle excitations sit on the positive side of the frequency axis, whereas the poles of hole excitations are on the negative side. This property stems from the fact that, by definition, $E_n > E_0$ for both cases, and holds only in the $T = 0$ limit. At finite temperature, other states apart from the ground state might take part in the thermal trace. These states make contribute with particle (hole) poles located at negative (positive) frequencies.

9.4 Spectral function

The spectral function $A(\boldsymbol{k}, \omega)$ is the physical quantity defined as:

$$A(\boldsymbol{k}, \omega) = -\pi^{-1} \operatorname{Im} G(\boldsymbol{k}, \omega). \tag{9.13}$$

To motivate the interpretation of the spectral function, let us first calculate its expression for the case of independent particles via Eq. (9.8):

$$A^{(0)}_n(\boldsymbol{k}, \omega) = -\pi^{-1} \operatorname{Im} G^{(0)}_{n,n}(\boldsymbol{k}, \omega) = \delta(\omega - \epsilon_n(\boldsymbol{k})). \tag{9.14}$$

The Dirac's delta arises upon taking the limit $\eta \to 0^+$. We read from this result that a particle in the state labeled by n can be added to the ground state only with energy $\omega = \epsilon_n(\boldsymbol{k})$. The spectral function $A^{(0)}_n(\boldsymbol{k}, \omega)$ can hence be interpreted as the energy resolution for a particle created in the state labeled by n, that is, like a density of states resolved for a certain quantum state.

We will now give three evidences to convince ourselves about this interpretation. Let us begin by deriving the spectral function for the interacting Green's function in

[2]We will consider that the ground state is non-degenerate, as this is the case of insulators

Eq. (9.11):

$$A_{\nu\nu'}(\omega) = \mathcal{Z}^{-1} \sum_{n,n'} e^{-\beta E_n} [\, \langle n|c_\nu|n'\rangle \, \langle n'|c^\dagger_{\nu'}|n\rangle \, \delta(\omega - (E_{n'} - E_n)) \\ + \, \langle n|c^\dagger_{\nu'}|n'\rangle \, \langle n'|c_\nu|n\rangle \, \delta(\omega - (E_n - E_{n'}))]. \tag{9.15}$$

First, we calculate the integral of $A_{\nu,\nu'}(\boldsymbol{k},\omega)$ for all frequencies:

$$\begin{aligned} &\int_{-\infty}^{\infty} \mathrm{d}\omega \, A_{\nu,\nu'}(\boldsymbol{k},\omega) \\ &= \mathcal{Z}^{-1} \sum_{n,n'} e^{-\beta E_n} [\, \langle n|c_\nu|n'\rangle \, \langle n'|c^\dagger_{\nu'}|n\rangle + \langle n|c^\dagger_{\nu'}|n'\rangle \, \langle n'|c_\nu|n\rangle] \\ &= \mathcal{Z}^{-1} \sum_{n} e^{-\beta E_n} \, \langle n|\{c_\nu, c^\dagger_{\nu'}\}|n\rangle \\ &= \delta_{\nu,\nu'}. \end{aligned} \tag{9.16}$$

The spectral function $A_\nu(\boldsymbol{k},\omega)$ is thus normalized so that its integral is equal to the number of electrons the state labeled by ν can host. Second, it is easy to check that $A_\nu(\boldsymbol{k},\omega) > 0$ for $\forall\omega \in \mathbb{R}$ and $\forall\boldsymbol{k} \in \mathrm{BZ}$. Third, it can be show [171] that the mean-number of particles in the state labeled by ν is:

$$\langle n_\nu \rangle = \langle c^\dagger_\nu c_\nu \rangle = \int_{-\infty}^{\infty} \mathrm{d}\omega \, A_\nu(\boldsymbol{k},\omega) n_F(\omega). \tag{9.17}$$

where $n_F(\omega)$ is the Fermi-Dirac distribution function. The spectral function is playing the role of a density of states in this expression.

The three arguments given here corroborate that the spectral function $A_\nu(\boldsymbol{k},\omega)$ can be interpreted as a ν-resolved density of states. Therefore, the complete density of states $\rho(\omega)$ of a system can be obtained from the trace of the spectral function:

$$\rho(\omega) = \mathcal{N}^{-1} \sum_{\boldsymbol{k}} \mathrm{tr}\, A(\boldsymbol{k},\omega). \tag{9.18}$$

$\mathcal{N}$ is the number of unit cells here. In conclusion, the density of states of the system can be extracted from the single-particle Green's function via the spectral function. This quantity can be used, for example, to determine if the system is an insulator and to calculate its gap.

9.5 Matsubara Green's functions

Until this point, our focus has been on retarded Green's functions. These Green's functions describe the propagation of excitations forward in time, and allow for the de-

termination of important quantities, such as the particle number. Nevertheless, in the condensed matter physics, it is common to find texts written in terms of a kind of more abstract Green's functions, called imaginary-time Green's functions. There are mainly two reasons for this: first, imaginary-time Green's functions admit a perturbative expansion which can be worked out in terms of Feynman diagrams. In addition, sums over frequencies – which often arise in diagramatic expansions – can be efficiently mapped to sums over poles of imaginary-time Green's functions, which facilitates their computation. Furthermore, retarded Green's functions can be derived from imaginary-time functions by analytical continuation.

Although imaginary-time Green's functions are not fundamental to understand our work, we offer here a brief introduction to them, which is intended to serve as a reference of the basic properties of these Green's functions. This decision is motivated by three points: First, the introduction of the self-energy feels more natural in the context of imaginary-time Green's functions, as it is a quantity defined usually in the language of Feynman diagrams. Second, most of the seminal works about the topological Hamiltonian are written in terms of these Green's functions, and we would like to be consistent with this notation. Third, we feel that it is sensible to present – at least briefly – these type of Green's functions in a thesis about an application of Green's functions in condensed matter physics, since they are commonly find in the literature, *e.g.* in the first works about cluster perturbation theory.

We will begin defining single-particle imaginary-time Green's functions and listing some of their remarkable properties, to then derive their frequency-regime expression. Finally, we will present the Lehmann representation for these Green's functions and their connection to retarded Green's functions.

9.5.1 Definition and properties

The imaginary-time formalism is based on the substitution[3] of $it \to \tau$, which is motivated by the similarity between the operator $\exp(-\beta H)$ and the time-evolution operator $\exp(-iHt)$. This substitution permits the expansion of both operators as time-ordered exponentials in the interaction picture, and leads hence to a simplified expression for the Green's function [171]. This expression can then be expanded conveniently within a perturbation theory approach, and computed (approximately) via Feynman diagrams. For a deeper look into this method, we refer to Refs. [38, 171, 172].

The single-particle imaginary-time Green's function, also called *Matsubara Green's function*, is defined as:

$$G_{\nu,\nu'}(\tau) = -\left\langle \hat{T} c_\nu(\tau), c^\dagger_{\nu'}(0) \right\rangle, \tag{9.19}$$

where the expectation value and $\hat{T}$ denote the thermal trace in Eq. (9.2) and time-

[3]This substitution has no physical meaning. It must be interpreted as a purely mathematical trick applied just for convenience.

ordering, respectively. If we expand the ordering in time, this expression reads:

$$G_{\nu,\nu'}(\tau) = -\theta(\tau)\left\langle c_\nu(\tau)c^\dagger_{\nu'}(0)\right\rangle + \theta(-\tau)\left\langle c^\dagger_{\nu'}(0)c_\nu(\tau)\right\rangle. \tag{9.20}$$

We will now prove two properties of Matsubara Green's functions which have important consequences when their transformation to frequency-regime is considered. First of all, let us study the convergence of $G_{\nu,\nu'}(\tau)$. We concentrate for that on the $\tau > 0$ case:

$$G_{\nu,\nu'}(\tau > 0) = -\mathcal{Z}^{-1}\,\mathrm{tr}\left(e^{-\beta H}e^{\tau H}c_\nu e^{-\tau H}c^\dagger_{\nu'}\right) \tag{9.21}$$

$$= -\mathcal{Z}^{-1}\sum_n e^{-(\beta-\tau)E_n}\,\langle n|c_\nu e^{-\tau H}c^\dagger_{\nu'}|n\rangle \tag{9.22}$$

where E_n and $|n\rangle$ are eigenvalues and eigenstates of the Hamiltonian H. The convergence of this function is not ensured for $\tau > \beta = (k_B T)^{-1}$, because the exponential in the sum grows fast as the energies of the excited states keep increasing. It can be similarly shown that this result applies also for $\tau < -\beta$. The convergence of $G_{\nu,\nu'}(\tau)$ is therefore ensured only for the domain $\tau \in (-\beta, \beta)$. Accordingly, we consider that the domain of the Matsubara Green's function is restricted to this region.

The second property of interest is the (anti)periodicity. Let us consider that the function $G_{\nu,\nu'}(\tau+\beta)$ for $\tau < 0$:

$$\begin{aligned} G_{\nu,\nu'}(\tau+\beta) &= -\mathcal{Z}^{-1}\,\mathrm{Tr}\left[e^{-\beta H}e^{(\tau+\beta)H}c_\nu e^{-(\tau+\beta)H}c^\dagger_{\nu'}\right] \\ &= -\mathcal{Z}^{-1}\,\mathrm{Tr}\left[e^{-\beta H}c^\dagger_{\nu'}e^{\tau H}c_\nu e^{-\tau H}\right] \\ &= \left\langle \hat{T}c_\nu(\tau)c^\dagger_{\nu'}\right\rangle \\ &= -G_{\nu,\nu'}(\tau). \end{aligned} \tag{9.23}$$

This property is written shortly as[4]:

$$G_{\nu,\nu'}(\tau+\beta) = -G_{\nu,\nu'}(\tau), \quad -\beta < \tau < 0. \tag{9.24}$$

9.5.2 Fourier transform to Matsubara frequencies

The transformation of Matsubara Green's functions from time to frequency-regime is worked out in this section. Unlike in the case of retarded Green's functions, the transformation here is driven by a Fourier series of discrete frequencies, since the domain of

[4]The Matsubara Green's function is periodic, instead of antiperiodic, for bosons.

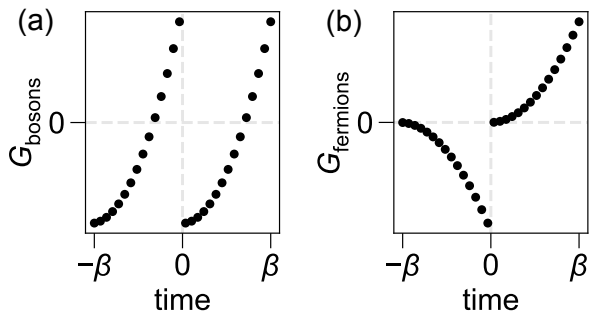

Figure 9.1: Illustration of the periodicity/antiperiodicity of the Matsubara Green's function for (a) bosons and (b) fermions.

τ was chosen to be the interval $\tau \in (-\beta, \beta)$:

$$G_{\nu,\nu'}(n) = \frac{1}{2}\int_{-\beta}^{\beta} \mathrm{d}\tau\, e^{i\pi n\tau/\beta} G_{\nu,\nu'}(\tau). \tag{9.25}$$

Let us consider now the antiperiodicity property proved in the previous section:

$$\begin{aligned} G_{\nu,\nu'}(n) &= \frac{1}{2}\int_{0}^{\beta} \mathrm{d}\tau\, e^{i\pi n\tau/\beta} G_{\nu,\nu'}(\tau) + \frac{1}{2}\int_{-\beta}^{0} \mathrm{d}\tau\, e^{i\pi n\tau/\beta} G_{\nu,\nu'}(\tau) \\ &= \frac{1}{2}\int_{0}^{\beta} \mathrm{d}\tau\, e^{i\pi n\tau/\beta} G_{\nu,\nu'}(\tau) + e^{-i\pi n}\frac{1}{2}\int_{0}^{\beta} \mathrm{d}\tau\, e^{i\pi n\tau/\beta} G_{\nu,\nu'}(\tau-\beta) \\ &= \frac{1}{2}(1-e^{-i\pi n})\int_{0}^{\beta} \mathrm{d}\tau\, e^{i\pi n\tau/\beta} G_{\nu,\nu'}(\tau). \end{aligned} \tag{9.26}$$

The factor $(1 - e^{-i\pi n})$ vanishes for n even. In conclusion, the frequency-regime expression for the Matsubara Green's function involves discrete frequencies ω_n which are odd multiples of π/β. The transformation between imaginary time to frequency reads finally:

$$G_{\nu,\nu'}(i\omega_n) = \int_{0}^{\beta} \mathrm{d}\tau\, e^{i\omega_n\tau} G_{\nu,\nu'}(\tau), \tag{9.27}$$

$$G_{\nu,\nu'}(\tau) = \frac{1}{\beta}\sum_{n=-\infty}^{\infty} e^{-i\omega_n\tau} G_{\nu,\nu'}(i\omega_n). \tag{9.28}$$

The frequencies ω_n are known as **Matsubara frequencies**. Notice that the separation between successive values for ω_n depends on the temperature. In fact, it decreases together with temperature, and become continuous in the $T = 0$ limit.

9.5.3 Relation between Matsubara and retarded Green's functions

The connection between retarded and Matsubara Green's functions is better identified by comparing their Lehmann representation. We demonstrated that the retarded Green's function can be written as [Eq. (9.11)]:

$$G_{\nu\nu'}(\omega) = \mathcal{Z}^{-1} \sum_{n,n'} e^{-\beta E_n} \left[\frac{\langle n|c_\nu|n'\rangle \ \langle n'|c^\dagger_{\nu'}|n\rangle}{\omega + i\eta - (E_{n'} - E_n)} + \frac{\langle n|c^\dagger_{\nu'}|n'\rangle \ \langle n'|c_\nu|n\rangle}{\omega + i\eta - (E_n - E_{n'})} \right]. \tag{9.29}$$

Following the same steps as those given in Sec. 9.3 to derive this equation, a similar representation can be obtained for the Matsubara Green's function:

$$G_{\nu\nu'}(i\omega_n) = \mathcal{Z}^{-1} \sum_{n,n'} e^{-\beta E_n} \left[\frac{\langle n|c_\nu|n'\rangle \ \langle n'|c^\dagger_{\nu'}|n\rangle}{i\omega_n + i\eta - (E_{n'} - E_n)} + \frac{\langle n|c^\dagger_{\nu'}|n'\rangle \ \langle n'|c_\nu|n\rangle}{i\omega_n + i\eta - (E_n - E_{n'})} \right] \tag{9.30}$$

The comparison between Eqs. (9.29) and (9.30) indicates that both the retarded Green's function $G_{\nu,\nu'}(\omega)$ and the Matsubara Green's function $G_{\nu,\nu'}(i\omega_n)$ can be obtained from the same function $G(z)$ defined as:

$$G_{\nu\nu'}(i\omega) = \mathcal{Z}^{-1} \sum_{n,n'} e^{-\beta E_n} \left[\frac{\langle n|c_\nu|n'\rangle \ \langle n'|c^\dagger_{\nu'}|n\rangle}{z + i\eta - (E_{n'} - E_n)} + \frac{\langle n|c^\dagger_{\nu'}|n'\rangle \ \langle n'|c_\nu|n\rangle}{z + i\eta - (E_n - E_{n'})} \right], \tag{9.31}$$

where z is a complex variable. This function $G(z)$, called **analytical continuation** of $G(\omega)$ and $G(i\omega_n)$, is analytical in the whole complex plane, except on the real axis. In fact, $G(i\omega_n)$ is obtained by evaluating $G(z)$ in discrete values of the imaginary axis, whereas the retarded function $G(\omega)$ is generated by substituting in $G(z)$ values for z which are infinitesimally close to the real axis, *i.e.* $G(\omega) = G(z \to \omega + i\eta)$. Furthermore, $G(z)$ is unique, in the sense that any other analytical continuation function should be identical to it [171].

In conclusion, once the Matsubara Green's function $G(i\omega_n)$ has been calculated, the retarded Green's function $G(\omega)$ can be obtained as $G(\omega) = G(\omega_n \to \omega + i\eta)$. This turns out to be handy in practice, as the Matsubara Green's function tends to be easier to calculate.

9.6 Topological invariants from Green's functions: topological Hamiltonian

Green's functions are considered in this work as a tool to investigate the topology of interacting systems. In this section, we will introduce the calculation of topological

invariants and diagnosis of topological phases in terms of Green's functions, using the so-called topological Hamiltonian.

The first topological invariants proposed in terms of single-particle Green's functions stemmed from topological-field theory methods [73–75]. The major drawback of these invariants is that their application in numerical approaches turns out to be complicate, as they require the evaluation of complex expressions involving Green's funtions. In 2012, Z. Wang *et al.* [42, 43] proposed a shortcut to overcome this difficulty, which consists in the diagnosis of topology via the Green's function at zero frequency. This alternative method simplifies the investigation of the topology in two aspects: On the one hand, it does not require the Green's function to be computed for all frequencies, but only at $\omega = 0$. On the other hand, it allows for the application of tools which are known for their use in the non-interacting case, like Wilson loops and EBRs – already introduced in this work.

The key insight which motivated this shortcut was the realization that the Green's function $G(\boldsymbol{k}, i\omega_n)$ is connected to the quantity $[i\omega_n - G^{-1}(\boldsymbol{k}, 0)]^{-1}$, via the following mapping [42]:

$$G(\boldsymbol{k}, i\omega_n, \lambda) = (1-\lambda)G(\boldsymbol{k}, i\omega_n) + \lambda[i\omega_n - G^{-1}(\boldsymbol{k}, 0)]^{-1}, \tag{9.32}$$

where $\lambda \in [0, 1]$ is a parameter driving the mapping. Under certain conditions, this connection is smooth, meaning that both ends share the same topological properties. Furthermore, the topological phase of $[i\omega_n - G^{-1}(\boldsymbol{k}, 0)]^{-1}$ is determined by its value at $i\omega_n = 0$, *i.e.* by $G(\boldsymbol{k}, 0)$. Summarizing, when a certain set of conditions are satisfied, .

As it was explored in Ref. [44], which is the result of a collaboration with Dominik Lessnich and other members of the group of Dr. Roser Valentí, if $G(\boldsymbol{k}, i\omega_n)$ satisfies the following conditions, the study of its topology can be tackled by exploring $G(\boldsymbol{k}, 0)$:

I. The spectral function $A(\boldsymbol{k}, \omega)$ has a finite gap around $\omega = 0$. This means that the ground state is non-degenerate with respect to one particle/hole excitations. We further assume that it is completely non-degenerate.

II. $G(\boldsymbol{k}, 0)$ is non-singular, *i.e.* neither of its eigenvalue vanishes.

It should be mentioned that we assume that the ground state, apart from being non-degenerate, respects the symmetries of the lattice. This assumption leaves some systems out of the scope of this work, for example, crystals with magnetically ordered ground states where the moments lower the symmetry of the lattice, as their ground states display lower symmetry than the Hamiltonian.

For the remaining of this section, we restrict ourselves to the physics at $T = 0$. In this limit, the Lehmann representation in Eq. (9.30) is simplified to the following

expression [5]:

$$G_{\nu\nu'}(i\omega) = \mathcal{Z}^{-1} \sum_n \left[\frac{\langle 0|c_\nu|n\rangle \, \langle n|c^\dagger_{\nu'}|0\rangle}{i\omega - (E_n - E_0)} + \frac{\langle 0|c^\dagger_{\nu'}|n\rangle \, \langle n|c_\nu|0\rangle}{i\omega - (E_0 - E_n)} \right]. \tag{9.33}$$

The condition-I above ensures that $E_0 \neq E_n$, for all eigenstates $|n\rangle$ of the Hamiltonian with $N \pm 1$ particles, where N is the number of particles in the ground state of energy E_0. Consequently, the Green's function at $i\omega = 0$ is hermitian, as it can be shown from Eq. (9.33):

$$\begin{aligned} [G_{\nu'\nu}(0)]^* &= \mathcal{Z}^{-1} \sum_n \left[\frac{\langle n|c'^\dagger_\nu|0\rangle \, \langle 0|c_\nu|n\rangle}{-(E_n - E_0)} + \frac{\langle n|c_\nu|0\rangle \, \langle 0|c^\dagger_{\nu'}|n\rangle}{-(E_0 - E_n)} \right] \\ &= G_{\nu\nu'}(0) \end{aligned} \tag{9.34}$$

Based on its hermiticity, Z. Wang *et al.* proposed using $H_T(\boldsymbol{k}) = -G^{-1}(\boldsymbol{k}, 0)$, dubbed **the topological Hamiltonian**, as an effective independent-particle Hamiltonian whose topology could be explored via conventional methods used for non-interacting systems. As we showed in chapters 3 and 5, these methods involve either the calculation of Wilson loops of occupied bands or the irreducible representations of such states. Let us denote $|\alpha(\boldsymbol{k})\rangle$ and eigenstate of $H_T(\boldsymbol{k})$ with eigenvalue $\mu_\alpha(\boldsymbol{k})$:

$$H_T(\boldsymbol{k}) \, |\alpha(\boldsymbol{k})\rangle = \mu_\alpha(\boldsymbol{k}) \, |\alpha(\boldsymbol{k})\rangle \, . \tag{9.35}$$

The state $|\alpha(\boldsymbol{k})\rangle$ is said to be a right zero (R-zero) if $\mu_\alpha(\boldsymbol{k}) < 0$, while it is called left zero (L-zero) if $\mu_\alpha(\boldsymbol{k}) > 0$. R-zeros play the role of occupied states in the analysis of the topological Hamiltonian.

Expressions for invariants proposed within the framework of topological band theory could be computed for the R-zeros of the topological Hamiltonian. Based on the connection in Eq. (9.32), it can be demonstrated that some of these invariants match with the aforementioned invariants derived in terms of topological-field theories, and are hence numerically more accessible alternatives to them. For example, the Chern number calculated for the R-zeros [42] matches with the hard-to-apply invariant N_2 proposed in Ref. [74]. Similarly, applying Fu-Kane's criterion to R-zeros [43] leads to a value for the invariant P_3 derived in Ref. [74] for time-reversal symmetric interacting systems.

Transitions between topologically different phases (in the same symmetry group) require changing the topology of the set of R-zeros via the exchange of states with L-zeros. In analogy with the non-interacting case, this involves closing the gap between R and L-zeros, which can not happen while $A(\omega, \boldsymbol{k})$ remains vanishing in a region around $A(\omega, \boldsymbol{k})$ [44]. Such a transition violates the condition I above for the applicability of the topological Hamiltonian. In addition, there exists another mechanism for the transition

[5] An alternative demonstration can be found in Ref. [44]

between different topological phases, which is absent for non-interacting systems. This phase transition consists in the violation of condition II: as the parameters governing the system are tuned, an eigenvalue of $G(\boldsymbol{k}, 0)$ vanishes at some point – equivalently, an eigenstate $\mu_\alpha(\boldsymbol{k})$ of $H_T(\boldsymbol{k})$ becomes diverging – and the topological Hamiltonian becomes ill defined. As we go on tuning the parameters, $G(\boldsymbol{k}, 0)$ turns again into a non-singular matrix, and the set of R-zeros hosts a topological phase different from the initial one. This mechanism was reported in an analysis of the phase transition in the interacting Su–Schrieffer–Heeger model [44].

The fact that $H_T(\boldsymbol{k})$ works as an effective Hamiltonian whose topology can be explored via techniques developed for non-interacting systems encouraged us to consider also the application of TQC to it. The first step in such an approach was to demonstrate that the symmetry group of $H_T(\boldsymbol{k})$ is the space group of the system – for non-degenerated ground states which preserve all symmetries of the Hamiltonian. Furthermore, $H_T(\boldsymbol{k})$ transforms under the symmetries in the same fashion as non-interacting Hamiltonians [44]. The formalism theory of symmetry representations and TQC can thus be applied straightforwardly to the topological Hamiltonian.

The rest of the section is devoted to shedding some light on the physical interpretation of the topological Hamiltonian. The discussion given below is inspired mainly by the ideas reported in Ref. [173]. Let us write the Green's function $G(\boldsymbol{k}, i\omega)$ in the following way, in terms of the independent-particle part $H_0(\boldsymbol{k})$ of the Hamiltonian:

$$G(\boldsymbol{k}, i\omega) = \frac{1}{i\omega - H_0(\boldsymbol{k}) - \Sigma(\boldsymbol{k}, i\omega)}, \tag{9.36}$$

$\Sigma(\boldsymbol{k}, i\omega)$ denotes here the **self-energy** of the electron. The self-energy can be defined as the sum of scattering diagrams that can not be split into two pieces by cutting a single propagator [38, 171], within the context of a perturbation theory based approach to Green's functions. Since such an approach lies out of the scope of this work, we could define the $\Sigma(\boldsymbol{k}, i\omega)$ as the the difference between the inverse of interacting and non-interacting single-particle Green's functions:

$$\Sigma(\boldsymbol{k}, i\omega) = G^{-1}(\boldsymbol{k}, i\omega) - G_0^{-1}(\boldsymbol{k}, i\omega), \tag{9.37}$$

where $G_0(\boldsymbol{k}, i\omega) = [i\omega - H_0(\boldsymbol{k})]^{-1}$ is the Green's function for independent particles [Eq. (9.8)]. This expression points out the fact that the information about interactions contained in the Green's function is encoded in $\Sigma(\boldsymbol{k}, i\omega)$.

According to Eqs. (9.36), the topological Hamiltonian can be written in the following form, in terms of the self-energy:

$$H_T(\boldsymbol{k}) = H_0(\boldsymbol{k}) + \Sigma(\boldsymbol{k}, 0). \tag{9.38}$$

This expression suggests that $H_T(\boldsymbol{k})$ could be interpreted as an effective Hamiltonian

that describes the renormalized-quasiparticle bands, but this perspective turns out to be a bit naive. The states $|\psi_\alpha(\boldsymbol{k})\rangle$ corresponding to the quasiparticles of the system would indeed be eigenstates of $H_0(\boldsymbol{k}) + \Sigma(\boldsymbol{k}, \omega)$ [173]:

$$[H_0(\boldsymbol{k}) + \Sigma(\boldsymbol{k}, \omega_\alpha)] \, |\psi_\alpha(\boldsymbol{k})\rangle = \omega_\alpha(\boldsymbol{k}) \, |\psi_\alpha(\boldsymbol{k})\rangle \, . \tag{9.39}$$

In this expression for the spectrum of quasiparticles, the self-energy depends (self-consistently) on the eigenvalue $\omega_\alpha(\boldsymbol{k})$, unlike in the topological Hamiltonian's spectrum where it is restricted to the value $\omega = 0$. Therefore, $H_T(\boldsymbol{k})$ is not the Hamiltonian corresponding to the quasiparticles of the system. It might be instead interpreted as the Hamiltonian of an auxiliary non-interacting system with the same topology as the genuine interacting system[6]. In fact, in Ref. [173], it was shown that for the interacting Thouless Pump's model [Sec. 3.4.3] the quasiparticle Hamiltonian fails to capture the topology, while the topological Hamiltonian turns out to be successful.

Another point which might be obscure about the topological Hamiltonian is the following: taking into account that particle/hole excitations can not propagate at $\omega = 0$ as $A(\boldsymbol{k}, \omega) = 0$ in a region around $\omega = 0$, how could the topology be captured by the Green's function at this frequency? It is captured because zero-energy boundary states are described by states which are, at the same time, eigenstates of $H_T(\boldsymbol{k})$ and the quasiparticle Hamiltonian with $\omega_\alpha = 0$ in Eq. (9.39), *i.e.* the projections onto the boundaries of these two Hamiltonians match, and the information about zero-energy boundary states is hence captured by $H_T(\boldsymbol{k})$.

9.7 Cluster perturbation theory: a method to calculate Green's functions

We briefly introduce cluster perturbation theory (CPT) and its implementation to obtain single-particle Green's functions for Hubbard models on a lattice. The basic idea behind CPT is to divide the lattice into a superlattice of clusters. The Hubbard model on each cluster is solved exactly, whereas the hoppings between sites belonging to different clusters are treated perturbatively. More details about the method and its applicability can be found in Refs. [175–179].

We consider the general form of the Hubbard Hamiltonian:

$$H = \sum_{\boldsymbol{r}\boldsymbol{r}'\sigma} t_{\boldsymbol{r}\sigma,\boldsymbol{r}'\sigma} c^\dagger_{\boldsymbol{r}\sigma} c_{\boldsymbol{r}'\sigma} + \sum_{\boldsymbol{r}} U n_{\boldsymbol{r}\uparrow} n_{\boldsymbol{r}\downarrow}. \tag{9.40}$$

where $c^\dagger_{\boldsymbol{r}\sigma}$ ($c_{\boldsymbol{r}\sigma}$) creates (annihilates) an electron with spin σ at site $\boldsymbol{r}$ and $t_{\boldsymbol{r}\sigma,\boldsymbol{r}'\sigma}$ is the hopping amplitude of an electron with spin σ from site $\boldsymbol{r}'$ to $\boldsymbol{r}$.

[6] This interpretation of the topological Hamiltonian resembles the idea of the Kohn-Sham Hamiltonian in DFT [174].

The kinetic term of Eq. (9.40) can be written in a form that shows the tiling of the lattice into clusters:

$$H = \sum_{ij} \mathbf{c}_i^\dagger \, t^{(i,j)} \mathbf{c}_j + \sum_{\boldsymbol{r}} U n_{\boldsymbol{r}\uparrow} n_{\boldsymbol{r}\downarrow}, \tag{9.41}$$

where $i, j = 1, ..., L$ with L the number of clusters in the crystal. $t^{(i,j)}$ is here the block of the hopping matrix containing terms which couple sites of the cluster ξ_i to those of cluster ξ_j, and $\mathbf{c}_j$ is the column-vector of annihilation operators corresponding to sites in cluster ξ_j. The Hamiltonian $H^{(i)}$ of a particular cluster is obtained by choosing from Eq. (9.41) the kinetic and interaction terms that involve only sites within the cluster ξ_i. Mathematically, this corresponds to taking a block matrix $t^{(i,i)}$ in the diagonal of the hopping matrix:

$$H^{(i)} = \mathbf{c}_i^\dagger t^{(i,i)} \mathbf{c}_i + \sum_{\boldsymbol{r} \in \xi_i} U n_{\boldsymbol{r}\uparrow} n_{\boldsymbol{r}\downarrow}. \tag{9.42}$$

The ground-state of $H^{(i)}$ is calculated with exact diagonalization [178, 180] and used to construct the cluster Green's function $G^{(i)}(i\omega)$:

$$G^{(i)}(i\omega) = \left[i\omega - t^{(i,i)} - \Sigma^{(i)}(i\omega) \right]^{-1}, \tag{9.43}$$

where $\Sigma^{(i)}(i\omega)$ is the self-energy of ξ_i. The main approximation of CPT consists in constructing the lattice self-energy $\Sigma(i\omega)$ as direct sum of cluster self-energies, i.e., as a block diagonal matrix where each block is the self-energy of a cluster:

$$\Sigma(i\omega) = \bigoplus_i \Sigma^{(i)}(i\omega). \tag{9.44}$$

The Dyson equation relating the lattice Green's function $G(i\omega)$ and self-energy $\Sigma(i\omega)$ reads:

$$[G(i\omega)]^{-1} = i\omega - t - \Sigma(i\omega), \tag{9.45}$$

where t is the hopping matrix. Combining Eqs. (9.43), (9.44) and (9.45) leads to the following expression for $G(i\omega)$:

$$[G(i\omega)]^{-1} = \bigoplus_i [G^{(i)}(i\omega)]^{-1} - t_{\text{inter}}. \tag{9.46}$$

Here, t_{inter} denotes the matrix obtained by removing the blocks in the diagonal of the hopping matrix t, *i.e.* the hopping matrix including only terms that couple different

clusters. Written in matrix form, Eq.(9.46) reads:

$$[G(i\omega)]^{-1} = \begin{bmatrix} [G^{(1)}(i\omega)]^{-1} & -t^{(1,2)} & \dots & -t^{(1,L)} \\ -t^{(2,1)} & [G^{(2)}(i\omega)]^{-1} & \dots & -t^{(2,L)} \\ \vdots & \vdots & \ddots & \vdots \\ -t^{(L,1)} & -t^{(L,2)} & \dots & [G^{(L)}(i\omega)]^{-1} \end{bmatrix}.$$

CPT inherits its name from the fact that Eq. (9.46) can be derived by isolating t_{inter} in Eq. (9.41), treating it as a perturbation to the rest of terms and conserving only first order terms [176, 181].

The Green's function $G(i\omega)$ in Eq. (9.46) is written in real-space. However, our focus is on the calculation of the Green's function in reciprocal space, $G(\boldsymbol{k}, i\omega)$, as the topological Hamiltonian and the $\boldsymbol{k}$-resolved spectral function $A(\boldsymbol{k}, \omega)$ are related directly to it. Due to the technicalities of the lattice's tiling into clusters, calculating $G(\boldsymbol{k}, i\omega)$ from Eq. (9.46) turns out to be more subtle than just taking a Fourier transform to reciprocal space. In the rest of this section, we go meticulously through this process.

We denote γ the Bravais lattice of the crystal and Γ the superlattice formed by the tiling into clusters ($\gamma \subset \Gamma$). When all clusters are of the same kind, that is, when all $H^{(i)}$ are related by a translation of γ, a supercell containing a single cluster may be chosen [see Figs. **9.2**(a) and Fig. **9.2**(b)]; otherwise, the primitive supercell of Γ will contain more than one primitive cells of γ. Let $\boldsymbol{r}$ and $\tilde{\boldsymbol{r}}$ indicate lattice vectors of γ and Γ, respectively. Every vector $\boldsymbol{r}$ can be decomposed in a univocal form as $\boldsymbol{r} = \tilde{\boldsymbol{r}} + \boldsymbol{R}$, where $\boldsymbol{R}$ is a vector of γ. The notation is illustrated in Fig. **9.3**(a) .

Furthermore, we denote $c^\dagger_{\boldsymbol{r}} = c^\dagger_{\tilde{\boldsymbol{r}},\boldsymbol{R}}$ the operator which creates an electron in the site $\boldsymbol{r}$ – we will not indicate other degrees of freedom, like the site of the WP, the orbital type or spin, for the sake of simplicity in the notation. We adopt the Fourier transform in Eq. (9.4a) to represent this creation operation in reciprocal space:

$$c^\dagger_{\boldsymbol{k}} = \mathcal{N}^{-1/2} \sum_r e^{i\boldsymbol{k}\cdot\boldsymbol{r}} = \mathcal{N}^{-1/2} \sum_{\tilde{\boldsymbol{r}},\boldsymbol{R}} e^{i\boldsymbol{k}\cdot(\tilde{\boldsymbol{r}}+\boldsymbol{R})}, \tag{9.47}$$

where $\mathcal{N}$ is the number of primitive unit cells in γ. In general terms, treating the coupling between clusters as a perturbation might break the translation symmetry of γ; for example, in the case shown in Fig. **9.2**(b), the diamond-diamond coupling within the cluster is treated in exact grounds, while it is considered perturbatively when it connects different clusters. Therefore, within CPT, the lattice Green's function could

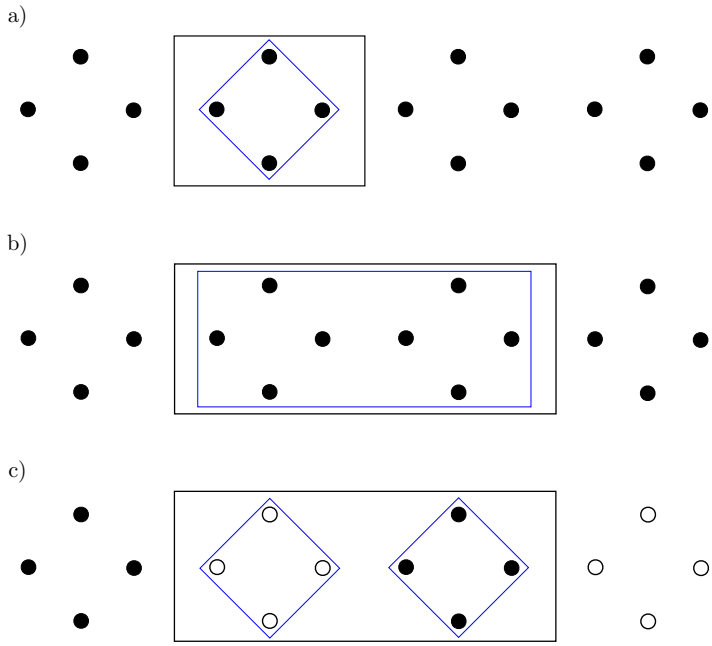

Figure 9.2: Different clusters and supercells of diamond-like chains. Supercells are marked with black lines, clusters with blue lines. a) Diamond chain, where a cluster contains a single diamond, and a supercell contains a single cluster. b) Diamond chain, with a cluster containing two diamonds and a supercell containing a single cluster. c) Diamond-like chain, constructed by placing successively two different diamonds. Each cluster contains a single diamond and the smallest supercell that can be chosen contains two clusters.

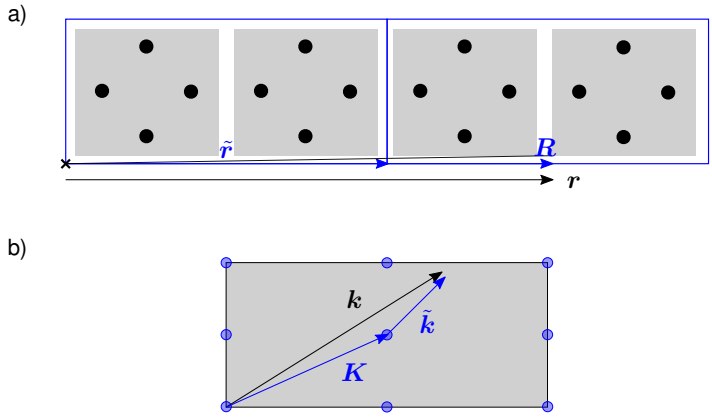

Figure 9.3: Illustration of the notation. (a) Example of a possible choice of the supercell (blue) in the HDC, where the unit cell is marked in grey, (b) Reciprocal structure, with the BZ in grey and sites of the superlattice denoted by blue dots.

have elements between different $\boldsymbol{k}$-vectors:

$$\begin{aligned} G(\boldsymbol{k},\boldsymbol{k}') &= \frac{1}{\mathcal{N}} \sum_{\boldsymbol{r},\boldsymbol{r}'} G_{\boldsymbol{r},\boldsymbol{r}'} e^{i\boldsymbol{k}\cdot\boldsymbol{r}} e^{-i\boldsymbol{k}'\cdot\boldsymbol{r}'} \\ &= \frac{1}{\mathcal{N}} \sum_{\substack{\tilde{\boldsymbol{r}},\tilde{\boldsymbol{r}}' \\ \boldsymbol{R},\boldsymbol{R}'}} G_{\tilde{\boldsymbol{r}}\boldsymbol{R},\tilde{\boldsymbol{r}}'\boldsymbol{R}'} e^{i\boldsymbol{k}\cdot(\tilde{\boldsymbol{r}}+\boldsymbol{R})} e^{-i\boldsymbol{k}'\cdot(\tilde{\boldsymbol{r}}'+\boldsymbol{R}')}, \end{aligned} \tag{9.48}$$

where $G_{\tilde{\boldsymbol{r}}\boldsymbol{R},\tilde{\boldsymbol{r}}'\boldsymbol{R}'}$ is a form of writing $G_{\boldsymbol{r},\boldsymbol{r}'}$ based on the decomposition $\boldsymbol{r} = \tilde{\boldsymbol{r}} + \boldsymbol{R}$ – the dependence on frequency will be omitted.

However, the invariance under translations of γ is not completely broken in CPT. The method preserves invariance with respect to translations by vectors of Γ. The lattice Green's function calculated by CPT [Eq. (9.46)] is hence diagonal when a Fourier transform with the reciprocal lattice of Γ is considered:

$$G_{\tilde{\boldsymbol{r}}\boldsymbol{R},\tilde{\boldsymbol{r}}'\boldsymbol{R}'} = \frac{1}{\mathcal{N}_\Gamma} \sum_{\boldsymbol{q}} G_{\boldsymbol{R},\boldsymbol{R}'}(\boldsymbol{q}) e^{i\boldsymbol{q}\cdot(\tilde{\boldsymbol{r}}-\tilde{\boldsymbol{r}}')} \tag{9.49}$$

where $\boldsymbol{q}$ denotes a vector in the BZ of Γ and $G_{\boldsymbol{R},\boldsymbol{R}'}(\boldsymbol{q},\boldsymbol{q}') \propto \delta_{\boldsymbol{q},\boldsymbol{q}'}$. This expression is midway between full reciprocal and real space expressions: reciprocal space between clusters ($\boldsymbol{q}$) and real space within a cluster ($\boldsymbol{R},\boldsymbol{R}'$). In CPT, the lattice Green's function in Eq. (9.46) is usually calculated in this representation. Substituting Eq. (9.49) in

Eq. (9.48) leads to:

$$G(\boldsymbol{k},\boldsymbol{k}') = \frac{\mathcal{N}_\Gamma}{\mathcal{N}} \sum_{\boldsymbol{R},\boldsymbol{R}'} \sum_{\boldsymbol{q}} G_{\boldsymbol{R},\boldsymbol{R}'}(\boldsymbol{q}) e^{-i\boldsymbol{k}\cdot\boldsymbol{R}} e^{i\boldsymbol{k}'\cdot\boldsymbol{R}'} \times \left(\frac{1}{\mathcal{N}_\Gamma}\sum_{\tilde{\boldsymbol{r}}} e^{i(\boldsymbol{q}-\boldsymbol{k})\cdot\tilde{\boldsymbol{r}}}\right)\left(\frac{1}{\mathcal{N}_\Gamma}\sum_{\tilde{\boldsymbol{r}}'} e^{i(-\boldsymbol{q}+\boldsymbol{k}')\cdot\tilde{\boldsymbol{r}}'}\right) \tag{9.50}$$

We consider the unambiguous decompositions $\boldsymbol{k} = \tilde{\boldsymbol{k}} + \boldsymbol{K}$ and $\boldsymbol{k}' = \tilde{\boldsymbol{k}}' + \boldsymbol{K}'$, where $\tilde{\boldsymbol{k}}$ and $\tilde{\boldsymbol{k}}'$ belong to the BZ of Γ, whereas $\boldsymbol{K}$ and $\boldsymbol{K}'$ to the reciprocal lattice of Γ. The terms between parentheses simplify then to:

$$\frac{1}{\mathcal{N}_\Gamma}\sum_{\tilde{\boldsymbol{r}}} e^{i(\boldsymbol{q}-\boldsymbol{k})\cdot\tilde{\boldsymbol{r}}} = \delta_{\boldsymbol{q},\tilde{\boldsymbol{k}}}, \tag{9.51}$$

which yields the following expression when it is applied to Eq. (9.50):

$$G(\boldsymbol{k},\boldsymbol{k}') = \frac{\mathcal{N}_\Gamma}{\mathcal{N}} \sum_{\boldsymbol{R},\boldsymbol{R}'} G_{\boldsymbol{R},\boldsymbol{R}'}(\tilde{\boldsymbol{k}}) e^{-i\boldsymbol{k}\cdot\boldsymbol{R}} e^{i\boldsymbol{k}'\cdot\boldsymbol{R}'} \delta_{\tilde{\boldsymbol{k}},\tilde{\boldsymbol{k}}'}. \tag{9.52}$$

The identity $\tilde{\boldsymbol{k}} = \tilde{\boldsymbol{k}}'$ holds for $\mathcal{N}/\mathcal{N}_\Gamma$ vectors in the BZ of γ, which differ by vectors $\boldsymbol{q}_s$ of the reciprocal lattice of Γ, such that $\delta_{\tilde{\boldsymbol{k}},\tilde{\boldsymbol{k}}'} = \sum_{s=1}^{\mathcal{N}/\mathcal{N}_\Gamma} \delta_{\boldsymbol{k}-\boldsymbol{k}',\boldsymbol{q}_s}$. According to this identity, and applying the fact that the Green's function in Eq. (9.46) satisfies $G_{\boldsymbol{R},\boldsymbol{R}'}(\tilde{\boldsymbol{k}}) = G_{\boldsymbol{R},\boldsymbol{R}'}(\boldsymbol{k})$ due to the invariance under translations by vectors of Γ, Eq. (9.52) can be rewritten as:

$$G(\boldsymbol{k},\boldsymbol{k}') = \frac{\mathcal{N}_\Gamma}{\mathcal{N}} \sum_{s=1}^{\mathcal{N}/\mathcal{N}_\Gamma} \sum_{\boldsymbol{R},\boldsymbol{R}'} G_{\boldsymbol{R},\boldsymbol{R}'}(\boldsymbol{k}) e^{-i\boldsymbol{k}\cdot\boldsymbol{R}} e^{i\boldsymbol{k}'\cdot\boldsymbol{R}'} \delta_{\boldsymbol{k}-\boldsymbol{k}',\boldsymbol{q}_s}. \tag{9.53}$$

This is the exact expression for the lattice Green's function within CPT, in reciprocal space. As aforementioned, the fact that it contains off-diagonal elements in $\boldsymbol{k}$ and $\boldsymbol{k}'$ is a consequence of the (potential) translation-symmetry breaking from the original lattice γ to the superlattice Γ. This property is thus an artifact of the CPT method – the genuine lattice Green's function must depend only on $\boldsymbol{k}$. Based on this idea, the off-diagonal terms are neglected in CPT by choosing $\boldsymbol{q}_s = \boldsymbol{0}$, which leads finally to the following expression:

$$G(\boldsymbol{k},i\omega) = \frac{\mathcal{N}_\Gamma}{\mathcal{N}} \sum_{\boldsymbol{R},\boldsymbol{R}'} G_{\boldsymbol{R},\boldsymbol{R}'}(\boldsymbol{k},i\omega)\; e^{-i\boldsymbol{k}\cdot(\boldsymbol{R}-\boldsymbol{R}')}. \tag{9.54}$$

This expression is known as the **periodization formula**. Let us summarize the procedure followed to calculate the single-particle Green's function $G(\boldsymbol{k},i\omega)$ within the CPT framework. First, the lattice is tiled into clusters, and the cluster Green's function is

calculated by neglecting couplings between these blocks. These hopping terms are then included as a perturbation of the rest of terms in the Hamiltonian, to calculate the Green's function $G_{\boldsymbol{R},\boldsymbol{R}'}(\boldsymbol{q}, i\omega)$ via Eq. (9.46). After that, the periodization formula in Eq. (9.54) is used to obtain the $\boldsymbol{k}$-resolved single-particle Green's function $G(\boldsymbol{k}, i\omega)$.

Once $G(\boldsymbol{k}, i\omega)$ is obtained, the spectral function $A(\boldsymbol{k}, \omega)$ can be calculated by taking its imaginary part, according to Eq. (9.13). The spectral function can be used to diagnose if the system is an insulator or a metal. It can also be used to determine the chemical potential, by matching its integral to the number of electrons; for example, at zero temperature and half filling, the chemical potential μ is determined by:

$$\int_{-\infty}^{\mu} d\omega \ \rho(\omega) = 1/2. \tag{9.55}$$

where $\rho(\omega)$ relates to the spectral function via Eq. (9.18).

It is interesting to emphasize that two approximations are involved in the CPT approach: on the one hand, hoppings between clusters are included as perturbations in the Hamiltonian. The precision of this approximation can be improved by increasing the size of clusters, as this is equivalent to increasing the number of hopping terms treated in exact grounds. On the other hand, even if the CPT Green's function is in not diagonal in $\boldsymbol{k}$-indices, we get rid of the blocks out of the diagonal and consider only those in the diagonal. This approximation is needed when the supercell is bigger than the primitive cell of the original lattice, so its impact on the quality of the results is minimized by considering a tiling which does not require a supercell structure. Whether such a tiling is realistic or not depends on the actual crystal structure of the material.

10 Hubbard Diamond Chain

The division between the interacting and non-interacting view on topology got reinforced as the characterization and classification of topological phases advanced substantially over the past years. In particular, the role of symmetries, both of spatial (crystalline) and of global type (e.g., time reversal) has been explored thoroughly in parallel in both domains [25, 28, 29, 66, 182].

A typical approach to classify topological phases of interacting matter is based on many-body invariants extracted, for instance, from the ground-state wave function [183]. A major drawback of this approach is, however, its impracticability to diagnose topological phases in real systems due to the complicated mathematical treatment of the invariants beyond the simplest cases. This problem is overcome efficiently in the classification of non-interacting topological phases. As it was explained in part I, although the topology can be diagnosed in terms of topological invariants also in this case, symmetry-indicators [28, 29] or TQC based approaches turn out to be more efficient for that task – at least when crystal symmetries can help classifying the phase. This fact motivates us to seek methods for classifying interacting topological phases alternative to topological invariants.

The purpose of this work is to explore the applicability and practicability of the TQC framework to diagnose symmetry-protected topological phases in interacting materials; specifically, we analyze the spectrum of single-particle Green's functions within the framework of TQC to investigate and detect certain interacting topological phases. We tackle this problem by invoking the concept of topological Hamiltonian [42, 173, 184], which is defined as the inverse of the single-particle Green's function at zero frequency.

As a proof of principle, we apply our approach to the example of a Hubbard chain of spinful electrons, namely the Hubbard diamond chain (HDC). This model is simple enough to allow us to calculate its phase-diagram through a combination of numerical methods and analytical invariants, yet it is rich enough to display different phases to test our approach, such as atomic and obstructed atomic limits which are connected adiabatically to band insulator phases, and a Mott insulator. The phase diagram of the model is calculated first with infinite Dynamical Matrix Renormalization Group

(iDMRG) [185, 186] and Variational Monte Carlo (VMC) [187–190] simulations. In addition, a many-body invariant capable of differentiating between all its phases is presented [191]. The computed phase diagram serves then as a reference to test our TQC and GF based method. The single-particle GFs are calculated within cluster perturbation theory [175–177, 179].

The analysis of the results shows that, in contrast to the mathematical difficulties in the calculation of many-body invariants when considering models beyond the simplest ones, the TQC Green's function – based approach may be a candidate to become a systematic method to characterize the topology of interacting insulating phases in material-specific models, at least for the cases when they are adiabatically connected to non-interacting phases. We also discuss explicitly the case of the SPT Mott phases.

The chapter is organized as follows: the HDC is introduced in Sec. 10.1. Its non-interacting phase diagram is described in detail in Sec. 10.2, while Sec. 10.3 is devoted to the analysis of the interacting phase diagram, which is used as reference when testing the GF based approach in Sec. 10.4. Finally, Sec. 10.5 contains the analysis of the HDC with SOC corrections. The conclusions obtained for each of these cases will be presented at the end of the corresponding section.

10.1 Extended Hubbard diamond chain

As illustrated in Fig. **10.1**(a), the HDC consists of a one-dimensional periodic arrangement (along x) of diamonds whose symmetries form the space group $Pmmm$ (No. 47). The lattice sites are at Wyckoff positions $2i$ and $2m$, and each of them contains a pair of spinful s-orbitals. These orbitals induce eight Kramers degenerate bands in reciprocal space. We will focus on the case of four electrons per unit cell, *i.e.* the half-filling case.

The model's Hamiltonian includes three different hopping parameters: (i) an intracell nearest-neighbor hopping t_1, (ii) an intracell next-nearest-neighbor coupling t_2, and (iii) an intercell coupling t_3. Onsite electron-electron correlations are included through a Hubbard term whose strength is controlled by the Hubbard parameter U. The full Hamiltonian, in the absence of spin-orbit coupling, is given by:

$$\begin{aligned}\mathcal{H} = &- t_3 \sum_{\sigma,j} \left(c^\dagger_{1,j,\sigma} c_{3,j+1,\sigma} + \text{h.c.} \right) + \sum_{\alpha,\beta} c^\dagger_{\alpha,j,\sigma} \; \mathbb{T}_{\alpha\beta} \; c_{\beta,j,\sigma} \\ &+ U \sum_{\alpha,j} n_{\alpha,j,\uparrow} n_{\alpha,j,\downarrow} + \mu \sum_{\alpha,j,\sigma} c^\dagger_{\alpha,j,\sigma} c_{\alpha,j,\sigma},\end{aligned} \tag{10.1}$$

where $c^\dagger_{\alpha,j,\sigma}$ ($c_{\alpha,j,\sigma}$) creates (annihilates) an electron of spin σ at site $\alpha \in \{0,1,2,3\}$ of the cell labeled by $j = 1, \ldots, \mathcal{N}$, where $\mathcal{N}$ denotes the number of unit cells and μ is the chemical potential – it is chosen such that the system is at half-filling. The matrix $\mathbb{T}_{\alpha\beta}$

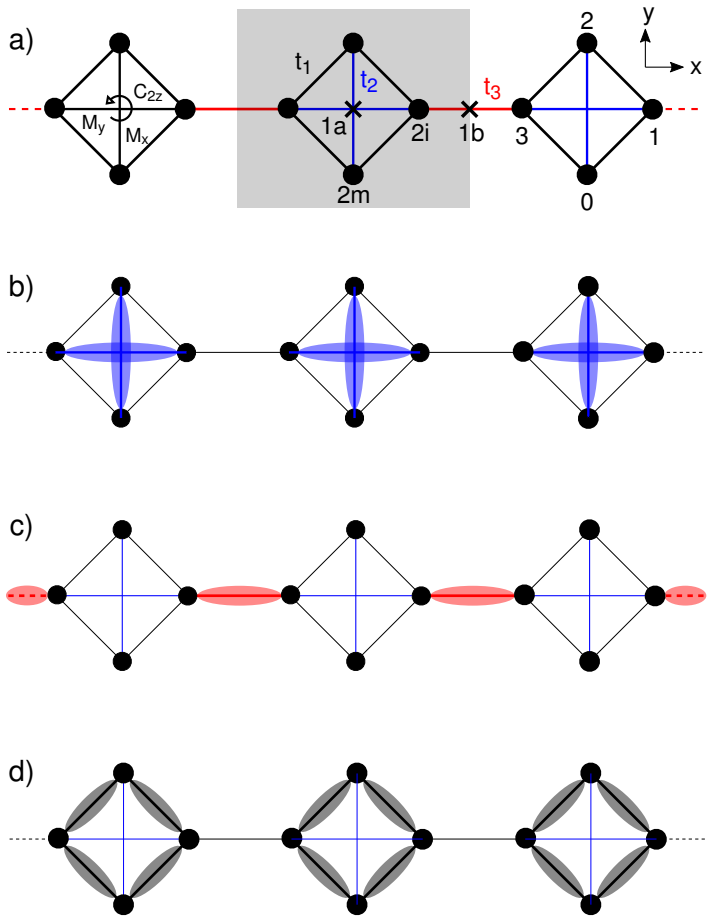

Figure 10.1: a) Atomic configuration of the extended diamond chain. The unit cell is marked with the grey background, WPs $1a$ and $1b$ are denoted with crosses and atomic sites at WPs $2i$ and $2m$ with solid black circles. The enumeration of orbitals adopted to write the Hamiltonian is also shown. Intracell hoppings t_1 and t_2 are indicated in black and blue lines, respectively, while intercell hopping t_3 is indicated in red. Black lines and circular arrow in the left diamond denote reflection planes and 2-fold rotation with respect to the z-axis, respectively. b)-d) Dominant coupling parameters for three different limiting cases: (b) $t_2 \gg t_1, t_3$, (c) $t_3 \gg t_1, t_2$, (d) $t_1 \gg t_2, t_3$.

that contains the intracell couplings t_1 and t_2 has the form

$$\mathbb{T} = -\begin{bmatrix} 0 & t_1 & t_2 & t_1 \\ t_1 & 0 & t_1 & t_2 \\ t_2 & t_1 & 0 & t_1 \\ t_1 & t_2 & t_1 & 0 \end{bmatrix}. \tag{10.2}$$

Actually, the HDC model can be understood as a one-dimensional version of the two-dimensional square lattice considered by Yao and Kivelson [192].

10.2 Non-interacting HDC

In this section, we study the phase diagram of the HDC without interaction, *i.e.* for the Hamiltonian in Eq. (10.1) with $U = 0$. Each phase will be studied in two steps: First, the symmetry properties of the single-particle band structure will be interpreted within in terms of band representations. Then, the many-body wave function of the ground state will be derived, and its transformation under the space group will be discussed.

Since the non-interacting Hamiltonian does not include spin-orbit corrections, we can base our symmetry analysis on the single-valued space group $Pmmm$. SOC corrections will be discussed in detail in Sec. 10.5. Furthermore, we will follow the notation for the irreps adopted in the *Bilbao Crystallographic Server* [96–98].

The orbitals in our model transform as the irrep A_1 of the corresponding site-symmetry groups, which are isomorphic to the point group[1] [see Fig. **10.1**(a)]. These orbitals induce the band representation $\rho = (A_1 \uparrow G)_{2i} \oplus (A_1 \uparrow G)_{2m}$ of the space group. Moreover, representations of little groups of the points Γ and X subduced by this representation can be decomposed as

$$\rho : \{2\Gamma_1^+ \oplus \Gamma_3^- \oplus \Gamma_4^-, 2X_1^+ \oplus X_3^- \oplus X_4^-\}. \tag{10.3}$$

The analytical phase diagram of the non-interacting Hamiltonian is shown in Fig. **10.2** for $t_2/t_1, t_3/t_1 > 0$. It contains two gapped[2] phases and a metallic phase. Let us comment briefly on the derivation of the phase diagram: We started from the Bloch states constructed from the considered s-orbitals. First, focused on the maximal k-points Γ and X, and calculated the states adapted to the symmetry of their little group irreps taking part in Eq. (10.3). Then, the change to the basis formed by these symmetry-adapted states was applied simplify the Hamiltonians $H(\Gamma)$ and $H(X)$ to block-diagonal form, according to Wigner's theorem. This step leaded to analytical expressions for the energy levels corresponding to the irreps $\Gamma_3^-, \Gamma_4^-, X_3^-$ and X_4^-,

[1] Note that C_{2v} is a subgroup of D_{2h}, where D_{2h} is the point group of an isolated diamond.

[2] In the actual context of this system, we say that a phase is gapped if its ground state is non-degenerate. In particular, in the noninteracting case, the band structures of gapped phases have valence and conduction bands separated by a gap.

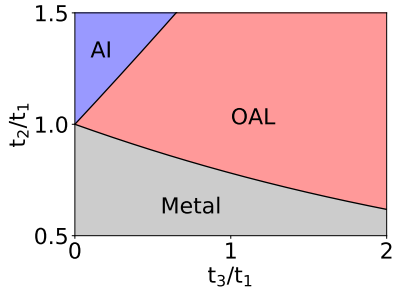

Figure 10.2: Phase diagram of the non-interacting diamond chain model at half-filling, the blue color represents the AI phase, red the OAL and grey the metallic phase.

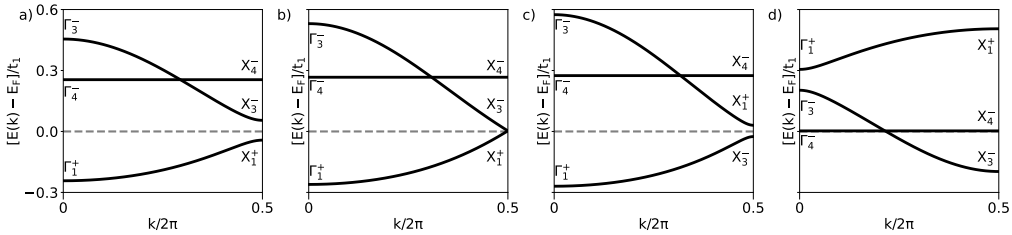

Figure 10.3: Band structure of the HDC for $U = 0$, where the lowest occupied band has been omitted as it is disconnected from the rest and it contains the irreps $\{\Gamma_1^+, X_1^+\}$ in the studied range of parameters. (a) AI phase ($t_2/t_1 = 1.2$, $t_3/t_1 = 0.2$). (b) Transition point between the AI and OAL phases ($t_2/t_1 = 1.2$, $t_3/t_1 = 0.264$). (c) OAL phase ($t_2/t_1 = 1.2$, $t_3/t_1 = 0.3$). (d) Metallic phase ($t_2/t_1 = 0.8$, $t_3/t_1 = 0.2$).

which are moreover linear in the hopping parameters. Analytical expressions were also obtained for the rest of irreps by further diagonalizing the corresponding 2×2 blocks. Finally, the realizable phases and boundaries between them were determined by studying the different possible arrangements (in energy) of irreps and the conditions set by them on the hopping parameters.

Atomic Insulator (AI) phase

In the limit $t_1 \to 0$, sites at WP $2i$ and WP $2m$ are decoupled. The sites at WP $2m$ form local dimers, while sites at WP $2i$ are connected along the periodic x direction and form a one-dimensional chain that can be adiabatically connected to the Su-Schrieffer-Heeger (SSH) chain. Particularly, when $t_3 \ll t_2$, sites at WP $2i$ form a chain that can be connected to the trivial SSH chain. This mapping is corroborated by the TQC based analysis of the band structure: The valence bands transform in the composite band representation $2(A_1 \uparrow G)_{1a}$, with occupied little group representations $2\Gamma_1^+$ and $2X_1^+$

[Fig. **10.3**(a)]. This representation can be induced from two Wannier functions whose charge centers are at the WP $1a$ and transform like s-orbitals under the action of the site-symmetry group of this site. Since the band representation of the occupied band of the trivial SSH-chain can also be induced by identical Wannier functions, we conclude that the occupied subspace of the diamond chain's spectrum can be adiabatically connected to two copies of the trivial SSH-chain and we classify this phase as an *atomic insulator* (AI).

Let us now derive the wave function of the many-body ground state of the chain in the AI phase in order to determine its symmetry properties. Since sites belonging to different diamonds (unit cells) are decoupled, the single-particle Hamiltonian H of the chain is a sum of Hamiltonians of diamonds:

$$H = \sum_j -t_2(c^\dagger_{0,j}c_{2,j} + c^\dagger_{1,j}c_{3,j}) + \text{h.c.} = \sum_j (H_{j,h} + H_{j,v}), \tag{10.4}$$

where $H_{j,2i}$ and $H_{j,2m}$ are the Hamiltonians for the dimers formed by sites at WPs $2i$ and $2m$, respectively. The Hamiltonian of the diamond in the j^{th}-cell is then $H_{j,2i} + H_{j,2m}$. We can thus construct the 2-particle[3] ground state of the diamond from the single-particle ground states of these dimer Hamiltonians.

Each of the dimer Hamiltonians coincides with the well-known Hamiltonian of the H_2^+ molecule. Their ground states are hence *bonding* states, whose creation operators are the following:

$$\psi^\dagger_{j,2i} = 1/\sqrt{2}(c^\dagger_{0,j} + c^\dagger_{2,j}), \tag{10.5a}$$

$$\psi^\dagger_{j,2m} = 1/\sqrt{2}(c^\dagger_{1,j} + c^\dagger_{3,j}). \tag{10.5b}$$

These states transform as the trivial representation A_1 of the point group D_{2h} of the diamond, which means that they are mapped to themselves – without acquiring any phase – under any transformation of D_{2h}. A more detailed description can be found in Appendix D.4.

Moreover, the states in Eqs. (10.5a) and (10.5b) are also eigenstates of the diamond's Hamiltonian. Accordingly, the creator operator for the 2-particle ground state of the diamond can be constructed as the Slater determinant of these dimer's ground states:

$$\mathcal{O}^\dagger_j = \psi^\dagger_{j,2i}\psi^\dagger_{j,2m}. \tag{10.6}$$

Finally, the $2\mathcal{N}$-particle ground state of the chain is created by the operator:

$$\psi^\dagger_{AI} = \prod_j \mathcal{O}^\dagger_j, \tag{10.7}$$

[3] As the Hamiltonian is diagonal in spin indices and the blocks of both spin indices are identical, we can solve for one of the spins and consider then that we have two copies of it.

where the product runs over all diamonds in the chain.

Let us comment on the transformation properties of this ground state under the space group. First, we consider translations. Any pair of operators $\mathcal{O}_i^\dagger$ and $\mathcal{O}_j^\dagger$ satisfies the commutation relation $[\mathcal{O}_i^\dagger, \mathcal{O}_j^\dagger] = 0$, as each of them is formed by an even number of single-particle creation operators. Therefore, $\psi_{AI}^\dagger$ is left invariant under all translation.

Regarding the rest of symmetries, we can restrict to analyzing the action of the generators of D_{2h} – this is equivalent to considering the coset representatives of the decomposition of the space group with respect to its translation subgroup. We choose these generators to be the mirror reflection M_y, the two-fold rotation C_{2z} and inversion I. The action of M_y on $\psi_{AI}^\dagger$ is trivial, as it leaves all diamonds invariant:

$$M_y \psi_{AI}^\dagger M_y^{-1} = \psi_{AI}^\dagger. \tag{10.8}$$

The action of C_{2z} and I might, however, be less trivial.

$$g\psi_{AI}^\dagger g^{-1} = g \ldots \mathcal{O}_{-1}^\dagger \mathcal{O}_0^\dagger \mathcal{O}_1^\dagger \ldots g^{-1} = \ldots \mathcal{O}_1^\dagger \mathcal{O}_0^\dagger \mathcal{O}_{-1}^\dagger \ldots \tag{10.9}$$

for $g = C_{2z}, M_y$. Nevertheless, the right-hand side of this equation turns out to be again $\psi_{AI}^\dagger$ due to the commutativity between creators of diamonds' ground states.

All in all, we have shown that the $2\mathcal{N}$-body ground state of the HDC in the AI phase is left invariant by all symmetries in the space group,*i.e.* it transforms as its trivial representation A_1.

The $4\mathcal{N}$-particle ground state is build up as the product of two copies of the $2\mathcal{N}$-body ground state in Eq. (10.7), each copy corresponding to one of the subspaces of spin.

$$\Psi_{AI}^\dagger = \prod_j \mathcal{O}_{j\uparrow}^\dagger \mathcal{O}_{j\downarrow}^\dagger. = \prod_{j,\sigma} \frac{1}{2}(c_{0,j,\sigma}^\dagger + c_{2,j,\sigma}^\dagger)(c_{1,j,\sigma}^\dagger + c_{3,j,\sigma}^\dagger). \tag{10.10}$$

This ground state also transforms as the trivial representation A_1 of the space group $Pmmm$.

Obstructed atomic limit (OAL)

When t_3 is the dominant hopping term ($t_3 \gg t_1, t_2$), the chain formed by orbitals at WP $2i$ can be mapped to the SSH chain in the topological phase, as these sites form dimers connected across neighboring unit cells [Fig. **10.1**(c)]. We thus expect the sites at WP 2i to contribute to the occupied subspace with a band of the same nature. This insight is again confirmed from the viewpoint of TQC framework: the valence bands transform in the $(A_1 \uparrow G)_{1a} \oplus (A_1 \uparrow G)_{1b}$ band representation with little group representations $2\Gamma_1^+$ and $X_1^+ \oplus X_3^-$ [**10.3**(c)]. Particularly, the band with little group irreps Γ_1^+ and X_3^- can be induced from s-like Wannier functions whose charge-center is in the WP $1b$, *i.e.* its states transform as the EBR $(A_1 \uparrow G)_{1b}$. This representation is

then connected to the one corresponding to valence band of the topological SSH-chain by considering the lowering of the symmetry from the space group $Pmmm$ of the HDC to the space group $P\bar{1}$ of the SSH-chain. On the basis of both this similarity with the topological SSH-chain and the fact that the band with irreps Γ_1^+ and X_3^- is induced from an empty WP, we identify the phase at $t_3 \gg t_2, t_1$ as an *obstructed atomic limit* (OAL). Notice that the remaining valence band, whose little group irreps are Γ_1^+ and X_1^+, is induced from the WP 2m – just as in the AI phase.

Even though irreps of valence bands are identical at Γ for both the AI and OAL phases, this resemblance does not hold for the X-point. There, the irrep X_1^+ of the highest-valence band in the AI phase is substituted by the irrep X_3^- in the OAL phase. Since these irreps have different two-fold rotation $\hat{C}_{2z}$ and reflection $\hat{M}_x$ [which maps a point (x, y, z) to $(-x, y, z)$] symmetry eigenvalues, it is not possible to connect these phases by a path in which the gap between valence and conduction bands does not close, without breaking these symmetries. Furthermore, they are phases distinguished by this symmetries.

Let us now derive the $4\mathcal{N}$-particle ground state of the HDC in the OAL phase. For this phase, the single-particle Hamiltonian of the chain is connected to:

$$H = \sum_j [\underbrace{-t_3 c^\dagger_{3,j+1} c^\dagger_{1,j} + \text{h.c.}}_{H_j} + \underbrace{(-t_2)(c^\dagger_{0,j} c_{2,j} + c^\dagger_{1,j} c_{3,j} + \text{h.c.})}_{H_{j,AI}}], \tag{10.11}$$

with $t_3 \gg t_2$. $H_{AI,j}$ is the Hamiltonian of the diamond in Eq. (10.4), and its ground state is the bonding state created by the operator $\psi^\dagger_{j,2i}$ in Eq. (10.5a). H_j is the Hamiltonian of the dimers formed by the sites at WP 2i, via the shortest intercell connections. Its ground state $\phi^\dagger_{j,2i}$ is therefore the bonding state centered on the border of between the j and $j+1$ unit cells:

$$\phi^\dagger_{j,2i} = 1/\sqrt{2}(c^\dagger_{1,j} + c^\dagger_{3,j+1}). \tag{10.12}$$

The energy levels of the bonding states created by $\phi^\dagger_{j,2i}$ and $\psi^\dagger_{j,2i}$ are $-t_3$ and t_2, respectively. These state are indeed the two lowest-energy eigenstates of the Hamiltonian in Eq. (10.11), as the energy levels of the antibonding states are both positive. Therefore, the 2-particle ground state of $H_j + H_{j,AI}$ is created by $\psi^\dagger_{j,2i}\phi^\dagger_{j,2i}$.

The $2\mathcal{N}$-ground state $\psi^\dagger_{OAL}$ of the chain can then be constructed through the product of this creation operators:

$$\psi^\dagger_{OAL} = \prod_j \psi^\dagger_{j,2i}\phi^\dagger_{j,2i} = \prod_j 1/2(c^\dagger_{0,j} + c^\dagger_{2,j})(c^\dagger_{1,j} + c^\dagger_{3,j+1}). \tag{10.13}$$

This creation operator is already invariant under all symmetries in the space group $Pmmm$, owing to the fact that it is the product commuting pairs of single-particle creation operators.

Finally, the creation operator for the $4\mathcal{N}$-particle ground state of the HDC in the

OAL is the product of two copies of Eq. (10.13), each copy corresponding to a spin index:

$$\Psi^{\dagger}_{OAL} = \prod_{j,\sigma} 1/2(c^{\dagger}_{0,j,\sigma} + c^{\dagger}_{2,j,\sigma})(c^{\dagger}_{1,j,\sigma} + c^{\dagger}_{3,j+1,\sigma}). \tag{10.14}$$

In conclusion, the $4\mathcal{N}$-particle ground state of the HDC in the OAL also transforms as the trivial representation A_1 of the space group $Pmmm$.

Metallic phase

For the last limiting case, where t_1 is the dominant hopping ($t_1 \gg t_2, t_3$) as it is shown in Fig. **10.1**d, the ground-state of a single-diamond is degenerate. Since t_3 is negligible, it follows from this degeneracy that the many-body ground-state of the HDC chain is also degenerate and therefore metallic, as it is confirmed by the presence of four partially filled bands in the band structure of Fig. **10.3**d, where the Fermi energy is pinned at the flat band (with little group representations Γ_4^- and X_4^-).

10.3 Topology of the interacting HDC

In this section, we will first calculate numerically the phase diagram of the interacting HDC. Then, we will present a mirror-reflection based invariant capable of differentiating between all the phases in the diagram.

10.3.1 Phase diagram of HDC for finite U

Both VMC and DMRG [in the matrix product state (MPS) formulation] are state-of-the-art techniques which are employed to approximate the ground state wave function of quantum many-body Hamiltonians. DMRG is one of the most prominent numerical method for the study of strongly-correlated one-dimensional systems, and has successfully been applied to a large variety of quantum models [193]. The MPS *Ansätze* can efficiently encode low-entangled quantum states, with systematically improvable accuracy. On the other hand, the VMC method applied in the present work relies on relatively simple variational wave functions, made of mean-field fermionic state supplemented by Jastrow correlators [187]. Despite its intrinsically biased nature, the VMC method represents a reliable tool for the study of the phase diagram of systems of interacting electrons beyond the perturbative limit, as in the case of Mott transitions in Hubbard-like models.

The DMRG based approach followed in this work to calculate the phase diagram of the interacting HDC consists in computing the ground-state wave function first, and exctracting from it the correlation length ξ [Eq. (D.2)] then. This procedure is motivated by the fact than ξ could be used as an indicator of the degeneracy of the ground state,

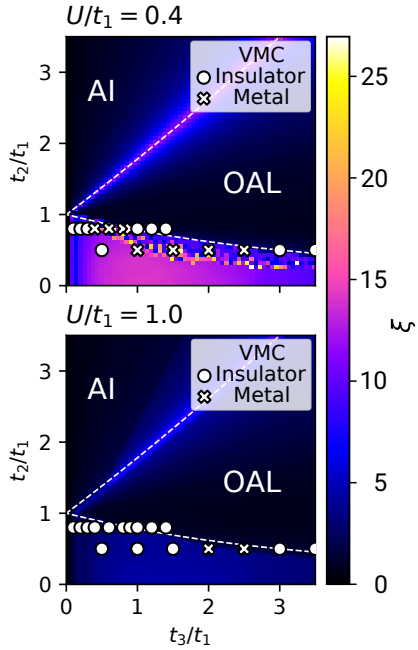

Figure 10.4: Phase diagram of the interacting diamond chain for $U/t_1 = 0.4$ and $U/t_1 = 1$ at half-filling determined from the calculation of the correlation length ξ in iDMRG (color map), as well as data points obtained by VMC at $t_2/t_1 = 0.8$ and $t_2/t_1 = 0.5$ for various t_3/t_1 indicating whether the system is in a metallic (crosses) or an insulating (circles) phase. The phase boundaries of the non-interacting phase diagram are given by the white, dashed lines.

as it takes a finite value for gapped phases, whereas it diverges (numerically) in metallic phases [194].

Based on this idea, we scanned the region of interest of the parameter space, calculating with iDMRG the correlation length at each point on it. The phase diagrams obtained this way for $U/t_1 = 0.4$ and $U/t_1 = 1$ are shown in Fig. **10.4** [see Appendix D.1 for additional calculations].

For $t_2/t_1 > 1$ and finite interaction U, the transition from the AI to OAL remains but slightly shifts to larger values of t_3/t_1 when increasing U/t_1 (see also Fig. **D.1** of Appendix D.1). Since all single-particle bands are either completely filled or empty in the gapped AI and OAL phases at $U = 0$, a small finite U only induces a renormalization of the electron bands without any drastic change. In analogy with the spinful SSH chain [191], both the AI and OAL phases are also smoothly connected to gapped valence bond analogues appearing at large U, without change of ground-state symmetry. As a result, the interacting analogues of the AI and OAL phases are each smoothly connected to a non-interacting atomic limit.

The $t_2 < t_1$ region requires deeper analysis for relatively small U. On the one hand, although formally the correlation length ξ diverges at the phase boundaries, in our data it is bounded by the maximal bond dimension. On the other hand, iDMRG tends to perform poorly for metallic or close-to-metallic systems, as it can be seen in Fig. **D.1**(a). We have therefore performed VMC simulations as well in order to corroborate the iDMRG results in the region where the metallic phase is observed ($t_2/t_1 < 1$). Our variational approach is based on Jastrow-Slater wave functions as described in Appendix D.2. The regions of gapped (insulator) and gapless (metallic) phases as determined by VMC are shown in Fig. **10.4** as circles and crosses, respectively.

The $t_2/t_1 < 1$ and $t_3/t_1 \ll t_2/t_1$ region shows a particularly interesting behavior. The metallic phase present in the non-interacting phase diagram is substituted by a gapped phase upon addition of electron interaction. This origin of the insulator phase suggests that it could be a Mott phase. Moreover, this gapped phase preserves all the symmetries of the space group $Pmmm$. Increasing t_3/t_1, the system either undergoes a transition into an intermediate metallic phase or, for sufficiently large values of U, it enters the OAL phase directly from the MI phase (compare the results for $U/t_1 = 0.4$ and $U/t_1 = 1$ in the region $t_2/t_1 = 0.8$ and $0 < t_3/t_1 < 1$ in Fig. **10.4**). With increasing U, the MI replaces an increasing proportion of the metallic region of the non-interacting model, while the extent of the bordering OAL phase remains largely unchanged.

10.3.2 Mott SPT phase and Many-Body Invariants

In this section, we establish the MI phase as an SPT phase and analyze the topology of the interacting phases in the HDC through many-body invariants.

We demonstrated in Sec. 10.2 that the many-body ground states of both the AI and OAL phases transform trivially under all symmetries of the space group. This is, in fact, a general property of all non-degenerate wave functions of even number of electrons with TRS which can be written as Slater determinants of single-particle wave functions. In order to prove this property, let us consider the non-degenerate Slater determinant of even number of particles created by:

$$\Psi_{SD}^{\dagger} = \prod_i c_i^{\dagger}, \tag{10.15}$$

where $c_i^{\dagger}$ creates a particle in a state that belongs, at the same time, to the spectra of the single-particle Hamiltonian and a certain $g \in Pmmm$, with eigenvalue $\lambda_{g,i}$. Due to TRS θ, the operator $\theta c_i^{\dagger} \theta^{-1}$ corresponds to an energetically degenerate eigenstate of g with eigenvalue $\lambda_{g,i}^*$. Since the many-body state is assumed to be non-degenerate, these two levels must be either both occupied or both unoccupied, that is, either they both are present or they both are absent in Eq. (10.15). However, the product of operators

always transforms trivially:

$$U_h c_i^\dagger (\mathcal{T} c_i^\dagger \mathcal{T}^{-1}) U_h^{-1} = |\lambda_{h,i}|^2 \; c_i^\dagger (\mathcal{T} c_i^\dagger \mathcal{T}^{-1}), \tag{10.16}$$

since $|\lambda_{h,i}|^2 = 1$, where U_h is the representation of h. In other words, any state described by a single Slater determinant transforms trivially provided all single-particle levels are either empty or fully occupied with both spin up and spin down. This condition is satisfied by all states that can be adiabatically connected to a non-interacting gapped state of spinful particles with time-reversal symmetry, in particular the AI and OAL phases. However, it is not applicable to the MI-phase, since the corresponding wave function is not a Slater determinant of single-particle wave functions. This fact enables its ground state to transform non-trivially under the space group, and we could take advantage of it to differentiate the phase from the AI and OAL.

As the symmetry properties (and topology) of the ground state can not change as long as the gap remains opened, we are free to choose specific points in the phase diagram for the study of each phase. In particular, let us consider for convenience the limit $t_3 = 0, t_2/t_1 \ll 1$ and small finite $U > 0$ for to elucidate the ground state of the MI phase. The Hamiltonian H of the chain is a sum of single-diamond interacting Hamiltonians $H_{d,i}$:

$$H = \sum_j \underbrace{\left[\sum_{\alpha,\beta} c^\dagger_{\alpha,j,\sigma} \; \mathbb{T}_{\alpha\beta} \; c_{\beta,j,\sigma} + U \sum_\alpha n_{\alpha,j,\uparrow} n_{\alpha,j,\downarrow} \right]}_{H_{d,i}} = \sum_j H_{d,j} \; , \tag{10.17}$$

where i labels the unit cell. As a consequence, we can construct the $4\mathcal{N}$-particle ground state of the interacting Hamiltonian H as the product of 4-particle ground states of $H_{d,j}$. The creation operator for such a 4-particle ground is:

$$\mathcal{O}^\dagger_{\mathrm{MI},j} = \frac{1}{\sqrt{2}} \left(\tilde{c}^\dagger_{\frac{\pi}{2},j,\uparrow} \tilde{c}^\dagger_{\frac{\pi}{2},j,\downarrow} - \tilde{c}^\dagger_{-\frac{\pi}{2},j,\uparrow} \tilde{c}^\dagger_{-\frac{\pi}{2},j,\downarrow} \right) \tilde{c}^\dagger_{0,j,\uparrow} \tilde{c}^\dagger_{0,j,\downarrow}. \tag{10.18}$$

where $\tilde{c}^\dagger_{k,j,\sigma} = 1/2 \sum_\alpha \exp(ik\alpha) c^\dagger_{\alpha,j,\sigma}$ are Fourier-transformed creation operators defined within a single diamond. Notice that $\mathcal{O}^\dagger_{\mathrm{MI},j}$ is not a single Slater determinant. Furthermore, it is odd with respect to two-fold rotations about the x- and y-axis (denoted C_{2x} and C_{2y}), as well as mirroring in the yz- and xz-planes (denoted M_x and M_y); in other words, it transforms as the irrep B_{1g} of the space group.

Finally, the many-body ground-state wave function of the chain in the MI-phase is

created by:

$$\begin{aligned}\Psi^{\dagger}_{MI} &= \prod_j \mathcal{O}^{\dagger}_{\mathrm{MI},j} \\ &= \prod_j \frac{1}{\sqrt{2}} \left(\tilde{c}^{\dagger}_{\frac{\pi}{2},j,\uparrow} \tilde{c}^{\dagger}_{\frac{\pi}{2},j,\downarrow} - \tilde{c}^{\dagger}_{-\frac{\pi}{2},j,\uparrow} \tilde{c}^{\dagger}_{-\frac{\pi}{2},j,\downarrow} \right) \tilde{c}^{\dagger}_{0,j,\uparrow} \tilde{c}^{\dagger}_{0,j,\downarrow}.\end{aligned} \tag{10.19}$$

From the transformation properties of $\mathcal{O}^{\dagger}_{AI}$, it follows that $\Psi^{\dagger}_{MI}$ is an eigenstate with eigenvalue $(-1)^{\mathcal{N}}$ (with $\mathcal{N}$ the number of diamonds in the chain) for any symmetry operation of $Pmmm$ whose rotational part is C_{2x}, C_{2y}, M_x or M_y. Consequently, the many-body ground state of the chain in the MI phase transforms as the irrep B_{1g} when the number of diamonds is odd. It can hence be distinguished from the trivial (AI) and obstructed (OAL) phases by, e.g., the mirror reflection eigenvalue of its ground-state: the observable $\langle M_x \rangle_{\Psi_0} = \langle \Psi_0 | M_x | \Psi_0 \rangle$. Nevertheless, these many-body expectation values can not distinguish the MI phase when $\mathcal{N}$ is even. They are unable to differentiate even between the AI and the OAL phase.

We circumvent this obstacle in the diagnosis by considering the expectation-values of partial mirror reflection operations proposed in Refs. [191,195] to diagnose interacting topological phases in systems with mirror symmetry (see Appendix D.3 for details on the case of the SSH model). We denote $M_{x;I}(\theta)$ the operator which acts as the M_x mirror reflection twisted by $U(1)$ symmetry on the states $j = 1, \ldots, L$ belonging to the interval I:

$$\hat{M}_{x;I}(\theta) : c^{\dagger}_{\alpha,j,\sigma} \longmapsto i e^{-i\theta} c^{\dagger}_{\beta,L-j+1,-\sigma} \left[B\right]_{\beta\alpha}, \tag{10.20}$$

while it leaves invariant the sites out of I.

Tab. **10.1** contains the values of $\langle M_{x,I}(\theta) \rangle_{\Psi_0}$ calculated for the ground states of the AI, OAL and MI phases corresponding to the operators in Eqs. (10.10), (10.14) and (10.19), respectively. When $\theta = \pi/2$ and odd L, the expectation value of the partial mirror operator takes the values 1, 0 and -1, *i.e.* a different value in each of the gapped phases. Therefore, the value of this ground-state expectation value provides us with a sharper diagnosis of the three gapped phases than $\langle M_x \rangle_{\Psi_0}$ [4].

A comment on the form of computing the expectation values $\langle M_x \rangle$ and $\langle M_{x,I}(\theta) \rangle$ for the AI and OAL is in order: These expectation values were calculated for the non-interacting many-body ground state operators in Eqs. (10.10) and (10.14), rather than for interacting ground states. This is justified by the fact that the non-interacting AI and OAL phases are adiabatically connected to their non-interacting counterparts. Indeed, according to this fact, the creation operators of these interacting ground states

[4] It should be mentioned that, as $M_{x,I}(\theta)$ is not rigorously a symmetry of the system, its expectation-value might change continuously within a given phase. Nevertheless, provided the correlation length remains short, the values it might adopt in each phase are expected to remain close enough from the ideal values in Tab. **10.1** to still allow us to identify the phase [191,195,196].

Phase	$\langle M_x \rangle_{\Psi_0}$	$\langle M_{x,I}(\theta) \rangle_{\Psi_0}$
AI	1	$\exp\left[-iQ_I(\theta - \frac{\pi}{2})\right]$
OAL	1	$\frac{1}{4}\exp\left[-iQ_I(\theta - \frac{\pi}{2})\right]\cos^2\theta$
MI	$(-1)^N$	$\exp\left[-iQ_I(\theta - \frac{\pi}{2})\right](-1)^L$

Table 10.1: Expectation values of the reflection operator and $U(1)$-twisted partial reflection operator evaluated for the ground states created the operators in Eqs. (10.10), (10.14) and (10.19). Q_I denotes the average total charge enclosed within the interval I.

can be written like Eqs. (10.10) and (10.14), by substituting the single-particle creation operators by those of quasiparticles with identical symmetry properties.

The MI phase in the HDC chain is not adiabatically connected to *any* non-interacting atomic limit, yet it can be continued to a state with no entanglement between the unit cells (the limit $t_3 \to 0$). A similar case was illuminated in Refs. [192,197]. Motivated by the similarity between these "local" Mott phases and the atomic limits of TQC, we coin the term **Mott atomic limit** to refer to gapped phases whose wave functions can not be written as Slater determinants of single-particle states, but as a product of entangled many-body states localized within the unit cell. The Hubbard diamond thus enriches the possible building blocks of quantum matter, and motivates the expansion of possible atomic limits to include Mott atomic limits.

10.4 Diagnosing topology from Green's functions

We explore now to which extent the topology of the interacting phases in the HDC model can be identified by analyzing the spectra of single-particle Green's functions in terms of TQC. For that, we calculate the Green's functions via cluster perturbation theory and invoke the concept of a topological Hamiltonian.

Whereas iDMRG and VMC are powerful methods to solve the ground state of many-body low-dimensional interacting systems, calculating Green's functions with them is not straightforward. CPT is a technique for calculating the Green's function of Hubbard models of strongly-correlated electrons. It consists in dividing the lattice into a (super)lattice of clusters and treating the couplings between clusters at leading order in perturbation theory. Since the Hubbard diamond chain is suitable for the clustering in diamonds, we could expect CPT to give accurate results.

We choose as a cluster a 4-site diamond (grey region in Fig. **10.1**a). With this choice, the 4-particle ground state of the diamond is calculated exactly for the interacting Hamiltonian, by setting $t_3 = 0$. The next step is to use this ground state to compute the Green's function of the cluster. Finally, the Green's function of the chain is obtained by considering a small t_3 and promoting the cluster Green's function. The spectral function

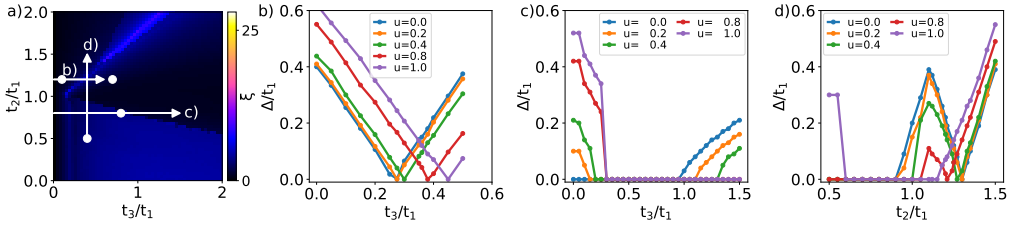

Figure 10.5: (a) Labeling of the paths considered in the CPT calculations over the iDMRG/VMC phase diagram obtained with $U/t_1 = 1.0$. (b), (c) and (d) show the evolution of the charge gap Δ/t_1 along the different paths as a function of the hopping parameter for different values of the $u = U/t_1$. A cluster containing a single unit cell has been used in CPT calculations.

can be extracted from the imaginary part of the Green's function.

We first check the reliability of the CPT results for the interacting HDC at half-filling. For that, we calculate the charge gap Δ/t_1 along the three paths on the phase diagram shown in Fig. **10.5**(a), for different values of the interaction strength U. In agreement with iDMRG and VMC results, we identify four phases: a metallic phase and three insulator phases characterized by the presence of a charge-gap in the spectral function.

The insulating phase at finite U, $t_2/t_1 < 1$ and $t_3/t_1 \ll 1$ shows a spectral function with a charge gap originated by the formation of upper and lower Hubbard bands (see Fig. **10.6**c). Hubbard bands are the typical feature of Mott insulators. This corroborates that local electron-electron interactions are responsible for a metal-to-Mott insulator transition in the HDC. The remaining two insulating phases are reminiscent of the non-interacting AI and OAL phases. The corresponding spectral functions suggest moreover that they are correlated insulators [see Figs. **10.6**(a) and (b)] describable in terms of quasiparticles. As U increases, phase transition between both phases is shifted towards larger values of t_3/t_1 [Fig. **10.5**(b)], which is in good agreement with the results of iDMRG and VMC calculations.

At $t_2/t_1 < 1$, and moderate values of U a metallic phase appears in a narrow region of intermediate t_3/t_1 values, between the Mott insulator and the interacting OAL phase (see Fig. **10.5**c). Furthermore, this gapless region is shifted to larger values of t_3/t_1 as the Hubbard-U parameter is increased – within the range of values considered for U. Even if these metallic phase and tendency are also observed via iDMRG and VMC, they survive to larger values of U in CPT calculations. The reason for this discrepancy could be that, according to our choice of cluster, t_3 is treated as a perturbation in our CTP approach, while it might become significant for the region where the transition between MI and OAL phases takes place.

Now that the capacity of CPT for capturing all the insulating phases of the HDC

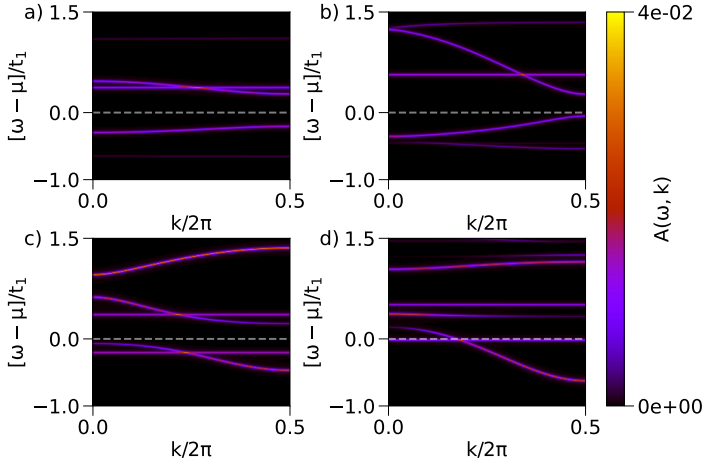

Figure 10.6: CPT spectral functions $A(\omega, k)$ calculated for $U/t_1 = 1$ at the marked cicles in Fig. **10.5**a. The Fermi-level is shown with dashed lines. Each spectral function is normalized to satisfy $\int \mathrm{d}\omega \sum_k A(\omega, k) = 1$, where the integral runs over the whole frequency domain. (a) AI ($t_2/t_1 = 1.2$, $t_3/t_1 = 0.1$), (b) OAL ($t_2/t_1 = 1.2$, $t_3/t_1 = 0.7$) , (c) MI ($t_2/t_1 = 0.5$, $t_3/t_1 = 0.4$), (d) Metallic phase ($t_2/t_1 = 0.8$, $t_3/t_1 = 0.8$).

has been checked, we construct the topological Hamiltonian and proceed with the determination of the topological nature of the AI and OAL insulating phases. The use of the topological Hamiltonian in this region is justified by the fact that $G(0, k)$ is non-singular for these insulating phases. In Fig. **10.7**, we show the bands of the topological Hamiltonian for both phases at U/t_1=1 together with their little group irreps at Γ and X. We note that the irreps of the occupied bands at small (large) values of t_3/t_1 [Figs. **10.7**(a) and (b), respectively] coincide with those of the non-interacting AI (OAL) phases (compare with Fig. **10.3**a and c, respectively), which corroborates that these interacting insulating phases are adiabatically connected to the non-interacting ones.

The MI phase, on the contrary, deserves special attention. In section 10.3.2 it was shown that there is not smoothly connected to any non-interacting limit. The Green's function obtained via CPT in this phase is singular at $\omega = 0$. The origin of this divergence is indeed the self-energy, which also diverges at $\omega = 0$, as it is shown in Fig. **10.8** for $t_2/t_1 = 0.5$, $t_3/t_1 = 0.4$ and $U/t_1 = 1.0$. In such a situation, the topological Hamiltonian is not applicable and the EBR description cannot be pursued.

We conclude that the TQC based analysis of the spectra of single-particle Green's functions (via the topological Hamiltonian) provides a possible new avenue to characterize correlated insulating phases, as far as they are smoothly connected to non-interacting limits. This excludes Mott phases which require a characterization beyond the single-particle Green's functions. Albeit this limitation, the approach can be straightforwardly

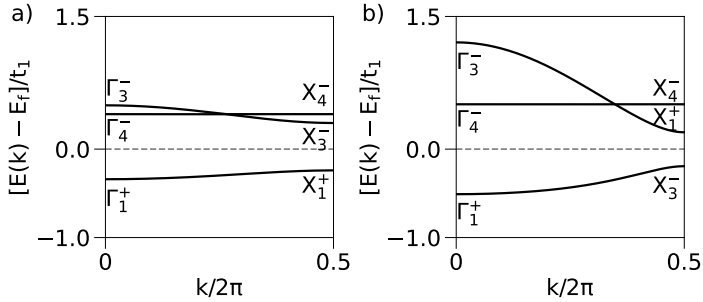

Figure 10.7: Spectrum and irreps of the topological Hamiltonian in the correlated insulating phases for $U/t_1 = 1$ in a) the AI phase ($t_2/t_1 = 1.2$, $t_3/t_1 = 0.1$) and b) the OAL phase ($t_2/t_1 = 1.2$, $t_3/t_1 = 0.7$). The lowest occupied band has been omitted.

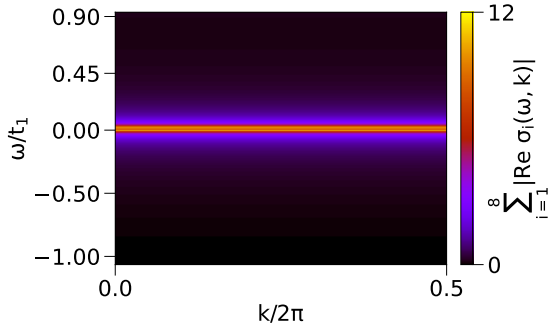

Figure 10.8: Sum of the absolute value of the real part of self-energy's eigenvalues $\sigma_i(\omega, k)$ in the MI phase. The drastic increase close to $\omega = 0$ is identified as a divergence of the self-energy.

applied to diagnose the topology of many correlated insulating phases in real materials, in contrast to many-body invariants which can be computed only for very specific models due to the analytical and numerical complexity of their calculation.

Moreover, motivated by the fact that the MI phase is connected to the limit of interacting-decoupled diamonds localized in the unit cell, we have introduced the concept of *Mott atomic limits*. These are insulator many-body phases whose ground state is induced from interacting clusters of electrons localized in the unit cell. In Ref. [65], which is the result of a collaboration held later with the group of Drs. Titus Neupert (University of Zurich) and Roser Valentí (Goethe University), Mott atomic limits have been defined properly and proposed as the generalization of non-interacting limits to the study of interacting topological insulators. The representation theory for two-particle Green's functions has also been developed in the mentioned work, and its capacity for fully classifying two-particle Mott atomic limits has been demonstrated [65].

10.5 HDC with spin-orbit coupling

While the spin-degree of freedom of electrons was effectively ignored in the previous analysis of the HDC, it is known that SOC corrections turn out to be significant in many materials. Here, we consider the reconsider the HDC with spinful electrons.

Because of the capacity of SOC for breaking the degeneracy of energy levels and bands, this effect is often responsible for gapped phases in materials that would be otherwise metallic. Based on this intuition, we could expect SOC to split the partially-filled bands in the metallic phase of the $U = 0$ HDC [see Fig. **10.3**(d)] into two sets of filled and empty bands, leading to an insulator phase.

On the other hand, the Mott insulator phase is originated in the HDC as a result of interactions on the metallic phase: When on-site electron interactions are considered, electrons tend to distribute themselves in such a way that Wannier functions inducing the partially-filled bands host on average a single electron.

Taking these two point into account, we could ask ourselves the following question: could we hope to observe the Mott phase in the HDC with SOC? The investigation presented in this section sheds light on this question. We begin by introducing the way to account for the spin of electrons in the model for the HDC. Then, we study the effect of this correction on the phase diagram. Finally, we focus on a particular point within the metallic phase of the HDC and analyze the interplay between SOC and interactions on it.

10.5.1 Model for spinful electrons in the HDC

Two ingredients of the model presented in Sec. 10.1 should be changed to account for the spin of the electrons: the transformation properties of Wannier functions in the unit cell, and the hopping parameters.

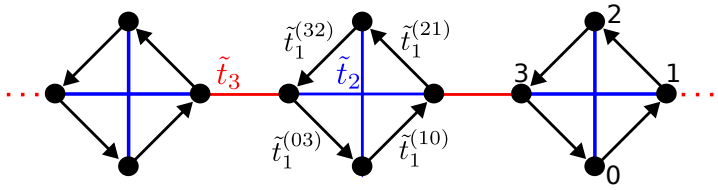

Figure 10.9: Hoppings included in the spinful model for the HDC. The actual matrix forms of the couplings are given in Eqs. (10.21), (10.22) and (10.22).

According to the discussion in Sec. 4.4, the action of symmetries on the spin-degree of freedom should be taken into account. The transformation of spin-indices is described by the matrices of SU(2). Since the symmetry group of the chain contains operations which map spin-up to spin-down, there is *a priori* no reason to restrict the analysis to only one of the spin subspaces.

Regarding the hoppings included in the model, the possibility for having couplings between spin-up and spin-down states should be considered, in principle. An efficient way to deal with this possibility is to consider that the hopping terms t_1, t_2 and t_3 of the spinless model are now 2×2 matrices, instead of scalars. Let us denote these matrices $\tilde{t}_1$, $\tilde{t}_2$ and $\tilde{t}_3$. The starting point to determine the form of the hoppings compatible with the space group is to consider that all hopping terms in the unit cell are different[5], as shown in Fig. **10.9**.

Next, we concentrate on the unit cell containing the origin, and to the check how the generators[6] of D_{2h} relate the hopping elements between them. The constrains set by time-reversal symmetry and the hermiticity of the Hamiltonian should also be taken into account.

By following this approach, we concluded that the most general spinful hopping matrices compatible with the symmetries of the HDC are the following:

$$\tilde{t}_2 = t_2 \, \mathbb{1}, \tag{10.21}$$

$$\tilde{t}_3 = t_3 \, \mathbb{1}, \tag{10.22}$$

$$\tilde{t}_1^{(10)} = \tilde{t}_1^{(21)} = \tilde{t}_1^{(32)} = \tilde{t}_1^{(03)} = \begin{bmatrix} t_1 & 0 \\ 0 & t_1^* \end{bmatrix}, \tag{10.23}$$

where $t_2, t_3 \in \mathbb{R}$ and $t_1 \in \mathbb{C}$. In conclusion, the spinful model for the HDC contains one more parameter than the spinless model, which is precisely $\mathrm{Im}\, t_1$. For the rest of the analysis, we equivalently express t_1 as $t_1 = |t_1| \exp(i\phi)$, and consider $|t_1|$ and $\phi \in [0, 2\pi]$

[5] Like in the spinless case, we restrict ourselves to the case where the hopping matrices where there is a single hopping matrix $\tilde{t}_2$.

[6] As aformentioned, we would have to go through all the generators of the space group (except lattice translations). In the case of $Pmmm$, as it is a symmorphic space group, this is equivalent to checking the action of the generators of D_{2h}, which is the group formed by the coset representatives in Eq. (4.25).

SV irrep	Γ_1^+	Γ_3^-	Γ_4^-	X_1^+	X_3^-	X_4^-
DV irrep	$\bar{\Gamma}_5$	$\bar{\Gamma}_6$	$\bar{\Gamma}_6$	$\bar{X}_5$	$\bar{X}_5$	$\bar{X}_6$

Table 10.2: Relation between irreps of little groups in the spinless (SV) and spinful (DV) cases. Every irrep of the spinless case can be considered to turn into the irrep that is below it when the model accounts for the spin. We are not being rigorous with the notation, as we are not using physically-irreducible irreps for the spinless case; trivial spin degeneracy should indeed be assumed for that case.

the parameters of the model. Despite ϕ being a cyclic parameter, not being related to the magnitude of t_1 and the spin subspaces being decoupled, we will interpret ϕ as the "strength" of the SOC, since $\phi = 0$ represents the spinless case.

These expressions for the hopping matrices lead to the most general spinful Hamiltonian in Eq. (10.1) compatible with the symmetries of the system. We see that, within this hopping range, it is not possible to couple spin-up and spin-down indices, so they keep on being good quantum numbers for the non-interacting part. Notice however that the blocks of the Hamiltonian are not identical anymore for both spin subspaces, unlike in the spinless case.

Concerning the notation for the application of representation theory to the study of the band structure, we would have to work with double-valued groups, which account properly for the transformation of the spin. Equivalently, we can restrict ourselves to the symmetries of single-valued groups, but adopting the notation for irreps of double-valued groups. The set of irreps at Γ and X of the band representation induced from spinful s-orbitals in WPs 2i and 2m is:

$$(\bar{E} \uparrow G)_{2i} \oplus (\bar{E} \uparrow G)_{2m} : \{2\bar{\Gamma}_5 \oplus 2\bar{\Gamma}_6, 2\bar{X}_5 \oplus 2\bar{X}_6\}. \tag{10.24}$$

10.5.2 Phase diagram for the spinful-indepentent electron HDC

Once the model for spinful electrons has been established, we turn our attention to the effect of ϕ on the phase diagram. Like in the spinless case, we apply at Γ and X changes to bases adapted to the symmetry of irreps in Eq (10.24). This allows us to derive analytical expressions for the actual energy level of each irrep, which facilitates the identification and classification – via TQC – of the phases. Furthermore, it turns out that ϕ enters these expressions always in terms of $\sin^2\phi$ or $\cos^2\phi$, thus it is enough to consider $\phi \in [0, \pi/2]$.

In order to understand the evolution of the phase diagram under ϕ, it is convenient to keep in mind how the relation between irreps used in both the spinless and spinful cases. This relation can be found in Tab. **10.2**:

The nature of the AI and OAL phases does not change upon inclusion of SOC. As it is shown in Fig. **10.10**, the band structures are reminiscent of the spinless AI and

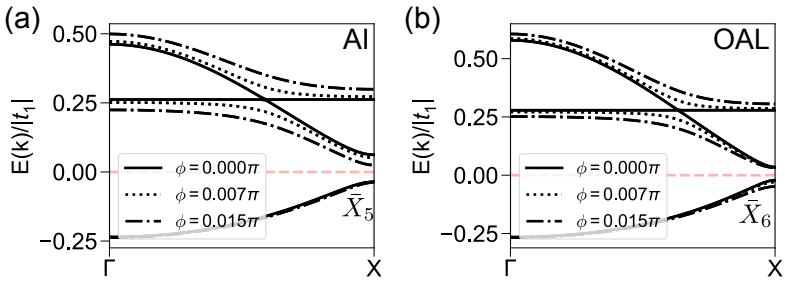

Figure 10.10: Band structures of the spinfull HDC for different values of ϕ. The red-dashed line indicates the chemical potential (calculated for $\phi = 0$). The lowest valence band, with irreps $\{\bar{\Gamma}_5, \bar{X}_5\}$, is omitted in the plots. (a) AI phase ($t_2/|t_1| = 1.2$, $t_3/|t_1| = 0.2$), with $\bar{X}_5$ as the irrep of the last valence band at X. (b) OAL phase ($t_2/|t_1| = 1.2$, $t_3/|t_1| = 0.3$), where $\bar{X}_6$ is the irrep of the last valence band at X.

$\Gamma(0,0,0) - \Sigma(k,0,0)$	$X(1/2,0,0) - \Sigma(k,0,0)$
$\Gamma_3^- \to \Sigma_1$	$X_3^- \to \Sigma_1$
$\Gamma_4^- \to \Sigma_4$	$X_4^- \to \Sigma_4$
$\bar{\Gamma}_6 \to \bar{\Sigma}_5$	$\bar{X}_6 \to \bar{\Sigma}_5$

Table 10.3: Compatibility relations for irreps of little groups in the line Σ connecting Γ to X.

OAL, and remain connected adiabatically to these. We will consequently refer to these spinful phases as AI and OAL.

Regarding the metallic phase, remember that its band structure displayed in the spinless case a partially-filled set of bands cut by the chemical potential [see Fig. **10.3**(d)]. These bands separate when a finite $\phi \in (0, \pi/2)$ is considered in the spinful model, as shown in Fig. **10.11**(a), and the system turns into an insulator. This metal-to-insulator transition can be understood in terms of irreps of little groups and their compatibility relations, shown in Tab. **10.3**: The bands are partially-filled for $\phi = 0$ because the irreps Γ_3^- and Γ_4^- subduce to different irreps Σ_1 and Σ_4 in the Γ-X line, allowing them to be connected. For a finite ϕ, these bands have the same irrep $\bar{\Gamma}_6$ at Γ, and they thus subduce to the same irrep $\bar{\Sigma}_5$ in the line. The hybridization between bands transforming as the same irrep opens then a gap between them, leading to a band structure without partially-filled bands.

We now tackle the classification of the insulator phase obtained by adding spin to the system. The irreps of its valence bands are $\bar{\Gamma}_5$ and $\bar{\Gamma}_6$ at Γ, $\bar{X}_5$ and $\bar{X}_6$ at X. The corresponding representation has two atomic limits: On the one hand, it can be written as $(\bar{E}_g \uparrow G)_{1a} \oplus (\bar{E}_u \uparrow G)_{1a}$, which corresponds to the induction from spinful s-like and

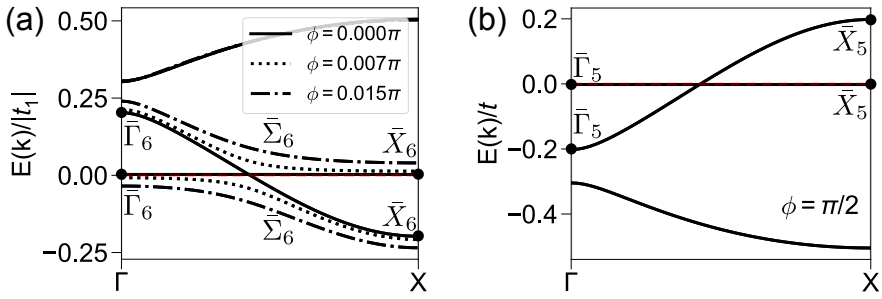

Figure 10.11: Band structures of the spinfull HDC for values of t_2 and t_3 that yield a metallic phase in the spinless case ($t_2/|t_1| = 0.8$, $t_3/|t_1| = 0.2$). The red-dashed line denotes the chemical potential, which lies at zero energy for the $\phi = 0$ case. (a) Band structures for different values of ϕ. The set of patially-filled bands separates in two, leading to the spectrum of an insulator. (b) Band structure with $\phi = \pi/2$.

Phase	Irreps of valence bands
AI	$2\bar{\Gamma}_5, 2\bar{X}_5$
OAL	$2\bar{\Gamma}_5, \bar{X}_5 \oplus \bar{X}_6$
SAI	$\bar{\Gamma}_5 \oplus \bar{\Gamma}_6, \bar{X}_5 \oplus \bar{X}_6$

Table 10.4: Irreps of little groups at maximal $\boldsymbol{k}$-points for the valence bands of each insulator phase, in the spinful HDC.

p-like orbitals sitting in WP 1a – the center of the cell [Fig. **10.12**(a)]. On the other hand, it could be decomposed as $(\bar{E}_g \uparrow G)_{1a} \oplus (\bar{E}_u \uparrow G)_{1a}$, which corresponds to placing the same kind of orbitals in WP 1b – border of the unit cell [Fig. **10.12**(b)]. We will refer to this insulator phase as **SOC-driven atomic insulator** (SAI).

The parameter ϕ has also influence on the lines where transitions between topologically different phases happen, as it is shown in Fig. **10.13**. As ϕ is increased, the transition between AI and OAL phases is shifted to smaller values of $t_3/|t_1|$, while that between the SAI and OAL phases takes place at larger values. The maximum variation with respect to the spinless case is achieved at $\phi = \pi/4$. If we keep increasing this parameter, the phase-transition lines move the other way around, until the SAI is substituted back by a metal at $\phi = \pi/2$.

The metallic phases at $\phi = 0$ and $\phi = \pi/2$ are not identical, although the band structures of both phases contain partially-filled bands. The difference is spotted by looking at these bands' irreps in Γ and X. These irreps are $2\bar{\Gamma}_6$ and $2\bar{X}_6$ for the $\phi = 0$ metallic phase [Fig. **10.11**(a)], whereas they are $2\bar{\Gamma}_5$ and $2\bar{X}_5$ for the metal at $\phi = \pi/2$ [Fig. **10.11**(b)]. Accordingly, partially-filled bands of these metallic phases have different

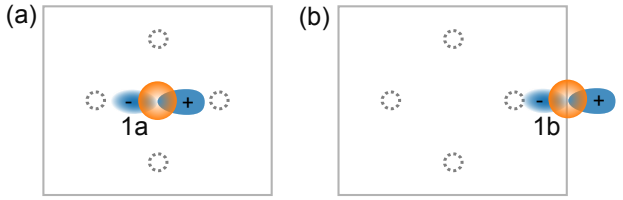

Figure 10.12: Possible atomic limits for the valence bands of the insulator obtained from the metal phase upon consideration of spin. s-like (p-like) orbitals are indicated in orange (blue). Atomic positions are marked with gray-dashed circles, and the unit cell coincides with box. (a) Induction from orbitals in WP 1a. (b) Induction from WP 1b. The orbitals sitting on the left border of the cell have been omitted.

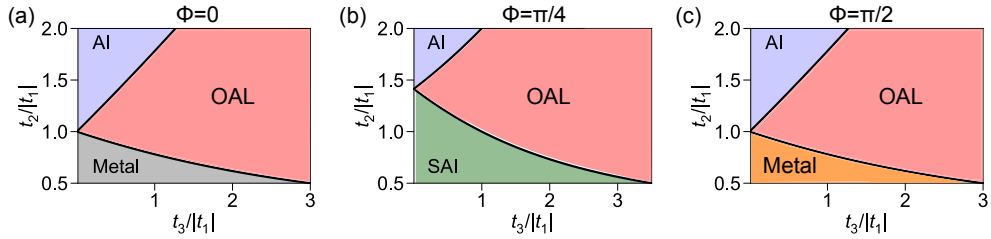

Figure 10.13: Phase diagram of the spinful HDC for different values of ϕ. (a) $\phi = 0$. (b) $\phi = \pi/4$. (c) $\phi = \pi/2$; the metallic phase here is different to that with $\phi = 0$, because the irreps of the partially-filled bands are different (see Fig. **10.11**).

atomic limits: while they are induced from a pair of spinful s-like orbitals sitting in WP 1a for $\phi = 0$, the orbitals are p-like at $\phi = \pi/2$ (also in WP 1a). Based on this difference in the nature of the orbitals, we might expect electron interactions to drive these metal phases to topologically different Mott insulators.

10.5.3 Interplay between SOC and electron interactions

For the rest of this chapter, we focus on gaining insight into the interplay between SOC and electron-electron interactions.

In the spinless model, we observed that electron interactions tend to drive the metal phase to a Mott insulator, while their effect is just a renormalization of bands in phases that were already insulators with $U = 0$ (AI and OAL). Therefore, upon addition of interactions, we could hope to observe Mott phases only at $\phi = 0$ and $\phi = \pi/2$, and a renormalization of bands in the AI, OAL and SAI phases for $0 < \phi < \pi/2$.

Let us consider the point with $t_2/|t_1|$ and $t_3/|t_1| = 0$ in the phase diagram, where the system is metallic for $\phi = 0$ and $\phi = \pi/2$. We will study the influence of ϕ and the interaction strength U on the system. The reason for choosing $t_3 = 0$ is that, as the

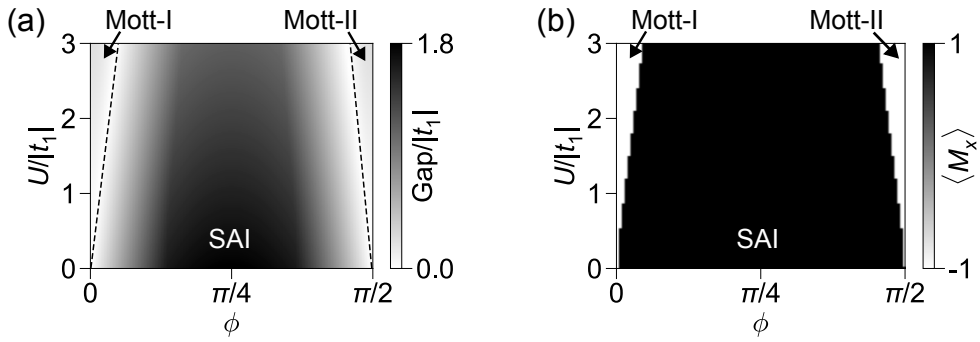

Figure 10.14: Exact diagonalization based calculations of a single diamond with $t_2/|t_1| = 0.5$. (a) Gap between the 4-particle ground state and first excited state energy of the diamond. (b) Expecation value of M_x reflection computed for the 4-particle ground state of the diamond.

diamonds making up the chain are decoupled, we can restrict the analysis to one of them. We have solved for the ground state and its energy level with exact diagonalization, also for the energy level of the first excited states. The difference in energy between the ground and first excited states is shown in Fig. **10.14**(a). The gap is finite where the phase is supposed to be the SAI, that is, where ϕ is the dominant parameter. It is also finite on the $\phi = 0$ and $\phi = \pi/2$ axes, where the system is expected to be in the Mott phase. However, we observe that transitions between Mott and SAI phases do not happen in the immediate vicinity of the these axes – as soon as we move out of them. Instead, it seems that the Mott phases survive when the interaction strength U dominates over ϕ.

In order to clarify this point, we consider the mirror symmetry M_x. We showed in Sec. 10.3 that its expectation value is $+1$ for any ground state which can be written as a Slater determinant, while it could take other values in the Mott insulator phases. It is therefore a good candidate to identify the nature of the observed phases. Fig. **10.14**(b) shows precisely the expectation value $\langle M_x \rangle$ computed for the ground state of the diamond. We see that $\langle M_x \rangle = +1$ for the SAI phase, as it is adiabatically connected to a band insulator (with SOC). However, $\langle M_x \rangle = -1$ for the gapped phases around the $\phi = 0$ and $\phi = \pi/2$ axes, which corroborates that they are Mott insulator phases.

In conclusion, we have shown that accounting for the spin of electrons enriches the phase diagram of the HDC. Upon addition of SOC, the AI and OAL just suffer from a renormalization of bands, while the metallic phase turns into an atomic insulator (SAI). Furthermore, at $\phi = \pi/2$, we have identified a metallic phase that is not connected to the gapless phase we had without SOC. These phases lead to Mott insulators upon consideration of local electron interactions. In fact, a deeper analysis of these Mott

phases might be promising, as they could belong to topologically distinct classes based on the fact that they originate from different metallic band structures. Finally, we have observed that the Mott phase survives to small values of ϕ, which suggests that relativistic effects and strong interactions might compete in certain group of materials. This tendency was reported in some Iridium based pyrochlore oxides [198].

11 Conclusions and outlook

It is time to summarize the results of this work and comment on the direction that future work could follow. Since the thesis is formed by four main projects, we will devote a section to each of them.

Band topology from a geometrical perspective of adiabatic transport. We have presented an alternative point of view to look into topology of band structures. In particular, we have shown how Berry phases and Wilson loops arise within the framework of adiabatic transport. Then, we have described the relationship between Wilson loops and localization of electrons, and shown the capacity of these mathematical objects for diagnosing topological phases in isolated sets of bands. This perspective is not limited to the single-band case, since it is directly applicable to the case where the set of states to be investigated contains multiple bands.

Although we got a grasp on the way symmetries constrain Wilson loops, there is still a lack of a general study about relationship between Wilson loops and crystal symmetries. In fact, determining and tabulating the constraints that crystal symmetries set in Wilson loops for any 230 space groups would be interesting. Such a map of Wilson loops would facilitate the identification of which Wilson loop is able to identify a certain topological phase in a system. Furthermore, this analysis could help us gain insight about the surface and edge states that a material with a certain topological phase might display, since Wilson loops' spectra are closely related to boundary modes [10].

***IrRep*: irreducible representations of *ab initio* band structures.** The software *IrRep* constitutes our contribution to the DFT based analysis of topological materials. It allows for a systematic calculation of symmetry eigenvalues and irreps of *ab initio* bands, as it works for all 230 non-magnetic space groups, with and without SOC. Currently, it includes interfaces to VASP, Quantum Espresso, Abinit and Wannier90, but its source code is structures in a form that facilitates the development of new interfaces.

Many additional features could be considered to be implemented in the future. First, we could consider implementing the calculation of irreducible correpresentata-

tions of magnetic groups, as the data needed for it is already available in the *Bilbao Crystallographic Server* [34, 72]. Secondly, including the possibility for computing the decomposition in terms of EBRs of the representation of a set of bands might be worth it, at least for space groups where the decomposition can be written unambiguously. Another interesting development would be to write interfaces for other DFT codes, like SIESTA [119] or the software MPB for the simulation of photonic crystals' band structures [199].

Topological quantum chemistry for heavy-fermion insulators. We have presented a TQC based analysis of the origin of topology in paramagnetic heavy-fermion insulators, which include mixed-valence and Kondo insulators. This approach consists in applying TQC to investigate how valence bands inherit their topological aspects from the interplay between dispersive $5d$ and almost-flat $4f$-bands. The analysis is applicable to the 230 non-magnetic space groups, with and without SOC. One of the main advantages of this approach is that it allows for a rigorous classification of topological phases which accounts for all crystal symmetries on an equal footing. Accordingly, the application of TQC to heavy-fermion insulators might lead to a renewed effort in the investigation of topological phases in this family of compounds, and therefore to the identification of new topological materials.

The approach has been tested with a particular material, SmB_6, for which it has lead to a more detailed classification of the material than in previous works. Moreover, we have concluded that the origin of topology in SmB_6 can be interpreted as the formation of valence bands mediated by the combination of irreps from $4f$ and $5d$-bands.

Based on the fact that $4f$-states tend to induce a relatively large number of bands, we conjecture that interplay between these and dispersive bands might yield to several disconnected sets of topological bands close to the Fermi level. On the boundaries of the material, these sets might be connected by midgap states. Furthermore, due to the proximity of these surface states to the Fermi level, they might be accessible to experimental probes. Our TQC based analysis might turn out to be helpful for the prediction of such surface modes, since it makes possible to classify every isolated set of bands separately.

Considering irreducible corepresentations of magnetic space groups [34] would be a promising next step for this project. We might hope that this implementation could allow for the characterization of topological phases in magnetically-ordered heavy-fermion insulators. In fact, the applicability of TQC to the rest of phases showing up in Kondo materials remains unexplored, as an option for future work.

Hubbard diamond chain. In this chapter, we have explored the possibility for extending the TQC formalism to interacting systems by applying it to the analysis of single-particle Green's functions. The approach has been tested in a particular system: the HDC. We have concluded that the TQC based analysis of Green's functions' spectra

is an efficient method for the identification and classification of the nature of interacting phases, as long as they are adiabatically connected to band insulators. The efficiency of the approach consists in the fact that it can be implemented numerically in a systematic way, in contrast to the computation of many-body topological invariants.

Our analysis illustrates that the Mott phase of the HDC is excluded from the applicability of the method, owing to the divergence of the self-energy at zero frequency in this phase. We conjectured that this phase requires the knowledge of 2-particle Green's functions, which has been confirmed in a later collaboration [65]. Moreover, the fact that this many-body phase stems from the diamond defined within the unit cell encouraged us to dub *Mott atomic limits* to such phases. Mott atomic limits have been classified in more detail in Ref. [65].

Although we focused here on the example of the one-dimensional HDC with space group $Pmmm$, the method we introduced can be easily extended to interacting systems and materials with other space groups and/or higher dimensions. This is advantageous with respect to many-body invariants calculations which are often not achievable for material-specific models due to the mathematical complexity of such a framework. Some possible direct extensions of the present work to materials are the two-dimensional version of the diamond chain (the square-octagon lattice) recently discussed in the context of organic networks [200], or the Shastry-Sutherland lattice materials which include insulating and metallic families [201]. Applying the formalism to materials in two and three dimensions requires calculating the Green's function and irreps of the topological Hamiltonian in four and eight high-symmetry points in the BZ, respectively, and to work with space groups that contain more symmetry operations and therefore are richer in EBRs. Since irreps of little groups in high-symmetry points and EBRs of all space groups are already available [96, 98], the extension of TQC we are proposing to real materials is of practical use and may lead to new insights in the quest for diagnosing topology in interacting systems.

Regarding the HDC, we have identified (without SOC) two atomic limits which are connected to non-interacting insulators (AI and OAL), and a metal phase that turns into a Mott insulator upon consideration of electron interactions. Specifically, we have demonstrated that the Mott phase is a symmetry protected topological phase which is not adiabatically connected to any band insulator. When SOC corrections are included in the model, the metal phase becomes an insulator (SAI) with an atomic limit that differs from the AI and OAL. Moreover, we have observed that the Mott phase survives to the addition of moderate SOC, which suggests that relativistic effects and electron interactions might compete in a certain class of materials, in accordance to Ref. [198].

To conclude, let us comment on the possible direction that (our) future efforts might follow in order to achieve a definitive extension of TQC to interacting systems. First of all, investigating the divergence of the self-energy in the Mott phase could be interesting. It might yield to a deeper insight on the nature of the Mott insulators and lead to a solution that would allow to a successful diagnosis of topological Mott phases through

single-particle Green's functions. Second, the discovery of the fact that higher-particle Green's functions can detect topological Mott phases might motivate the development of efficient numerical techniques for the calculation of two-particle Green's functions – for example, an extension of CPT to such Green's functions. Third, since the addition of SOC leads to two metal phases whose partially filled bands have different atomic limits, the HDC might be a promising platform for the investigation about Mott atomic limits. Finally, the demonstrated usefulness of Green's functions might turn out to be encouraging for the development of ways to avoid the wannierization in the calculation of Green's functions.

A Abbreviations

Abbreviation	Definition
QHE	Quantum Hall effect
TCI	Topological-crystalline insulator
TQC	Topological quantum chemistry
WP	Wyckoff position
EBR	Elementary band representation
DFT	Density Functional Theory
CLI	Command line interface
CICE	Concentric intersecting coplanar ellipses
MI	Mott insulator
SAI	SOC-driven atomic insulator
HEK	Hall efektu kuantikoa
KTK	Kimika topologiko kuantikoa
HDK	Hubbarden diamante katea

B Group theory definitions

Definition 1 : The **site-symmetry group**, or stabilizer group, of a site $\boldsymbol{q}$ is the group of symmetries $G_{\boldsymbol{q}}$ which leave $\boldsymbol{q}$ fixed. $G_{\boldsymbol{q}}$ is indeed a subgroup of the space group G (*i.e.* $G_{\boldsymbol{q}} \subset G$) which does not include lattice translations. The site-symmetry group $G_{\boldsymbol{q}}$ is said to be maximal if there does not exist a group H such that $G_{\boldsymbol{q}} \subset H \subset G$.

Definition 2 : The crystallographic **orbit** of a site $\boldsymbol{q}$ is the set of positions $\{g\boldsymbol{q} \mid g \in G\}$ related to it by the symmetry operations of the space group G. Notice that the orbit of every site is infinite owing to the infinite number of translations in G.

Definition 3 : The **Wyckoff position** of a site classifies the elements of its orbit which belong to the primitive unit cell. The multiplicity of a Wyckoff position is given by the number of elements in it, *i.e.* the number of positions within the primitive unit cell that are symmetrically equivalent to the original site.

Definition 4 : A Wyckoff position is said to be a **maximal** if the site-symmetry group of any of its site is a maximal.

C Topological quantum chemistry for heavy-fermion insulators: supplemental material

C.1 Details of DFT calculations

The Vienna Ab Initio Simulation package [164] has been used to perform the **ab initio calculations** of SmB_6. A plane-wave cutoff of 500 eV was used in the self-consistent calculation of the ground-state density and the BZ was sampled with a grid of $9\times9\times9$. Spin-orbit corrections have been included in the calculations. Lattice parameters and atomic positions were taken from Ref. [202] and the General Gradient Approximation was used for the exchange-correlation term in the Perdew Burke Ernzerhof [137] parametrization. We employed the software *IrRep* [77] to calculate the irreps of little groups at maximal $\boldsymbol{k}$-points. The data obtained from this package has been analyzed with the software *CheckTopologicalMat* [30, 104] to compute the topological-invariants.

C.2 Excluding potential band-crossings on high-symmetry lines, planes and generic points

In this appendix, we comment on the potential existence of accidental band crossings between valence and conduction bands in SmB_6. For that, we first need to show how symmetries constrain the form of the Hamiltonian on a $\boldsymbol{k}$-point in the BZ.

Let $\hat{H}(\boldsymbol{k})$ be the Hamiltonian operator restricted to bands that potentially cross at particular $\boldsymbol{k}$-point. We consider that the states on these bands transform as the same pirrep $D^{\boldsymbol{k}}$, as otherwise they could not hybridize. $\hat{H}(\boldsymbol{k})$ can be written in the following

form:

$$\hat{H}(\boldsymbol{k}) = \sum_{ij} h_{ij}(\boldsymbol{k}) \, |i\rangle\langle j| \, , \tag{C.1}$$

where $|i\rangle$ and $|j\rangle$ run over the states adapted to the symmetry of the pirrep of bands that (potentially) cross. For a symmetry operation $g_{\boldsymbol{k}}$ in the little group of $\boldsymbol{k}$:

$$\begin{aligned} g_{\boldsymbol{k}}^{-1} \hat{H}(\boldsymbol{k}) g_{\boldsymbol{k}} &= \sum_{ij} h_{ij}(\boldsymbol{k}) g_{\boldsymbol{k}}^{-1} \, |i\rangle\langle j| \, g_{\boldsymbol{k}} \\ &= \sum_{ijmn} h_{ij}(\boldsymbol{k}) [D^{\boldsymbol{k}\dagger}(g_{\boldsymbol{k}})]_{mi} \, |m\rangle\langle n| \, D^{\boldsymbol{k}}_{jn}(g_{\boldsymbol{k}}) \end{aligned} \tag{C.2}$$

Since $\hat{H}(\boldsymbol{k})$ must commute with all the operations in the little group of $\boldsymbol{k}$, the matrix elements $h_{ij}(\boldsymbol{k})$ must satisfy the following equation:

$$h_{mn}(\boldsymbol{k}) = \sum_{ij} [D^{\boldsymbol{k}\dagger}(g_{\boldsymbol{k}})]_{mi} h_{ij}(\boldsymbol{k}) D^{\boldsymbol{k}}_{jn}(g_{\boldsymbol{k}}) \tag{C.3}$$

Eq. (C.3) might set constrains on the matrix elements $h_{ij}(\boldsymbol{k})$ and therefore, describes how crystal symmetries determine the form of $\hat{H}(\boldsymbol{k})$.

Let θ be the matrix of an antiunitary symmetry in the little group of $\boldsymbol{k}$. The matrix in the pirrep $D^{\boldsymbol{k}}$ of such a symmetry can be written as the combination of a unitary matrix U and the complex conjugation operator $\mathcal{K}$, i.e. $D^{\boldsymbol{k}}(\theta) = U\mathcal{K}$. $\hat{H}(\boldsymbol{k})$ should also commute with θ, which imposes the following constrain on the matrix elements $h_{ij}(\boldsymbol{k})$:

$$h^*_{mn}(\boldsymbol{k}) = \sum_{ij} U^\dagger_{mi} h_{ij}(\boldsymbol{k}) U_{jn} \tag{C.4}$$

In the rest of this appendix, we will go case by case through all symmetry-lines and planes in the BZ. We will derive the most general form of $\hat{H}(\boldsymbol{k})$ that is compatible with the symmetry of the little group of each on each line and plane by applying Eqs. (C.3) and (C.4), to later argument that the probability for having gap-closing points is zero. Finally, we will discard the existence of crossings in generic $\boldsymbol{k}$-points.

Line Δ : $(0, k_y, 0)$

The closing of the gap between valence and conduction bands would involve a touching of states that transform as the pirreps $\bar{\Delta}_6$. We denote $|i\rangle$ and $|j\rangle$ the symmetry-adapted states of one of the Δ_6 pirreps and $|i'\rangle$ and $|j'\rangle$ those of the other Δ_6 pirrep.

Let us consider the matrix elements $h_{ii}(\Delta)$, $h_{ii'}(\Delta)$ and $h_{ij}(\Delta)$ in Eq. (C.1). Instead of checking case by case the constrains set by all symmetries in G_Δ, it is sufficient to consider only the action of the generators (see Tab. **C.1**). In particular, applying

Eq. (C.3) for the four-fold rotation C_{4y}:

$$h_{ij} = -ih_{ij} \Rightarrow h_{ij} = 0. \tag{C.5}$$

In the same spirit, $h_{i'j'} = h_{ij'} = h_{i'j} = 0$. The action of the reflection m_z:

$$\begin{aligned} h_{ii} &= h_{jj}, \\ h_{ii'} &= h_{jj'}. \end{aligned} \tag{C.6}$$

In addition, $h_{i'i'} = h_{j'j'}$ and $h_{i'i} = h_{j'j}$. Since the points in the plane Δ are not time-reversal invariant, we cannot choose this operation as the antiunitary representative. Nevertheless, we can select the combination of inversion and time-reversal symmetry, i.e. $I\mathcal{T}$, which does belong to the little group. By applying the action of the unitary part U of $I\mathcal{T}$ (see Tab. **C.1**) in Eq. (C.4), we obtain the constrain that all matrix elements of $\hat{H}(\Delta)$ must be real functions. Altogether, the most general form of the matrix $H(\Delta)$ compatible with the symmetries in the basis $\{|i\rangle, |i'\rangle, |j\rangle, |j'\rangle\}$ is the following:

$$H(\Delta) = \begin{bmatrix} a(k_y) & b(k_y) & 0 & 0 \\ b(k_y) & a'(k_y) & 0 & 0 \\ 0 & 0 & a(k_y) & b(k_y) \\ 0 & 0 & b(k_y) & a'(k_y) \end{bmatrix}, \tag{C.7}$$

where $a(k_y)$, $a'(k_y)$ and $b(k_y)$ are real functions whose particular shape depends on the microscopic details of the crystal. The eigenvalues of this matrix are

$$E_{\pm}(k) = \frac{1}{2}[a(k_y) + a'(k_y)] \pm \sqrt{\frac{1}{2}[a(k_y) - a'(k_y)]^2 + b^2(k_y)}. \tag{C.8}$$

The square root in Eq. (C.8) should vanish to have a band crossing. This requires $a(k_y) = a'(k_y)$ and $b(k_y) = 0$ to be satisfied simultaneously. The first condition is met at the intersection k_y of two curves, whereas the second equation defines the point k'_y. The coincidence $k_y = k'_y$ requires fine-tuning of the material's microscopic features, thus it is impossible that two bands that transform as $\bar{\Delta}_6$ cross.

Since the Hamiltonian corresponding to $\bar{\Delta}_7$ bands is identical to (C.7), it is impossible to have a crossing between $\bar{\Delta}_7$ bands without the infinitely-accurate tunning of the system's microscopic parameters.

Line T: $(1/2, 1/2, k_z)$

The generators of the little cogroup of a point $(1/2, 1/2, k_z)$ in the line-T are shown in Tab. **C.2**, together with their matrices in the representations $\bar{T}_6$ and $\bar{T}_7$. Since matrices are identical to those of the generators of the little group G_Δ in Tab. **C.1**, the form of the most general Hamiltonian compatible with G_T is that given in (C.7). Therefore, having

Table C.1: Matrices for the generators of the little cogroup of G_Δ in the representations $\bar{\Delta}_6$ and $\bar{\Delta}_7$.

pirrep	$\{4^+_{010}\|000\}$	$\{m_{001}\|000\}$	$\mathcal{T}\{I\|000\}$
$\bar{\Delta}_6$	$\begin{pmatrix} e^{i3\pi/4} & 0 \\ 0 & e^{-i3\pi/4} \end{pmatrix}$	$\begin{pmatrix} 0 & e^{i\pi/4} \\ e^{i3\pi/4} & 0 \end{pmatrix}$	$\begin{pmatrix} 0 & -1 \\ 1 & 0 \end{pmatrix}$
$\bar{\Delta}_7$	$\begin{pmatrix} e^{-i\pi/4} & 0 \\ 0 & e^{i\pi/4} \end{pmatrix}$	$\begin{pmatrix} 0 & e^{-i3\pi/4} \\ e^{-i\pi/4} & 0 \end{pmatrix}$	$\begin{pmatrix} 0 & -1 \\ 1 & 0 \end{pmatrix}$

Table C.2: Matrices for the generators of the little cogroup of G_T in the representations $\bar{T}_6$ and $\bar{T}_7$.

pirrep	$\{4^+_{001}\|000\}$	$\{m_{100}\|000\}$	$\mathcal{T}\{I\|000\}$
$\bar{T}_6$	$\begin{pmatrix} e^{i3\pi/4} & 0 \\ 0 & e^{-i3\pi/4} \end{pmatrix}$	$\begin{pmatrix} 0 & e^{i\pi/4} \\ e^{i3\pi/4} & 0 \end{pmatrix}$	$\begin{pmatrix} 0 & -1 \\ 1 & 0 \end{pmatrix}$
$\bar{T}_7$	$\begin{pmatrix} e^{-i\pi/4} & 0 \\ 0 & e^{i\pi/4} \end{pmatrix}$	$\begin{pmatrix} 0 & e^{-i3\pi/4} \\ e^{-i\pi/4} & 0 \end{pmatrix}$	$\begin{pmatrix} 0 & -1 \\ 1 & 0 \end{pmatrix}$

crossings between bands that transform as the same pirrep in the line-T is improbable.

Line $\Lambda : (k, k, k)$

We show in Tab. **C.3** the generators of the little cogroup of the points in the line-Λ and their matrices in the irreducible representations $\bar{\Lambda}_4$, $\bar{\Lambda}_5$ and $\bar{\Lambda}_6$. It is straightforward to show that the form of the Hamiltonian for two bands that transform as $\bar{\Lambda}_6$ is identical to (C.7). Therefore, in practical terms, two bands that transform as $\bar{\Lambda}_6$ cannot cross.

Let us now look into the potential crossing of two bands that transform as the pirrep $\bar{\Lambda}_4\bar{\Lambda}_5$. We consider the basis $\{|4\rangle, |4'\rangle, |5\rangle, |5'\rangle\}$, where $|4\rangle$ and $|4'\rangle$ are states adapted to the symmetry of $\bar{\Lambda}_4$ whereas $|5\rangle$ and $|5'\rangle$ are adapted to $\bar{\Lambda}_5$. It is clear from Tab. **C.3** that the states of $\bar{\Lambda}_4$ and $\bar{\Lambda}_5$ cannot have matrix elements between them, i.e. $h_{45} = h_{45'} = h_{4'5} = h_{4'5'}$. Consequently, we can write the matrix of $\hat{H}(\Lambda)$ as

$$H(\Lambda) = \begin{pmatrix} h_1 & 0 \\ 0 & h_2 \end{pmatrix}, \tag{C.9}$$

where h_4 and h_5 are 2×2 blocks corresponding to the $\bar{\Lambda}_4$ and $\bar{\Lambda}_5$ irreducible representations, respectively. The subspaces spanned by the states adapted to these irreducible representations are not invariant under the $I\mathcal{T}$, which means that these operation con-

Table C.3: Matrices for the generators of the little cogroup of G_Λ in the representations $\bar{\Lambda}_4$, $\bar{\Lambda}_5$ and $\bar{\Lambda}_6$.

irrep	$\{3^+_{111}\|000\}$	$\{m_{1\bar{1}0}\|000\}$	$\mathcal{T}\{I\|000\}$
$\bar{\Lambda}_6$	$\begin{pmatrix} e^{-i\pi/3} & 0 \\ 0 & e^{i\pi/3} \end{pmatrix}$	$\begin{pmatrix} 0 & -1 \\ 1 & 0 \end{pmatrix}$	$\begin{pmatrix} 0 & -1 \\ 1 & 0 \end{pmatrix}$
$\bar{\Lambda}_4$	1	$-i$	
$\bar{\Lambda}_5$	-1	i	

nects both subspaces. Indeed, the matrix of $I\mathcal{T}$ takes the following off-diagonal form:

$$\bar{\Lambda}_4\bar{\Lambda}_5(I\mathcal{T}) = \begin{pmatrix} 0 & -\mathbb{1} \\ \mathbb{1} & 0 \end{pmatrix}, \tag{C.10}$$

where $\mathbb{1}$ is the 2×2 identity matrix. By applying (C.9) and (C.10) in (C.4) yields the constrain $h_5 = h_4^*$. Altogether, the most general form of $H(\Lambda)$ compatible with the symmetries of the little group is

$$H(\Lambda) = \begin{bmatrix} a(k_y) & b^*(k_y) & 0 & 0 \\ b(k_y) & a'(k_y) & 0 & 0 \\ 0 & 0 & a(k_y) & b(k_y) \\ 0 & 0 & b^*(k_y) & a'(k_y) \end{bmatrix}, \tag{C.11}$$

The eigenvalues of (C.11) are given by

$$E_\pm(k) = \frac{1}{2}[a(k_y) + a'(k_y)] \pm \sqrt{\frac{1}{2}[a(k_y) - a'(k_y)]^2 + |b(k_y)|^2}. \tag{C.12}$$

The crossing of both bands requires $a(k) = a'(k)$, $\mathrm{Re}\{b\}(k) = 0$ and $\mathrm{Im}\{b\}(k) = 0$ to be satisfied at the same k. As these conditions require fine-tuning of the microscopic details of the system, the probability for a crossing of two $\bar{\Lambda}_4\bar{\Lambda}_5$-bands is zero.

Generic points

The little group of a generic point only contains the antiunitary symmetry $I\mathcal{T}$, appart from the identity. As this group has a single pirrep $\bar{GP}_2\bar{GP}_2$, we have to focus on the crossing between two bands that transform as this pirrep. Let us denote $|1\rangle$ and $|2\rangle$ the states on the first band, while $|1'\rangle$ and $|2'\rangle$ those on the second band. Furthermore, we choose as basis the set of states sorted as $\{|1\rangle, |1'\rangle, |2\rangle, |2'\rangle\}$. The Hamiltonian $\hat{H}(GP)$

can be written in this basis in the following form:

$$H(k_x, k_y, k_z) = \begin{pmatrix} h_{11} & h_{21}^\dagger \\ h_{21} & h_{22} \end{pmatrix}. \tag{C.13}$$

Moreover, the matrix of $I\mathcal{T}$ in $\bar{G}\bar{P}_2\bar{G}\bar{P}_2$ is

$$\bar{G}\bar{P}_2\bar{G}\bar{P}_2(I\mathcal{T}) = \begin{pmatrix} 0 & -1 \\ 1 & 0 \end{pmatrix}. \tag{C.14}$$

Then, Eq. (C.4) takes the following form:

$$\begin{pmatrix} 0 & \mathbb{1} \\ -\mathbb{1} & 0 \end{pmatrix} H(k_x, k_y, k_z) \begin{pmatrix} 0 & -\mathbb{1} \\ \mathbb{1} & 0 \end{pmatrix}, = [H(k_x, k_y, k_z)]^* \tag{C.15}$$

The eigenvalues of this matrix are

$$\begin{aligned} E_\pm(\boldsymbol{k}) =& \frac{1}{2}[a(\boldsymbol{k}) + a'(\boldsymbol{k})] \\ & \pm \sqrt{[a(\boldsymbol{k}) - a'(\boldsymbol{k})]^2 + |b(\boldsymbol{k})|^2 + |c(\boldsymbol{k})|^2}. \end{aligned} \tag{C.16}$$

There will be a crossing of bands at a point $\boldsymbol{k}$ if the conditions $a(\boldsymbol{k}) = a'(\boldsymbol{k})$, $\mathrm{Re}[b(\boldsymbol{k})] = 0$, $\mathrm{Im}[b(\boldsymbol{k})] = 0$, $\mathrm{Re}[c(\boldsymbol{k})] = 0$ and $\mathrm{Im}[c(\boldsymbol{k})] = 0$ are satisfied simultaneously. Since this would require fine-tuning of the parameters that govern the system, the probability for having a crossing of bands on a generic $\boldsymbol{k}$-point is zero.

In conclusion, having crossings between bands that transform as the same pirrep in symmetry-lines and planes is impossible in practical terms, as it would require fine-tuning of the system's microscopic parameters. The probability for having band crossings in generic $\boldsymbol{k}$-points is also zero. As a consequence, all the phases in Tab. **8.2** correspond to insulators, including the DFT band structure of SmB_6.

D Hubbard Diamond Chain: supplemental information

D.1 DMRG calculations

The Density Matrix Renormalization Group (DMRG) algorithm is one of the most powerful and unbiased numerical methods for one-dimensional and quasi one-dimensional systems [203]. Our calculations have been performed using the infinite DMRG (iDMRG) method [185], which is an extension of standard DMRG to infinite systems, as implemented in the TeNPy package [204].

We initialize the algorithm on a two-diamond unit cell as the half-filled product state $|\Psi\rangle_0 = |\downarrow,\downarrow,\uparrow,\uparrow,\downarrow,\downarrow,\uparrow,\uparrow\rangle$, with the sites ordered as given in Fig. **10.1**. From there, we build a matrix product state (MPS) representation of the form

$$|\Psi\rangle = \sum_{j_1 \cdots j_N} M^{[1]j_1} M^{[2]j_2} \ldots M^{[N]j_N} |j_1, j_2, \ldots, j_N\rangle, \tag{D.1}$$

where each $M^{[n]j_n}$ is a $\chi_n \times \chi_{n+1}$ matrix, and N the number of sites. We employ the commonly used two-site update, which sweeps through the system and iteratively optimizes the matrices by minimizing the energy locally with respect to our Hamiltonian, keeping the number of electrons fixed. The procedure is repeated until the convergence criteria are fulfilled ($\Delta E < 10^{-10}$ eV and $\Delta S < 10^{-4}$ UNIT).

Having calculated the ground-state, we compute the correlation length, which, in the DMRG context, is defined as

$$\xi = -\frac{N}{\log|\eta_2|}, \tag{D.2}$$

with η_2 denoting the second largest eigenvalue of the transfer matrix T [204]. While gapped phases are characterized by a finite correlation length, metallic phases, have a

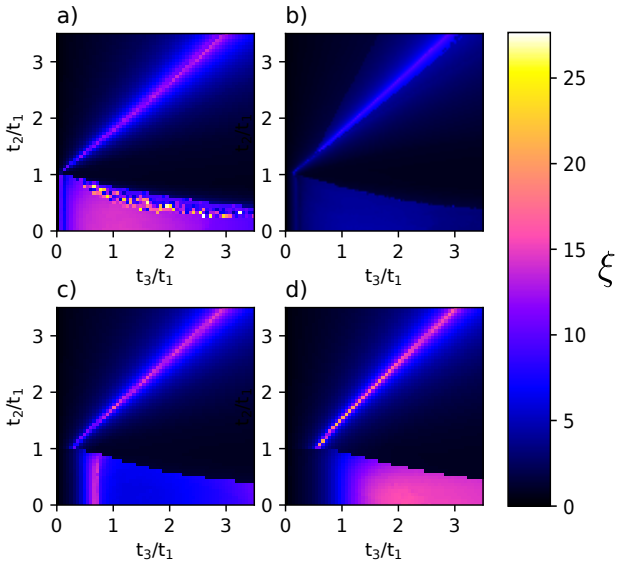

Figure D.1: iDMRG calculations for the HDC model showing the correlation length ξ for Hubbard interaction strengths a) $U/t_1 = 0.4$, b) $U/t_1 = 1.0$, c) $U/t_1 = 2.0$ and d) $U/t_1 = 4.0$. The maximal bond dimension is set to $\chi = 128$.

diverging ξ [194]. The resulting phase diagrams are presented in Fig. **D.1**. The non-interacting phase diagram as shown in Fig. **10.2** is certainly recognizable in the DMRG results.

Although formally, the correlation length ξ diverges at the phase boundaries, it only assumes a large finite value in our data, since it is bounded by the maximal bond dimension, which is set to $\chi = 128$. For metallic, or close-to-metallic systems, DMRG performs generally poorly, resulting in points that are not fully converged close the lower phase boundary for $U = 0.4$ in Fig. **D.1**a).

For $t_2 = 0$ and $t_3 \ll t_1$, we expect a Mott-insulating phase for any finite value of U. Increasing the Hubbard interaction, the short-range correlated Mott region in the lower left hand corner of the phase diagram extends further to the right. Increasing t_3, the system either undergoes a transition into an intermediate metallic phase or, for sufficiently large values of U, it enters the OAL phase directly. The exact value of U at which the intermediate phase is completely suppressed is hard to pinpoint, due to the strong drift observed in the data.

Fixing $t_2/t_1 = 0.3$ and $U/t_1 = 1.0$, we plot the correlation length ξ and the entanglement entropy S against t_3/t_1 for different maximal bond dimensions χ in Fig. **D.2**. With increasing χ, we note that the position of the peak t_{max} shifts to higher values of t_3/t_1 as shown in the inset of the figure. Extrapolating this behavior to infinitely large values of χ suggests that the Mott-metal transition is suppressed, and the system enters

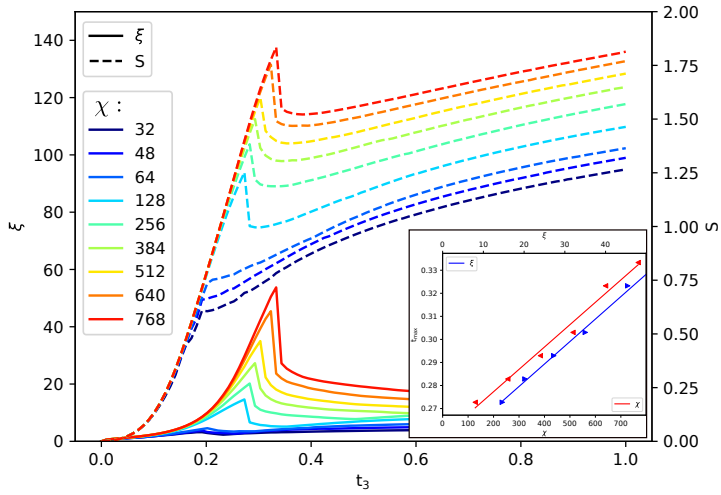

Figure D.2: Correlation length ξ (solid line) and entanglement entropy S (dashed line) plotted against t_3/t_1 for $U/t_1 = 1.0$ and $t_2/t_1 = 0.3$ for different values of χ.

the OAL phase directly.

Using finite DMRG, we calculate the charge gap crossing the AI-OAL phase boundary at $t_2/t_1 = 1.2$ with $U/t_1 = 1.0$ on a chain of 20 diamonds (80 sites). As in the non-interacting case, we observe a closure of the charge gap at the transition.

D.2 Variational Monte Carlo calculations

To strengthen our results for the phase diagram of the diamond chain, we also perform variational Monte Carlo (VMC) calculations in the region of the phase diagram in which the metallic phase is observed ($t_2/t_1 < 1$). Our variational approach is based on Jastrow-Slater wave functions of the form

$$|\Psi_{var}\rangle = \mathcal{J}_n \mathcal{J}_s |\Phi_0\rangle, \tag{D.3}$$

in which long-range Jastrow correlators, $\mathcal{J}_n$ and $\mathcal{J}_s$, are applied onto an uncorrelated fermionic state, $|\Phi_0\rangle$, to introduce non-trivial electron-electron correlations. This class of variational states has been shown to accurately describe both metallic and Mott insulating phases in one dimension [188]. The variational *Ansatz* of Eq. (D.3) features

long-range density-density and spin-spin Jastrow factors,

$$\mathcal{J}_n = \exp\left(\sum_{i,j}\sum_{\alpha,\beta} v_{\alpha,i;\beta,j} n_{\alpha,i} n_{\beta,j}\right), \tag{D.4}$$

$$\mathcal{J}_s = \exp\left(\sum_{i,j}\sum_{\alpha,\beta} u_{\alpha,i;\beta,j} S^z_{\alpha,i} S^z_{\beta,j}\right), \tag{D.5}$$

and the non-interacting state $|\Phi_0\rangle$. Although the simplest choice for $|\Phi_0\rangle$ is the ground-state of the Hamiltonian with $U = 0$, here we adopt a more general scheme, in which we consider the ground-state of an auxiliary quadratic Hamiltonian [187].

$$\begin{aligned}\mathcal{H}_0 = &\sum_{i,j}\sum_{\alpha,\beta}\Bigg[\sum_{\sigma} t_{\alpha,i;\beta,j}\; c^\dagger_{\alpha,i,\sigma} c_{\beta,j,\sigma} + H.c. \\ &+ \Delta_{\alpha,i;\beta,j}\; (c^\dagger_{\alpha,i,\uparrow} c^\dagger_{\beta,j,\downarrow} + c^\dagger_{\beta,j,\uparrow} c^\dagger_{\alpha,i,\downarrow}) + H.c.\Bigg] \\ &+ \Delta_{\mathrm{AF}} \sum_{j}\sum_{\alpha}\left[e^{i\pi(j+\alpha)} c^\dagger_{\alpha,j,\uparrow} c_{\alpha,j,\downarrow} + H.c.\right].\end{aligned} \tag{D.6}$$

$\mathcal{H}_0$ contains hopping terms ($t_{\alpha,i;\beta,j}$) and singlet pairing terms ($\Delta_{\alpha,i;\beta,j}$) up to fifth-neighbors, and a Néel magnetic field (Δ_{AF}). In order to minimize the variational energy of the trial state, all the parameters of $\mathcal{H}_0$ and the Jastrow pseudopotentials ($v_{\alpha,i;\beta,j}$, $u_{\alpha,i;\beta,j}$) are optimized by means of the stochastic reconfiguration technique [187, 205].

When scanning the phase diagram of the diamond chain, we can discriminate between metallic and insulating phases by computing two distinct observables. On the one hand, we can evaluate the density-density structure factor $N(q) = \langle n_{-q} n_q \rangle_{var}$, where $n_q = N^{-1}\sum_{j,\alpha} n_{\alpha,j}\exp(iqj)$ is the Fourier transform of the density operator and $\langle\cdots\rangle_{var}$ indicates the expectation value with respect to the variational state (D.3). The absence (presence) of a charge gap is signalled by the linear (quadratic) behavior of $N(q)$ for $q \to 0$ [188, 189, 206]. On the other hand, we can compute the expectation value of the localization parameter introduced in Ref. [207], namely

$$z_L = \left\langle \exp\left(\frac{2\pi i}{N}\sum_{j,\alpha} j n_{\alpha,j}\right)\right\rangle_{var}. \tag{D.7}$$

In the thermodynamic limit, $|z_L| \to 0$ in a metallic phase, while $|z_L| \to 1$ in an insulating phase [188] (see Fig. **D.3** for an example).

We performed VMC calculations for $U/t_1 = 0.4$ and $U/t_1 = 1$, $t_2/t_1 = 0.5$ and $t_2/t_1 = 0.8$, and different values of t_3/t_1. The results are reported in Fig. **10.4**, on top of the DMRG phase diagram.

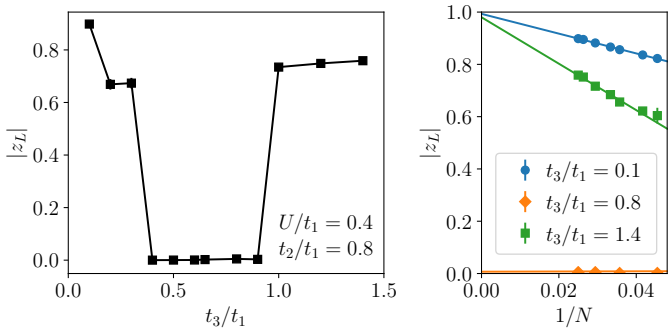

Figure D.3: Localization parameter z_L [Eq. (D.7)] computed by variational Monte Carlo for $U/t_1 = 0.4$ and $t_2/t_1 = 0.8$. Left panel: $|z_L|$ for a system of $N = 40$ diamonds (160 sites) and different values of t_3/t_1. We observe a metallic phase ($|z_L| \approx 0$) sandwiched between two insulating phases (finite $|z_L|$). Right panel: finite size scaling of $|z_L|$ at $t_3/t_1 = 0.1$ (insulator), 0.8 (metal), 1.4 (insulator).

D.3 Benchmarking the topological invariants with the Su-Schrieffer-Heeger model

Let us consider the fixed point Su-Schrieffer-Heeger (SSH) model described by the Hamiltonian

$$H(\alpha) = \sum_{j=1}^{N-1} b_j^\dagger a_{j+1} + e^{-i\alpha} b_N^\dagger a_1 + \text{h.c} \tag{D.8}$$

where we have inserted a $U(1)$ flux by twisting the boundary conditions by $e^{-i\alpha}$. Let us define basis transformed fermions as

$$\begin{aligned} f_{j+\frac{1}{2}}^\dagger &= \frac{1}{\sqrt{2}}(b_j^\dagger - a_{j+1}^\dagger), \\ \widetilde{f}_{j+\frac{1}{2}}^\dagger &= \frac{1}{\sqrt{2}}(b_j^\dagger + a_{j+1}^\dagger), \end{aligned} \tag{D.9}$$

for $j = 1, \ldots, N-1$ and

$$\begin{aligned} f_{\frac{1}{2}}^\dagger(\alpha) &= \frac{1}{\sqrt{2}}(b_N^\dagger - e^{-i\alpha} a_1^\dagger), \\ \widetilde{f}_{\frac{1}{2}}^\dagger(\alpha) &= \frac{1}{\sqrt{2}}(b_N^\dagger + e^{-i\alpha} a_1^\dagger), \end{aligned} \tag{D.10}$$

then the groundstate takes the form

$$|\Psi(\alpha)\rangle_{\text{SSH}} = \prod_j f^\dagger_{j+\frac{1}{2}}|0\rangle, \tag{D.11}$$

where $\prod_j f^\dagger_{j+1/2} = f^\dagger_{1/2}(\alpha) f^\dagger_{3/2} \dots f^\dagger_{N-1/2}$. First we compute the groundstate eigenvalue for the mirror operator $\hat{M}_x$ which has the following action

$$\hat{M}_x : \begin{bmatrix} a^\dagger \\ b^\dagger \end{bmatrix}_j \mapsto \begin{bmatrix} b^\dagger \\ a^\dagger \end{bmatrix}_{N-j+1}. \tag{D.12}$$

therefore, it can be immediately read off that

$$\hat{M}_x : \begin{bmatrix} f^\dagger_{j+\frac{1}{2}} \\ f^\dagger_{\frac{1}{2}}(\alpha) \end{bmatrix} \mapsto \begin{bmatrix} -f^\dagger_{N-j+\frac{1}{2}} \\ -e^{-i\alpha} f^\dagger_{\frac{1}{2}}(-\alpha) \end{bmatrix}, \tag{D.13}$$

using which one can explicitly show that

$${}_{\text{SSH}}\langle\Psi(\alpha)|\hat{M}_x|\Psi(\alpha)\rangle_{\text{SSH}} = (-1)^{\frac{N}{2}(N-1)+1}\cos(\alpha). \tag{D.14}$$

This quantity by itself does not carry topological information. Furthermore when $\alpha = 0$, the quantity still depends on N itself and not just its parity. Instead as shown in Ref. [[196]], one may define a many-body invariant as

$$\begin{aligned} \gamma_{\text{SSH}} &:= e^{\oint \mathrm{d}\alpha_{\text{SSH}}\langle\Psi(\alpha)|\partial_\alpha|\Psi(\alpha)\rangle_{\text{SSH}}} \\ &= \frac{{}_{\text{SSH}}\langle\Psi(\pi)|\hat{M}_x|\Psi(\pi)\rangle_{\text{SSH}}}{{}_{\text{SSH}}\langle\Psi(0)|\hat{M}_x|\Psi(0)\rangle_{\text{SSH}}} = -1. \end{aligned} \tag{D.15}$$

Further, it is known that the interaction classification of class A insulators with additional mirror reflection symmetry with $M_x^2 = +1$ is given by the cobordism group $\Omega^2_{\text{pin}^c}(\text{pt.}) = \mathbb{Z}_4$. Therefore the above many-body invariant is not capable of detecting such a classification. In order to capture the refined interacting classification, the partial reflection operation may be used. We consider the $U(1)$-twisted partial mirror reflection operator $\hat{M}_{x,I}(\theta)$ which acts on the interval I containing sites $j = 1$ to $j = L$. The operator acts as

$$\hat{M}_{x,I}(\theta) : \begin{bmatrix} a^\dagger \\ b^\dagger \end{bmatrix}_j \mapsto e^{-i\theta} \begin{bmatrix} b^\dagger \\ a^\dagger \end{bmatrix}_{L-j+1}. \tag{D.16}$$

While the action of $\hat{M}_{x,I}(\theta)$ in the bond basis takes the form

$$\begin{aligned}\hat{M}_{\theta,I} : f^\dagger_{\frac{1}{2}} &\mapsto \left(b^\dagger_N - e^{-i\theta} b^\dagger_L\right)/\sqrt{2} \\ : f^\dagger_{L+\frac{1}{2}} &\mapsto \left(e^{-i\theta} a^\dagger_1 - a^\dagger_{L+1}\right)/\sqrt{2} \\ : f^\dagger_{j+\frac{1}{2}} &\mapsto -e^{-i\theta} f_{L-j+\frac{1}{2}},\end{aligned} \tag{D.17}$$

for $j \in [1, \ldots, L-1]$. For all other operators, the partial reflection acts trivially. The partial reflection eigenvalue can be computed as

$$\begin{aligned}&\langle \Psi_{SSH} | \hat{M}_{\theta,I} | \Psi_{SSH} \rangle = \\ &= \langle 0 | f_{N-\frac{1}{2}} \cdots f_{\frac{1}{2}} \hat{M}_{\theta,I} f^\dagger_{\frac{1}{2}} \underbrace{f^\dagger_{\frac{3}{2}} \cdots f^\dagger_{L-\frac{1}{2}}}_{L-1} f^\dagger_{L+\frac{1}{2}} \underbrace{f^\dagger_{L+\frac{3}{2}} \cdots f^\dagger_{N-\frac{1}{2}}}_{N-L-1} \hat{M}^{-1}_{\theta,I} \hat{M}_{\theta,I} | 0 \rangle \\ &= (-1)^{L-1} e^{-i(L-1)\theta} \langle 0 | f_{L+\frac{1}{2}} f_{\frac{1}{2}} f_{N-\frac{1}{2}} \cdots f_{\frac{3}{2}} \underbrace{f^\dagger_{L-\frac{1}{2}} \cdots f^\dagger_{\frac{3}{2}}}_{L-1} \underbrace{f^\dagger_{L+\frac{3}{2}} \cdots f^\dagger_{N-\frac{1}{2}}}_{N-L-1} \hat{M}_{\theta,I} \left(f^\dagger_{\frac{1}{2}} f^\dagger_{L+\frac{1}{2}}\right) \hat{M}^{-1}_{\theta,I} \hat{M}_{\theta,I} | 0 \rangle \\ &= (-1)^{L-1+\sum_{n=1}^{L-2} 1} e^{-i(L-1)\theta} \langle 0 | f_{L+\frac{1}{2}} f_{\frac{1}{2}} \hat{M}_{\theta,I} \left(f^\dagger_{\frac{1}{2}} f^\dagger_{L+\frac{1}{2}}\right) \hat{M}^{-1}_{\theta,I} \hat{M}_{\theta,I} | 0 \rangle \\ &= \frac{1}{4} (-1)^{\frac{L}{2}(L-1)} e^{-i(L-1)\theta} \langle 0 | f_{L+\frac{1}{2}} f_{\frac{1}{2}} \left(b^\dagger_N - e^{-i\theta} b^\dagger_L\right) \left(e^{-i\theta} a^\dagger_1 - a^\dagger_{L+1}\right) | 0 \rangle \\ &= \frac{i}{2} e^{-iL\theta} \sin\theta (-1)^{L(L-1)/2},\end{aligned} \tag{D.18}$$

where we have used the shorthand $M_{\theta,I}$ for $M_{x,I}(\theta)$. It can be seen that for $\theta = \pm\pi/2$ and L even, the partial reflection operation produces a phase of $\pm i$ which is a topological diagnostic of $\mathbb{Z}_4 = \Omega^2_{\text{pin}^c}$. Conversely, if we consider odd L i.e site-centred inversion we obtain $\text{Arg}\left({}_{\text{SSH}}\langle \Psi | \hat{M}_{\theta,0} | \Psi \rangle_{\text{SSH}}\right) \in \{0, \pi\}$ which implies a $\mathbb{Z}_2$ invariant.

D.4 Analysis of a single diamond

In this Appendix we show the application of TQC to the Green's function of a single diamond, which may serve as checkpoint to test our approach before tackling the periodic chain. We have calculated the single-particle Green's function and spectral function of the diamond with exact diagonalization at representative points within the AI, metal and Mott phases. We have also computed the topological Hamiltonian and analyzed its spectrum in the framework of TQC.

D.4.1 Atomic insulator

The point representing the AI phase is located at $t_2/t_1 = 1.5$. The single-particle spectrum, of the diamond with $U = 0$ is shown in Fig. **D.4**a, while Figs. **D.4**b and Figs. **D.4**c show the spectral function and Green's function with $U/t_1 = 1$, respectively. The electronic structure with $U \neq 0$ is adiabatically connected to the $U = 0$ limit, as the

peaks in the spectral function and poles in the Green's function retain the features of the non-interacting electronic structure in Fig. **D.4**a. Accordingly, the lowest (highest) two levels in the spectrum of the topological Hamiltonian also have in correspondence wave functions transforming as irreps Γ_1^+ (Γ_3^- and Γ_4^-).

The single-particle spectrum in the AI phase (equivalently, the spectrum of the topological Hamiltonian) can be interpreted in terms of the quantum physics of the H_2^+ molecule, since the Hamiltonian H_{diam}^{AI} of the diamond in the AI phase is adiabatically connected to the following limit:

$$H_{diam}^{AI} = -t_2 \sum_{\sigma} c_{1\sigma}^{+} c_{3\sigma} - t_2 \sum_{\sigma} c_{0\sigma}^{+} c_{2\sigma} + \text{h.c.} \tag{D.19}$$

In order to interpret the symmetry properties of the spectrum in Fig. **D.4**a, let us write the point group D_{2h} of the diamond as two slightly different coset decompositions:

$$D_{2h} = \{E, M_z, C_{2x}, M_y\} \cup I\{E, M_z, C_{2x}, M_y\}, \tag{D.20a}$$
$$\{E, M_z, C_{2y}, M_x\} \cup I\{E, M_z, C_{2y}, M_x\}. \tag{D.20b}$$

The first term on the right of Eq. (D.19) is the Hamiltonian of a H_2^+ molecule formed by the two sites of the diamond that are on the x-axis in Fig. **10.1**a. Its ground state is dubbed *bonding* state and it is even with respect to the both cosets in Eq. (D.20a), thus it transforms as the irrep Γ_1^+. The excited state is known as *anti-bonding* state due to the node positioned between both sites and it is even with respect to the first coset in Eq. (D.20a) and odd under the second, so it transforms as the irrep Γ_3^-. Both states are spatially distributed along the x-axis joining the sites.

The second term on the right of Eq. (D.19) is also the Hamiltonian of a H_2^+ dimer, but composed by the two sites of the diamond that are out of the x-axis. Accordingly, its eigenstates spread on the direction normal to the x-axis. Whereas its bonding state is even with respect to all the symmetries in D_{2h} and transforms as Γ_1^+, the anti-bonding state is odd under the operations in the second coset of Eq. (D.20b) and transforms as Γ_4^-.

The anti-bonding states coincide with the states transforming as Γ_3^- and Γ_4^- in the single-particle spectrum shown in Fig. **D.4**a and they are degenerate in energy, as both terms in Eq. (D.19) share the same coupling constant t_2. Considering that t_1 does not vanish in the whole AI phase, bonding states will hybridize and as a result, neither of the states transforming as Γ_1^+ in Fig. **D.4**a will be pure bonding states nor they will be degenerate in energy.

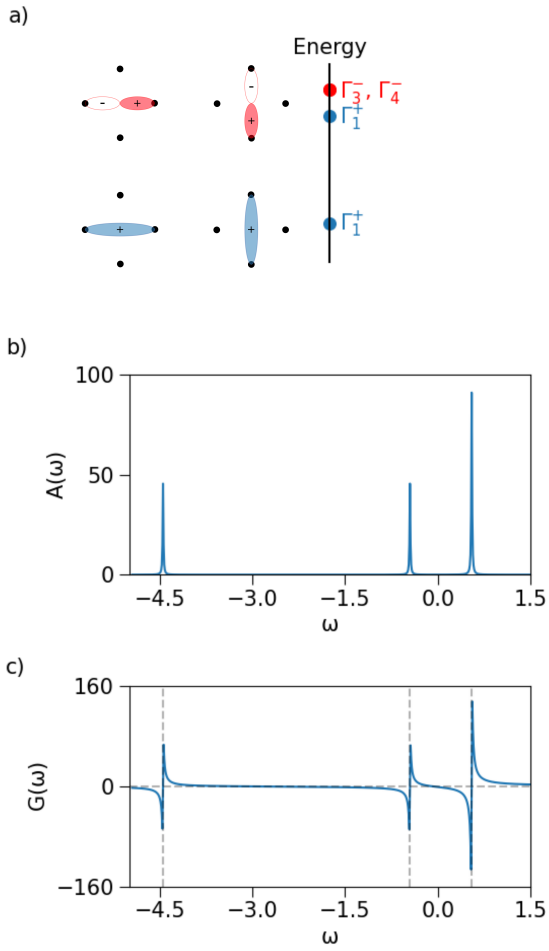

Figure D.4: Analysis of the single diamond in the AI phase with $t_2/t_1 = 1.5$. (a) Single-particle spectrum with $U = 0$, where the bonding states whose combinations give raise to states transforming as Γ_1^+ and anti-bonding states transforming as Γ_3^- and Γ_4^- are shown. (b) and (c) show the traces of single-particle spectral function and Green's function computed with $U/t_1 = 1$, respectively.

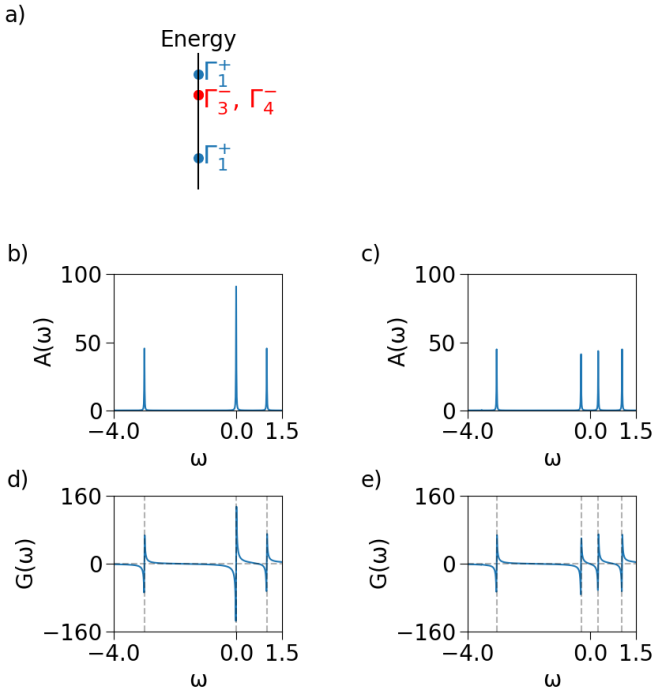

Figure D.5: Analysis of the diamond with $t_2/t_1 = 0.5$. (a), (b) and (d) show the single-particle spectrum and traces of the spectral function and Green's function in the metal phase with $U = 0$, while (c) and (e) contain the traces of the spectral function and Green's function in the Mott phase with $U/t_1 = 1$.

D.4.2 Metal and Mott phases

We choose $t_2/t_1 = 0.5$ with $U = 0$ as the point representing the metallic phase. As it can be seen in the single-particle spectrum in Fig. **D.5**a, the levels corresponding to irreps Γ_3^- and Γ_4^- are not separated by a gap. Accordingly, the spectral function in Fig. **D.5**b and Green's function in Fig. **D.5**d contain a peak and a pole at $\omega = 0$, respectively. The spectrum of the topological Hamiltonian is also characterized by the absence of a finite gap between the second and third levels [44].

The single-particle spectral function computed with $U/t_1 = 1.0$ (Fig. **D.5**c) shows the formation of Hubbard bands giving raise to a charge gap in the Mott phase and each Hubbard band has in correspondence a pole in the Green's function (Fig. **D.5**e). The symmetric distribution of these poles around $\omega = 0$ forces the Green's function to have eigenvalues that vanish at that frequency, giving raise to a singularity in the topological Hamiltonian $H_T = -G^{-1}(0)$.

Bibliography

[1] K. v. Klitzing, G. Dorda, and M. Pepper, *"New Method for High-Accuracy Determination of the Fine-Structure Constant Based on Quantized Hall Resistance"*, Physical Review Letters **45**, 494–497 (1980).

[2] C. L. Kane and E. J. Mele, *"Quantum Spin Hall Effect in Graphene"*, Phys. Rev. Lett. **95**, 226801 (2005).

[3] C. L. Kane and E. J. Mele, *"Z_2 Topological Order and the Quantum Spin Hall Effect"*, Physical Review Letters **95**, 146802 (2005).

[4] B. A. Bernevig and S.-C. Zhang, *"Quantum Spin Hall Effect"*, Phys. Rev. Lett. **96**, 106802 (2006).

[5] B. A. Bernevig, T. L. Hughes, and S.-C. Zhang, *"Quantum Spin Hall Effect and Topological Phase Transition in HgTe Quantum Wells"*, Science **314**, 1757–1761 (2006).

[6] M. König, S. Wiedmann, C. Brüne, A. Roth, H. Buhmann, L. W. Molenkamp, X.-L. Qi, and S.-C. Zhang, *"Quantum Spin Hall Insulator State in HgTe Quantum Wells"*, Science **318**, 766–770 (2007).

[7] L. Fu, C. L. Kane, and E. J. Mele, *"Topological Insulators in Three Dimensions"*, Physical Review Letters **98**, 106803 (2007).

[8] J. E. Moore and L. Balents, *"Topological invariants of time-reversal-invariant band structures"*, Physical Review B **75**, 121306 (2007).

[9] R. Roy, *"Topological phases and the quantum spin Hall effect in three dimensions"*, Physical Review B **79**, 195322 (2009).

[10] L. Fidkowski and A. Kitaev, *"Topological phases of fermions in one dimension"*, Physical Review B **83**, 075103 (2011).

[11] M. Z. Hasan and C. L. Kane, *"Colloquium: Topological insulators"*, Rev. Mod. Phys. **82**, 3045–3067 (2010).

[12] P. Roushan, J. Seo, C. V. Parker, Y. S. Hor, D. Hsieh, D. Qian, A. Richardella, M. Z. Hasan, R. J. Cava, and A. Yazdani, *"Topological surface states protected from backscattering by chiral spin texture"*, Nature **460**, 1106–1109 (2009).

[13] H. Zhang, C.-X. Liu, X.-L. Qi, X. Dai, Z. Fang, and S.-C. Zhang, *"Topological insulators in Bi2Se3, Bi2Te3 and Sb2Te3 with a single Dirac cone on the surface"*, Nature Phys. **5**, 438–442 (2009).

[14] T. Zhang, P. Cheng, X. Chen, J.-F. Jia, X. Ma, K. He, L. Wang, H. Zhang, X. Dai, Z. Fang *et al., "Experimental Demonstration of Topological Surface States Protected by Time-Reversal Symmetry"*, Physical Review Letters **103**, 266803 (2009).

[15] A. Altland and M. R. Zirnbauer, *"Nonstandard symmetry classes in mesoscopic normal-superconducting hybrid structures"*, Physical Review B **55**, 1142–1161 (1997).

[16] A. P. Schnyder, S. Ryu, A. Furusaki, and A. W. W. Ludwig, *"Classification of topological insulators and superconductors in three spatial dimensions"*, Physical Review B **78**, 195125 (2008).

[17] S. Ryu, A. P. Schnyder, A. Furusaki, and A. W. W. Ludwig, *"Topological insulators and superconductors: tenfold way and dimensional hierarchy"*, New Journal of Physics **12**, 065010 (2010).

[18] L. Fu and C. L. Kane, *"Topological insulators with inversion symmetry"*, Physical Review B **76**, 045302 (2007).

[19] L. Fu, *"Topological Crystalline Insulators"*, Phys. Rev. Lett. **106**, 106802 (2011).

[20] T. Neupert and F. Schindler, *"Topological Crystalline Insulators"*, in *Topological Matter*. Springer International Publishing, 2018, 31–61.

[21] J. C. Y. Teo, L. Fu, and C. L. Kane, *"Surface states and topological invariants in three-dimensional topological insulators: Application to $Bi_{1-x}Sb_x$"*, Physical Review B **78**, 045426 (2008).

[22] T. H. Hsieh, H. Lin, J. Liu, W. Duan, A. Bansil, and L. Fu, *"Topological crystalline insulators in the SnTe material class"*, Nature Communications **3**(2012).

[23] Y. Tanaka, Z. Ren, T. Sato, K. Nakayama, S. Souma, T. Takahashi, K. Segawa, and Y. Ando, *"Experimental realization of a topological crystalline insulator in SnTe"*, Nature Physics **8**, 800–803 (2012).

[24] F. Schindler, Z. Wang, M. G. Vergniory, A. M. Cook, A. Murani, S. Sengupta, A. Y. Kasumov, R. Deblock, S. Jeon, I. Drozdov *et al., "Higher-order topology in bismuth"*, Nature Physics **14**, 918–924 (2018).

[25] B. Bradlyn, L. Elcoro, J. Cano, M. G. Vergniory, Z. Wang, C. Felser, M. I. Aroyo, and B. A. Bernevig, *"Topological quantum chemistry"*, Nature **547**, 298–305 (2017).

[26] J. Cano, B. Bradlyn, Z. Wang, L. Elcoro, M. G. Vergniory, C. Felser, M. I. Aroyo, and B. A. Bernevig, *"Building blocks of topological quantum chemistry: Elementary band representations"*, Physical Review B **97**, 035139 (2018).

[27] B. Bradlyn, L. Elcoro, M. G. Vergniory, J. Cano, Z. Wang, C. Felser, M. I. Aroyo, and B. A. Bernevig, *"Band connectivity for topological quantum chemistry: Band structures as a graph theory problem"*, Physical Review B **97**, 035138 (2018).

[28] H. C. Po, A. Vishwanath, and H. Watanabe, *"Symmetry-based indicators of band topology in the 230 space groups"*, Nature Communications **8**, 50 (2017).

[29] Z. Song, T. Zhang, Z. Fang, and C. Fang, *"Quantitative mappings between symmetry and topology in solids"*, Nature Communications **9**(2018).

[30] M. G. Vergniory, L. Elcoro, C. Felser, N. Regnault, B. A. Bernevig, and Z. Wang, *"A complete catalogue of high-quality topological materials"*, Nature **566**, 480–485 (2019).

[31] J. Zak, *"Symmetry Specification of Bands in Solids"*, Physical Review Letters **45**, 1025–1028 (1980).

[32] J. Zak, *"Band representations and symmetry types of bands in solids"*, Physical Review B **23**, 2824–2835 (1981).

[33] J. Zak, *"Band representations of space groups"*, Physical Review B **26**, 3010–3023 (1982).

[34] L. Elcoro, B. J. Wieder, Z. Song, Y. Xu, B. Bradlyn, and B. A. Bernevig, *"Magnetic topological quantum chemistry"*, Nature Communications **12**(2021).

[35] H. Watanabe, H. C. Po, and A. Vishwanath, *"Structure and topology of band structures in the 1651 magnetic space groups"*, Science Advances **4**(2018).

[36] J. Kondo, *"Resistance Minimum in Dilute Magnetic Alloys"*, Progress of Theoretical Physics **32**, 37–49 (1964).

[37] N. F. Mott, *"Metal-Insulator Transition"*, Reviews of Modern Physics **40**, 677–683 (1968).

[38] P. Coleman, *Introduction to Many-Body Physics*. Cambridge University Press, nov 2015.

[39] P. Coleman, *"Heavy Fermions: electrons at the edge of magnetism"*, arXiv e-prints(2006).

[40] P. Coleman, *"Heavy Fermions and the Kondo Lattice: a 21st Century Perspective"*, arXiv e-prints arXiv:1509.05769(2015).

[41] C. Xu and J. E. Moore, *"Stability of the quantum spin Hall effect: Effects of interactions, disorder, and Z_2 topology"*, Physical Review B **73**, 045322 (2006).

[42] Z. Wang and S.-C. Zhang, *"Simplified Topological Invariants for Interacting Insulators"*, Physical Review X **2**, 031008 (2012).

[43] Z. Wang, X.-L. Qi, and S.-C. Zhang, *"Topological invariants for interacting topological insulators with inversion symmetry"*, Physical Review B **85**, 165126 (2012).

[44] D. Lessnich, S. M. Winter, M. Iraola, M. G. Vergniory, and R. Valentí, *"Elementary band representations for the single-particle Green's function of interacting topological insulators"*, Physical Review B **104**, 085116 (2021).

[45] A. Shitade, H. Katsura, J. Kuneš, X.-L. Qi, S.-C. Zhang, and N. Nagaosa, *"Quantum Spin Hall Effect in a Transition Metal Oxide Na_2IrO_3"*, Physical Review Letters **102**, 256403 (2009).

[46] M. Dzero, K. Sun, V. Galitski, and P. Coleman, *"Topological kondo insulators"*, Physical review letters **104**, 106408 (2010).

[47] T. Takimoto, *"SmB6: A Promising Candidate for a Topological Insulator"*, Journal of the Physical Society of Japan **80**, 123710 (2011).

[48] M. Dzero, K. Sun, P. Coleman, and V. Galitski, *"Theory of topological Kondo insulators"*, Physical Review B **85**, 045130 (2012).

[49] M. Dzero, J. Xia, V. Galitski, and P. Coleman, *"Topological Kondo Insulators"*, Annual Review of Condensed Matter Physics **7**, 249–280 (2016).

[50] V. Alexandrov, M. Dzero, and P. Coleman, *"Cubic Topological Kondo Insulators"*, Physical Review Letters **111**, 226403 (2013).

[51] M. Neupane, N. Alidoust, S.-Y. Xu, T. Kondo, Y. Ishida, D. J. Kim, C. Liu, I. Belopolski, Y. J. Jo, T.-R. Chang *et al.*, *"Surface electronic structure of the topological Kondo-insulator candidate correlated electron system SmB6"*, Nature Communications **4**(2013).

[52] F. Lu, J. Zhao, H. Weng, Z. Fang, and X. Dai, *"Correlated Topological Insulators with Mixed Valence"*, Physical Review Letters **110**, 096401 (2013).

[53] N. Xu, X. Shi, P. K. Biswas, C. E. Matt, R. S. Dhaka, Y. Huang, N. C. Plumb, M. Radović, J. H. Dil, E. Pomjakushina *et al.*, *"Surface and bulk electronic structure of the strongly correlated system SmB_6 and implications for a topological Kondo insulator"*, Physical Review B **88**, 121102 (2013).

[54] T.-R. Chang, T. Das, P.-J. Chen, M. Neupane, S.-Y. Xu, M. Z. Hasan, H. Lin, H.-T. Jeng, and A. Bansil, *"Two distinct topological phases in the mixed-valence compound YbB_6 and its differences from SmB_6"*, Physical Review B **91**, 155151 (2015).

[55] Y. Choi, J. Kemmer, Y. Peng, A. Thomson, H. Arora, R. Polski, Y. Zhang, H. Ren, J. Alicea, G. Refael *et al.*, *"Electronic correlations in twisted bilayer graphene near the magic angle"*, Nature Physics **15**, 1174–1180 (2019).

[56] Y. Choi, H. Kim, Y. Peng, A. Thomson, C. Lewandowski, R. Polski, Y. Zhang, H. S. Arora, K. Watanabe, T. Taniguchi *et al.*, *"Correlation-driven topological phases in magic-angle twisted bilayer graphene"*, Nature **589**, 536–541 (2021).

[57] X. Liu, Z. Wang, K. Watanabe, T. Taniguchi, O. Vafek, and J. I. A. Li, *"Tuning electron correlation in magic-angle twisted bilayer graphene using Coulomb screening"*, Science **371**, 1261–1265 (2021).

[58] Z.-D. Song and B. A. Bernevig, *"Magic-Angle Twisted Bilayer Graphene as a Topological Heavy Fermion Problem"*, Physical Review Letters **129**, 047601 (2022).

[59] A. A. Soluyanov and D. Vanderbilt, *"Wannier representation of $\mathbbZ_2$ topological insulators"*, Phys. Rev. B **83**, 035108 (2011).

[60] G. Kresse and J. Hafner, *"Ab initio molecular dynamics for liquid metals"*, Physical Review B **47**, 558–561 (1993).

[61] X. Gonze, B. Amadon, G. Antonius, F. Arnardi, L. Baguet, J.-M. Beuken, J. Bieder, F. Bottin, J. Bouchet, E. Bousquet *et al.*, *"The Abinit project: Impact, environment and recent developments"*, Computer Physics Communications **248**, 107042 (2020).

[62] A. H. Romero, D. C. Allan, B. Amadon, G. Antonius, T. Applencourt, L. Baguet, J. Bieder, F. Bottin, J. Bouchet, E. Bousquet *et al.*, *"ABINIT: Overview and focus on selected capabilities"*, The Journal of Chemical Physics **152**, 124102 (2020).

[63] P. Giannozzi, O. Andreussi, T. Brumme, O. Bunau, M. B. Nardelli, M. Calandra, R. Car, C. Cavazzoni, D. Ceresoli, M. Cococcioni *et al.*, *"Advanced capabilities for materials modelling with Quantum ESPRESSO"*, Journal of Physics: Condensed Matter **29**, 465901 (2017).

[64] G. Pizzi, V. Vitale, R. Arita, S. Blügel, F. Freimuth, G. Géranton, M. Gibertini, D. Gresch, C. Johnson, T. Koretsune *et al.*, *"Wannier90 as a community code: new features and applications"*, Journal of Physics: Condensed Matter **32**, 165902 (2020).

[65] M. O. Soldini, N. Astrakhantsev, M. Iraola, A. Tiwari, M. H. Fischer, R. Valentí, M. G. Vergniory, G. Wagner, and T. Neupert, *"Interacting topological quantum chemistry of Mott atomic limits"*, arXiv e-prints arXiv:2209.10556(2022).

[66] S. Rachel, *"Interacting topological insulators: a review"*, Reports on Progress in Physics **81**, 116501 (2018).

[67] D. J. Thouless, M. Kohmoto, M. P. Nightingale, and M. den Nijs, *"Quantized Hall Conductance in a Two-Dimensional Periodic Potential"*, Physical Review Letters **49**, 405–408 (1982).

[68] D. C. Tsui, *"Nobel Lecture: Interplay of disorder and interaction in two-dimensional electron gas in intense magnetic fields"*, Reviews of Modern Physics **71**, 891–895 (1999).

[69] F. Schindler, A. M. Cook, M. G. Vergniory, Z. Wang, S. S. P. Parkin, B. A. Bernevig, and T. Neupert, *"Higher-order topological insulators"*, Science Advances **4**(2018).

[70] T. Zhang, Y. Jiang, Z. Song, H. Huang, Y. He, Z. Fang, H. Weng, and C. Fang, *"Catalogue of topological electronic materials"*, Nature **566**, 475–479 (2019).

[71] F. Tang, H. C. Po, A. Vishwanath, and X. Wan, *"Comprehensive search for topological materials using symmetry indicators"*, Nature **566**, 486–489 (2019).

[72] Y. Xu, L. Elcoro, Z.-D. Song, B. J. Wieder, M. G. Vergniory, N. Regnault, Y. Chen, C. Felser, and B. A. Bernevig, *"High-throughput calculations of magnetic topological materials"*, Nature **586**, 702–707 (2020).

[73] X.-L. Qi, T. L. Hughes, and S.-C. Zhang, *"Topological field theory of time-reversal invariant insulators"*, Physical Review B **78**, 195424 (2008).

[74] Z. Wang, X.-L. Qi, and S.-C. Zhang, *"Topological Order Parameters for Interacting Topological Insulators"*, Physical Review Letters **105**, 256803 (2010).

[75] G. E. Volovik, *"Topological invariant for superfluid 3He-B and quantum phase transitions"*, JETP Letters **90**, 587–591 (2009).

[76] B. Bradlyn and M. Iraola, *"Lecture notes on Berry phases and topology"*, SciPost Physics Lecture Notes(2022).

[77] M. Iraola, J. L. Mañes, B. Bradlyn, M. K. Horton, T. Neupert, M. G. Vergniory, and S. S. Tsirkin, *"IrRep: Symmetry eigenvalues and irreducible representations of ab initio band structures"*, Computer Physics Communications **272**, 108226 (2022).

[78] J. Gao, Q. Wu, C. Persson, and Z. Wang, *"Irvsp: To obtain irreducible representations of electronic states in the VASP"*, Computer Physics Communications **261**, 107760 (2021).

[79] A. Matsugatani, S. Ono, Y. Nomura, and H. Watanabe, *"qeirreps: An open-source program for Quantum ESPRESSO to compute irreducible representations of Bloch wavefunctions"*, Computer Physics Communications **264**, 107948 (2021).

[80] M. Iraola, N. Heinsdorf, A. Tiwari, D. Lessnich, T. Mertz, F. Ferrari, M. H. Fischer, S. M. Winter, F. Pollmann, T. Neupert *et al.*, *"Towards a topological quantum chemistry description of correlated systems: The case of the Hubbard diamond chain"*, Physical Review B **104**, 195125 (2021).

[81] J. E. Avron, *"Adiabatic quantum transport"*, in *Quantum Symmetries/Symetries Quantiques: Proceedings of the Les Houches Summer School, Session Lxiv, Les Houches, France, 1 August - 8 September, 1995 (Les Houches Summer School proceedings)*. Elsevier, Amsterdam, 1998.

[82] J. E. Avron, R. Seiler, and L. G. Yaffe, *"Adiabatic theorems and applications to the quantum hall effect"*, Communications in Mathematical Physics **110**, 33–49 (1987).

[83] T. Eguchi, P. B. Gilkey, and A. J. Hanson, *"Gravitation, gauge theories and differential geometry"*, Physics Reports **66**, 213–393 (1980).

[84] M. Nakahara, *Geometry, Topology and Physics*. CRC Press, oct 2018.

[85] T. Kato, *"On the Adiabatic Theorem of Quantum Mechanics"*, Journal of the Physical Society of Japan **5**, 435–439 (1950).

[86] G. Nenciu, *"Linear adiabatic theory. Exponential estimates"*, Communications in Mathematical Physics **152**, 479–496 (1993).

[87] R. Resta, *"The quantum-mechanical position operator and the polarization problem"*, in *AIP Conference Proceedings*. AIP, 1998.

[88] J. Zak, *"Berry's phase for energy bands in solids"*, Physical Review Letters **62**, 2747–2750 (1989).

[89] J. D. Cloizeaux, *"Analytical Properties of n-Dimensional Energy Bands and Wannier Functions"*, Physical Review **135**, A698–A707 (1964).

[90] G. Nenciu, *"Existence of the exponentially localised Wannier functions"*, Communications in Mathematical Physics **91**, 81–85 (1983).

[91] T. Thonhauser and D. Vanderbilt, *"Insulator/Chern-insulator transition in the Haldane model"*, Physical Review B **74**, 235111 (2006).

[92] C. Brouder, G. Panati, M. Calandra, C. Mourougane, and N. Marzari, *"Exponential Localization of Wannier Functions in Insulators"*, Physical Review Letters **98**, 046402 (2007).

[93] J. Cano, B. Bradlyn, Z. Wang, L. Elcoro, M. Vergniory, C. Felser, M. Aroyo, and B. A. Bernevig, *"Topology of Disconnected Elementary Band Representations"*, Physical Review Letters **120**, 266401 (2018).

[94] M. B. de Paz, M. G. Vergniory, D. Bercioux, A. García-Etxarri, and B. Bradlyn, *"Engineering fragile topology in photonic crystals: Topological quantum chemistry of light"*, Phys. Rev. Research **1**, 032005 (2019).

[95] D. Vanderbilt, *Berry Phases in Electronic Structure Theory: Electric Polarization, Orbital Magnetization, and Topological Insulators*. Cambridge University Press, 2018.

[96] L. Elcoro, B. Bradlyn, Z. Wang, M. G. Vergniory, J. Cano, C. Felser, B. A. Bernevig, D. Orobengoa, G. de la Flor, and M. I. Aroyo, *"Double crystallographic groups and their representations on the Bilbao Crystallographic Server"*, Journal of Applied Crystallography **50**, 1457–1477 (2017).

[97] M. I. Aroyo, J. M. Perez-Mato, C. Capillas, E. Kroumova, S. Ivantchev, G. Madariaga, A. Kirov, and H. Wondratschek, *"Bilbao Crystallographic Server: I. Databases and crystallographic computing programs"*, Zeitschrift für Kristallographie - Crystalline Materials **221**, 15 – 27 (2006).

[98] M. I. Aroyo, A. Kirov, C. Capillas, J. M. Perez-Mato, and H. Wondratschek, *"Bilbao Crystallographic Server. II. Representations of crystallographic point groups and space groups"*, Acta Crystallographica Section A Foundations of Crystallography **62**, 115–128 (2006).

[99] B. J. Wieder and B. A. Bernevig, *"The Axion Insulator as a Pump of Fragile Topology"*, arXiv preprint arXiv:1810.02373(2018).

[100] L. Fidkowski, I. Klich, and T. Jackson, *"From bulk invariants to edge modes via the entanglement spectrum"*, Tech. Rep., (2011).

[101] M. Taherinejad, K. F. Garrity, and D. Vanderbilt, *"Wannier center sheets in topological insulators"*, Physical Review B **89**, 115102 (2014).

[102] A. Alexandradinata, X. Dai, and B. A. Bernevig, *"Wilson-loop characterization of inversion-symmetric topological insulators"*, Physical Review B **89**, 155114 (2014).

[103] M. B. de Paz, C. Devescovi, G. Giedke, J. J. Saenz, M. G. Vergniory, B. Bradlyn, D. Bercioux, and A. García-Etxarri, *"Tutorial: Computing Topological Invariants in 2D Photonic Crystals"*, Advanced Quantum Technologies **3**, 1900117 (2019).

[104] M. G. Vergniory, B. J. Wieder, L. Elcoro, S. S. P. Parkin, C. Felser, B. A. Bernevig, and N. Regnault, *"All topological bands of all nonmagnetic stoichiometric materials"*, Science **376**(2022).

[105] *Teoría de Grupos: Aplicación a la Mecánica Cuántica.* URSS, 2000.

[106] D. B. Litvin and V. Kopský, *"Seitz notation for symmetry operations of space groups"*, Acta Crystallographica Section A Foundations of Crystallography **67**, 415–418 (2011).

[107] X. Zhou, C.-H. Hsu, H. Aramberri, M. Iraola, C.-Y. Huang, J. L. Mañes, M. G. Vergniory, H. Lin, and N. Kioussis, *"Novel family of topological semimetals with butterflylike nodal lines"*, Physical Review B **104**, 125135 (2021).

[108] X. Zhou, C.-H. Hsu, C.-Y. Huang, M. Iraola, J. L. Mañes, M. G. Vergniory, H. Lin, and N. Kioussis, *"Glide symmetry protected higher-order topological insulators from semimetals with butterfly-like nodal lines"*, npj Computational Materials **7**(2021).

[109] C. Bradley and A. P. Cracknell, *The Mathematical Theory of Symmetry in Solids.* Oxford University Press, 2009.

[110] J. L. Mañes, *"Fragile phonon topology on the honeycomb lattice with time-reversal symmetry"*, Physical Review B **102**, 024307 (2020).

[111] C. Devescovi, M. García-Díez, I. Robredo, M. B. de Paz, J. Lasa-Alonso, B. Bradlyn, J. L. Mañes, M. G. Vergniory, and A. García-Etxarri, *"Cubic 3D Chern photonic insulators with orientable large Chern vectors"*, Nature Communications **12**(2021).

[112] B. Bradlyn, J. Cano, Z. Wang, M. G. Vergniory, C. Felser, R. J. Cava, and B. A. Bernevig, *"Beyond Dirac and Weyl fermions: Unconventional quasiparticles in conventional crystals"*, Science **353**(2016).

[113] V. Peri, Z.-D. Song, M. Serra-Garcia, P. Engeler, R. Queiroz, X. Huang, W. Deng, Z. Liu, B. A. Bernevig, and S. D. Huber, *"Experimental characterization of fragile topology in an acoustic metamaterial"*, Science **367**, 797–800 (2020).

[114] A. Alexandradinata, J. Höller, C. Wang, H. Cheng, and L. Lu, *"Crystallographic splitting theorem for band representations and fragile topological photonic crystals"*, Physical Review B **102**, 115117 (2020).

[115] L. Elcoro, Z. Song, and B. A. Bernevig, *"Application of induction procedure and Smith decomposition in calculation and topological classification of electronic band structures in the 230 space groups"*, Physical Review B **102**, 035110 (2020).

[116] H. C. Po, H. Watanabe, and A. Vishwanath, *"Fragile Topology and Wannier Obstructions"*, Physical Review Letters **121**, 126402 (2018).

[117] J. Cano and B. Bradlyn, *"Band Representations and Topological Quantum Chemistry"*, Annual Review of Condensed Matter Physics **12**, 225–246 (2021).

[118] J. Cano, L. Elcoro, M. I. Aroyo, B. A. Bernevig, and B. Bradlyn, *"Topology invisible to eigenvalues in obstructed atomic insulators"*, Physical Review B **105**, 125115 (2022).

[119] J. M. Soler, E. Artacho, J. D. Gale, A. García, J. Junquera, P. Ordejón, and D. Sánchez-Portal, *"The SIESTA method for ab initio order-N materials simulation"*, Journal of Physics: Condensed Matter **14**, 2745–2779 (2002).

[120] S. S. Tsirkin, I. Souza, and D. Vanderbilt, *"Composite Weyl nodes stabilized by screw symmetry with and without time-reversal invariance"*, Physical Review B **96**, 045102 (2017).

[121] F. Schindler, M. Brzezińska, W. A. Benalcazar, M. Iraola, A. Bouhon, S. S. Tsirkin, M. G. Vergniory, and T. Neupert, *"Fractional corner charges in spin-orbit coupled crystals"*, Physical Review Research **1**, 033074 (2019).

[122] J. F. Khoury, A. J. E. Rettie, M. A. Khan, N. J. Ghimire, I. Robredo, J. E. Pfluger, K. Pal, C. Wolverton, A. Bergara, J. S. Jiang *et al.*, *"A New Three-Dimensional Subsulfide Ir_2In_8S with Dirac Semimetal Behavior"*, Journal of the American Chemical Society **141**, 19 130–19 137 (2019).

[123] J. F. Khoury, A. J. E. Rettie, I. Robredo, M. J. Krogstad, C. D. Malliakas, A. Bergara, M. G. Vergniory, R. Osborn, S. Rosenkranz, D. Y. Chung *et al.*, *"The Subchalcogenides Ir_2In_8Q (Q = S, Se, Te): Dirac Semimetal Candidates with Re-entrant Structural Modulation"*, Journal of the American Chemical Society **142**, 6312–6323 (2020).

[124] I. Robredo, M. G. Vergniory, and B. Bradlyn, *"Higher-order and crystalline topology in a phenomenological tight-binding model of lead telluride"*, Physical Review Materials **3**, 041202 (2019).

[125] M.-Á. Sánchez-Martínez, I. Robredo, A. Bidaurrazaga, A. Bergara, F. de Juan, A. G. Grushin, and M. G. Vergniory, *"Spectral and optical properties of $Ag_3Au(Se_2,Te_2)$ and dark matter detection"*, Journal of Physics: Materials **3**, 014001 (2019).

[126] J. Ibanez, F. de Juan, and I. Souza, *"Assessing the role of interatomic position matrix elements in tight-binding calculations of optical properties"*, SciPost Physics **12**(2022).

[127] J. Ibañez Azpiroz, I. Souza, and F. de Juan, *"Directional shift current in mirror-symmetric* BC_2N*"*, Phys. Rev. Research **2**, 013263 (2020).

[128] A. Togo and I. Tanaka, *"`Spglib`: a software library for crystal symmetry search"*, arXiv e-prints arXiv:1808.01590(2018).

[129] P. E. Blöchl, *"Projector augmented-wave method"*, Physical Review B **50**, 17 953–17 979 (1994).

[130] G. Kresse and D. Joubert, *"From ultrasoft pseudopotentials to the projector augmented-wave method"*, Physical Review B **59**, 1758–1775 (1999).

[131] M. Torrent, F. Jollet, F. Bottin, G. Zérah, and X. Gonze, *"Implementation of the projector augmented-wave method in the ABINIT code: Application to the study of iron under pressure"*, Computational Materials Science **42**, 337–351 (2008).

[132] Official repository of Irrep in Github, https://github.com/stepan-tsirkin/irrep.

[133] K. Yamada, K.-i. Takada, S. Hosoya, Y. Watanabe, Y. Endoh, N. Tomonaga, T. Suzuki, T. Ishigaki, T. Kamiyama, H. Asano *et al.*, *"Three-Dimensional Antiferromagnetic Order and AnisotropicMagnetic Properties in* Bi_2CuO_4*"*, Journal of the Physical Society of Japan **60**, 2406–2414 (1991).

[134] D. Thomas, J.-C. Boivin, and J. Tréhoux, *"Étude structurale de* $CuBi_2O_4$*"*, Bulletin de la Société française de Minéralogie et de Cristallographie **99**, 193–196 (1976).

[135] B. J. Wieder, Y. Kim, A. Rappe, and C. Kane, *"Double Dirac Semimetals in Three Dimensions"*, Physical Review Letters **116**, 186402 (2016).

[136] N. Marzari, *"Ab-initio Molecular Dynamics for Metallic Systems. PhD Thesis"*(1996). https://inis.iaea.org/search/search.aspx?orig_q=RN:30045813

[137] J. P. Perdew, K. Burke, and M. Ernzerhof, *"Generalized Gradient Approximation Made Simple"*, Physical Review Letters **77**, 3865–3868 (1996).

[138] Pseudo Dojo database of pseudopotentials, http://www.pseudo-dojo.org/index.html.

[139] M. van Setten, M. Giantomassi, E. Bousquet, M. Verstraete, D. Hamann, X. Gonze, and G.-M. Rignanese, *"The PseudoDojo: Training and grading a 85 element optimized norm-conserving pseudopotential table"*, Computer Physics Communications **226**, 39–54 (2018).

[140] J. Xiao and B. Yan, *"First-principles calculations for topological quantum materials"*, Nature Reviews Physics **3**, 283–297 (2021).

[141] F. Schindler, S. S. Tsirkin, T. Neupert, B. A. Bernevig, and B. J. Wieder, *"Topological zero-dimensional defect and flux states in three-dimensional insulators"*, Nature Communications **13**(2022).

[142] I. Robredo, N. B. M. Schröter, A. Reyes-Serrato, A. Bergara, F. de Juan, L. M. Schoop, and M. G. Vergniory, *"Theoretical study of topological properties of ferromagnetic pyrite CoS_2"*, Journal of Physics D: Applied Physics **55**, 304004 (2022).

[143] Z. Zhang, Z.-M. Yu, G.-B. Liu, and Y. Yao, *"A phonon irreducible representations calculator"*, arXiv e-prints arXiv:2201.11350(2022).

[144] R. González-Hernández, C. Pinilla, and B. Uribe, *"Quasinodal spheres and the spin Hall effect: The case of YH_3 and CaTe"*, Physical Review B **106**, 125135 (2022).

[145] Z. Zhang, Z.-M. Yu, G.-B. Liu, Z. Li, S. A. Yang, and Y. Yao, *"MagneticKP: A package for quickly constructing $\boldsymbol{k}\cdot\boldsymbol{p}$ models of magnetic and non-magnetic crystals"*, arXiv e-prints arXiv:2205.05830(2022).

[146] P. M. Lenggenhager, X. Liu, T. Neupert, and T. Bzdušek, *"Triple nodal points characterized by their nodal-line structure in all magnetic space groups"*, Physical Review B **106**, 085128 (2022).

[147] P. Mlkvik, C. Ederer, and N. A. Spaldin, *"Influence of germanium substitution on the structural and electronic stability of the competing vanadium dioxide phases"*, arXiv e-prints arXiv:2207.06153(2022).

[148] R. González-Hernández, C. Pinilla, and B. Uribe, *"Axion insulators protected by C_2T symmetry, their K-theory invariants, and material realizations"*, Physical Review B **106**, 195144 (2022).

[149] K. Andres, J. E. Graebner, and H. R. Ott, *"4f-Virtual-Bound-State Formation in $CeAl_3$ Low Temperatures"*, Physical Review Letters **35**, 1779–1782 (1975).

[150] P. W. Anderson, *"Localized Magnetic States in Metals"*, Physical Review **124**, 41–53 (1961).

[151] P. Fazekas and B. H. Brandow, *"Application of the Gutzwiller method to the periodic Anderson model"*, Physica Scripta **36**, 809–819 (1987).

[152] J. R. Schrieffer and P. A. Wolff, *"Relation between the Anderson and Kondo Hamiltonians"*, Physical Review **149**, 491–492 (1966).

[153] M. A. Ruderman and C. Kittel, *"Indirect Exchange Coupling of Nuclear Magnetic Moments by Conduction Electrons"*, Physical Review **96**, 99–102 (1954).

[154] A. Menth, E. Buehler, and T. H. Geballe, *"Magnetic and Semiconducting Properties of SmB_6"*, Physical Review Letters **22**, 295–297 (1969).

[155] F. Steglich, J. Aarts, C. D. Bredl, W. Lieke, D. Meschede, W. Franz, and H. Schäfer, *"Superconductivity in the Presence of Strong Pauli Paramagnetism: $CeCu_2Si_2$"*, Physical Review Letters **43**, 1892–1896 (1979).

[156] N. Grewe and F. Steglich, *"Chapter 97 Heavy fermions"*, in *Handbook on the Physics and Chemistry of Rare Earths*. Elsevier, 1991, 343–474.

[157] H. v. Löhneysen, A. Rosch, M. Vojta, and P. Wölfle, *"Fermi-liquid instabilities at magnetic quantum phase transitions"*, Reviews of Modern Physics **79**, 1015–1075 (2007).

[158] Q. Si and S. Paschen, *"Quantum phase transitions in heavy fermion metals and Kondo insulators"*, physica status solidi (b) **250**, 425–438 (2013).

[159] R. M. Martin and J. W. Allen, *"Theory of mixed valence: Metals or small gap insulators (invited)"*, Journal of Applied Physics **50**, 7561 (1979).

[160] S. Paschen and Q. Si, *"Quantum phases driven by strong correlations"*, Nature Reviews Physics **3**, 9–26 (2020).

[161] V. Alexandrov, P. Coleman, and O. Erten, *"Kondo Breakdown in Topological Kondo Insulators"*, Physical Review Letters **114**, 177202 (2015).

[162] M. Ye, J. W. Allen, and K. Sun, *"Topological crystalline Kondo insulators and universal topological surface states of SmB_6"*, arXiv e-prints arXiv:1307.7191(2013).

[163] H. Weng, J. Zhao, Z. Wang, Z. Fang, and X. Dai, *"Topological Crystalline Kondo Insulator in Mixed Valence Ytterbium Borides"*, Physical Review Letters **112**, 016403 (2014).

[164] G. Kresse and J. Furthmüller, *"Efficient iterative schemes for ab initio total-energy calculations using a plane-wave basis set"*, Phys. Rev. B **54**, 11 169–11 186 (1996).

[165] P. Thunström and K. Held, *"Topology of SmB_6 determined by dynamical mean field theory"*, Physical Review B **104**, 075131 (2021).

[166] J. D. Denlinger, J. W. Allen, J. S. Kang, K. Sun, J. W. Kim, J. H. Shim, B. I. Min, D.-J. Kim, and Z. Fisk, *"Temperature Dependence of Linked Gap and Surface State Evolution in the Mixed Valent Topological Insulator SmB6"*, arXiv e-prints arXiv:1312.6637(2013).

[167] H. Miyazaki, T. Hajiri, T. Ito, S. Kunii, and S. ichi Kimura, *"Momentum-dependent hybridization gap and dispersive in-gap state of the Kondo semiconductor SmB_6"*, Physical Review B **86**, 075105 (2012).

[168] A. D. Becke and E. R. Johnson, *"A simple effective potential for exchange"*, The Journal of Chemical Physics **124**, 221101 (2006).

[169] C.-J. Kang, J. Kim, K. Kim, J. Kang, J. D. Denlinger, and B. I. Min, *"Band Symmetries of Mixed-Valence Topological Insulator: SmB6"*, J. Phys. Soc. Jpn. **84**, 024722 (2015).

[170] R. P. Feynman, *"Space-Time Approach to Non-Relativistic Quantum Mechanics"*, Reviews of Modern Physics **20**, 367–387 (1948).

[171] H. Bruus and K. Flensberg, *Many-Body Quantum Theory in Condensed Matter Physics: An Introduction*. Oxford University Press, 2004.

[172] M. Peskin and D. Schroeder, *An Introduction to Quantum Field Theory*, ser. Advanced book classics. Avalon Publishing, 1995.

[173] Z. Wang and B. Yan, *"Topological Hamiltonian as an exact tool for topological invariants"*, Journal of Physics: Condensed Matter **25**, 155601 (2013).

[174] W. Kohn and L. J. Sham, *"Self-Consistent Equations Including Exchange and Correlation Effects"*, Physical Review **140**, A1133–A1138 (1965).

[175] C. Gros and R. Valentí, *"Cluster expansion for the self-energy: A simple many-body method for interpreting the photoemission spectra of correlated Fermi systems"*, Physical Review B **48**, 418–425 (1993).

[176] D. Sénéchal, D. Perez, and D. Plouffe, *"Cluster perturbation theory for Hubbard models"*, Physical Review B **66**, 075129 (2002).

[177] D. Sénéchal, D. Perez, and M. Pioro-Ladrière, *"Spectral Weight of the Hubbard Model through Cluster Perturbation Theory"*, Physical Review Letters **84**, 522–525 (2000).

[178] D. Sénéchal, *"An introduction to quantum cluster methods"*, arXiv e-prints arXiv:0806.2690(2008).

[179] F. Manghi, *"Multi-orbital cluster perturbation theory for transition metal oxides"*, Journal of Physics: Condensed Matter **26**, 015602 (2013).

[180] E. Dagotto, *"Correlated electrons in high-temperature superconductors"*, Reviews of Modern Physics **66**, 763–840 (1994).

[181] S. Pairault, D. Sénéchal, and A.-M. S. Tremblay, *"Strong-Coupling Expansion for the Hubbard Model"*, Physical Review Letters **80**, 5389–5392 (1998).

[182] Z. Song, T. Zhang, and C. Fang, *"Diagnosis for Nonmagnetic Topological Semimetals in the Absence of Spin-Orbital Coupling"*, Physical Review X **8**, 031069 (2018).

[183] Q.-R. Wang and Z.-C. Gu, *"Towards a Complete Classification of Symmetry-Protected Topological Phases for Interacting Fermions in Three Dimensions and a General Group Supercohomology Theory"*, Physical Review X **8**, 011055 (2018).

[184] V. Gurarie, *"Single-particle Green's functions and interacting topological insulators"*, Physical Review B **83**, 085426 (2011).

[185] I. P. McCulloch, *"Infinite size density matrix renormalization group, revisited"*, arXiv e-prints arXiv:0804.2509(2008).

[186] M. P. Zaletel, R. S. K. Mong, and F. Pollmann, *"Topological Characterization of Fractional Quantum Hall Ground States from Microscopic Hamiltonians"*, Physical Review Letters **110**, 236801 (2013).

[187] F. Becca and S. Sorella, *Quantum Monte Carlo Approaches for Correlated Systems*. Cambridge University Press, nov 2017.

[188] M. Capello, F. Becca, M. Fabrizio, S. Sorella, and E. Tosatti, *"Variational Description of Mott Insulators"*, Physical Review Letters **94**, 026406 (2005).

[189] M. Capello, F. Becca, S. Yunoki, and S. Sorella, *"Unconventional metal-insulator transition in two dimensions"*, Physical Review B **73**, 245116 (2006).

[190] L. F. Tocchio, C. Gros, R. Valentí, and F. Becca, *"One-dimensional spin liquid, collinear, and spiral phases from uncoupled chains to the triangular lattice"*, Physical Review B **89**, 235107 (2014).

[191] F. Pollmann and A. M. Turner, *"Detection of symmetry-protected topological phases in one dimension"*, Physical Review B **86**, 125441 (2012).

[192] H. Yao and S. A. Kivelson, *"Fragile Mott Insulators"*, Physical Review Letters **105**, 166402 (2010).

[193] U. Schollwöck, *"The density-matrix renormalization group in the age of matrix product states"*, january 2011 Special Issue, , Annals of Physics **326**. 96–192 (2011).

[194] M. B. Hastings and T. Koma, *"Spectral Gap and Exponential Decay of Correlations"*, Communications in Mathematical Physics **265**, 781–804 (2006).

[195] H. Shapourian, K. Shiozaki, and S. Ryu, *"Many-Body Topological Invariants for Fermionic Symmetry-Protected Topological Phases"*, Phys. Rev. Lett. **118**, 216402 (2017).

[196] K. Shiozaki, H. Shapourian, and S. Ryu, *"Many-body topological invariants in fermionic symmetry-protected topological phases: Cases of point group symmetries"*, Phys. Rev. B **95**, 205139 (2017).

[197] Y. Fuji, F. Pollmann, and M. Oshikawa, *"Distinct Trivial Phases Protected by a Point-Group Symmetry in Quantum Spin Chains"*, Physical Review Letters **114**, 177204 (2015).

[198] D. Pesin and L. Balents, *"Mott physics and band topology in materials with strong spin–orbit interaction"*, Nature Physics **6**, 376–381 (2010).

[199] S. Johnson and J. Joannopoulos, *"Block-iterative frequency-domain methods for Maxwell's equations in a planewave basis"*, Optics Express **8**, 173 (2001).

[200] T.-J. Liu, M. A. Springer, N. Heinsdorf, A. Kuc, R. Valentí, and T. Heine, *"Semimetallic square-octagon two-dimensional polymer with high mobility"*, Physical Review B **104**, 205419 (2021).

[201] Y. Ishii, G. Sala, M. B. Stone, V. O. Garlea, S. Calder, J. Chen, H. K. Yoshida, S. Fukuoka, J. Yan, C. dela Cruz *et al.*, *"Magnetic properties of the Shastry-Sutherland lattice material $BaNd_2ZnO_5$"*, Physical Review Materials **5**, 064418 (2021).

[202] A. Yanase and H. Harima, *"Band Calculations on YbB_{12}, SmB_6 and CeNiSn"*, Progress of Theoretical Physics Supplement **108**, 19–25 (1992).

[203] S. R. White, *"Density-matrix algorithms for quantum renormalization groups"*, Physical Review B **48**, 10 345–10 356 (1993).

[204] J. Hauschild and F. Pollmann, *"Efficient numerical simulations with Tensor Networks: Tensor Network Python (TeNPy)"*, SciPost Physics Lecture Notes(2018).

[205] S. Sorella, *"Wave function optimization in the variational Monte Carlo method"*, Physical Review B **71**, 241103 (2005).

[206] R. P. Feynman, *"Atomic Theory of the Two-Fluid Model of Liquid Helium"*, Phys. Rev. **94**, 262–277 (1954).

[207] R. Resta and S. Sorella, *"Electron Localization in the Insulating State"*, Phys. Rev. Lett. **82**, 370–373 (1999).